Cool Stars and Contingencies: Stellar Characterisation in the Solar Neighbourhood

Adam D. Rains

A thesis submitted for the degree of
Doctor of Philosophy
of The Australian National University

Australian
National
University

July 2021

Declaration

I declare that the research presented in this thesis represents original work that I carried out during my candidature at the Australian National University, except for contributions to multi-author papers incorporated in the thesis where my contributions are specified in this Statement of Contribution.

- **A. D. Rains**, M. J. Ireland, T. R. White, L. Casagrande, I. Karovicova, 2020, *'Precision angular diameters for 16 southern stars with VLTI/PIONIER'*, MNRAS, 493, 2377

- **A. D. Rains**, M. Žerjal, M. J. Ireland, T. Nordlander, M. S. Bessell, L. Casagrande. C. A. Onken, M. Joyce, J. Kammerer, H. Abbot, 2021, *'Characterization of 93 Southern TESS Candidate Planet Hosts and a New Photometric [Fe/H] Relation for Cool Dwarfs'*, MNRAS, 504, 5788

For both these papers, I conducted all analysis, wrote the entirety of the text, and prepared all tables and figures. Additionally, for paper 2, I conducted most of the telescope observations using the ANU 2.3 m Telescope. For the first paper the only exceptions (unless otherwise stated in the text) were: initial target selection and some initial introductory text by Prof. Michael J. Ireland; and code to work with limb darkening coefficients from the STAGGER grid by Dr Timothy R. White. For the second, the only exceptions (unless otherwise stated in the text) were: MARCS model spectra and associated description text from Dr Thomas Nordlander; *SkyMapper* target crossmatching by Dr Chris A. Onken; data reduction pipeline development by Dr Marusa Zerjal; and observations by Dr Maruša Žerjal, Jens Kammerer, and Harrison Abbot. All co-authors reviewed the papers, gave advice, answered questions, and participated generally in discussions and planning.

Chapter 3 documents the FunnelWeb Survey as it was originally planned prior to its cancellation in November 2019. My key contribution was on the development and testing of a FunnelWeb specific sky tiling algorithm based on code originally developed for the Taipan Survey by Dr Marc White. I was also involved in survey observing strategy discussions, particularly where it related to tiling. Other than text describing the TAIPAN instrument, originally written by Dr. Kyler Kuehn, I prepared all text, figures (barring Figure 3.3, which was prepared by Prof. Michael J. Ireland), and tables unless otherwise stated in the text.

I also made contributions to the following articles during the course of my candidature:

- M. Žerjal, **A. D. Rains**, M. J. Ireland, G. Zhou, J. Kammerer, A. Wallace, B. J. Orenstein, T. Nordlander, H. Abbot, S. Chang, 2021, *'A spectroscopically confirmed Gaia-selected sample of 318 new young stars within ~200 pc'*, MNRAS, 503, 938

- L. Casagrande, J. Lin, **A. D. Rains**, F. Liu, S. Buder, J. Horner, M. Asplund, G. F. Lewis, S. L. Martell, T. Nordlander, D. Stello, Y. -S. Ting, R. Wittenmyer, J. Bland-Hawthorn, A. R. Casey, G. M. De Silva, V. D'Orazi, K. C. Freeman, M. R. Hayden, J. Kos, K. Lind, K. J. Schlesinger, S. Sharma, J. D. Simpson, D. B. Zucker, T. Zwitter, 2020, *'Effective temperature calibration from the InfraRed Flux Method in the Gaia system'*, (submitted.), arXiv:2011.02517

- T. R. Bedding, S. J. Murphy, D. R. Hey, D. Huber, T. Li, B. Smalley, D. Stello, T. R. White, W. H. Ball, W. J. Chaplin, I. L. Colman, J. Fuller, E. Gaidos, D. R. Harbeck, J. J. Hermes, D. L. Holdsworth, G. Li, Y. Li, A. W. Mann, D. R. Reese, S. Sekaran, J. Yu, V. Antoci, C. Bergmann, T. M. Brown, A. W. Howard, M. J. Ireland, H. Isaacson, J. M. Jenkins, H. Kjeldsen, C. McCully, M. Rabus, **A. D. Rains**, G. R. Ricker, C. G. Tinney, R. K. Vanderspek, 2020, *'Very regular high-frequency pulsation modes in young intermediate-mass stars'*, Nature, 581, 7807, 147

For the first of these I substantially contributed to telescope observations, data reduction, and data reduction pipeline development. For the second, I tested the developed relations against cool dwarf benchmarks. For the third, I contributed to telescope observations.

Adam D. Rains
12th July, 2021

Abstract

The coming decades will see stellar parameters like temperature, radius, and metallicity produced for many millions of new stars as part of both current and upcoming massive stellar surveys. However, for any new insights into stellar or Galactic physics to reach their full potential, these parameters need to be calibrated by a library of benchmark stars whose properties are as fundamental and model independent as possible. Thus was the motivation for my PhD work as presented here: to extend the currently available library of stellar standards, and to use this library as part of the calibration strategy for upcoming stellar spectroscopic surveys.

For stellar temperature and radius, there is nothing more accurate or precise than when these properties are calculated from the angular diameters measured by long-baseline optical interferometry. Using VLTI/PIONIER, I inducted a new set of 10 stars into the ranks of stellar benchmarks, and confirmed another six with higher precision than ever before. These results, precise to the 1% level, will serve as critical benchmarks for all current and future surveys in Galactic archaeology.

One such survey was the planned FunnelWeb Survey. A low resolution spectroscopic survey of two million of the brightest stars in the southern hemisphere, FunnelWeb was built around the novel TAIPAN instrument and its ability to rapidly reconfigure its 150 optical fibres in parallel. This high-multiplex capability and broad range in targeted magnitudes combined to provide unique challenges in optimising survey efficiency and yield. Here I present a sky tiling algorithm for this class of survey, including a six step priority scale and overlapping magnitude bins, able to efficiently allocate observing fields to a high level of survey completeness.

A more traditional survey involves observing stars one at a time using a high efficiency spectrograph with greater resolving power. WiFeS on the ANU 2.3 m Telescope is one such instrument, and is well suited to a survey of exoplanet host stars identified by NASA's TESS Mission. The result was the spectroscopic characterisation of 92 cool dwarfs and transit light curve modelling of 100 planet candidates. Given known complexities modelling cool dwarf atmospheres, I quantified model deficiencies at predicting optical fluxes, and developed an empirical photometric relation to determine cool dwarf metallicity independently of spectroscopy. This large and uniform sample will prove instrumental to future demographic studies of planets around cool dwarfs—a historically small, but now rapidly growing sample thanks to TESS.

My PhD research has provided new insight into the stars and planets of the Solar Neighbourhood and improved our ability to calibrate broader surveys of our Galaxy as a whole. While I have demonstrated the strength of tried and tested methods, my work has made apparent the need for non-traditional analysis techniques for dealing with challenging regions of the parameter space—techniques that should be well suited to the data-rich environment stellar astronomers will soon find themselves in.

Acknowledgements

"Was he leaving home, or going home?"

Ursula K. Le Guin, *City of Illusions*

I leave my PhD a better researcher, a more effective communicator, and generally a better person due in no small part to the many people I'm about to thank. I didn't really have the best idea of who I was or what I wanted to do with myself when I started in 2017, but the past four and a half years have given me some much more satisfactory answers to those questions.

Firstly, I'd like to thank my supervisors and close collaborators, without whom none of this would have been possible: Mike Ireland for setting high research standards and for always helping me to see the big picture; Luca Casagrande for the support and photometric wizardry; Mike Bessell for the helpful observing tips and being a fount of knowledge on both the science and history of cool dwarfs; Maruša Žerjal for the frequent mutual commiserations and the stellar surveys we invented along the way; Tim White for helpfully sharing the highs—and lows—of optical interferometry; and Thomas Nordlander for the theoretical perspectives on all things spectra. Together you somehow managed to impart a modicum of stellar astrophysics knowledge and academic rigour to this now thoroughly reformed engineer.

At the start of my masters degree in 2015 I certainly did not foresee the full implications of my decision to become involved with the Mount Stromlo Observatory outreach program—especially as someone who had never before given a presentation without reading from a *literal* script. While I wasn't particularly involved during my masters, I really fell headfirst into the waters of outreach and science communication in 2017. Nearly four and a half years later and I'm currently the most senior student member of MSO's outreach program, have been involved in more than 170 outreach events, find myself a mentor to newer outreachers, and serve on the ACT coordinating committee for National Science Week. I'd like to specifically thank Brad Tucker and Brittany Carter for the encouragement, support, and opportunities. Without you, I would not be a science communicator—something that has given a not–insubstantial amount of meaning to my non–PhD hours. Thanks as well to the many others who have been part of the outreach program over the years whom I have learnt a great deal from.

Thanks to the rotating roster of people I've had the pleasure of calling officemates during my PhD: Rajika Kuruwita, Adam Thomas, Eloise Birchall, Matthew Alger, and Lara Cullinane. Be it friendly chats, soliciting advice, rubber ducking, venting, or just silly office in–jokes, I've greatly appreciated and benefited from your company over the years.

Turns out other offices played host to some alright people over the years too, people whom I have enjoyed sharing many a lunch table, meeting room, or hallway chat with. In alphabetical, but probably not exhaustive, order: Harrison Abbot, Ayan Acharyya, Dilyar Barat, Joao Bento, Tim Crundall, Natalia Eiré Sommer, Isabella Gerrard, Jonah Hansen, Meridith Joyce,

Jens Kammerer, Umang Malik, Sarah McIntyre, Madeleine McKenzie, Rajsekhar Mohapatra, Stephanie Monty, Karlie Noon, Wei Shen Oh, Fiona Panther, Ryan Ridden-Harper, Matt Roth, Piyush Sharda, Jamie Soon, Margaret Streamer, Georgina Taylor, Philip Taylor, Alec Thomson, Alex Wallace, Ella Wang, Haiyang Wang, and Henry Zovaro. Thanks as well to Michelle Cicolini and Howard Coyle for, quite frankly, keeping the school running.

I appear to be a bit of an anomaly in that I've managed to live in the same house for the entire duration of my studies in Canberra, but that doesn't mean I don't have more than a single house worth of people to thank for being housemates over that time. Thanks to Rajika Kuruwita, Joao Bento, Jesse Pratt, Dylan Porter, and Marc Carlton for making my home life both pleasant and stable—hope I didn't monopolise the kitchen *too* much.

Thanks to my regular–until–the–pandemic–deemed–otherwise tabletop RPG group: Byron Williams, Georgia-Cate Westcott, Connor Gourlay, and Alex Dullow. Bonus thanks to Byron, as well as Morgan Smith and Paul McKibbin, for being my MIGW and PAX buddies many years running. Thanks to Elizabeth Whitty for the (often long) chats about life and research.

Thanks to my friends and family back home in Queensland for giving me somewhere warm and sociable to flee to and (usually) forget about astronomy for a while: Louisa Rains, Frank Rains, Ryan Rains, Liam Rains, Piper Rains, Jesse Browning, Matthew Hurley, Amber Hurley, Sam Hooper, and Marcus Hooper. Now that there are a few little ones in the mix or on the way, I'm keen to eventually play Science Uncle. Thanks as well to my friends abroad in Nicole Davis and Chani Nava for the regular chats and trans–Pacific support.

Finally, special thanks to my good friends Philip Taylor and Eloise Birchall for the endless support. They always do helpful things like 'offer sound life advice', 'read thesis drafts and provide extensive comments', and 'insist I take care of my mental health'—all of which I genuinely appreciate and have proven immensely helpful over the years.

Anyway, enjoy the thesis I guess!

This PhD was completed primarily at Mount Stromlo Observatory in the Australian Capital Territory, the land of the Ngunnawal and Ngambri peoples. Siding Spring Observatory in New South Wales, the site of the ANU 2.3 m and Anglo–Australian Telescopes, is the land of the Gamilaraay people. I would like to acknowledge and celebrate the traditional custodians of these lands, the first astronomers, and pay my respects to elders both past and present. Sovereignty was never ceded.

Contents

List of Figures

List of Tables

Chapter 1

Introduction

There is much to consider when one sets out with the goal of determining precise and accurate stellar properties. This is especially true in the knowledge that the most fundamental of these properties—mass, age, and chemical composition—are also the *most difficult* to determine. From this starting point, a number of questions naturally arise. Firstly, one could ask, what *are* these properties, and how might we observe or model them? How are we currently limited in our understanding or capability to answer this question? Can we know some stars better than others, and if so can they be used as reference objects to calibrate against? The Galaxy is large, so how best to study stars at scale? And, finally, how does our understanding of these stars relate to any planets they might host?

This PhD, over three separate but interconnected projects, touches on each of these broad questions. Such a wide array of questions posed necessitates breadth in introductory content, with this chapter structured as follows: Section 1.1 introduces the fundamental properties of stars and how astronomers measure them; Section 1.2 gives an overview of some of the prominent gaps currently limiting our understanding of the stars; Section 1.3 outlines the importance of stellar benchmarks, particularly in light of certain gaps in our knowledge; Section 1.4 broadly summarises the current state of observational stellar astrophysics from the perspective of current and upcoming massive surveys; Section 1.5 links stellar astrophysics to that of its exoplanetary counterpart, giving particular attention to exoplanet demographics by way of transiting planet surveys; Section 1.6 presents an outline of the thesis as whole; and Section 1.7 lists the key contributions of this thesis to stellar and exoplanetary astrophysics.

1.1 The Fundamental Properties of Stars

The most fundamental properties of a star are its mass, age, *intrinsic* chemical composition, and rotational velocity[1]. A star of a given mass, age, intrinsic chemical composition, and rotational velocity will then have a given radius, temperature, surface gravity, *atmospheric* chemical composition, and luminosity. These are all more directly observable quantities, but our ability to measure them is modulated by the star's position in the Galaxy and composition of the intervening gas and dust—more distant and the star will appear fainter, too much dust and the star will appear redder as the dust selectively scatters blue light. Further uncertainties

[1]Discussed here in the context of determining stellar ages through *gyrochronology*.

are introduced here on Earth by our atmosphere, telescopes, and instrumentation, as well as any limitations in available computational resources or our current understanding of physics.

With that in mind, this section serves to provide a broad overview of the multitude of methods at our disposal to determine the fundamental properties of stars. We start with stellar mass, $M_\star$, in Section 1.1.1; followed by age in Section 1.1.2; temperature, $T_{\rm eff}$, in Section 1.1.3; flux and luminosity, $L_\star$, in Section 1.1.4; radius, $R_\star$, in Section 1.1.5; surface gravity, $\log g$, in Section 1.1.6; before finishing with chemistry and metallicity, [Fe/H][2] in Section 1.1.7.

1.1.1 Mass

The mass of a star is its most fundamental property. While chemistry modulates stellar evolution, it is the mass that ultimately dictates how a star will evolve and how spectacular the end of its life will be. Determining the masses of stars is critical to understanding them—both individually, and in aggregate. Following is a brief summary of the various techniques used to determine stellar mass, noting that only the first—dynamical masses from binaries or disks—is a fundamental technique. For a much more thorough overview on mass determination, see the review by Serenelli et al. (2021). For an overview of the stellar Initial Mass Function (IMF)—the relative number of stars formed as a function of stellar mass—see Bastian et al. (2010).

Taking a step back first, it is useful to go over a few of the basics of stellar evolution for intermediate-mass ($\sim 1.25 - 3\,M_\odot$), low-mass ($\sim 0.4 - 1.25\,M_\odot$) and very-low mass ($\lesssim 0.4\,M_\odot$) stars. For the purpose of our discussion here, we consider three major phases to the life-cycle of a star. The first is the pre-main sequence, which occurs while a star is still undergoing gravitational contraction and has yet to begin fusing hydrogen into helium within its core. The second is the main sequence, where hydrogen burning begins and where a star will spend most of its life—anywhere from a few billion years for the largest of intermediate-mass stars, to longer than the current age of the Universe for the smallest very low-mass stars. The third is the post-main sequence—a broad category for everything that happens after a star reaches the main sequence turn-off, runs out of hydrogen to burn in its core, and begins fusing hydrogen around its inert helium core. During this time, the star will gradually increase in luminosity and radius as it moves through the sub-giant and giant branches, with the largest able to eventually initiate the fusion of helium, before ending their lives as a white dwarf. For more detail, see Kippenhahn et al. (2012).

Figure 1.1 (top) shows the theoretical path pre-main sequence stars take during their mass-dependent contraction to the main sequence. The near-vertical tracks are known as Hayashi Tracks (Hayashi 1961) and dominate the pre-main sequence of the lowest mass stars. These merge into the more diagonal or even horizontal evolution of Henyey tracks (Henyey et al. 1955) for those stars larger than $\sim 0.5\,M_\odot$, and dominate pre-main sequence evolution for stars above $\sim 3\,M_\odot$. Figure 1.1 (bottom) shows the evolution of stars from the zero-age main sequence through main sequence and post main sequence.

[2]Note that throughout this document 'metallicity' will be used interchangeably with [Fe/H]—the logarithmic iron abundance—where the square bracket notation indicates that the abundance has been scaled by the Solar value (i.e. [Fe/H] = 0 is Solar). [Fe/H] is a common proxy for the actual metallicity [M/H] in stellar astrophysics.

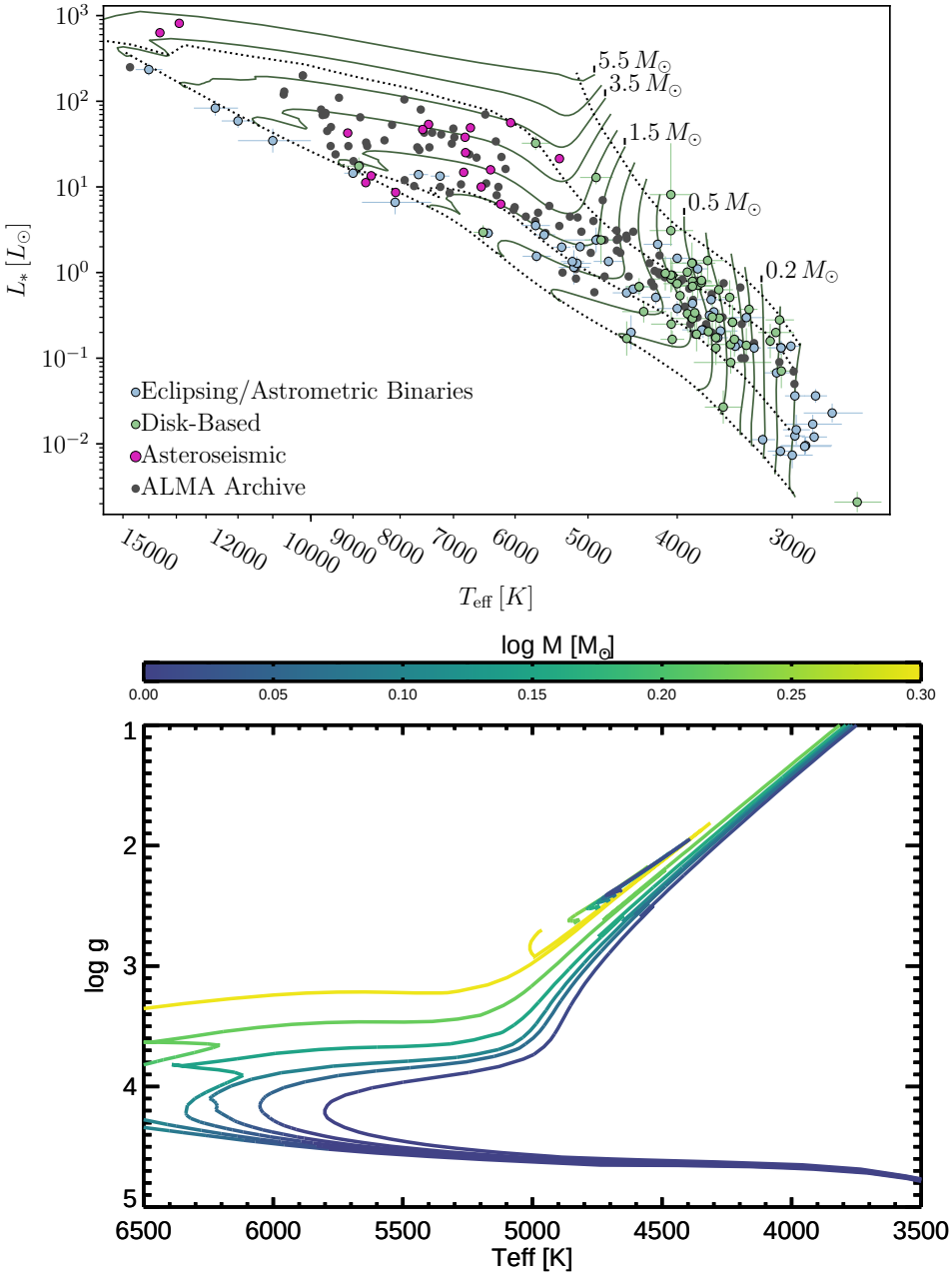

Figure 1.1: Pre- and post-main sequence stellar evolution for stars of different masses, both reproduced from Serenelli et al. (2021). **Top:** Pre-main sequence theoretical evolutionary tracks (MIST, Choi et al. 2016) in $L_\star$ as a function of $T_{\rm eff}$, with observed benchmark masses overplotted. The black dotted lines are isochrones at ages 0.1, 1, 10, and 100 Myr, with only 0.1 – 10 Myr plotted for the highest masses. Note that the lowest mass stars descend almost vertically to the main sequence via Hayashi Tracks (Hayashi 1961), whereas higher mass stars reach the main sequence sooner following a combination of Hayashi and Henyey Tracks (Henyey et al. 1955). **Bottom:** Post-main sequence stellar evolution shown using PARSEC isochrones (Bressan et al. 2012) for tracks of constant age. Note that as higher mass stars age, they become more luminous (corresponding to *lower* $\log g$) and ascend the red giant branch, whilst their lower mass counterparts do not appreciably change on the same timescales.

Dynamical Masses

Binary systems are the source of the most precise fundamental stellar mass measurements. The reason for this is that an object's gravity is the only way—short of tallying its every constituent particle—to probe its mass, and this is unobservable for single stars. Binary stars on the other hand each orbit their common centre of mass, making their masses directly observable through their Keplerian orbits. This requires us to be able to measure the velocities of each stellar component, however, most binary systems are not aligned edge-on to our telescopes. Radial velocity (RV) measurements are only able to measure the line of sight component of the true velocity, so for all non-edge-on systems only the *minimum* mass, modulated by the orbital inclination, can be determined spectroscopically.

This is not so for the most useful binary systems, the so-called 'double-lined eclipsing binaries'. For these systems, spectral features from *both* stars can be seen in their combined spectrum for radial velocity analysis, and not only must their inclination be near-edge-on to transit, but the precise inclination can be determined via a transit light curve analysis. A joint analysis of both sets of observations allows for tight constraints on *absolute* stellar masses and radii, temperatures, and the system geometry. There are many specific examples of this at a variety of masses and ages, particularly for low-mass stars which have historically challenged models (e.g. Torres & Ribas 2002; Morales et al. 2009; Kraus et al. 2011; Murphy et al. 2020), but for complete reviews, see Andersen (1991) and Torres et al. (2010).

For resolved binaries however, it is possible to use other techniques to fully constrain binary orbits. These methods primarily rely on astrometry from high-spatial resolution instruments or techniques (e.g. Woitas et al. 2003; Dupuy et al. 2009; Köhler et al. 2012; Mann et al. 2019), perhaps including precision space-based astrometry (e.g. Söderhjelm 1999; Benedict et al. 2016) from the *Hubble Space Telescope*, or dedicated astrometric missions like *Hipparcos* (ESA 1997) or *Gaia* (Gaia Collaboration et al. 2016a).

Fundamental masses such as these are critical, as they can be used to develop empirical mass relations based on an easily observable property like luminosity, applicable to a wider sample of stars. For stars that evolve on moderate–to–fast timescales, however, any such relation must include the effect of age, resulting in a mass–luminosity–*age* relation. This is problematic as model–independent ages are incredibly difficult to determine for the vast majority of stars (see Section 1.1.2 for more information). The situation is very different however for the lowest mass stars with $M_\star \lesssim 0.7\,M_\odot$, which don't evolve on appreciable timescales once they arrive on the main sequence. This is shown in Figure 1.2, reproduced from Mann et al. (2019), which shows that these low-mass stars have negligible change in luminosity on Gyr timescales. Thus, at least for the accuracy currently available, these stars can be assumed to follow a more simple mass–luminosity relation[3], which allows for the development of broadly applicable empirical mass relations (e.g. Henry & McCarthy 1993; Delfosse et al. 2000; Benedict et al. 2016; Mann et al. 2019).

For young, disk-bearing stars, it is also possible to obtain dynamical masses, not from the orbit of a stellar companion, but by measuring and modelling rotation of gas in the disk

[3]With the influence of [Fe/H] consistent with zero, and the remaining $\simeq$ 2% scatter hypothesised to be the result of a missing parameter like age/activity/rotation or other elemental abundances, or possibly underestimated measurement uncertainties (Mann et al. 2019).

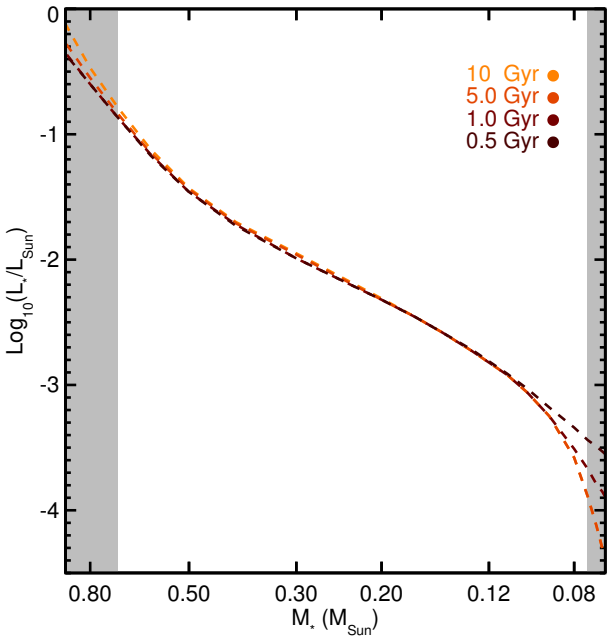

Figure 1.2: Cool dwarf $M_\star$ vs $L_\star$ relationship as a function of age, as reproduced from Mann et al. (2019) using models from Baraffe et al. (2015). Note that for stars with $0.1 \lesssim M_\star \lesssim 0.7\,M_\odot$, the stars do not appreciably age on timescales close to the age of the Universe. On long timescales, those stars more massive than this clearly show signs of evolution, whereas those less massive have a longer pre-main sequence lifetime, and may even be below the hydrogen burning limit and are thus brown dwarfs.

itself via millimetre-wave interferometry (e.g. Rosenfeld et al. 2012; Czekala et al. 2015, 2016, 2017; Simon et al. 2017). Whilst more model dependent than the work on binaries above, the technique does have the advantage of directly measuring the masses of *isolated* (i.e. not in binary systems) pre-main sequence stars.

Microlensing

Microlensing, the process whereby the gravity of a foreground object—typically a star, but also brown dwarfs and free-floating planets—temporarily 'lenses' and increases the brightness of a distant coincident background star, is able to measure the masses of isolated objects (e.g. Zhu et al. 2016; Chung et al. 2017; Shin et al. 2017). While the ability, in principle, to measure the mass of *any* isolated star is tremendously useful, microlensing events are the result of incredibly rare chance alignments, with the foreground object typically being too faint to easily follow-up.

Asteroseismology

Techniques to study stars can only observe their exteriors, leaving us blind to the complex physics occurring within. The sole exception to this asteroseismology[4]. Analogous to the study of

[4]Noting that neutrino astrophysics is currently only applicable to the Sun and other energetic sources like supernovae or blazars.

seismology here on the Earth, asteroseismology allows for the study of stellar interiors and densities as revealed through global stellar oscillations. This allows for determination of stellar properties like densities, masses, radii, and even stellar ages. As with exoplanetary astrophysics, to be discussed later, asteroseismology has benefited tremendously from the continuous time-series photometry from space-based missions like *CoRoT* (Auvergne et al. 2009), *Kepler* (Borucki et al. 2010), *K2* (Howell et al. 2014), and *TESS* (the Transiting Exoplanet Survey Satellite, Ricker et al. 2015). Prior to these missions, there were only a few tens of stars with asteroseismic properties—now there are thousands. For foundational reviews on the topics, see Christensen-Dalsgaard (1984), Brown & Gilliland (1994), and Christensen-Dalsgaard (2004). For more modern reviews post-*Kepler*, see Chaplin & Miglio (2013), Hekker & Christensen-Dalsgaard (2017), and García & Ballot (2019).

Asteroseismology involves studying the power spectrum distribution of stellar pulsations (e.g. Cox 1980; Unno 1989; Christensen-Dalsgaard 2002). These pulsations, and their various harmonics, can be classified as either pressure or acoustic modes at higher frequencies, gravity modes at lower frequencies, or mixed modes with properties of both. While detailed modelling to reproduce observed pulsation frequencies is the most accurate approach to determine stellar mass and radius, simpler empirical relations based on scaled Solar values can be used to great effect (e.g. García & Ballot 2019). At its most precise, asteroseismic masses can be precise to ∼4% (e.g Silva Aguirre et al. 2017), and have the strength of being much more widely applicable than dynamical masses which are limited to binary or disk-bearing stars.

Spectroscopic

Where dynamical masses rely on observing velocities or positions, and asteroseismic masses rely on the analysis of time series pulsations, there are spectroscopic techniques successfully benchmarked against their more fundamental counterparts. These include measurement of the precise shape of hydrogen lines in red giant stars for 10 – 15% precision in mass (Bergemann et al. 2016), measurement of photospheric carbon and nitrogen abundances in red giants to give ∼14% precision in mass (Martig et al. 2016; Ness et al. 2016), and measuring the lithium abundances of Solar twins—the depletion of which is strongly mass dependent (do Nascimento et al. 2009). While less precise than either dynamical or asteroseismic masses, these techniques can be more easily applied to fainter stars or in greater numbers, as they require only a single epoch medium–to–high resolution spectrum, rather than continuous monitoring.

Theoretical Stellar Evolution Models

The most model–dependent approach is fitting observed properties like temperature, luminosity, and [Fe/H] to theoretical models of stellar evolution (e.g. Edvardsson et al. 1993; Ng & Bertelli 1998; Pont & Eyer 2004; Berger et al. 2020). The most widely used models are one-dimensional, with some of the most common being: BaSTI (Bag of Stellar Tracks and Isochrones, Pietrinferni et al. 2004); the Y^2 isochrones (Yonsei-Yale, Demarque et al. 2004); the Victoria-Regina models (VandenBerg et al. 2006); DSEP (Dartmouth Stellar Evolution Database, Dotter et al. 2008); PARSEC (PAdova and TRieste Stellar Evolution Code, Bressan et al. 2012); and MESA (Modules for Experiments in Stellar Astrophysics, Paxton et al. 2010) and MIST (MESA Isochrones and Stellar Tracks, Dotter 2016). The input parameters for the

evolution of a single star are $M_\star$, the stellar mass; Z, the metal mass fraction; Y, the helium mass fraction; and the so called 'mixing length' parameter, used to parameterise stellar convection in 1D (see Section 1.2.1 for more information). These models are then run over evolutionary time scales, and at each time step the modelled star will have a given temperature, radius, surface gravity, luminosity, and set of surface abundances—all observable properties that can be used as constraints during fitting.

There are both theoretical and observational challenges to this technique however. On the theoretical side, we do not understand the physics driving all stars equally. For instance there are known issues reproducing the radii of low-mass stars, suspected to be the result of magnetic fields (see Section 1.2.2 for an overview). More generally, since fitting is typically done to observed values of temperature, metallicity, and luminosity (via an absolute magnitude), any uncertainties in determining these parameters will propagate to errors in the fitted mass or age. For stars outside of the Solar Neighbourhood, uncertainty in distance or interstellar extinction, as well as unresolved binarity, are further cause for concern. This is more fraught for the youngest of stars, which might be more active, still accreting, have disk emission, dust obscuration, or uncertain extinction—all resulting in uncertain luminosities and temperatures. Even with precise observational constraints, best results are only obtained for those stars that have begun to evolve off the main sequence, where the model tracks are not so closely packed (see Figure 1.1). Despite these caveats, the era of observational surveys makes these issues smaller than they ever were, and models continue to improve. See Section 5 of Serenelli et al. (2021) for more information.

1.1.2 Age

While mass is the more fundamental parameter, at least it has at least one method of directly observing it in other stars. There is no such luck with stellar age. There is but one fundamental technique—measuring the decay of long-lived isotopes—and it has the rather restrictive limitation of requiring rocky material to do so and thus is only applicable to the Sun. What is left are several semi-fundamental techniques, alongside model-dependent, empirical, and statistical approaches, noting that no single method is suitable for all ages or stellar masses. For a full review of these techniques, the interested reader should see the excellent reviews by Soderblom (2010) on general age determination, and Soderblom et al. (2014) for age determination specifically for young stars, whose hierarchy and grouping of techniques we adopt here.

Fundamental and Semi-Fundamental

Our only fundamental stellar dating technique, that is one where we understand all of the underlying physical process and have ample available data, is that of measuring the radioactive decay of long-lived isotopes. While recent years have given us two interstellar interlopers to the Solar System in the form of 'Oumuamua[5] (Meech et al. 2017) and 2I/Borisov[6] (Jewitt & Luu

[5] www.minorplanetcenter.net/mpec/K17/K17UI1.html
[6] www.minorplanetcenter.net/mpec/K19/K19RA6.html

2019), we cannot sample material orbiting arbitrary stars in the Galaxy, leaving this technique solely applicable to the Sun.

The first semi-fundamental technique is nucleocosmochronometry, which concerns itself with measuring the decay of uranium or thorium in high signal-to-noise ratio (SNR) spectra of individual stars. Although distance independent and based on well-understood physics, the technique is really only applicable to metal-poor stars where the atomic lines of interest are unblended. See the review by Cowan et al. (1991).

Kinematic ages are another semi-fundamental technique, applicable to young groups of stars born from the same cluster. Stars are born together in clusters and over time, influenced by their initial velocities and the Galactic potential, they disperse. Under the assumption that the birth of the cluster corresponds to when it is smallest in volume, given the present-day positions and velocities of a set of stars, their orbits can be traced back in time (e.g. Makarov 2007; Fernández et al. 2008; Gagné et al. 2018; Crundall et al. 2019). Beyond this core assumption, there are few others, and the technique has the strength of being model independent. Historically a key difficulty was the limited number of stars with good quality parallaxes and radial velocities, though the *Gaia* Mission has effectively solved this problem (Gaia Collaboration et al. 2016b; Brown et al. 2018, 2021).

The Lithium Depletion Boundary (LDB) is the final semi-fundamental technique, applicable for young clusters 20-200 Myr old. Pre-main sequence stars see their core temperature rise as they continue to contract, eventually reaching the threshold (~3 million K) beyond which they are able to burn (and thus deplete) lithium (e.g. Chabrier et al. 1996). This depletion occurs on a mass-dependent timescale, the physics of which is well-understood and insensitive to various physical and modelling parameters (Burke et al. 2004). When observing a cluster, it is thus possible to see a luminosity boundary separating the stars with detectable lithium versus those without. It is important to note that this technique does not require measuring the *abundance* of lithium, as will be discussed later, only *detecting* lithium within an order of magnitude in abundance. The main limitations of the technique are that it can only be applied to stellar clusters, and the fact that the age range probed does not go past the zero age main sequence (ZAMS) or currently cover the ages of nearby star-forming regions—all of which which would require prohibitively long observations of faint stars using current 8–10 m telescopes.

Model-dependent

While we can determine model-based ages for single stars using the same approach outlined in Section 1.1.1, this ultimately amounts to fitting a single data point. Better results are achieved—and more stringent tests on models applied—when fitting for the age of a coeval group of stars spanning a range of stellar masses, but importantly sharing only a single age and chemical composition. At its simplest this could be any binary system, but is also applicable to clusters of stars. For excellent summaries, see Sections 8.4 and 9.0 respectively in Soderblom (2010).

Returning once more to asteroseismology (for an introduction, see Section 1.1.1), its insight into stellar interiors can be leveraged to determine stellar ages (e.g. Christensen-Dalsgaard 1984; Ulrich 1986; Otí Floranes et al. 2005; Mazumdar 2005; Lebreton & Montalbán 2009) or evolutionary state (e.g. Bedding et al. 2011, who used asteroseismology to distinguish between hydrogen and helium burning red giants). While mass and radius can be determined using

the global seismic properties as part of scaling relations, more detailed modelling is typically required to determine the age of a star. This takes the form of extracting and modelling the full spectrum of various oscillation modes, and involves coupling stellar evolution models to models of stellar pulsations. An excellent summary and comparison of various modelling pipelines can be seen in in Silva Aguirre et al. (2017), who cite an average uncertainty in age of 10%. While these ages are likely better than those from other techniques, they share the same limitations and sensitivity to input physics as isochrone fitting. As before, see the reviews by Chaplin & Miglio (2013), Hekker & Christensen-Dalsgaard (2017), and García & Ballot (2019) for more information.

Empirical and Statistical

Empirical methods are typically calibrated to the model-dependent ages from clusters using relatively easily observed properties. Gyrochronology is the first and, as the name implies, is the relationship between stellar rotation and age. Challenges with this technique include measuring rotation for stars without prominent rotation signatures; stars with differential rotation at different stellar latitudes; and observed scatter both within a cluster of stars the same age, and between clusters of similar ages. For details, see Barnes (2007) and Mamajek & Hillenbrand (2008) for calibrations between rotation, age, and colour. For more general reviews on the rotational evolution of stars, see Barnes (2009), Irwin & Bouvier (2009), and Mamajek (2009).

The second empirical method to be discussed are age-activity relations. Activity in this case refers to stellar emission, such as optical chromospheric emission from the Ca II H and K resonance lines and Hα from the hydrogen Balmer series (e.g. Lyra 2005; Herbig 1985), ultra-violet chromospheric emission from Mg II hk lines (e.g. Cardini & Cassatella 2007), and coronal emission in the form of soft x-rays (e.g. Güdel et al. 1997)—the latter two not observable from the ground. Of these, Ca II H and K emission has been the most well studied, in large part due to long term monitoring at Mount Wilson, California, USA (Noyes et al. 1984; Baliunas et al. 1995). The principle advantage of Ca II activity measures are that they are easy to obtain from ground-based low-resolution spectra, and while there is some variation with activity, the trend with age is typically stronger. Concerns include how these measures are affected by stellar rotation or metallicity.

Finally, measurement of the stellar lithium abundance is the single star equivalent of measuring the lithium depletion boundary of a cluster. While the lithium 6 708 Å feature is readily apparent in medium-resolution spectra, line formation is highly sensitive to temperature, non-local thermodynamic equilibrium (non-LTE)[7] effects (Lind et al. 2009), and potentially also rotation or starspots (Soderblom et al. 1993)—thus introducing much greater model-dependency and uncertainty than for the lithium depletion boundary technique.

1.1.3 Temperature

The atmospheric temperature of a star is one of the simpler stellar properties to determine, but is not without its challenges. Our historical understanding of stellar temperatures was initially not

[7]Where 'LTE', local thermodynamic equilibrium, is a simplifying assumption made in most model 1D model atmospheres. See Section 1.2.4 for an overview.

as a continuous physical property, but as a number of discrete classes and subclasses in the form of the spectral type system—OBAFGKM[8](LTY)[9]. Each of these subclasses is typically defined by a set of so called spectral type standards and the strength of their particular spectroscopic features (e.g. the strength of TiO features in stars of spectral class K and M).

A set of optical spectra for main sequence stars (i.e. those stars fusing hydrogen in their cores) can be seen in Figure 1.3, covering almost the entire spectral sequence from O through M—or roughly a factor of 10 in temperature. One can see two main ways temperature affects stellar spectra. The first is the overall shape of the spectrum, particularly where the peak of stellar flux occurs—not displayed for the hottest and coolest stars, being in the ultraviolet (UV) and infrared (IR) respectively. The second is the intensity of atomic or molecular absorption features—many of which are sensitive to temperature. The selected temperature determination methods to be discussed below can be based on either—or even both—of these features.

Optical Interferometry

Most of stellar astrophysics is done without ever actually resolving the stars you observe. The reason for this is entirely understandable of course: even the closest stars are phenomenally distant, which renders all but a select few stars point sources. The implication however is clear: in most cases, the size of a star is not a directly measured property. Enter interferometry.

The resolution of a single-dish telescope is set by the diameter of its primary mirror and the wavelength at which it observes. Large telescopes, however, are both costly and technically challenging to build, and require adaptive optics to overcome the blurring effect imposed by atmospheric turbulence (known as *seeing*). An interferometer on the other hand draws its resolution from the separations (known as *baselines*) between the various telescopes in its array—perhaps hundreds of metres distant. Whilst the process of combining this light is a highly non-trivial active process (requiring the constant modulation of path lengths), the result is that resolution is now decoupled from both telescope size and atmospheric seeing, and is typically at least an order of magnitude better than even the largest single-dish telescopes. Thus, while most stellar observations see their stars only as point sources, optical interferometry is critically able to resolve the angular size of its targets.

At the time of writing, it has now been a century since the first angular diameter was measured using interferometry—Betelgeuse, or α Orionis, measured by Albert Michelson and Francis Pease in 1921 using the 100 inch reflector at Mount Wilson Observatory, California, USA (Michelson & Pease 1921). To this day Mount Wilson continues to have a strong tradition of optical interferometry with the CHARA Array (Centre for High-Angular Resolution Astronomy), where long term programs exist to calibrate the temperature scale of dwarf stars (e.g. Boyajian et al. 2012a,b, 2013, 2014), verify the results from asteroseismology (e.g. Huber et al. 2012; White et al. 2013), and characterise exoplanet host stars (e.g. Baines et al. 2009; von Braun et al. 2011, 2014; White et al. 2018). Other stellar diameter work has been done at PTI, the Palomar Testbed Interferometer at Palomar Observatory, California, USA (e.g. van Belle

[8]Ideally known by a whimsical and self-deprecating mnemonic like *Only Boring Astronomers Find Gratitude Knowing Mnemonics*, and not the sexist one you were likely taught.

[9]Where L, T, and Y spectral types refer to substellar objects—brown dwarfs—not undergoing nuclear fusion, the first confirmed discoveries of which were only in 1995 (Rebolo et al. 1995; Nakajima et al. 1995).

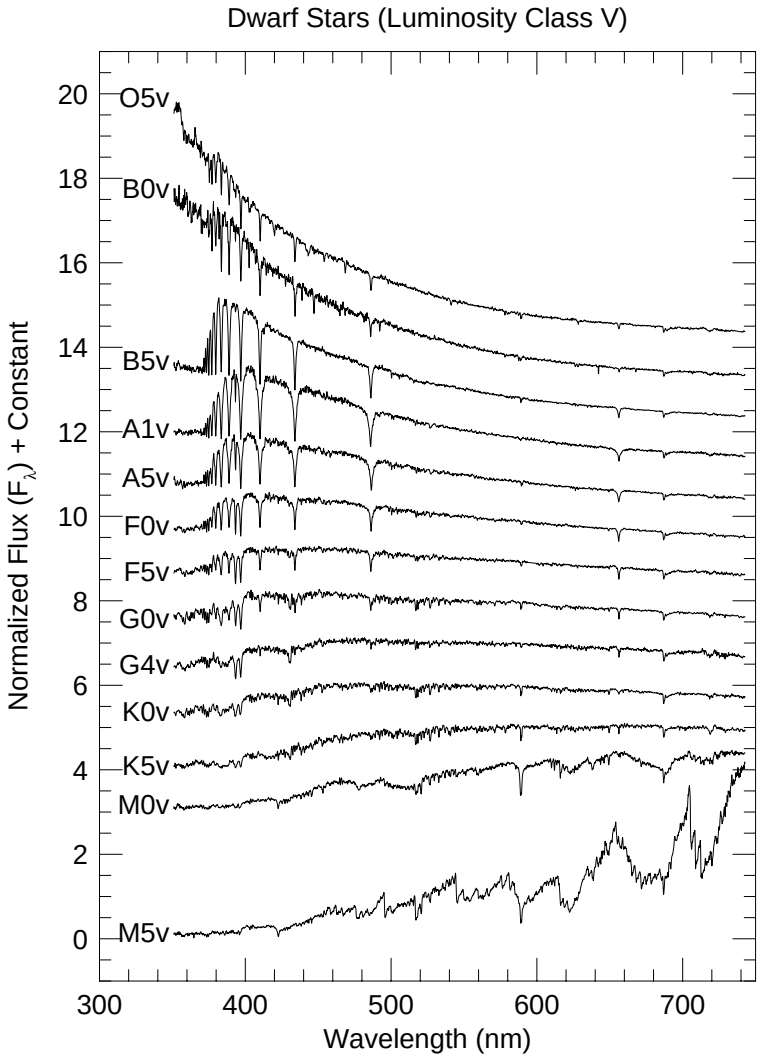

Figure 1.3: Spectra of dwarf stars, O through M, as reproduced from astronomy lecture material by Richard Pogge using spectra from Jacoby et al. (1984). Note that hotter stars emit more light at shorter wavelengths, cooler stars at redder wavelengths, and that the very coolest stars become dominated by intense molecular absorption. These spectral types have the following $T_{\rm eff}$ per the temperature sequence by Pecaut & Mamajek (2013): O5V ~41 400 K; B0V ~31 400 K; B5V ~15 700 K; A1V ~9 300 K; A5V ~8 100 K; F0V ~7 220 ; F5V ~6 550 K; G0V ~5 930 K; G4V ~5 680 K; K0V ~5 270 K; K5V ~4 440 K; M0V ~3 850 K; M5V ~3 060 K.

& von Braun 2009; van Belle et al. 1999); NPOI, the Navy Precision Optical Interferometer[10] in Flagstaff, Arizona, USA (e.g. Baines et al. 2018); SUSI, the Sydney University Stellar Interferometer at Narrabri Observatory, New South Wales, Australia (Davis et al. 1999); and—perhaps most critically for present day optical interferometry in the Southern Hemisphere—the VLTI, the Very Large Telescope Interferometer at Paranal Observatory, Antofagasta Region,

[10]Note that this facility was originally known as the Navy Prototype Optical Interferometer (NPOI), and also briefly the Navy Optical Interferometer (NOI)

Chile (Haguenauer et al. 2010).

Whilst it may seem strange to begin a section on stellar temperature by discussing size and spatial resolution at length, it is critical to understanding how we actually define and benchmark the temperatures of stars. When we refer to the temperature of a star, we are typically talking about what is known as the *effective temperature*, $T_{\rm eff}$. The effective temperature of a star is the temperature at which a black body of the same size would radiate the same amount of energy. This can be formulated as:

$$T_{\rm eff} = \left(\frac{L_\star}{4\pi\sigma R_\star^2} \right)^{1/4} \tag{1.1}$$

where $T_{\rm eff}$ is the effective temperature of the star, $L_\star$ is the stellar luminosity, $R_\star$ is the stellar radius, and σ is the Stefan-Boltzmann constant. Formulating it this way though has the downside of introducing a dependence on distance, which is required to measure the physical radius. Reformulating in terms of the angular diameter and observed stellar flux, rather than absolute luminosity, results in the following:

$$T_{\rm eff} = \left(\frac{4 f_{\rm bol}}{\sigma {\theta_{\rm LD}}^2} \right)^{1/4} \tag{1.2}$$

where $f_{\rm bol}$ is the bolometric stellar flux (i.e. the total flux received at Earth) and $\theta_{\rm LD}$ is the limb-darkened[11] angular diameter of the star. Both these terms can be determined relatively independently of models, thus demonstrating the key strength of optical interferometry to produce near-model-independent values of $T_{\rm eff}$. As such, interferometric temperatures form the foundation of the stellar temperature scale, with their role as benchmarks discussed in Section 1.3.

The Infrared Flux Method

The second most precise method of determining $T_{\rm eff}$ was developed in the late 1970s (Blackwell & Shallis 1977; Blackwell et al. 1979, 1980) and is known as the InfraRed Flux Method (IRFM). As its name implies, the IRFM works with near-infrared (NIR) photometry, typically in the *2MASS* (Skrutskie et al. 2006) J, H, and K_S bands, the prevalence of which enables it to be applied to far larger samples of stars than are accessible to interferometry. The basis of the method is the following relationship:

$$\frac{\mathcal{F}_{\rm Bol}({\rm Earth})}{\mathcal{F}_{\lambda_{\rm IR}}({\rm Earth})} = \frac{\sigma T_{\rm eff}^4}{\mathcal{F}_{\lambda_{\rm IR}}(T_{\rm eff}, \log g, [{\rm Fe/H}])} \tag{1.3}$$

where $\mathcal{F}_{\rm Bol}({\rm Earth})$ is the observed *bolometric* flux and $\mathcal{F}_{\lambda_{\rm IR}}({\rm Earth})$ is the observed infrared *monochromatic* flux—both measured at the top of Earth's atmosphere, $\sigma T_{\rm eff}^4$ is the surface bolometric flux, and $\mathcal{F}_{\lambda_{\rm IR}}(T_{\rm eff}, \log g, [{\rm Fe/H}])$ is the model surface infrared monochromatic flux as a function of the stellar temperature ($T_{\rm eff}$), surface gravity ($\log g$), and metallicity ([Fe/H]).

[11] Limb darkening is the wavelength–dependent phenomenon where the centre of the stellar disk is brighter than the edge (or 'limb'). This is the result of an observer seeing the deeper and warmer layers of the star when looking straight on, but only the cooler surface layers when looking towards the limb. Critically for our discussion here, it affects how stellar flux relates to angular diameter.

By using a relationship based on the *ratios* of bolometric to monochromatic observed and surface fluxes, the dependence on stellar angular diameter is removed—thus obviating the need to resolve the star as in interferometry.

While the final term, $\mathcal{F}_{\lambda_{\rm IR}}(T_{\rm eff}, \log g, [{\rm Fe/H}])$, is based on synthetic spectra interpolated to the given stellar parameters, it is only weakly model dependent. The reason for this is that for stars warmer than ∼4 200 K, wavelengths longer than ∼1.2 μm sample the Rayleigh-Jeans tail of the spectral energy distribution. This region is overwhelmingly dominated by the smooth spectral continuum, and as a result is mostly independent of $\log g$ and [Fe/H], and only linearly dependent on $T_{\rm eff}$. It is important to note, however, that for stars *cooler* than ∼4 200 K, this is no longer true, and chemical effects become much more pronounced.

This insensitivity to the effects of gravity or metallicity means that the technique is widely applicable to large samples of stars, with the core uncertainty being interstellar reddening (e.g. Bell & Gustafsson 1989; Alonso et al. 1996; Casagrande et al. 2006; Ramírez & Meléndez 2005; González Hernández & Bonifacio 2009; Casagrande et al. 2010, 2020). Modern $T_{\rm eff}$ scales are thus made by benchmarking IRFM temperatures against those from interferometry, which generally show a high level of consistency (e.g. Casagrande et al. 2014).

Spectral Types and Spectral Features

The two methods of temperature determination discussed so far rely on stellar fluxes, and not individual spectral features like atomic or molecular lines. Line formation, however, is a temperature sensitive process, and there exist a bevy of spectroscopic techniques for $T_{\rm eff}$ determination. While the spectral features in question are often easy to observe—even at low or moderate resolutions—line formation is a complicated process depending on temperature, pressure, chemistry, and stellar rotation. Given this complexity, measurements often have the downside of introducing additional degeneracies or model dependencies. As such, temperatures obtained from these techniques must be benchmarked against their more fundamental interferometric or IRFM counterparts. Whilst that is a significant downside, these techniques are less sensitive to the effect of interstellar reddening, which strongly affects the photometry used to determine stellar fluxes.

The first of these techniques is the oldest: the spectral typing of stars. There are two core components to our modern spectral type system which discretises the physically continuous properties of temperature and luminosity. The first is the 1D temperature sequence OBAFGKM, first put in that form by the pioneering research of Annie Jump Cannon as part of her work on the HD catalogue (e.g. Cannon & Pickering 1918). In this system, stars are classified by the strengths of their atomic or molecular features, starting with helium lines in hot O stars, through molecular TiO bands in cool M stars.

Later work by William Wilson Morgan, Philip C. Keenan, and Edith Kellman (Morgan et al. 1943) refined this, and extended it to a second dimension in the form of stellar luminosity. These classes were labelled with Roman numerals (e.g. V for dwarfs, IV for subgiants, III for giants, etc), and defined on the basis of gravity sensitive features. At this point however, the only widely studied stars of spectral type M were giants, and the field would have to wait for deeper surveys and more sensitive IR detectors begin to extend this system to the faintest of

stars, specifically late[12] K and M dwarfs (e.g. Kirkpatrick et al. 1991, 1995). It took longer still for the spectral type system to be extended to the sub-stellar regime, where the IR surveys *2MASS* (Two Micron All Sky Survey, Skrutskie et al. 2006) and *WISE* (Wide-field Infrared Survey Explorer, Wright et al. 2010) proved instrumental in assembling a sample of these very cool and faint objects (e.g. Rebolo et al. 1995; Nakajima et al. 1995; Kirkpatrick et al. 1999; Kirkpatrick 2005), with the first Y dwarf not confirmed until 2011 (Cushing et al. 2011). Whilst spectral typing is useful in a qualitative or descriptive sense, its 2D nature fails to account for the chemical composition of stars, and modern systems generally use more physically meaningful parameters. Still though, one cannot overstate its importance in early stellar astrophysics.

More modern quantitative techniques include line depth ratios of different atomic lines (e.g. Gray & Johanson 1991; Gray 1994; Kovtyukh et al. 2003), and the fitting of hydrogen Balmer line profiles (e.g. Fuhrmann 1998; Barklem et al. 2002; Nissen et al. 2007; Fuhrmann 2008). A more widely used method, particularly for Solar-type stars (e.g. Bensby et al. 2003; Santos et al. 2004; Sneden et al. 2004; Bensby et al. 2014), involves measuring $T_{\rm eff}$ by requiring excitation balance for the abundances of specifically chosen Fe I and Fe II lines, the populations of which are both temperature and pressure sensitive (see Takeda et al. 2002 for an overview). Care must be taken however, as systematic offsets in temperature from the IRFM have been observed (e.g. Ramírez & Meléndez 2004; Santos et al. 2004), along with surface gravity offsets as compared to gravities derived from observed fluxes, model masses, and *Hipparcos* parallaxes (Allende Prieto et al. 1999; Santos et al. 2004). Further, the atmospheric conditions assumed for the technique, particularly that of ionisation equilibrium, is not reproduced in model atmospheres (Yong et al. 2004; Allende Prieto et al. 2004), and there are known non-LTE effects for the lower main sequence (Bensby et al. 2014).

Template Matching

Finally, there are methods that rely on matching or interpolating a grid of spectra or photometry that well samples the stellar parameter space (i.e. generally at least $T_{\rm eff}$, $\log g$, and [Fe/H]). While the details of the algorithm can vary (e.g. χ^2 minimisation, cross correlation, weighted mean), this technique ultimately draws its accuracy from **a)** how well sampled the grid is, and **b)** how well the grid points are representative of reality. This latter point is particularly important, as these techniques can equally use grids of observed spectra (e.g. Katz et al. 1998), synthetic spectra (e.g. Recio-Blanco et al. 2006; Zwitter et al. 2008), synthetic photometry (e.g. Bessell et al. 1998; Houdashelt et al. 2000), a combination of synthetic spectra and photometry (e.g. Allende Prieto et al. 2006; Lee et al. 2008; Mann et al. 2015), or are general use packages like *ULySS* (Koleva et al. 2009). If using an observed grid, the technique is ultimately only as accurate as how well constrained the benchmark stars acting as grid points are, whereas a synthetic grid is subject to model limitations or systematics. For excellent summaries of spectral template matching, see the introductions of Wu et al. (2011) and Xiang et al. (2015), and for an introduction to synthetic spectra see Section 1.1.7.

[12]Where the terms 'late' and 'early' when applied to stars means cooler and hotter respectively, though the exact temperature often depends on context. In this case, late K is used to refer to the coolest few spectral classes (e.g. K7 through K9), as compared to mid (K4 through K6) or early (K1 through K3) K dwarfs.

1.1.4 Flux and Luminosity

Stellar flux is one of the more readily observable stellar properties, whose determination is complicated mostly by one's ability to accurately characterise system throughput (i.e. instrument, telescope, and atmosphere), the difficulty in measuring ultraviolet or infrared fluxes from the ground (e.g. Code et al. 1976), wavelength dependent interstellar extinction, the precision to which the zeropoints of various photometric systems are known, and in some cases limitations associated with model spectra or fluxes. Taking all this into account, the total stellar flux observed at Earth, known as the bolometric flux or $f_{\rm bol}$, is defined as:

$$f_{\rm bol} = \int_0^\infty f_\lambda \, d\lambda \tag{1.4}$$

where f_λ is the flux at a given wavelength λ arriving at the top of Earth's atmosphere, corrected for the effect of interstellar extinction and system throughput; and $f_{\rm bol}$ is the total flux integrated over all wavelengths. With a stellar distance, the definition of the stellar luminosity $L_\star$ quickly follows:

$$L_\star = 4\pi f_{\rm bol} D^2 \tag{1.5}$$

where $L_\star$ is the stellar luminosity, and D is the distance to the star.

In practice, however, one does not need to observe a star at all wavelengths as not all wavelengths contribute equally to flux. Flux is an incredibly temperature dependent property and wavelengths far outside the peak of emission do not contribute strongly. Further, following from the discussion of the IRFM in Section 1.1.3, emission at very short or NIR-longward wavelengths are almost independent of non-$T_{\rm eff}$ stellar parameters like gravity and [Fe/H]. As such, it is generally sufficient to use some combination of optical and NIR photometry in well characterised photometric systems, optical or NIR flux-calibrated spectra, and their synthetic equivalents (e.g. to fill in for regions with so-called 'telluric' contamination from Earth's atmosphere) to determine stellar fluxes. Given, however, the the distance dependency of determining stellar luminosity, there also exist spectroscopic indicators useful for stars without reliable parallaxes or where extinction is uncertain (e.g. Kudritzki et al. 2020).

With a large sample of stars, empirical relations can be developed (e.g. Mann et al. 2015), and synthetic grids built and tested (e.g. Casagrande & VandenBerg 2014, 2018a,b). These relations or grids often take the form of *bolometric corrections*—literally the fractional 'missing' flux outside of a given photometric band—which are easy to deploy given the abundance of literature photometry available from ground and space based photometric surveys. For a more detailed overview of flux determination, zeropoints, bolometric corrections, and flux standards, see Casagrande & VandenBerg (2014), Casagrande & VandenBerg (2018a), and Casagrande & VandenBerg (2018b).

1.1.5 Radius

We now turn to stellar radius—a readily measurable property, but one which varies dramatically over the lifetime of a star. For most stars, a reliable parallax is necessary for precise radius determination, but thanks to *Gaia* this is easier than ever. This section is relatively brief, as radius determination methods like eclipsing binary stars, optical interferometry, asteroseismology, and

stellar evolution modelling have already been discussed for other stellar parameters.

Detached Double-Lined Eclipsing Binaries

Detached double-lined eclipsing binaries, whilst incredibly rare, are the source of the most precise stellar radii, and are almost entirely model independent (see Andersen 1991 and Torres et al. 2010 for reviews). The word 'detached' here is critical though, as it means the stars are non-interacting and can be assumed more representative of similar single star systems. The combination of simultaneous radial velocity and transit light curve analysis is incredibly powerful, and as described in Section 1.1.1, allows use of these benchmark systems as stringent tests of theoretical models (e.g. Stassun et al. 2014; Feiden 2015).

Angular Diameters

Stellar angular diameters, when combined with a now readily available distance measured from stellar parallax, provide stellar radii as follows:

$$R_\star = \frac{1}{2}\theta_{\rm LD} D \tag{1.6}$$

where $R_\star$ is the stellar diameter, $\theta_{\rm LD}$ is the limb darkened angular diameter, and D is the distance to the star. While this can be applied to any star, either by calculating $\theta_{\rm LD}$ from a measured $T_{\rm eff}$ and $f_{\rm bol}$ using Equation 1.2, or using empirical surface brightness relations (e.g. Hindsley & Bell 1989; di Benedetto 1995; van Belle 1999; Mozurkewich et al. 2003; Kervella et al. 2004a; di Benedetto 2005; Boyajian et al. 2014), the most precise results are achieved for those stars with measured interferometric angular diameters. For more detail, see the overview of interferometry given in Section 1.1.3.

1.1.6 Surface Gravity

Stellar spectroscopy does not grant *direct* insight into either the mass or radius of an observed star. What is observable, however, is the surface gravity of the star:

$$g = \frac{GM_\star}{R_\star^2} \tag{1.7}$$

where g is the surface gravity, typically presented in logarithmic form as $\log g$; G is Newton's gravitational constant; $M_\star$ is the stellar mass; and $R_\star$ is the stellar radius. Since this contains information on both mass and radius, it can be used as a proxy for stellar luminosity or atmospheric pressure when modelling, the latter of which, critically, affects the formation of atomic and molecular lines. Thus, grids of synthetic spectra (see Section 1.1.7) typically use the three physical dimensions of $T_{\rm eff}$, $\log g$, and [Fe/H]—all of which are readily able to be determined spectroscopically.

While $\log g$ can of course be obtained directly from a measured mass and radius, or from asteroseismology (e.g. Pinsonneault et al. 2014; Silva Aguirre et al. 2015, 2017), these parameters can be challenging to determine in the absence of a reliable parallax or asteroseismic observations. More generally, it is possible to determine $\log g$ spectroscopically using the

pressure-sensitive wings of strong atomic lines (Blackwell & Willis 1977), pressure-sensitive molecular lines themselves like MgH (Bell et al. 1985), or more general spectral template fitting as described in Section 1.1.3. The use of pressure-sensitive atomic or molecular features was particularly important in the era before the widespread availability of stellar parallaxes, such as being able to distinguish dwarfs and giants for the *Kepler* input catalogue (Mann et al. 2012). See Nissen & Gustafsson (2018) for an overview of determining $\log g$ in the context of high-precision abundance determination.

1.1.7 Atmospheric Chemistry

The final fundamental stellar parameter to be discussed is the chemistry of a star—specifically its *atmospheric* chemistry. The emphasis here is to distinguish what we can actually *measure* from the *global* or *intrinsic* properties of the star as a whole. Stars of different masses experience different rates of energy or matter transport, nuclear burning, gravitational settling, and elemental diffusion in their interiors. This means that the *surface* chemistry accessible to our observations is not necessarily representative of the intrinsic chemistry of the star as a whole. We have no method of insight into the global elemental abundances of stars, only what their atmospheres reveal to us—even if such results are biased by events like dredge-up[13] events in giant stars (e.g. Smith & Lambert 1985), pollution by accreted refractory material (e.g. Zuckerman et al. 2003; Spina et al. 2018), the time dependent depletion of lithium abundances (e.g. Mentuch et al. 2008), or stellar activity (Spina et al. 2020).

We thus must resort to working with what we can measure, and for the measurement of stellar bulk metallicity or elemental abundances this is primarily atomic or molecular absorption as measured from stellar spectra—the higher the resolution the better. While this absorption is obviously a strong function of chemistry, it is also strongly affected by the atmospheric temperature, which influences the relative populations of atomic energy levels plus the thermal broadening of lines, and pressure, which determines the atomic or molecular equilibrium conditions as well as the amount of collisional line broadening. For an example of this, see how absorption changes as a function of spectral type in Figure 1.3. The hottest of these stars display absorption from a well-defined spectral *continuum*, and it is with reference to this continuum that abundances are measured.

This becomes far more challenging at cool temperatures where innumerable overlapping molecular lines begin to dominate the spectrum, rendering the location of the true continuum unknown. This can be seen in Figure 1.4, which shows the absorption contribution for atoms, the hydrides MgH and CaH, and the oxide TiO, used to compute a synthetic spectrum for an M2 dwarf at Solar composition. These molecules, along with many others, dominate the spectra of cool stars and render difficult the ability to accurately model their atmospheres. For a specific discussion on these difficulties, see Section 1.2.3.

We briefly touched on one method to determine the bulk metallicity of a star when discussing template fitting in Section 1.1.3. While this might be sufficient for determining [Fe/H], measuring the abundances of additional elements is generally a more involved process. Accordingly, here we will discuss two general use techniques in the form of spectral line equivalent

[13] A 'dredge-up' event is when convective mixing brings fusion products from the stellar interior to the surface.

width measurements and spectral synthesis, as well as a specific example uniquely applicable to cool dwarfs. For a thorough review of these topics, see the reviews Allende Prieto (2016), Nissen & Gustafsson (2018), and Jofré et al. (2019).

Equivalent Widths

The equivalent width of a spectral line—defined as the width of a *completely opaque* rectangle with equal area—is directly sensitive to the associated elemental abundance given two sets of physical constraints. The first is an accurate set of stellar parameters. The second—which is the core complexity of measuring abundances—is knowledge of the 'curve of growth' for the line and element in question. This curve describes how line width W correlates with the number of absorbing atoms, N, being proportional ($W \propto N$) for weak lines (the 'linear' part of the curve), being almost independent ($W \propto \sqrt{\ln N}$) for saturated lines (the 'flat' or 'saturated' part of the curve), before finally the line wings are able to dominate ($W \propto \sqrt{N}$) for the strongest of lines (the 'damping' or 'square-root' part of the curve, Hubeny & Mihalas 2014). This progression means that it is critical to *carefully select* a set of lines for any abundance analysis, with weaker lines, which show the greatest sensitivity to abundance, being generally considered the best to use, as well as ensuring any chosen lines are unblended—hence the need for high spectral resolution. Abundances measured from equivalent widths are often highly accurate, but at the cost of being time consuming or even bespoke (e.g. Meléndez et al. 2009; Ramírez et al. 2014; Tucci Maia et al. 2014; Nissen 2015; Spina et al. 2016). While automated approaches exist (e.g. Blanco-Cuaresma et al. 2014b), one of the largest sources of error is typically in the placement of the continuum and associated normalisation (Jofré et al. 2017) which is sometimes more reliably done manually.

Spectral Synthesis

As compared to measuring equivalent widths, which considers individual lines, spectral synthesis endeavours to model the entire spectrum. This is an intensive process, requiring a model atmosphere (e.g. MARCS, Gustafsson et al. 2008; ATLAS, Castelli & Kurucz 2003; STAGGER, Magic et al. 2013), a radiative transfer code (e.g. `Turbospectrum`, Plez 2012), atomic or molecular line lists (e.g. VALD, Ryabchikova et al. 2015; ExoMol, Tennyson et al. 2016; Kurucz, Kurucz 2011), and software enabling the automatic determination of abundances (e.g. SME, Spectroscopy Made Easy, Valenti & Piskunov 1996). Combined, these can not only produce the aforementioned grids of model spectra typically varying in $T_{\rm eff}$, $\log g$, [Fe/H], and ζ, the so-called 'microturbulence parameter'[14], but also enable detailed abundance analysis such as is done in modern large spectroscopic surveys like GALAH (De Silva et al. 2015; Buder et al. 2021), APOGEE (Majewski et al. 2017; Pérez et al. 2016), and the *Gaia*-ESO Survey (Gilmore et al. 2012; Smiljanic et al. 2014).

The benefits of spectral synthesis are that it can be done reliably and repeatably at scale, and can work with blended lines where the measurement of equivalent widths would not be possible. One must, however, ensure that their data are of sufficiently high SNR (e.g. Heiter

[14] ζ is a model parameter used to account for non-thermal gas motions in a star which result in additional line broadening.

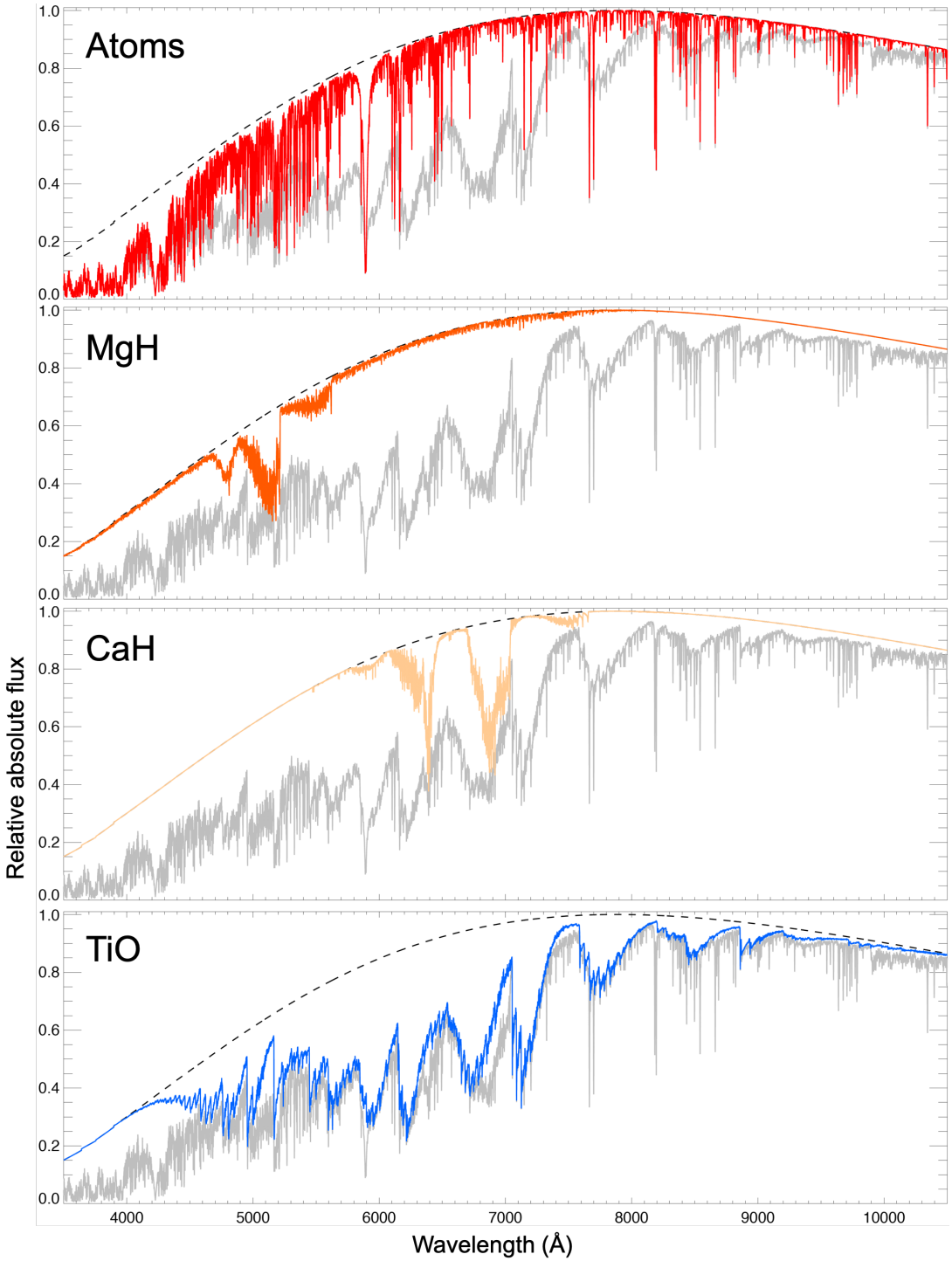

Figure 1.4: Theoretical absorption due to atoms and several dominant molecular species in the atmosphere of an ~M2V dwarf ($T_{\rm eff}$ = 3 500 K, $\log g$ = 5.5, [Fe/H] = 0.0). The dotted black lines are the true spectral continuum, the coloured lines are atomic or molecular absorption, and the grey line the resulting spectrum. Note how at optical wavelengths there is no way to determine the true spectral continuum—the typical point of reference for measuring the strength of absorption features and their corresponding chemical abundances—from an emergent spectrum. Reproduced from work by Thomas Nordlander using synthetic MARCS spectra. For a full description of of these models, see Section 4.5.1 in Chapter 4.

et al. 2014, Smiljanic et al. 2014), take care to properly correct spectral regions affected by absorption by Earth's atmosphere (e.g. Sameshima et al. 2018), and avoid errors introduced by incorrect wavelength calibration (e.g. Hinkel et al. 2016; Jofré et al. 2017). Other issues arise during analysis or from the synthetic spectra themselves, such a ζ being partially degenerate with other stellar parameters (e.g. Brewer et al. 2015), a scaled Solar abundance pattern not being valid for all stars (e.g. Brewer et al. 2015), issues arising from the assumed geometry of model atmospheres (Heiter & Eriksson 2006), biased fitting due to incomplete line lists (see Section 1.2.3 for more detail), and non-LTE effects (see Section 1.2.4 and Asplund 2005).

Cool Dwarf Colour-M_K Relations

Due to the dominance of molecular absorption in the atmospheres of cool stars, their chemistry has a profound impact on the shape of their spectrum, particularly in the optical where this absorption is strongest (see Figure 1.4). For a fixed stellar mass, this results in metal-rich stars being *less* luminous at optical wavelengths than a metal–poor counterpart—an effect largely absent for NIR photometry (see Allard et al. 1997, Baraffe et al. 1998, and Chabrier & Baraffe 2000 for theoretical perspectives), especially the metallicity insensitive K band at 2.4 μm commonly used in the development of empirical mass–luminosity relations for cool dwarfs (e.g. Henry & McCarthy 1993; Delfosse et al. 2000; Benedict et al. 2016; Mann et al. 2019).

This first became observationally apparent in Delfosse et al. (2000) when developing such empirical mass relations, where the authors noted "the V band $M_\star/L_\star$ diagram represents direct evidence for an intrinsic dispersion around the mean $M_\star/L_\star$ relation", which can be seen in Figure 1.5. Future papers took advantage of this (e.g. Bonfils et al. 2005; Johnson & Apps 2009; Schlaufman & Laughlin 2010; Neves et al. 2012; Hejazi et al. 2015; Dittmann et al. 2016), using absolute K band magnitudes as proxies for $M_\star$, and the scatter in an optical-NIR colour (typically $V - K$) as a metallicity indicator. These relations are trained on samples of binary metallicity benchmark F/G/K–K/M systems from which metallicity can more easily be inferred from the hotter F/G/K primary stars and propagated to the cooler K/M secondaries under the assumption that stars in binary systems formed together and thus share a common chemistry (see Section 1.3.2 for an overview of these benchmarks). As more such binaries over a greater range of metallicities were discovered over the years, these provided increasingly robust relations applicable to a wider sample of stars.

Note, however, that these relations are only possible due to the slow rate of evolution of stars with $M_\star < 0.7\,M_\odot$ once on the main sequence, meaning that the dispersion in magnitude is overwhelmingly the result of stellar chemistry, not stellar evolution (see Figure 1.2). As a result, this approach is only applicable for isolated main sequence stars, and will give erroneous results if used for stars still contracting to the main sequence, or unresolved binaries.

1.2 Gaps in Our Knowledge

As has now been well established, there are a multitude of ways for us to know the stars, yet there remain some obvious gaps in our knowledge. Some are due to the computational complexity of modelling stars, such the phenomenon of stellar convection—an inherently

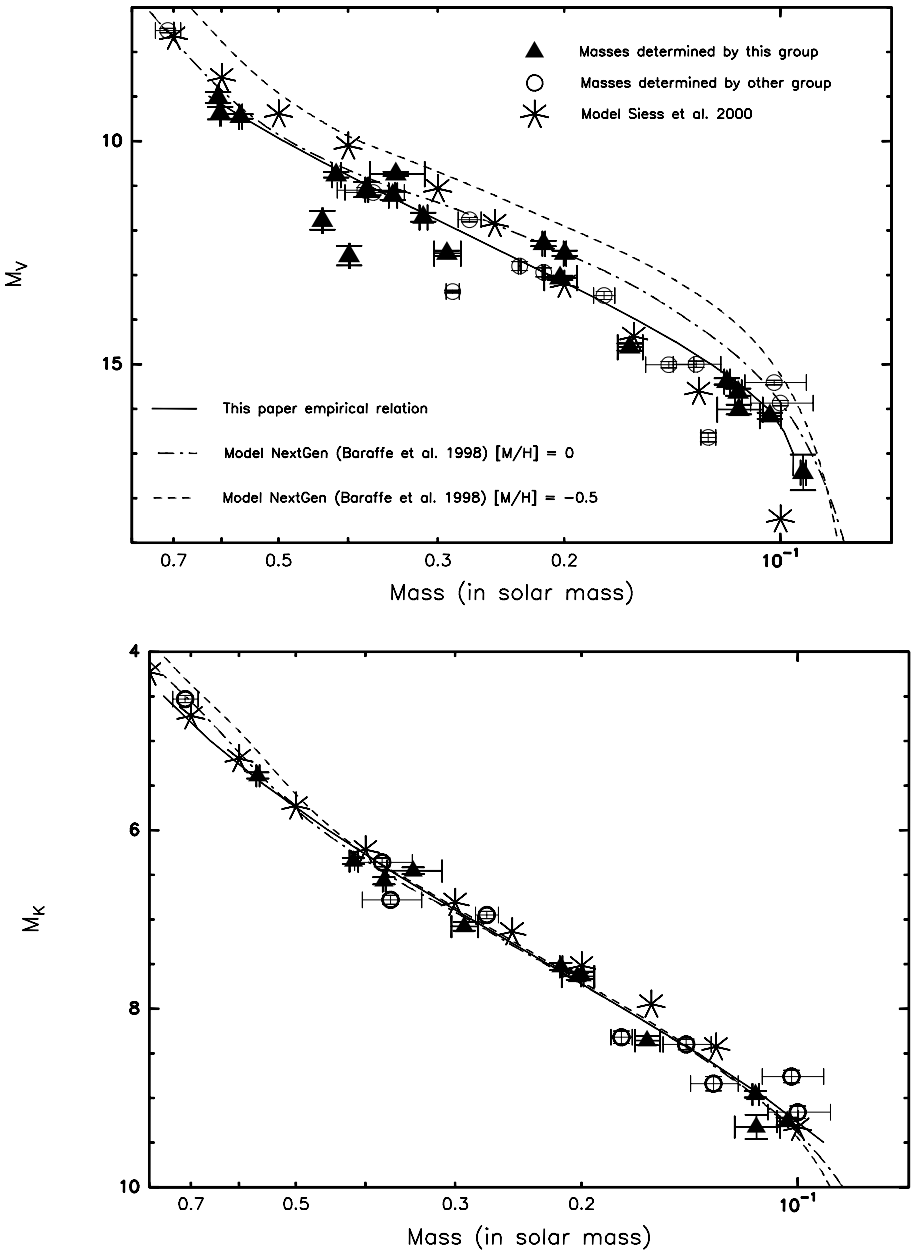

Figure 1.5: $M_\star$–$L_\star$ comparisons for cool dwarfs with $0.1 \lesssim M_\star \lesssim 0.7\,M_\odot$ from Delfosse et al. (2000). The solid black lines are the empirical mass relations developed by the authors, the dashed and dash-dotted lines are 5 Gyr theoretical isochrones from Baraffe et al. (1998) with [M/H] of −0.5 and 0.0 respectively, and the asterisks represent 5 Gyr Solar metallicity models from Siess et al. (2000). **Top:** $M_\star$–$L_\star$ relation when using the absolute V band magnitude, M_V, as a proxy for $L_\star$. Note the significant scatter about the fitted relation and wide separation of the theoretical isochrones, with the lower metallicity tracks being more luminous. This effect is due to increasing molecular opacity in the optical with metallicity, resulting in lower luminosity for a given mass. **Bottom:** Same as previous, but using the absolute K band magnitude, M_K, instead as the $L_\star$ proxy. Note the tight agreement between the fitted relation and theoretical tracks, indicating the relative insensitivity of NIR K band magnitudes to metallicity.

three dimensional, nonlinear, and time-dependent process—often parameterised under a one–dimensional framework known as mixing length theory (MLT, Section 1.2.1). Other gaps are due to our lack of understanding of the physical phenomena themselves, as is common with how magnetic fields result from and impact stellar properties, activity, and evolution (Section 1.2.2). Other uncertainties still stem not from stellar astrophysics, but atomic and molecular physics, and how atoms and molecules behave in a radiation field to absorb or emit light (Section 1.2.3), as well as how we model these processes (Section 1.2.4). Combined, these gaps in our understanding complicate the study of stellar astrophysics.

1.2.1 Mixing Length

While it is possible to run physically realistic radiative hydrodynamical models of stellar interiors and physical phenomena like convection in three dimensions, it is currently computationally unrealistic to do so on evolutionary timescales. As such, most stellar modelling is undertaken using one dimensional stellar evolution codes (e.g. the Victoria-Regina models, VandenBerg et al. 2006; DSEP, Dotter et al. 2008; and MIST, Dotter 2016) more feasibly able to model stars varying in mass and chemical composition over their entire life cycle.

The so-called 'Mixing Length Theory' (Vitense 1953; Böhm-Vitense 1958) is a widely used one dimensional parameterisation of stellar convection used in such models. The titular 'mixing length', $\alpha_{\rm MLT}$, describes the vertical distance—or mean free path—travelled by a rising 'parcel' of hot gas before it disperses. While $\alpha_{\rm MLT}$ is not relevant in regions of highly efficient convection deep in the star, in near surface convection zones a higher value indicates that heat is transported more readily. Such a simple formulation of such a complex problem necessitates a bevy of nonphysical simplifying assumptions, like solely vertical 1D gas paths, symmetry between rising and descending gas, and a rigid boundary at the edge of stellar convection zones (see the introduction of Joyce & Chaboyer 2018a for a more detailed overview). While there have been efforts to, for example, calibrate the mixing length to more physically realistic 3D models (e.g. Ludwig et al. 1999, Trampedach et al. 2014, Arnett et al. 2015, Magic et al. 2015), MLT remains a mainstay in theoretical stellar astrophysics.

Care must then be taken when using 1D stellar evolution models. For example, the optimal mixing length depends on stellar $T_{\rm eff}$ and $\log g$ (e.g. Trampedach et al. 2014), and is correlated with metallicity for stars on the giant branch (e.g. Tayar et al. 2017). Further, Solar-calibrated mixing length values are inappropriate for modelling metal-poor stars and fail to reproduce their observed stellar properties (e.g. Joyce & Chaboyer 2018a).

1.2.2 Magnetic Fields & Stellar Activity

Magnetic fields have long challenged our naive astrophysical assumptions at a variety of scales. From the stellar astrophysics perspective alone, magnetic fields affect stellar convection (e.g. Feiden 2016); the equivalent widths of spectral features (e.g. Flores et al. 2016; Yana Galarza et al. 2019); the determination of stellar parameters like $T_{\rm eff}$ and [Fe/H] (Spina et al. 2020); and the radii of low-mass double-lined eclipsing binary benchmark systems via inflation (e.g. Ribas 2006; López-Morales 2007; Morales et al. 2008, 2009; Torres 2010; Kraus et al. 2011; Feiden & Chaboyer 2012). For a general review on magnetic fields, see Donati & Landstreet (2009). Stellar activity—a related phenomenon—also presents a barrier to the detection of exoplanets,

as features such as stellar spots can produce signals that mimic or mask those of exoplanets (e.g. Haywood et al. 2014).

1.2.3 Atomic and Molecular Line Lists and Opacities

While model atmospheres at cool temperatures demonstrate reasonable performance in the NIR (e.g. Baraffe et al. 1997, 1998), there have long been issues in the optical (e.g. Baraffe et al. 1998; Reylé et al. 2011; Mann et al. 2013c). The core reason for this disagreement lies in the complexity of cool atmospheres, where the low temperatures allow for the formation of an array of oxides and hydrides which dominate the spectral profile (as can be seen in Figure 1.4). Given the dominance of these molecules, the impact of not accurately knowing their wavelengths or line depths can be severe (e.g. Plez et al. 1992; Masseron et al. 2014), particularly for TiO (e.g. Hoeijmakers et al. 2015; McKemmish et al. 2019) which dominates absorption in the optical.

A more general concern, applicable to warmer stars also, is in the use of scaled Solar abundances for other stars. While appropriate for stars of similar chemical composition to the Sun, this assumed relation is not always valid (e.g. Brewer et al. 2015, and Veyette et al. 2016 for the C/O ratio specifically). Care should be taken when analysing or modelling these stars, as these chemical differences can have profound effects on atmospheric structure or opacities (e.g. Gustafsson et al. 2008; Saffe et al. 2018).

1.2.4 Model Atmospheres

Most stellar atmosphere models—and thus the model spectra derived from them—are computed using several simplifying approximations: a single spatial dimension in the radial direction, time–independence, hydro*static* as opposed to hydro*dynamic*, and local thermodynamic equilibrium (LTE). While these approximations give reasonable model agreement in certain cases, in others they demonstrate substantial departures from reality. For detailed overviews of these topics, see the introductions in Lind (2010) and Amarsi (2016). For a review of how the approximation of LTE influences spectral line formation and our measurements, see Asplund (2005).

Stars are dynamic objects, and modelling their atmospheres as one dimensional and time–independent fails to capture the complexity of their atmospheres and the resulting impact phenomena like granulation has on spectral line formation (e.g. Dravins et al. 1981; Dravins & Nordlund 1990; Asplund et al. 2000). This necessitates the use of the aforementioned Mixing Length Theory to approximate convection, as well as other model parameters like ζ, the microturbulence, to account for line broadening due unmodeled turbulent gas motions. While it then seems obviously preferable to employ more realistic models, any extra complexity in the form of additional spatial or temporal dimensions, or viewing angles severely increases computational and storage requirements. This is especially true if the intent is to build a library of stellar models covering a range of temperatures, metallicities, and gravities (e.g. Magic et al. 2013).

Under LTE conditions gas temperature varies slowly in space where it and the gas pressure solely determine the excitation and ionisation fractions of different atomic or molecular species (via the Boltzmann and Saha Distributions respectively). So called ‘non–LTE’ effects describe how radiative transitions drive material away from these distributions and change the depths and

shapes of spectral lines. This can severely impact the measurement of elemental abundances (especially in metal poor or giant stars, e.g. Thévenin & Idiart 1999, Bergemann et al. 2012, Lind et al. 2012), the shape of spectroscopic temperature indicators like the hydrogen Balmer series (e.g. Amarsi 2016), and potentially the estimation of $\log g$ for stars on the lower main sequence (Bensby et al. 2014). Modelling stars in non–LTE conditions greatly increases model complexity as the radiative transfer equation becomes non–linear and non–local, with model computation now needing many more iterations to converge. In addition to this, more detailed atomic data is required, and this is unavailable for most atoms and transitions. For reviews on these topics, see Gustafsson & Jørgensen (1994) and Asplund (2005).

1.3 The Importance of Stellar Benchmarks

Having now spent some time getting familiar with the many methods of stellar characterisation at our disposal, it is worthwhile considering how to best ensure agreement between these varied approaches. This is important, because not only do we need to ensure consistency between techniques, but also consistency within different implementations of the same technique. This brings us to the topic of stellar benchmarks.

There are two typical and somewhat overlapping meanings when labelling a star a benchmark or standard. The first, and the most relevant to this PhD, are stars that have at least some of their properties determined through fundamental methods with as little dependence on models as possible. These can be stars with dynamical masses, interferometric temperatures or radii, or those with asteroseismic measurements—to name a few. An early and particularly noteworthy example is Capella A, a ~104 day period binary consisting of two evolved stars, whose orbit and and component masses were precisely determined using the stellar interferometer at Mount Wilson (Anderson 1920)—the same instrument used to measure the angular diameter of Betelgeuse mentioned previously. These results were subsequently used by Arthur Eddington to develop an early stellar mass–luminosity relation, substantially increasing the ability to advance stellar models (Eddington 1930).

The second are those stars elevated to reference status even if they don't necessarily have fundamentally determined parameters. This can include stars used as 'type specimens' to define the spectral type scale, analogous to the use of the term in biology (see e.g. the spectral type scale, and associated notes, by Pecaut & Mamajek 2013). Alternatively, it could refer to libraries of bright, well-studied stars such as the 34 *Gaia* FGK Benchmark Stars which span a variety of masses, ages, and metallicities (Blanco-Cuaresma et al. 2014a; Heiter et al. 2015).

The availability of such benchmarks, and the breadth of the parameter space covered by them, has only become more important as stellar astrophysics moves further in the direction of large surveys and big data. In essence, they are the foundation that stellar astrophysics is built upon.

1.3.1 Optical Interferometric Standards

Optical interferometry is the source of the most precise and accurate stellar angular diameters, temperatures, and radii (excepting those from relatively rare eclipsing binaries). Given this

accuracy and precision, these stars are understandably used as the basis for testing models, building empirical relations, and form the foundation of the temperature scale.

The angular diameters from optical interferometry are used to build empirically calibrated surface brightness relations which relate the colour and brightness of a star to its angular diameter (e.g. Hindsley & Bell 1989; di Benedetto 1995; van Belle 1999; Mozurkewich et al. 2003; Kervella et al. 2004a; di Benedetto 2005; Boyajian et al. 2014) thus superseding prior theoretical relations (e.g. Wesselink 1969; Barnes & Evans 1976). While this has obvious applicability for determining the temperatures and radii of individual stars, such relations can also be used to determine the distances to eclipsing binaries (e.g. Lacy 1977; Southworth et al. 2005), and calibrate cosmological distance relations such as the Cepheid period-luminosity relation (e.g. di Benedetto 1995; Fouque & Gieren 1997; Kervella et al. 2004b; Groenewegen 2007; Storm et al. 2011a,b). Interferometric temperatures, on the other hand, form the foundation of the temperature scale, and are what techniques like the IRFM are benchmarked upon (e.g. Casagrande et al. 2020). Meanwhile radii from interferometry can be used to test stellar models (e.g. Berger et al. 2006; von Braun et al. 2012; Joyce & Chaboyer 2018b), and characterise exoplanet hosts (e.g. van Belle & von Braun 2009; Baines & Armstrong 2011; von Braun et al. 2012, 2014; White et al. 2018).

However, the existing set of interferometric standards is neither complete nor free of problems. The principal reasons for this are twofold. Firstly, the technique has incredibly bright restrictions on limiting magnitude—by the standards of other techniques—which severely limits the pool of suitable targets. Secondly, there are challenges associated with both conducting and calibrating observations. Calibration in this context refers to the process of correcting for atmospheric and instrumental effects and, particularly at small angular resolutions, is a non-trivial exercise at best. There are recent examples of large systematic differences between measurements from separate beam combiners, or between interferometry and the IRFM (Casagrande et al. 2014; White et al. 2018; Karovicova et al. 2018; Tayar et al. 2020)—with $T_{\rm eff}$ differences of up to several hundred K. Additionally, simple parameterisations of surface brightness as a single photometric colour have been shown to be sensitive to metallicity, which reflects limitations in our coverage of the chemical dimension. This latter point has implications beyond stellar astrophysics, all the way up to the accuracy of the extragalactic distance scale (e.g. Storm et al. 2011b; Mould et al. 2019).

1.3.2 Cool Dwarf Metallicity Standards

As already touched upon, determining the chemistry of stars with cool atmospheric temperatures is a challenging task due to their inherent complexity and the difficulty associated with modelling them. It is wonderfully ironic then that these stars are the most common in the Universe, and most likely planet hosts, thus making the task of finding a suite of suitable benchmarks all the more important. Fortunately, however, for our benchmarks here we once again turn to binary systems.

Binaries form together, and it is now accepted that such pairs share not only a common origin, but also a common chemical composition (see e.g. Desidera et al. 2004 and Hawkins et al. 2020 for studies on F/G/K+F/G/K binaries). The implication here, under the assumption that this also applies to F/G/K+K/M binaries, is that such systems make for excellent chemical benchmarks

when studying cool atmospheres. Models and techniques for abundance determination in F/G/K stars are more reliable and established, and propagating the results to the K/M secondary allows for critical constraints when studying the coolest of stars.

A few potential cool dwarf specific applications enabled by such calibrations include: building photometric [Fe/H] relations (e.g. Bonfils et al. 2005; Johnson & Apps 2009; Schlaufman & Laughlin 2010; Neves et al. 2012); calibrating line-by-line studies at high-spectroscopic resolution (e.g. Bean et al. 2006a; Önehag et al. 2012; Passegger et al. 2016; Lindgren et al. 2016; Souto et al. 2020); and developing [Fe/H] relations from [Fe/H]–sensitive molecular indices in low-resolution spectra (e.g. Rojas-Ayala et al. 2010, 2012; Terrien et al. 2012; Mann et al. 2013a; Newton et al. 2014). This latter sample is particularly important as the of ease obtaining low-resolution spectra at volume allows for a much larger sample of secondary calibrators with NIR [Fe/H] estimations suitable for calibrating optical surveys.

1.4 The Current State of Observational Stellar Astrophysics

Let's now consider the state of observational stellar astrophysics as a whole. Large dedicated surveys—be they photometric or spectroscopic, ground based or space based—are changing both the scope and detail with which we can study the stars. Most moderately bright stars now have multi-band photometry extending from the optical into the infrared, with most of these targets also having space-based positions, proper motions, and parallaxes from *Gaia*. Millions of stars now have spectra as part of the several large ongoing spectroscopic surveys, and hundreds of thousands of stars have high-quality, space-based time-series photometry from NASA missions like *Kepler* (Borucki et al. 2010) and *TESS* (Transiting Exoplanet Survey Satellite, Ricker et al. 2015). This wealth of data allows us to find and study rare objects more easily, and to more reliably implement non-traditional analysis techniques like data-driven approaches reliant not on stellar models, but on the quality of stellar benchmarks—ideally obtained from the most fundamental of the techniques discussed above.

1.4.1 Ground-Based Photometric Surveys

Multi-band photometry is useful in constraining stellar temperature, luminosity, and in certain cases metallicity (e.g. Casagrande et al. 2019; Carrillo et al. 2020). Critically, it is also easier to obtain in bulk—and for fainter stars—than spectroscopy. The benefit of all-sky photometric surveys towards knowing the stars is thus clear, and now hundreds of millions of stars have been observed. For the optical and near-infrared, the Sloan Digital Sky Survey (SDSS, York et al. 2000) and Pan-STARRS Survey (Kaiser et al. 2002, 2010; Chambers et al. 2016) have targeted the Northern Hemisphere, with the SkyMapper Southern Sky Survey (Keller et al. 2007) covering the south. In the infrared, *2MASS* (Skrutskie et al. 2006) observed the *entire* sky and was the *de facto* standard source catalogue prior to *Gaia*. Combined, these provide information over roughly 2 000 nm in wavelength for moderately bright stars, and is foundational to most stellar astrophysics.

For stars fainter than $r\sim16$, the future of ground-based surveys however will fundamentally change when LSST (the Legacy Survey of Space and Time, Ivezić et al. 2019), begins operations using the 8.4 m telescope at the Vera C. Rubin Observatory, Coquimbo Region, Chile. LSST

will push many magnitudes fainter than any previous optical survey (to $r{\sim}27.5$), and aims to visit each location close to 1 000 times over 10 years. In doing so it will produce photometry for ~20 billion stars—an order of magnitude more than *Gaia*—and allow for the first time the study of very distant or faint Milky Way components. Operating from as a large a telescope as it will though, LSST will have a comparatively faint saturation limit compared to current photometric surveys, allowing for it to complement, rather than supersede, the aforementioned surveys.

1.4.2 Ground-Based Spectroscopic Surveys

While in certain cases it is possible to infer metallicities from photometry, spectroscopy is needed to gain insight into elemental abundances for chemical studies, radial velocities for kinematics, and stellar emission for studying activity. Spectroscopy, however, is much more expensive to obtain than photometry in terms of both number of pixels and integration time—even when considering that all modern spectroscopic surveys have multi-object instruments. Any such survey must then carefully consider its science goals, for the potential design-space is large, comprising: total stars observed; spectroscopic resolution; wavelength coverage; SNR; and temporal coverage. No single instrument can effectively maximise all of these, and while several upcoming surveys are able to work at a variety of resolutions, they are typically world–leading in at most two of these categories.

Surveys at low-to-medium spectroscopic resolution ($R \lesssim 10\,000$) typically require shorter exposure times, and as such are able to target larger numbers of stars. They're excellent for determining basic stellar parameters like $T_{\rm eff}$, $\log g$, and [Fe/H], as well as discovering or following up rare objects. This category includes the historical SEGUE (Sloan Extension for Galactic Understanding and Exploration, Yanny et al. 2009, Rockosi et al. 2009) and RAVE (the RAdial Velocity Experiment, Steinmetz et al. 2006) surveys, the planned FunnelWeb Survey, and ongoing LAMOST Survey (Large Sky Area Multi-Object Fibre Spectroscopic Telescope, Cui et al. 2012).

High-resolution surveys are necessary to determine the full suite of elemental abundances, study resolved stellar populations, and probe the chemical fingerprints of the Milky Way's accretion history. Current high-resolution surveys include APOGEE (Apache Point Observatory Galactic Evolution Experiment, Majewski et al. 2017) and GALAH (GALactic Archaeology with HERMES, De Silva et al. 2015), along with the upcoming 4MOST (4-metre Multi-Object Spectrograph Telescope, de Jong & 4MOST Consortium 2016) and SDSS-V (Sloan Digital Sky Survey 5, Kollmeier et al. 2017) surveys—the latter two of which will also have low resolution modes, allowing for complementary science.

Sky Tiling and Scheduling

One important aspect that must not be overlooked when operating at the scale these surveys do is *efficiency*. These surveys are multi-year operations, and typically observe targets spanning a range of magnitudes—potentially varying in brightness by factors of hundreds or even thousands. While photometric surveys are able to have fixed pointings to observe all stars in a field (only limited by depth and angular resolution), spectroscopic surveys must disperse their light and are limited to observing a fixed amount of targets per field as set by the number of optical

fibres. Thus spectroscopic surveys, particularly in the case of surveys aiming for completion via some metric (e.g. magnitude), have more of an optimisation problem on their hands—which targets to observe with which telescope pointing with which exposure time. While there have been a variety of different approaches over the years for both stellar and extragalactic surveys (e.g. Campbell et al. 2004; Robotham et al. 2010; Yuan et al. 2012; Tempel et al. 2020a), each ultimately must vary with the goals of the survey, as well as instrument and telescope specifics.

1.4.3 *Gaia*

Arguably the single greatest boon for observational stellar astrophysics in the last decade is the *Gaia* Mission (Gaia Collaboration et al. 2016a). The successor to the astrometric *Hipparcos* Satellite (ESA 1997; Perryman et al. 1997), *Gaia* will measure the positions, parallaxes, and proper motions for more than a billion stars—a factor of 400 greater than its predecessor and more objects than any other survey. Further setting *Gaia* apart are its two non-astrometric instruments: the Radial Velocity Spectrometer (RVS, Cropper et al. 2018) which will produce medium resolution spectra (R~10 500) centred on the Ca NIR triplet ($847 < \lambda < 874$ nm); and the Blue and Red Photometers (BP/RP, Jordi et al. 2010) which will produce low-resolution spectrophotometry using two filters ($330 < \lambda_{B_P} < 680$ nm, and $640 < \lambda_{R_P} < 1\,000$ nm) as well as in unfiltered white light ($350 < \lambda_G < 1\,000$ nm). Combined, *Gaia* will produce complete positional and kinematic information (including radial velocities), chemical abundances, spectral energy distributions, stellar parameters, and reddening for an incredible number stars—thus providing all the components necessary to investigate Galactic dynamics and chemical evolution on a heretofore unprecedented scale.

At the time of writing, *Gaia* has had three public data releases: DR1 (Gaia Collaboration et al. 2016b), DR2 (Brown et al. 2018), and EDR3 (*Early* DR3, Brown et al. 2021). While *Gaia* has yet to release spectra or chemical information, it has already changed how stellar astrophysics is done. It is now the standard positional and input catalogue for stellar surveys (superseding *2MASS*); in providing parallaxes for vastly more stars makes clear luminosities and radii for all stars in the extended Solar Neighbourhood—reducing confusion between distant giants and faint dwarfs, and providing a more reliable and standardised input catalogue for transiting exoplanet surveys (e.g. Stassun et al. 2019); and allows Galactic dynamics to be done at scale enabling studying the accretion history of the Milky Way (e.g. Belokurov et al. 2018; Haywood et al. 2018; Helmi et al. 2018; Myeong et al. 2019) or the history and structure of local moving groups (e.g. Gagné & Faherty 2018; Cantat-Gaudin et al. 2018; Zari et al. 2018; Meingast & Alves 2019; Kounkel & Covey 2019; Crundall et al. 2019; Quillen et al. 2020). Not since *2MASS* has stellar astrophysics seen such a change in data availability, and our knowledge of the Galaxy will only continue to improve as *Gaia* data is paired with other upcoming spectroscopic and photometric surveys.

1.4.4 Machine Learning and Data-Driven Analysis

Such a data-rich era has brought with it an increase in the use of machine learning and data-driven approaches to problem solving. Whilst the use of non-traditional analysis techniques in astrophysics isn't new, the widespread public availability of large astrophysical datasets and

access to diverse sets of benchmark objects to serve as training samples is only increasing. For a somewhat recent overview of the topic, see Ball & Brunner (2010).

Why machine learning though? As has hopefully been conveyed by now, stellar astrophysics is a terribly complicated affair, and there is much we don't yet know, aren't able to model in detail, or is time consuming to determine via traditional means. Machine learning algorithms—when used carefully—can help us quickly find or exploit complex patterns and peculiarities in our data that might otherwise be missed or inaccessible. Note, however, that these algorithms are not equally well–suited for all problems or domains, and that treating them as 'black boxes', or deploying them carelessly, is just as likely to produce nonsense as anything physically meaningful.

Some examples of such techniques, and their astrophysical applications, include: t-SNE (t-distributed Stochastic Neighbour Embedding, van der Maaten & Hinton 2008, e.g. Traven et al. 2017); neural networks (e.g. Gulati et al. 1994; von Hippel et al. 1994; Bailer-Jones et al. 1998; Bailer-Jones 2000; Snider et al. 2001; Hon et al. 2018); LLE (Locally Linear Embedding, Roweis & Saul 2000, e.g. Daniel et al. 2011), PCA (Principal Component Analysis, Pearson 1901, Hotelling 1936, Jolliffe 2002; e.g. Bailer-Jones et al. 1998, McGurk et al. 2010) and data-driven algorithms like the Cannon (Ness et al. 2015, e.g. Ho et al. 2017, Ness et al. 2016, Abolfathi et al. 2018, Buder et al. 2018, Behmard et al. 2019, Rice & Brewer 2020, Birky et al. 2020). Most of the cited applications are on machine learning as applied to stellar spectra, where the main goal is typically to determine the corresponding set of stellar parameters, e.g. $T_{\rm eff}$, $\log g$, and [Fe/H]. While this is fundamentally a *regression* problem—i.e. the prediction of continuous numerical values—a stellar spectrum might consist of thousands of pixels, and the mapping between the stellar parameters and spectrum itself is highly non-trivial. At their core then, these algorithms tend to involve a process of *dimensionality reduction* where our data, in this case a stellar spectrum, is mapped from the high-dimensional spectral pixel space to a lower dimensional space representing our stellar parameters.

For such regression algorithms to be useful, they first need to be *trained* and *validated* using a set of reference objects with known stellar parameters (or *labels*). These objects are the very stellar benchmarks discussed in Section 1.3, and the ultimate success of any machine learning or data-driven algorithm relies on their properties being both diverse and well constrained. One of the key strengths of these techniques is that, provided a sufficiently large and diverse training sample is available, they can be used to study stars where models have known limitations, for example M-dwarfs in Birky et al. (2020).

1.5 From Stars to Planets

In addition to big data, one other marker of the modern era of astronomy is the coming of age of exoplanetary astrophysics. The field has developed substantially since the first exoplanet discoveries in the 1990s, and at the time of writing we now know of more than 4 300 planets orbiting stars other than our own[15]. While some of these are similar to the planets of the Solar System, vast numbers—and even entire classes of planet—are not, causing us to rethink our naive assumptions about planet formation. The Universe is stranger than we first thought, and

[15] https://exoplanetarchive.ipac.caltech.edu/

objects like super-Earths (e.g. Rivera et al. 2005), short-period giant planets (e.g. Mayor & Queloz 1995), tightly packed rocky planets (e.g. Gillon et al. 2017), circumbinary planets (e.g. Doyle et al. 2011), and even pulsar planets (e.g. Wolszczan & Frail 1992)—the first exoplanets to be discovered—continue to give astronomers much to puzzle over.

There are a number of different exoplanet detection methods, with each being sensitive to different populations of planets. All are important in order to understand the full diversity of exoplanets and study their demographics. Just as important, however, is understanding the stars they orbit, especially for the techniques which only indirectly detect planets.

1.5.1 Exoplanet Detection

The two most productive methods of planet detection do not observe said planets directly, only the influence they have on their host stars. The first is the radial velocity technique, which detects the Doppler shift of a stellar spectrum as the star orbits the centre of mass common to it and its planet. RV observations are, with few exceptions, necessary to determine planet masses and thus planet densities when combined with radii from another technique. While sensitive to planets at a variety of orbital inclinations, unless the inclination is known, only the *minimum planet mass*, $M_P \sin i$, can be determined from the line of sight component of the Doppler shift:

$$K = \sqrt{\frac{G}{(1-e^2)}} M_P \sin i (M_\star + M_P)^{-1/2} a^{-1/2} \tag{1.8}$$

where K is the radial velocity semi-amplitude[16], G is Newton's gravitational constant, e is the orbital eccentricity, M_P is the mass of the planet, $M_\star$ is the mass of the host star, and a is the orbital semi-major axis. Importantly, since measurement of K requires observing precise shifts in spectral absorption lines, the technique is sensitive to anything that would reduce either the number of lines or their depth like rapid stellar rotation (e.g. Galland et al. 2005) or low stellar metallicity (e.g. Fischer & Valenti 2005; Santos et al. 2003; Sozzetti et al. 2006). For a more detailed summary of finding planets via the RV method, see the review chapter by Lovis & Fischer (2010) in Seager (2011).

RV observations, particularly when hunting for small rocky planets, make use of some of the most stable and highest spectral resolution instruments on the planet. The most successful of these by far is HARPS (High-Accuracy Radial velocity Planetary Searcher, Mayor et al. 2003), used as part of the HARPS Survey, but other successful surveys include the Anglo-Australia Planet Search (Tinney et al. 2001), CARMENES (Calar Alto high-Resolution search for M dwarfs with Exoearths with Near-infrared and optical Echelle Spectrographs, Quirrenbach et al. 2014), and ELODIE (Baranne et al. 1996) and CORALIE (Queloz et al. 2000)—the precursors to HARPS.

The transit method is the second technique, and the more relevant to this thesis. Another indirect technique, but this time rather than detecting the planet via the gravitational influence it exerts on its host star, we are instead observing the dimming of the stellar host as the planet eclipses it. Alone it is able to determine precision radii and orbits for planets, but greater

[16]Where the semi-amplitude is defined as $(v_{\max} - v_{\min})/2$, where $v_{\max}$ and $v_{\min}$ are the maximum and minimum line of sight radial velocities respectively.

constraints can be obtained when combined with RV observations. Given the known inclination from transit modelling, RV observations can be used to determine mass and density for the planet. Accordingly, transiting planets are the planets we understand the best. For more detail on transit fitting, see the review chapter by Winn (2010) in Seager (2011).

Geometrically these alignments are rare—most planets do not transit, especially those more distant from their stars[17]. Observe a large enough sample of stars for long periods of time though, and you can still be successful. Herein lies the strategy of most transiting exoplanet surveys: obtaining *simultaneous* time series photometry on entire fields of stars. Following this approach, there are a number of successful ground-based surveys for transiting exoplanets. The two most successful are WASP (Wide Angle Search for Planets, Pollacco et al. 2006) and HATNet/HATSouth (Hungarian Automated Telescope Network, Bakos et al. 2004, and its southern counterpart, Bakos et al. 2013), which operate from multiple hemispheres and continents. Others include KELT (Kilodegree Extremely Little Telescope, Pepper et al. 2007), NGTS (Next-Generation Transit Survey, Wheatley et al. 2018), MASCARA (Multi-site All-Sky CAmeRA, Talens et al. 2017), TRAPPIST (Transiting Planets and Planetesimals Small Telescope, Jehin et al. 2011), and the MEarth Project (looking specifically at *M*-dwarfs for *Earth*-like planets, Irwin et al. 2008).

Collectively these surveys have discovered hundreds of planets, and greatly pushed forward the field. However, as diverse as their instrumentation and survey strategies may be, they still have one critical limitation: they're observing from the ground.

Kepler and *TESS*

Our understanding of planets fundamentally changed with the advent of space based survey telescopes like *Kepler* (Borucki et al. 2010) and *TESS* (the Transiting Exoplanet Survey Satellite, Ricker et al. 2015). The primary strength of these missions is their ability to survey the sky for weeks, months, or even years at a time uninfluenced by weather or the day/night cycle as ground-based facilities are.

To date *Kepler* and *K2* (*Kepler*'s follow-up mission after the failure of its second reaction wheel used for pointing, Howell et al. 2014), have discovered nearly 2 800 planets, with more than 3 000 candidates awaiting confirmation[18]. *Kepler* offered higher photometric precision than most ground-based facilities, and by observing the same field for several years was able to detect planets with periods measured in months or years, rather than weeks or days. The primary disadvantage of *Kepler*, other than it observing a northern field inaccessible to southern telescopes, was that most of the stars it found planets around were faint, and not well suited to ground-based precision-RV follow-up using small-to-intermediate class telescopes.

TESS can be thought of as a shallow, all-sky successor to *Kepler* addressing this limitation. Whereas *Kepler* had only a single camera and telescope pointing, *TESS* has four cameras, each of which had 26 somewhat overlapping pointings during its primary mission. The result is that *TESS* is able to observe nearly the entire sky, over which bright stars are roughly evenly distributed. Thus, while each camera has a far smaller collecting area than *Kepler* (0.95 m vs

[17]The reason for this is that a close-in planet might still transit its star if misaligned by e.g. 10°, but the angular tolerance is much lower for more distant stars.

[18]https://exoplanetarchive.ipac.caltech.edu/docs/counts_detail.html

0.1 m diameters for Kepler and *TESS* respectively), *TESS* is finding many planets more easily studied from the ground, with the brightest of these likely being among *the most* amenable of all planets to future atmospheric or chemical characterisation via transmission spectroscopy—something that requires very high SNR. While *TESS*'s reduced sensitivity is causing it to miss planets *Kepler* would have found, this only increases the importance of ground-based time-series follow-up for detecting the additional ~50% of transiting planets missed by *TESS* (Ballard 2019). Crucially, *TESS*'s photometric bandpass is redder than *Kepler*'s, making it well suited to observe cool dwarfs whose flux peaks in the NIR. The *TESS* mission is ongoing, and is now in its extended mission. To date, *TESS* has already confirmed more than 120 planets, and has more than 2 600 planets awaiting further confirmation[18] (many of which are short period massive planets around relatively faint stars).

1.5.2 Exoplanet Demographics

With the thousands of confirmed and candidate planets detected by *Kepler*, *K2*, and *TESS*, we have a large enough sample of planets to begin studying the demographics of planets—albeit with many gaps remaining. What is the distribution of planets as a function of orbital period and eccentricity? How does planet formation vary as a function of stellar spectral type or chemical composition? Or what does the planet distribution look like as a function of planet mass, radius, or age?

We have at least partial answers to some of these questions. The success of ground-based RV surveys like HARPS, and space-based transit surveys like *Kepler* and *K2* continue to further constrain exoplanet occurrence rates as a function of period, radius/mass, and spectral type (e.g. Mayor et al. 2011, Howard et al. 2012, Fressin et al. 2013, and Hsu et al. 2019 for F/G/K stars; Dressing & Charbonneau 2013, Dressing & Charbonneau 2015, Hardegree-Ullman et al. 2019, and Hsu et al. 2020 for M dwarfs). We know that giant planets on short period orbits preferentially orbit metal-rich stars (Fischer & Valenti 2005), and that giant planets of any kind are rare around low-mass stars (e.g. Johnson et al. 2010; Fressin et al. 2013; Montet et al. 2014). Perhaps the most compelling discovery yet though is that of the so called 'exoplanet radius valley'.

This feature, first discovered observationally by Fulton et al. (2017) for planets around F/G/K stars observed by the California-*Kepler* Survey (Figure 1.6), presents as a bimodality in the distribution of exoplanet radii as determined from *Kepler*. Proposed mechanisms for sculpting the gap typically invoke atmospheric mass loss via either star-planet interactions (such as photoevaporation, where weakly held planetary atmospheres are stripped via stellar flux, e.g. Owen & Wu 2013, Lee et al. 2014, Lopez & Fortney 2014, Lee & Chiang 2016, Owen & Wu 2017, Lopez & Rice 2018) or planetary evolution alone (such as core-powered mass loss, where light planetary atmospheres are eroded by the cooling luminosity from the planet's own rocky core, e.g. Ikoma & Hori 2012, Ginzburg et al. 2018, Gupta & Schlichting 2019, Gupta & Schlichting 2020). It has since been seen for *K2* planets (Hardegree-Ullman et al. 2020) and cool dwarfs from both *Kepler* and *K2* ($T_{\rm eff} < 4,700$ K, Cloutier & Menou 2020), thus providing encouraging evidence for it being a real feature.

The fortune of exoplanetary astrophysics, however, is tied up with that of stellar counterpart—one cannot truly characterise a planet without first understanding its star. This point is partic-

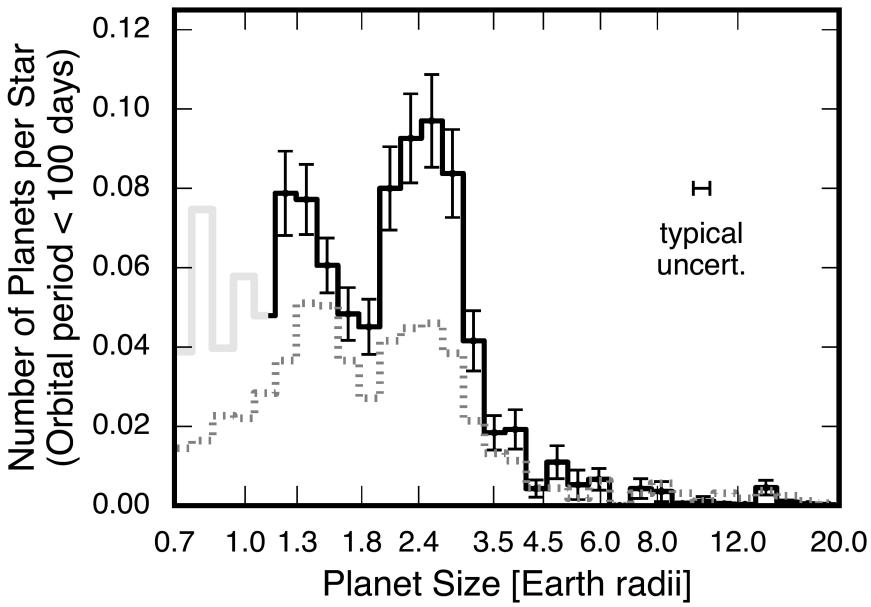

Figure 1.6: Completeness-corrected distribution of close-in exoplanet radii measured as part of the California-*Kepler* Survey in Fulton & Petigura (2018) for host stars with $4\,700 \lesssim T_{\rm eff} \lesssim 6\,500$ K. The black line shows the number of planets per star with periods less than 100 days *after* completeness-correction, and the dotted line shows the arbitrarily scaled size distribution of just the ~900 detected planets. Note the bimodal shape of both distributions, where the peak around 1.3 $R_\oplus$ corresponds to a population of mostly rocky super-Earths, and the peak around 3.0 $R_\oplus$ to a population of sub-Neptunes with more substantial atmospheres (for reference, Uranus and Neptune have radii of ~4.0 $R_\oplus$ and ~3.9 $R_\oplus$ respectively). The gap itself is thought to be the signature of exoplanet atmospheric mass loss, whereby these sub-Neptunes lose their atmospheres either through interior physical processes or star–planet interactions. This feature only becomes apparent with **a)** a large enough sample of planets; and **b)** host star temperatures and radii known to sufficiently high precision (typically a few %), which is the principal limiting factor in knowing the properties of such transiting planets.

ularly salient when considering transiting planets like those used to discover the radius valley. Analysis of transit light curves yields $R_P/R_\star$, the radius *ratio* between star and planet, not R_P alone. The implication then is that planetary radii can only be known as well as that of their host star's.

When determined solely from photometry and mostly without parallaxes, the stars from the California-*Kepler* Survey—the sample of stars used to discover the radius valley—had radius uncertainties of ~40%. When adding spectroscopic constraints and stellar modelling this decreased to ~11% (Johnson et al. 2017), with a corresponding decrease in planet radii uncertainty from ~42% to ~12%. It was with this precision that Fulton et al. (2017) first observed the radius valley. With the addition of precise stellar parallaxes from *Gaia* DR2 (Brown et al. 2018), Fulton & Petigura (2018) re-derived *physical* stellar radii (as compared to the model-based parameters from Fulton et al. 2017) for all their stars via the Stefan-Boltzmann relation. This further reduced their stellar and exoplanetary radii uncertainties to ~3% and

~5% respectively, allowing them to study the feature—and thus exoplanet demographics—in much greater detail than was possible before with poorly constrained stellar hosts.

It is clear then that understanding stars, ideally through fundamental or fundamentally-calibrated techniques, is critical to understanding their planets. By targeting bright and nearby stars, *TESS* will discover the planets most amenable to atmospheric characterisation, as well as a larger sample of planets around low-mass stars than either *Kepler* or *K2*. These planets will add exciting new dimensions to our understanding of planet formation, evolution, and chemistry, but only if we understand their hosts. Fortunately, however, the data-rich present and future of observational astrophysics is making this easier than ever before.

1.6 Thesis Outline

Having now provided the broad, but necessary, background information critical to placing this work in context, we can now move onto the remainder of this PhD thesis which is structured as follows:

- Chapter 2 presents the results of a VLTI/PIONIER interferometric survey of 16 southern stars designed to broaden the sample of temperature benchmarks available to calibrate current and future massive spectroscopic surveys. This work was published as Rains et al. (2020).

- Chapter 3 presents an overview of the FunnelWeb Survey—a planned massively-multiplexed, low resolution spectroscopic survey of two million of the brightest Southern Hemisphere stars—and presents the survey strategy and efficient observing field generation algorithm. Following the cancellation of FunnelWeb in late 2019, this work remains unpublished.

- Chapter 4 presents the results of a spectroscopic survey of 93 southern cool dwarf candidate exoplanet hosts, and characterisation of the 100 candidate planets, as identified by NASA's *TESS* mission. This work was published as Rains et al. (2021).

- Chapter 5 summarises and puts into context the work presented in this thesis, and outlines future work in the fields of stellar benchmarks, stellar parameters, non-traditional analysis techniques, ground-based stellar spectroscopic surveys, and exoplanet demographics around low mass stars.

1.7 Contributions

My main contributions to stellar and exoplanetary astrophysics are:

- I established 10 new stars as ~1% precision interferometric stellar temperature and radius benchmarks, and confirmed no substantial problems with my sample of six existing southern benchmarks (Chapter 2).

- I developed an efficient observing field generation algorithm suitable for a massively multiplexed stellar spectroscopic survey covering a wide range in magnitude (Chapter 3).

- I quantified systematics at optical wavelengths in the current generation of MARCS synthetic spectra for cool dwarfs which would otherwise bias spectral and photometric fitting and the determination of $T_{\rm eff}$ and [Fe/H] (Chapter 4).
- I developed a new photometric [Fe/H] relation—using for the first time widely available *Gaia* photometry—based on a calibration sample of 69 binary systems and accurate to ± 0.19 dex for isolated main sequence cool dwarfs (Chapter 4).
- I observed further tentative evidence that the exoplanet radius gap is present for planets around cool dwarfs—the first such evidence using *TESS*. These planets will be crucial in broadening the currently limited sample around cool dwarfs suitable for demographic studies (Chapter 4).

Chapter 2

Precision angular diameters for 16 southern stars with VLTI/PIONIER

This chapter is published in Monthly Notices of the Royal Astronomical Society as **A. D. Rains**; M. J. Ireland; T. R. White; L. Casagrande; I. Karovicova; *'Precision angular diameters for 16 southern stars with VLTI/PIONIER'*, 2020 MNRAS, 493, 2377.

2.1 Abstract

In the current era of *Gaia* and large, high signal to noise stellar spectroscopic surveys, there is an unmet need for a reliable library of fundamentally calibrated stellar effective temperatures based on accurate stellar diameters. Here we present a set of precision diameters and temperatures for a sample of 6 dwarf, 5 sub-giant, and 5 giant stars observed with the PIONIER beam combiner at the VLTI. Science targets were observed in at least two sequences with five unique calibration stars each for accurate visibility calibration and to reduce the impact of bad calibrators. We use the standard PIONIER data reduction pipeline, but bootstrap over interferograms, in addition to employing a Monte-Carlo approach to account for correlated errors by sampling stellar parameters, limb darkening coefficients, and fluxes, as well as predicted calibrator angular diameters. The resulting diameters were then combined with bolometric fluxes derived from broadband *Hipparcos-Tycho* photometry and MARCS model bolometric corrections, plus parallaxes from *Gaia* to produce effective temperatures, physical radii, and luminosities for each star observed. Our stars have mean angular diameter and temperatures uncertainties of 0.8% and 0.9% respectively, with our sample including diameters for 10 stars with no pre-existing interferometric measurements. The remaining stars are consistent with previous measurements, with the exception of a single star which we observe here with PIONIER at both higher resolution and greater sensitivity than was achieved in earlier work.

2.2 Introduction

Precision determination of fundamental stellar properties is a critical tool in the astronomers' toolkit in their mission to understand the night sky. Among the most useful of these properties are the effective temperature (or surface temperature) and physical radius of a star, which, for an individual star, provides insight into its evolutionary state, and aids in the understanding

of exoplanetary systems—particularly for putting limits on stellar irradiation or for situations where planet properties are known only relative to their star, as is the case for radii from transits (e.g. Baines et al. 2008; van Belle & von Braun 2009; von Braun et al. 2011, 2012). More broadly, when looking at populations of stars, well-constrained parameters offer observational constraints for stellar interior and evolution models (e.g. Andersen 1991; Torres et al. 2010; Piau et al. 2011; Chen et al. 2014), the calibration of empirical relations (e.g. the photometric colour-temperature scale, Casagrande et al. 2010), and detailed study of exoplanet population demographics (e.g. Howard et al. 2012; Fressin et al. 2013; Petigura et al. 2013; Fulton & Petigura 2018). However, the utility of knowing these properties precisely is matched by the difficulty inherent in measuring them. Precision observations are complicated, and most methods exist only as indirect probes of these properties, or have substantial model dependencies, limiting us to only a small subset of the stars in the sky.

Long-baseline optical interferometry, with its high spatial resolutions, is one such technique, capable of *spatially resolving* the photospheric discs of the closest and largest of stars. These arrays of telescopes have resolutions an *order of magnitude* better than the world's current largest optical telescopes fed by extreme adaptive optics systems (∼10 mas), and several orders of magnitude better than those unable to correct for the effect of atmospheric seeing at all (∼1−2 arcsec). This amounts to a resolution finer than 0.5−1.0 mas for modern interferometers, with typical errors of a few percent. When combined with bolometric flux measurements and precision parallaxes, temperature and physical radii can be determined with a similar few percent level of precision (e.g. Huber et al. 2012; White et al. 2018; Karovicova et al. 2018).

Increasing the sample of stars with fundamentally calibrated effective temperatures is critical in the era of *Gaia* (Gaia Collaboration et al. 2016b) and ground based high-SNR spectroscopic surveys such as GALAH (De Silva et al. 2015), APOGEE (Allende Prieto et al. 2008), and the upcoming SDSS-V (Kollmeier et al. 2017)). Internal errors on modern techniques for spectroscopic temperature determination are at the level of $< 1.5\%$ (e.g. using the Cannon, Ho et al. 2016, trained on values from more fundamental techniques, see Nissen & Gustafsson 2018 for a summary), meaning that in order to be useful, diameter calibration at the level of $< 1\%$ is required to put these surveys on an absolute scale. Whilst possible to measure $T_{\rm eff}$ spectroscopically, it is not yet possible to calibrate temperature scales at the < 100 K level from spectra alone (particularly when using different analysis techniques, e.g. Lebzelter et al. 2012), as non-local thermodynamic equilibrium and 3D effects become important, particularly for where $\log g$ and [Fe/H] remain uncertain (e.g. Yong et al. 2004; Bensby et al. 2014). Angular diameters offer a direct approach to determining $T_{\rm eff}$ when combined with precision flux measurements, such as those readily available from the *Hipparcos-Tycho* (Høg et al. 2000), *Gaia* (Gaia Collaboration et al. 2016b; Brown et al. 2018), and *WISE* (Wright et al. 2010) space missions.

Here we present precision angular diameters, effective temperatures, and radii for 16 southern dwarf, subgiant, and giant stars, 10 of which have no prior angular diameter measurements. We accomplish this using PIONIER, the Precision Integrated-Optics Near-infrared Imaging ExpeRiment (Bouquin et al. 2011), the shortest-wavelength (H-band, $\lambda\sim1.6\,\mu$m), highest precision beam combiner at the Very large Telescope Interferometer (VLTI), on the longest available baselines in order to extend the very small currently available library of 1% level diameters.

2.3 Observations and Data Reduction

2.3.1 Target Selection

The primary selection criteria for our target sample was for southern dwarf or subgiant stars lacking existing precision interferometric measurements with predicted angular diameters > 1.0 mas such that they could be sufficiently resolved using the longest baselines of the VLTI. Stars were checked for known multiplicity using *SIMBAD*, the *Washington Double Star Catalogue* (Mason et al. 2001), the *Sixth Catalog of Orbits of Visual Binary Stars* (Hartkopf et al. 2001), and the *9th Catalogue of Spectroscopic Binary Orbits* (Pourbaix et al. 2004) and ruled out accordingly. The list of science targets can be found in Table 2.1 along with literature spectroscopic $T_{\rm eff}$, $\log g$, and [Fe/H]. All targets are brighter than $H{\sim}3.1$, limiting available high precision photometry to the space-based *Hipparcos-Tycho*, *Gaia*, and *WISE* missions, with *2MASS* notably being saturated for most targets. Where uncertainties on $\log g$, and [Fe/H] were not available, conservative uncertainties of 0.2 dex and 0.1 dex were adopted respectively.

Figure 2.1 presents a $(B-V)$ colour-magnitude diagram of the same targets using *Tycho-2* $B_{\rm T}$ and $V_{\rm T}$ photometry (converted using the relations from Bessell 2000), and *Gaia* DR2 parallaxes to calculate the absolute $V_{\rm T}$ magnitudes. Overplotted are ~Solar metallicity (Z=0.058) BASTI evolutionary tracks (Pietrinferni et al. 2004). Given that these targets are within the extent of the Local Bubble ($\lesssim$ 70 pc, e.g. Leroy 1993; Lallement et al. 2003), we assume that they are unreddened. Distances are calculated incorporating the systematic parallax offset of -82 ± 33 μas found by Stassun & Torres (2018).

τ Cet, ϵ Eri, δ Eri, 37 Lib, and β Aql form part of an overlap sample with the PAVO beam combiner (Ireland et al. 2008) on the northern CHARA array (ten Brummelaar et al. 2005), with diameters to be published in White et al. (in prep) enabling consistency checks between the northern and southern diameter sample.

2.3.2 Calibration Strategy

The principal data product for the interferometric measurement of stellar angular diameters is the *fringe visibility*, V, which can be defined as the ratio of the *amplitude* of interference fringes, and their *average intensity* as follows:

$$V = \frac{\text{fringe amplitude}}{\text{average fringe intensity}} \tag{2.1}$$

where V varies between 0, for completely resolved targets (e.g. resolved discs, well-separated binary components), and 1 for completely unresolved targets (i.e. a point source). V is a function of both the projected baseline and the wavelength of observation, combining to give a characteristic *spatial frequency* at which observations are made.

When performing ground-based interferometric observations in real conditions, the combined effect of atmospheric turbulence and instrumental factors (e.g. optical aberrations) is to reduce the measured science target visibility $V_{\rm sci,measured}$ from its true value. To account for this, calibrator stars are observed to obtain a measure of the combined atmospheric and instrumental transfer function $V_{\rm system}$ in order to calibrate the $V_{\rm sci,measured}$ and determine their true value of $V_{\rm sci,corrected}$. Ideal calibrators meet four criteria: they are single unresolved point-sources to

Table 2.1: Science targets

Star	HD	RA[a] (hh mm ss.ss)	DEC[a] (dd mm ss.ss)	SpT[b]	V_T^c (mag)	H^d (mag)	$T_{\rm eff}$ (K)	$\log g$ (dex)	[Fe/H] (dex)	$v \sin i$ (km s^{-1})	Plx[a] (mas)	Refs
τ Cet	10700	01 44 02.23	-16 03 58.32	G8V	3.57	1.8	5310 ± 17	4.44 ± 0.03	-0.52 ± 0.01	1.60	277.52 ± 0.52	1,1,1,2
α Hyi	12311	01 58 46.77	-62 25 48.93	F0IV	2.87	1.9	7165 ± 64	3.67 ± 0.20	0.07 ± 0.10	118.00	51.55 ± 0.83	3,4,4,5
χ Eri	11937	01 55 58.59	-52 23 32.60	G8IV	3.80	1.9	5135 ± 80	3.42 ± 0.10	-0.18 ± 0.07	4.50	57.38 ± 0.33	6,6,6,7
95 Cet A	20559	03 18 22.68	-1 04 10.02	-	5.60	-	4684 ± 71	2.64 ± 0.14	-0.15 ± 0.05	1.60	15.63 ± 0.18	8,8,8,9
ϵ Eri	22049	03 32 54.82	-10 32 30.58	K2V	3.81	1.9	5049 ± 48	4.45 ± 0.09	-0.15 ± 0.03	4.08	312.22 ± 0.47	1,1,1,10
δ Eri	23249	03 43 14.80	-10 14 23.33	K0+IV	3.62	1.7	5027 ± 48	3.66 ± 0.10	0.07 ± 0.03	6.79	110.22 ± 0.42	1,1,1,10
40 Eri A	26965	04 15 13.98	-8 19 56.63	K0V	4.51	2.6	5098 ± 32	4.35 ± 0.10	-0.36 ± 0.02	2.10	198.57 ± 0.51	1,1,1,2
37 Lib	138716	15 34 11.03	-11 56 04.05	K1III-IV	4.72	2.3	4816 ± 70	3.05 ± 0.19	-0.05 ± 0.06	4.50	35.19 ± 0.25	8,8,8,9
β TrA	141891	15 55 08.13	-64 34 03.16	F1V	2.85	2.2	7112 ± 64	4.22 ± 0.07	-0.29 ± 0.10	69.63	79.43 ± 0.58	3,11,4,10
λ Sgr	169916	18 27 58.19	-26 34 39.01	K1IIIb	2.92	0.4	4778 ± 37	2.66 ± 0.10	-0.11 ± 0.03	3.81	38.78 ± 0.63	12,13,12,14
δ Pav	190248	20 08 46.71	-67 48 47.04	G8IV	3.62	2.0	5604 ± 38	4.26 ± 0.06	0.33 ± 0.03	0.32	164.05 ± 0.36	1,1,1,10
ϵ Ind	209100	22 03 29.14	-57 12 11.15	K5V	4.83	2.3	4649 ± 74	4.63 ± 0.01	-0.13 ± 0.06	2.00	274.80 ± 0.25	1,8,1,15
HD131977	131977	14 57 29.15	-22 34 37.56	K4V	5.88	3.1	4507 ± 58	4.76 ± 0.06	0.12 ± 0.03	7.68	170.01 ± 0.09	16,17,17,10
η Sco	155203	17 12 09.22	-44 45 34.45	F5IV	3.36	2.3	6724 ± 106	3.65 ± 0.20	-0.29 ± 0.10	150.00	45.96 ± 0.44	18,4,4,19
β Aql	188512	19 55 18.84	06 24 16.90	G8IV	3.81	1.9	5062 ± 57	3.54 ± 0.14	-0.19 ± 0.05	22.28	74.76 ± 0.36	8,8,8,10
HR7221	177389	19 09 53.30	-69 34 31.31	K0IV	5.41	3.1	5061 ± 26	3.49 ± 0.09	-0.05 ± 0.02	-	27.04 ± 0.09	12,12,12,-

Notes: [a]Gaia Brown et al. (2018) - note that Gaia parallaxes listed here have not been corrected for the zeropoint offset, [b]SIMBAD, [c]Tycho Høg et al. (2000), [d]2MASS Skrutskie et al. (2006)

References for spectroscopic $T_{\rm eff}$, $\log g$, [Fe/H], and $v \sin i$: 1. Delgado Mena et al. (2017), 2. Jenkins et al. (2011), 3. Blackwell & Lynas-Gray (1998), 4. Erspamer & North (2003), 5. Royer et al. (2007), 6. Fuhrmann et al. (2017), 7. Schröder et al. (2009), 8. Ramírez et al. (2013), 9. Massarotti et al. (2008), 10. Martínez-Arnáiz et al. (2010), 11. Allende Prieto et al. (2004), 12. Alves et al. (2015), 13. Liu et al. (2007), 14. Hekker & Meléndez (2007), 15. Torres et al. (2006), 16. Boyajian et al. (2012b), 17. Valenti & Fischer (2005), 18. Casagrande et al. (2011), 19. Mallik et al. (2003),

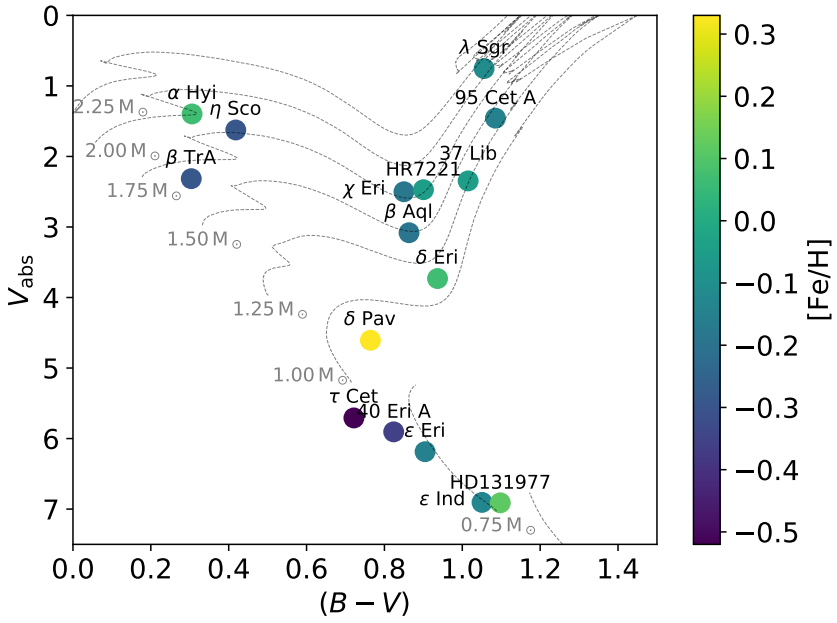

Figure 2.1: $(B-V)$ colour magnitude diagram for science targets with overplotted BASTI evolutionary tracks for Z= 0.058

the interferometer, have no close companions or other asymmetries (e.g. oblate due to rapid rotation), and are both proximate on sky and close in magnitude to the science target. Being close on sky ensures they are similarly affected by atmospheric turbulence (and thus suffer from the same systematics), and similar in magnitude ensures the detector can be operated in the same mode (e.g. same exposure time and gain). Their status of isolated or single stars means that their observation is insensitive to projected baseline geometry.

With all of these criteria met, and calibrator observations taking place immediately before or after science target observations, the measured calibrator visibility $V_{\mathrm{cal,measured}}$ can be used to determine V_{system} provided a prediction of the *true* calibrator visibility $V_{\mathrm{cal,predicted}}$ is available in the from of a predicted limb darkened angular diameter $\theta_{\mathrm{LD,cal}}$. In practice the significance of the dependency on knowing the (typically unmeasured) diameter of a calibrator is minimised by choosing calibrators much smaller in angular size than their respective science targets (ideally $\theta_{\mathrm{LD,cal}} \leq \frac{1}{2}\theta_{\mathrm{LD,sci}}$ in practice), such that even large $\theta_{\mathrm{LD,cal}}$ uncertainties do not significantly change $V_{\mathrm{cal,measured}}$ for the mostly/entirely unresolved calibrator. This is formalised below in Equations 2.2 and 2.3:

$$V_{\mathrm{sci,corrected}} = \frac{V_{\mathrm{tar,measured}}}{V_{\mathrm{system}}} \tag{2.2}$$

with

$$V_{\mathrm{system}} = \frac{V_{\mathrm{cal,measured}}}{V_{\mathrm{cal,predicted}}} \tag{2.3}$$

This is not feasible in practice, particularly for stars as bright as those considered here,

where it is difficult to find unresolved (yet bright) neighbouring stars. Given this limitation, the decision was made to observe a total of five calibrators per science target which, on average, meet the criteria. This lead to the observation of two separate CAL-SCI-CAL-SCI-CAL sequences—one for *bright*, but often more distant and resolved, stars, and another for those more *faint*, but closer and less resolved. Calibrators from bright and faint sequences have $\theta_{\rm LD,cal}$, on average, $0.59\theta_{\rm LD,sci}$, and $0.47\theta_{\rm LD,sci}$ respectively. This large number of calibrators allows for the possibility of unforeseen bad calibrators (e.g. resolved binaries) without compromising on the ability to calibrate the scientific observations.

Calibrators were selected using *SearchCal*[1] (Bonneau et al. 2006, 2011), and the `pavo_ptsrc` IDL calibrator code (maintained within the CHARA/PAVO collaboration), with the the list of calibrators used detailed in Table A.2.

Interstellar extinction was computed for stars more distant than 70 pc using intrinsic stellar colours from Pecaut & Mamajek (2013) for the main sequence and Aller et al. (1982) for spectral types III, II, Ia, Ib, with the subgiant branch interpolated as being halfway between spectral types V and III. We note that this approach is, at best, an approximation, but more complete or modern catalogues of intrinsic stellar colours are not available, and 3-dimensional dust maps (e.g. Green et al. 2015, 2018) are incomplete for the southern hemisphere. With intrinsic colours in hand, B, V, $H_{\rm P}$, $B_{\rm T}$, $V_{\rm T}$, and $R_{\rm P}$ photometry could be corrected for the effect of reddening using the extinction law of Cardelli et al. (1989) implemented in the `extinction`[2] python package. This approach was not applied to *WISE* photometry however for the joint reasons of being less subject to extinction in the infrared, and what extinction (or even emission, e.g. Fritz et al. 2011) occurs being difficult to parameterise and not covered by the same relations that hold at optical wavelengths.

Angular diameters for calibrators were predicted using surface brightness relations from Boyajian et al. (2014), prioritising those with *WISE* $W3$ or $W4$ magnitudes to minimise the effect of interstellar reddening. A $(V-W3)$ relation was used for 59 stars, the majority of our calibrator sample, with Johnson V band magnitudes converted from *Tycho*-2 catalogue $V_{\rm T}$ band (Høg et al. 2000) per the conversion outlined in Bessell (2000), and another three with unavailable or saturated $W3$ using a $(V-W4)$ relation.

The remaining three stars lacked *WISE* magnitudes altogether, and whilst a $(B-V)$–[Fe/H] relation (converting $B_{\rm T}$ to B, also per Bessell 2000) from Boyajian et al. (2014) was used for HD 16970A ([Fe/H]=0.0, Gray et al. 2003), HD 20010A and HD 24555 lack literature measurements of [Fe/H] which the simpler $(B-V)$ relation is highly sensitive to. To get around both this sensitivity and the saturated nature of *2MASS* photometry for such bright stars, $(V-K)$ was computed from $(V_{\rm T}-R_{\rm P})$ via a third order polynomial fit to the photometry of a million synthetic stars ($4\,500 < T_{\rm eff} < 7\,500$, $2 < \log g < 5$, $-1 < [Fe/H] < 0.5$) using the methodology and software of Casagrande & VandenBerg (2014, 2018a). This fit was:

$$Y = 0.2892625 + 0.643771X + 2.5184359X^2 - 1.121815X^3 \tag{2.4}$$

where Y and X are the $(V-K)$ and $(V_{\rm T}-R_{\rm P})$ colours respectively.

[1] https://www.jmmc.fr/searchcal_page.htm
[2] https://github.com/kbarbary/extinction

2.3.3 Interferometric Observations

VLTI (Haguenauer et al. 2010) PIONIER (Bouquin et al. 2011) observations were undertaken in service mode during ESO periods 99, 101, and 102 (2017-2019), using the four 1.8 m Auxiliary Telescopes on the two largest configurations: A0-G1-J2-J3 and A0-G1-J2-K0 (58-132 m and 49-129 m baselines respectively). The service mode observations had the constraint of clear skies and better than 1.2 arcsec seeing. Two 45 min CAL-SCI-CAL-SCI-CAL sequences were observed per target, with each target having five calibrator stars in total (with one shared between each sequence). In practice this looked something like CAL1-SCI-CAL2-SCI-CAL3 and CAL1-SCI-CAL4-SCI-CAL5, but with the calibrators in each sequence ordered by their respective sidereal time constraints (i.e. by taking into account shadowing from the four Unit Telescopes). PIONIER was operated in GRISM mode (6 spectral channels) for the entirety of the program.

PIONIER observations are summarised in Table 2.2. Note that δ Eri, 40 Eri A, and β TrA were reobserved to complete both bright and faint sequences, with both τ Cet, and ϵ Ind serving as useful inter-period diagnostics of identical sequences.

We note that all targets had sequences observed over at least two nights, with the exception of 37 Lib and β Aql which had their bright and faint sequences observed on the same night. As discussed in detail by Lachaume et al. (2019), there are correlated uncertainties for observations taken within a given night (e.g. atmospheric effects, instrumental drifts), reducing the accuracy of the resulting diameter fits. The consequence of this for these two stars is that any systematics in wavelength scale calibration are the same for both sequences.

2.3.4 Wavelength Calibration

The accuracy of model fits to visibility measurements depends not only on the uncertainties in the observed visibilities, but the spatial frequencies at which we measure them. The spatial frequencies here are also the working resolution of the interferometer, and any uncertainties in the baseline length or wavelength scale will affect the results. Uncertainties in the wavelength scale dominate this, with the effective wavelength conservatively having an accuracy of ±1% (Bouquin et al. 2011) or even ±2% (per the PIONIER manual[3]), whereas the VLTI baseline lengths are known to cm precision resulting in an uncertainty of ±0.02% for the shortest baselines.

PIONIER's spectral dispersion is known to change with time, and is calibrated once per day by the instrument operations team at Paranal. This calibration is identical to a single target observation in all respects save its use of an internal laboratory light source, with the resulting fringes used as a Fourier transform spectrometer to measure the effective wavelength of each channel. Effective wavelengths, accurate to ~1.5%, are then assumed 'constant' for all subsequent observations that night. Calibration data were downloaded from the ESO Archive where, at least for service mode observations, they are stored under the program ID 60.A-9209(A).

Another aspect of instrumental stability to be considered is whether the piezo hardware used to construct each interferometric scan of path delay is constant with respect to time. This

[3] https://www.eso.org/sci/facilities/paranal/instruments/pionier/manuals.html

Table 2.2: Observing log. Note that five unique calibrators were observed per science target, though some later needed to be excluded due to factors such as binarity.

Star	UT Date	ESO Period	Sequence Type	Baseline	Calibrator HD	Calibrators Used
ϵ Ind	2017-07-22	99	faint	A0-G1-J2-K0	205935, 209952, 212878	3
α Hyi	2017-07-24	99	faint	A0-G1-J2-K0	1581, 15233, 19319	2
χ Eri	2017-07-24	99	bright	A0-G1-J2-K0	1581, 11332, 18622	2
β TrA	2017-07-25	99	bright	A0-G1-J2-K0	128898, 136225, 165040	3
37 Lib	2017-07-25	99	bright	A0-G1-J2-K0	132052, 141795, 149757	3
37 Lib	2017-07-25	99	faint	A0-G1-J2-K0	136498, 139155, 149757	3
α Hyi	2017-07-26	99	bright	A0-G1-J2-J3	1581, 11332, 18622	2
χ Eri	2017-07-27	99	faint	A0-G1-J2-J3	10019, 11332, 18622	2
ϵ Ind	2017-08-17	99	bright	A0-G1-J2-K0	197051, 209952, 219571	3
τ Cet	2017-08-17	99	faint	A0-G1-J2-K0	9228, 10148, 18978	3
λ Sgr	2017-08-26	99	faint	A0-G1-J2-J3	166464, 167720, 175191	2
τ Cet	2017-08-26	99	bright	A0-G1-J2-J3	9228, 17206, 18622	2
95 Cet A	2017-08-26	99	bright	A0-G1-J2-J3	16970A, 19994, 22484	3
δ Pav	2017-08-27	99	faint	A0-G1-J2-J3	192531, 197051, 197359	3
95 Cet A	2017-09-01	99	faint	A0-G1-J2-J3	16970A, 19866, 20699	3
ϵ Eri	2017-09-04	99	faint	A0-G1-J2-J3	16970A, 21530, 25725	2
40 Eri A	2017-09-04	99	faint	A0-G1-J2-J3	24780, 26409, 27487	3
ϵ Eri	2017-09-05	99	bright	A0-G1-J2-J3	16970A, 20010A, 24555	3
λ Sgr	2017-09-08	99	bright	A0-G1-J2-J3	165634, 169022, 175191	2
δ Pav	2017-09-12	99	bright	A0-G1-J2-J3	169326, 197051, 191937	3
δ Eri	2017-09-24	99	faint	A0-G1-J2-J3	16970A, 23304, 26464	3
β TrA	2018-04-18	101	faint	A0-G1-J2-J3	128898, 140018, 143853	3
β Aql	2018-06-04	101	bright	A0-G1-J2-J3	182835, 189188, 194013	3
β Aql	2018-06-04	101	faint	A0-G1-J2-J3	182835, 193329, 189533	3
ϵ Ind	2018-06-04	101	bright	A0-G1-J2-J3	197051, 209952, 219571	3
HD131977	2018-06-05	101	faint	A0-G1-J2-J3	129008, 133649, 133670	3
HR7221	2018-06-05	101	bright	A0-G1-J2-J3	161955, 165040, 188228	3
ϵ Ind	2018-06-06	101	faint	A0-G1-J2-J3	205935, 209952, 212878	3
η Sco	2018-06-06	101	bright	A0-G1-J2-J3	135382, 158408, 160032	2
HD131977	2018-06-06	101	bright	A0-G1-J2-J3	129502, 133627, 133670	3
HR7221	2018-06-06	101	faint	A0-G1-J2-J3	165040, 172555, 173948	2
η Sco	2018-06-07	101	faint	A0-G1-J2-J3	152236, 152293, 158408	1
τ Cet	2018-08-06	101	bright	A0-G1-J2-J3	4188, 9228, 17206	3
β TrA	2018-08-07	101	bright	A0-G1-J2-J3	128898, 136225, 165040	3
τ Cet	2018-08-07	101	faint	A0-G1-J2-J3	9228, 10148, 18978	3
δ Eri	2018-11-25	102	bright	A0-G1-J2-J3	16970A, 20010A, 24555	3
δ Eri	2018-11-26	102	faint	A0-G1-J2-J3	16970A, 23304, 26464	3
40 Eri A	2018-11-26	102	bright	A0-G1-J2-J3	26409, 26464, 33111	3
40 Eri A	2018-11-26	102	faint	A0-G1-J2-J3	24780, 26409, 27487	3

is not a standard part of the instrument's daily calibration routine, however, and PIONIER lacks the internal laser source required to simply perform this procedure. As such, particularly given the potential for this being a limiting factor in high precision observations, several studies have sought to investigate the stability of PIONIER via a variety of means.

Kervella et al. (2017), seeking to measure the radii and limb darkening of α Centauri A and B, were limited by this uncertainty, and spent time investigating both its magnitude and long term stability. They used the binary system HD 123999, well constrained from two decades of monitoring (Boden et al. 2000, 2005; Tomkin & Fekel 2006; Konacki et al. 2010; Behr et al.

2011), as a dimensional calibrator, and compared literature orbital solutions to those derived from their PIONIER observations. The result was a wavelength scaling factor determined through comparison of best-fit semi-major axis values from Boden et al. (2005), Konacki et al. (2010), and the authors' of $\gamma = 1.00481 \pm 0.00412$, where γ is a multiplicative offset in the PIONIER wavelength scale, and its uncertainty the fractional standard deviation of each measurement of the semi-major axis. This uncertainty of 0.41% was then added in quadrature with all derived angular diameters instead of the 2% quoted in the PIONIER manual. These results were also found to be consistent (within 0.8σ) with another binary, HD 78418, also studied by Konacki et al. (2010) yielding $\gamma = 1.00169$, though with only two points this served only as a check.

Gallenne et al. (2018), as part of their investigation into red-clump stars, also spent time confirming the wavelength scale of PIONIER using a different approach: through spectral calibration in conjunction with the second generation VLTI instrument GRAVITY (Eisenhauer et al. 2011). Through interleaved observations with both instruments over two half nights of the previously characterised binary TZ For (Gallenne et al. 2016), they studied the orbital separation of the binary, taking advantage of GRAVITY's internal laser reference source (accurate to $< 0.02\%$) for calibration. Combining data they found a relative difference of 0.35% in the measured separations, consistent with Kervella et al. (2017), which was taken to be the systematic uncertainty of the PIONIER wavelength calibration. The authors do not report a *systematic* offset equivalent to γ from Kervella et al. (2017), only a relative uncertainty, with subsequent work involving authors of both investigations using only this relative value (Gallenne et al. 2019).

Lachaume et al. (2019), and the associated Rabus et al. (2019), undertook investigation into the statistical uncertainties and systematics when using PIONIER to measure diameters for under-resolved low-mass stars. They make use of the findings of Gallenne et al. (2018) and take the uncertainty on the central wavelength of each spectral channel, and thus the spatial frequency itself, to be $\pm 0.35\%$. Rather than applying this uncertainty to the x-axis spatial frequency values during modelling, they instead translate the error to a y-axis uncertainty in visibility. During modelling, the uncertainties are sampled and treated as a correlated systematic source of error for all observations taken on a single night with the same configuration, and uncorrelated otherwise.

With these recent results in mind, the wavelength calibration strategy for this work is to use the spectral dispersion information calibration available on each night, and adopt an uncertainty of 0.35% on our wavelength scale per the conclusions of Kervella et al. (2017) and Gallenne et al. (2018). Following the approach of subsequent investigations (Rabus et al. 2019; Lachaume et al. 2019; Gallenne et al. 2019), we do not consider a systematic offset in the wavelength scale. For the results described here, this relative uncertainty is added in quadrature with all bootstrapped angular diameter uncertainties.

2.3.5 Data Reduction

A single CAL-SCI-CAL-SCI-CAL sequence generates five interferograms and a single dark exposure per target (each consisting of 100 scans), plus a set of flux splitting calibration files known as a 'kappa matrix' (consisting of four files, each with a separate telescope shutter open).

This produces 34 files per observational sequence, though this can be more in practice if more observations are required to replace those of poor quality. This raw data can be accessed and downloaded in bulk through the ESO archive [4].

`pndrs`[5] (Bouquin et al. 2011), the standard PIONIER data reduction pipeline, was used to go from raw data to calibrated squared visibility (V^2) measurements of our science targets. During reduction the exposures are averaged together, to produce 36 V^2 points for each of the two science target observations (six wavelength channels on six independent baselines), resulting in 72 V^2 points for the entire sequence. `pndrs` uses the calibrators in the bracketed sequence to determine the instrumental and atmospheric transfer function by interpolating in time.

The python package `reach`[6], written for this project, was used to interface with `pndrs` to perform simple tasks such as providing files of calibrator estimated diameters, and using the standard `pndrs` script reading functionality to exclude bad calibrators (e.g. binaries) or baselines (e.g. lost tracking) from being using for calibration. `reach` also exists to perform the more complex task of accurate V^2 uncertainty estimation considering correlated or non-Gaussian errors. Similar to the approach of Lachaume et al. (2014, 2019), we perform a bootstrapping algorithm on the calibrated interferograms within each given CAL-SCI-CAL-SCI-CAL sequence, in combination with Monte Carlo sampling of the predicted calibrator angular diameters, and science target stellar parameters ($T_{\rm eff}$, $\log g$, and [Fe/H]) and magnitudes, for calculation of limb darkening coefficients, bolometric fluxes (see Sections 2.4.1-2.4.5), radii, and luminosities.

Our bootstrapping implementation samples (with repeats) the five interferograms of each science or calibrator target in the sequence independently, rather than sampling from the combined 10 science and 15 calibrator interferograms respectively. In addition, predicted calibrator angular diameters are sampled at each step from a normal distribution using the uncertainties on the colour-angular diameter relations. The results as presented here were bootstrapped 5 000 times, fitting for both $\theta_{\rm UD,sci}$ and $\theta_{\rm LD,sci}$, and calculating $f_{\rm bol}$, $T_{\rm eff}$, radius ($R_\star$), and luminosity ($L_\star$) once per iteration. Final values for each parameter, as well as each ${V_{\rm tar,corrected}}^2$ point (for the plots in Figure 2.2), and their uncertainties were calculated through the mean and standard deviations of the resulting probability distributions. The Monte Carlo/diameter fitting process was then completed once more in its entirety, but sampling our interferometry derived $T_{\rm eff}$ values in place of their literature equivalents from Table 2.1. The effect of this is for our limb darkening coefficients and bolometric fluxes to be sampled with less scatter by using values with smaller and more consistent uncertainties, in effect 'converging' to the final reported values in Table 2.4.

[4] https://archive.eso.org/cms.html
[5] https://www.jmmc.fr/data_processing_pionier.htm
[6] https://github.com/adrains/reach

2.4 Results

2.4.1 Limb Darkened Angular Diameters

A linearly-limb darkened disc model is a poor fit to both real and model stellar atmospheres, but in order to properly resolve the intensity profile and take advantage of higher order limb darkening laws (e.g. Equation 2.5 below, from Claret 2000), one must resolve beyond the first lobe of the visibility profile:

$$\frac{I(\mu)}{I(1)} = 1 - \sum_{k=1}^{4} a_k (1 - \mu^{\frac{k}{2}}) \tag{2.5}$$

where $I(1)$ is the specific intensity at the centre of the stellar disc, $\mu = \cos(\gamma)$ with angle γ between the line of sight and emergent intensity, k the polynomial order, and a_k the associated coefficient.

In the first and second lobes, the visibilities of a 4-term limb darkening law are nearly indistinguishable from linearly darkened model of slightly different diameter and appropriate coefficient. We thus model the intensity profile with a four term law, interpolating the 3D STAGGER grid of model atmospheres (Magic et al. 2015) initially with the $T_{\rm eff}$, $\log g$, and [Fe/H] given in Table 2.1, then a second and final time using the resulting estimate of the interferometric $T_{\rm eff}$. Note that STAGGER assumes $v \sin i = 0\,{\rm km\,s^{-1}}$, however the fastest rotating stars in our sample are too hot for the grid (discussed below), minimising the influence of this limitation.

For the results presented here, obtained at the highest resolution possible at the VLTI, we resolve only the first lobe for all stars bar λ Sgr (see Section 2.4.2). This means that we do not resolve the intensity profile well enough to take full advantage of higher order polynomial limb darkening laws. Given this limitation, the best approach, which can be considered analogous to reducing the resolution of the model to the resolution of the data available, would be an equivalent linear coefficient to the four term model described above. The so called 'equivalent linear coefficient' is the coefficient that gives the same side-lobe height for both models, though with a slightly smaller value of $\theta_{\rm LD}$ of the order $0.4 - 0.5\%$, corrected for by the scaling factor s_λ. This is formalised in White et al. (in prep).

For each target we fitted a modified linearly limb darkened disc model per Hanbury Brown et al. (1974):

$$V^2 = C\left(\left(\frac{1-u_\lambda}{2} + \frac{u_\lambda}{3}\right)^{-1}\left[(1-u_\lambda)\frac{J_1(x)}{x} + u_\lambda(\pi/2)^{1/2}\frac{J_{3/2}(x)}{x^{3/2}}\right]\right)^2 \tag{2.6}$$

with

$$x = \pi B s_\lambda \theta_{\rm LD} \lambda^{-1} \tag{2.7}$$

where V is the calibrated fringe visibility, C is an intercept scaling term, u_λ is the wavelength dependent linear limb darkening coefficient, s_λ the wavelength dependent diameter scaling term, $J_n(x)$ is the n^{th} order Bessel function of the first kind, B is the projected baseline, and λ is the observational wavelength. Fitting was performed using `scipy`'s *fmin* minimisation routine with a χ^2 loss function.

The intercept term C, and diameter scaling parameter s_λ, are the sole modifications to the

standard linearly darkened disc law. In the ideal case where all calibrators are optimal and the system transfer function is estimated perfectly, C would not be required as the calibrated visibilities would never be greater than 1. With non-ideal calibrators however, the calibration is imperfect and this is no longer the case. Deviations from $V^2 \leq 1$ are generally small, but in the case of our bright science targets with faint calibrators, `pndrs` had significant calibration issues, something discussed further in Section 2.4.3. Thus, whilst the fitting was done simultaneously on data from all sequences, each sequence of data was fit with a separate value of C. We also fit for the uniform disc diameter $\theta_{\rm UD}$ using Equation 2.6, but set $u_\lambda = 0$ for the case of no limb darkening.

Usage of the STAGGER grid also confers another advantage: the ability to compute u_λ for each wavelength channel of PIONIER, rather than the grid being defined broadly for the entire H-band as in Claret & Bloemen (2011). Thus, when fitting Equation 2.6, u_λ is actually a vector of length 6 - one for each of the PIONIER wavelength channels ($\lambda \approx 1.533, 1.581, 1.629, 1.677, 1.7258, 1.773\,\mu$m). STAGGER however covers a limited parameter space, with the coolest stars in our sample (ϵ Ind, HD 131977), and the hottest (α Hyi, η Sco, β Aql), falling outside the grid bounds. For these stars, the grid of Claret & Bloemen (2011) is interpolated (with microturbulent velocity of $2\,{\rm km\,s^{-1}}$) for the sampled parameters and used instead, which in practice means $u_{\lambda,1-6}$ are identical, and $s_{\lambda,1-6} = 1.0$. Table A.3 quantifies the difference in $\theta_{\rm LD}$ obtained using each of these two approaches.

Figure 2.2 shows V^2 fits for each of our science targets, with point colour corresponding to the observational wavelength (where darker points correspond to redder wavelengths). Note that fitting for both $\theta_{\rm UD}$ and $\theta_{\rm LD}$ was done once per bootstrapping iteration, such that these plots use the mean and standard deviations of the final distributions for each V^2 point, C, u_λ, s_λ, and $\theta_{\rm LD}$. To aid readability by showing only a single diameter fit for each star, each sequence of data has been normalised by its corresponding value of C.

Final values for $\theta_{\rm UD}$ and $\theta_{\rm LD}$ fits, with the systematic uncertainty of PIONIER's wavelength scale added in quadrature, are presented in Table 2.4, and adopted u_λ and s_λ in Table A.4.

2.4.2 Limb Darkening of λ Sgr

Figure 2.3 shows a zoomed in plot of the λ Sgr fit, focusing on the resolved sidelobe. Comparing the model fits to the uniform disc curve, the effect of limb darkening is clear. However, with only a single star from our sample being this well resolved, it is difficult to comment on whether the observed limb darkening is consistent with models. Using PIONIER Kervella et al. (2017) found their α Centauri A and B results to be significantly less limb darkened than both 1D and 3D model atmosphere predictions. A similar investigation at the CHARA Array is ongoing, with results to be published as White et al. (in prep).

2.4.3 Transfer Function Calibration

In the case of perfect calibration, that is to say the influence of the system transfer function on the measured visibilities has been entirely removed, V^2 should be $0 \leq V^2 \leq 1$ and consistent with a limb darkened disc model for single stars. For many of our sequences, this was not the case, resulting in significant calibration issues where measured V^2 was systematically higher

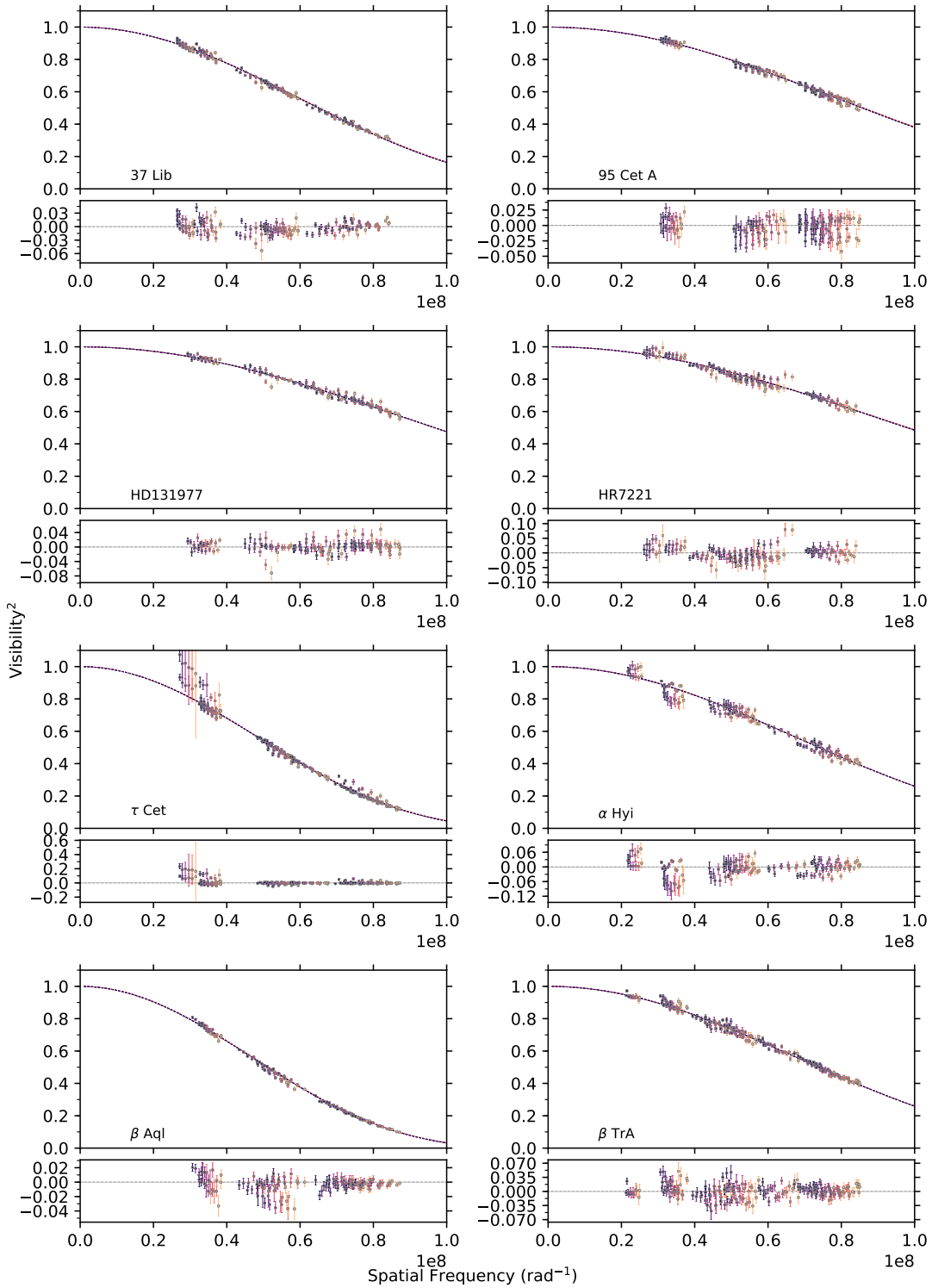

Figure 2.2: V^2 fits using final means and standard deviations from bootstrapped distributions. Point colour corresponds to one of the six PIONIER wavelength channels, with darker points being redder wavelengths.

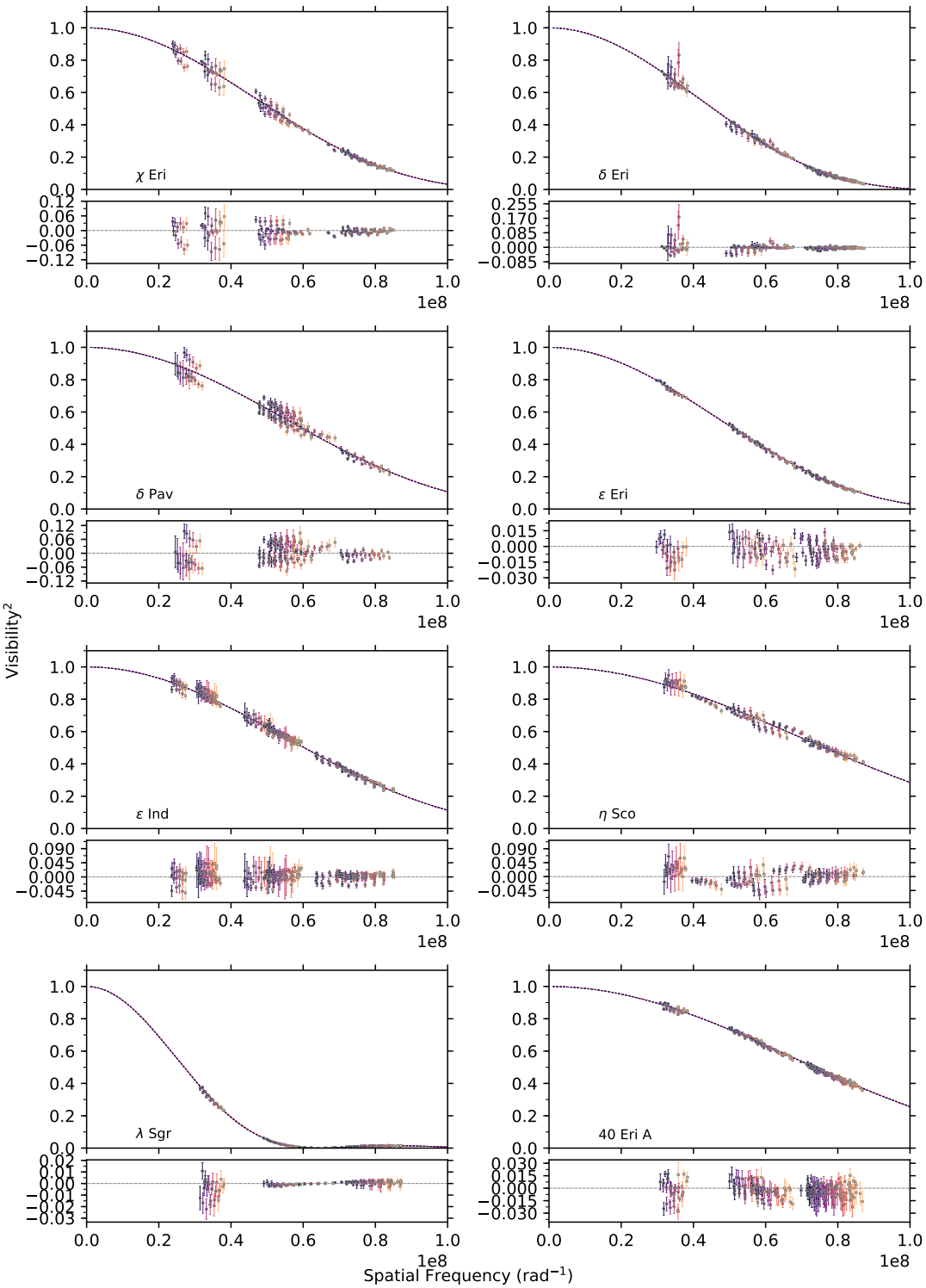

Figure 2.2: *– continued*

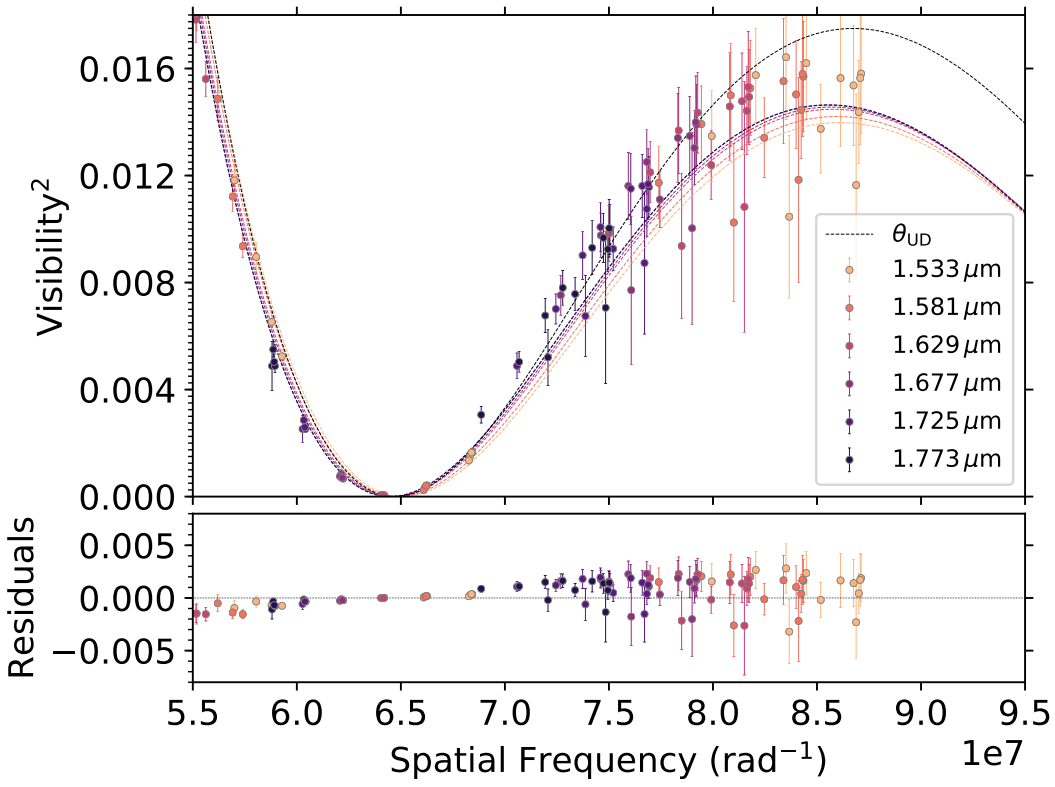

Figure 2.3: Zoomed in view of λ Sgr sidelobe and limb darkening effects.

than the model, necessitating our modification of the intercept for the standard linear limb darkening law in Equation 2.6.

Table 2.3 shows the best fit intercept parameter for each observational sequence, where every star in a given sequence was observed with the same integration time. Recalling that *bright* sequences were those preferencing similarity in science and calibrator target magnitudes, and *faint* sequences were those prioritising science-calibrator on-sky separation, our mean C values are as follows: $C_{\text{bright}} = 1.04 \pm 0.03$, $C_{\text{faint}} = 1.05 \pm 0.03$. This difference is marginal, but is not without precedent (as discussed below), and indeed non-linear behaviour at high visibility due to the difference in brightness between science and calibrator is a known, if unaddressed, issue with PIONIER.

Wittkowski et al. (2017) encountered high V^2 at short baselines, systematically above model predictions, when imaging both the carbon AGB star R Scl (H~0.49), and the nearby resolved K5/M0 giant υ Cet (H~0.27) for comparison and validation. Both targets were observed with the same selection of calibrators: HD 6629 (H~2.90), HR 400 (H~1.85), ξ Scl (H~2.65), HD 8887 (H~4.29), HD 9961 (H~3.91), HD 8294 (H~4.36), and HR 453 (H~3.72), on average being nearly 3 magnitudes fainter than the science and check targets. They conclude the systematic as being most likely caused by either this difference in magnitude or airmasses between the science and calibrator targets, and took it into account by excluding the short baseline V^2 data during modelling and image synthesis.

Table 2.3: Fitted intercept parameter C for each observational sequence.

Star	Period	Sequence	C_{LD}	C_{UD}
37 Lib	99	bright	1.007 ± 0.007	1.006 ± 0.007
37 Lib	99	faint	1.045 ± 0.006	1.045 ± 0.006
95 Cet A	99	bright	1.028 ± 0.010	1.027 ± 0.010
95 Cet A	99	faint	1.064 ± 0.006	1.063 ± 0.006
HD131977	101	bright	1.009 ± 0.007	1.009 ± 0.007
HD131977	101	faint	1.034 ± 0.009	1.034 ± 0.009
HR7221	101	bright	1.032 ± 0.008	1.031 ± 0.008
HR7221	101	faint	1.010 ± 0.007	1.009 ± 0.007
τ Cet	99	bright	1.021 ± 0.013	1.018 ± 0.013
τ Cet	101	bright	1.067 ± 0.012	1.064 ± 0.012
τ Cet	99	faint	1.108 ± 0.014	1.105 ± 0.014
τ Cet	101	faint	1.072 ± 0.011	1.070 ± 0.011
α Hyi	99	bright	1.044 ± 0.008	1.043 ± 0.008
α Hyi	99	faint	1.016 ± 0.018	1.015 ± 0.018
β Aql	101	bright	1.017 ± 0.008	1.014 ± 0.008
β Aql	101	faint	1.051 ± 0.010	1.048 ± 0.010
β TrA	99	bright	1.064 ± 0.010	1.064 ± 0.010
β TrA	101	bright	1.090 ± 0.007	1.089 ± 0.007
β TrA	101	faint	1.041 ± 0.009	1.040 ± 0.009
χ Eri	99	bright	1.090 ± 0.022	1.087 ± 0.022
χ Eri	99	faint	1.073 ± 0.009	1.070 ± 0.009
δ Eri	102	bright	1.091 ± 0.023	1.084 ± 0.023
δ Eri	99	faint	1.055 ± 0.006	1.050 ± 0.006
δ Eri	102	faint	1.020 ± 0.005	1.015 ± 0.005
δ Pav	99	bright	1.049 ± 0.022	1.048 ± 0.022
δ Pav	99	faint	1.018 ± 0.029	1.017 ± 0.029
ϵ Eri	99	bright	1.011 ± 0.008	1.008 ± 0.008
ϵ Eri	99	faint	1.049 ± 0.008	1.046 ± 0.008
ϵ Ind	99	bright	1.004 ± 0.008	1.003 ± 0.008
ϵ Ind	101	bright	1.043 ± 0.009	1.042 ± 0.009
ϵ Ind	99	faint	1.080 ± 0.024	1.079 ± 0.024
ϵ Ind	101	faint	1.005 ± 0.008	1.003 ± 0.008
η Sco	101	bright	1.061 ± 0.010	1.060 ± 0.010
η Sco	101	faint	1.169 ± 0.029	1.169 ± 0.029
λ Sgr	99	bright	1.029 ± 0.027	0.994 ± 0.027
λ Sgr	99	faint	1.036 ± 0.022	1.003 ± 0.023
40 Eri A	102	bright	0.998 ± 0.011	0.997 ± 0.011
40 Eri A	99	faint	1.078 ± 0.006	1.077 ± 0.006
40 Eri A	102	faint	1.045 ± 0.005	1.043 ± 0.005

Observations to image granulation on π Gru ($H\sim -1.71$) in Paladini et al. (2018) were also subject to the same systematic. The two calibrators used, HD 209688 ($H\sim$1.44) and HD 215104 ($H\sim$2.61), were both substantially fainter than the science target by $\geq$ 3 magnitudes. The authors do not go into detail about how they addressed the miscalibration other than adding a flat 5% systematic relative uncertainty to their data.

The corresponding mean difference between our science target and 'good' (i.e. used) calibrator magnitudes in H is $\Delta H_{\mathrm{bright}} = 0.95$, and $\Delta H_{\mathrm{faint}} = 1.69$. If the issue indeed stems from ΔH being large, then the marginal difference we observe in C is at least consistent with the bright sequences on average having a lower ΔH.

2.4.4 Bolometric Fluxes

Determination of $T_{\rm eff}$ requires measurement of $f_{\rm bol}$, the bolometric flux received at Earth, which can be done through one of several techniques, each with precedent in optical interferometry literature. All are only accurate to the few percent level, primarily due to uncertainties on the adopted zero points used to convert fluxes, either real or synthetic, to magnitudes and vice versa.

The least model dependent approach is to use a combination of spectrophotometry and broadband photometry from the science target itself, in combination with synthetic equivalents for missing or contaminated regions, to construct the flux calibrated spectral energy distribution of the star from which $f_{\rm bol}$ can be determined. White et al. (2018) implemented this procedure, using the methodology outlined in Mann et al. (2015).

A related technique is to employ a library of flux calibrated template spectra covering a range of spectral types, e.g. the *Pickles Atlas* (115-2 500 nm, Pickles 1998), in lieu of spectrophotometry from the targets themselves. Fits are then performed to target broadband photometry using library spectra of adjacent spectral types. This was the approach taken by e.g. van Belle et al. (2007), van Belle et al. (2008), Boyajian et al. (2012a), Boyajian et al. (2012b), Boyajian et al. (2013), and White et al. (2013), which lacks the limitations associated with synthetic spectra (e.g. due to modelling assumptions such as one-dimensional and hydrostatic models, or models satisfying local thermodynamic equilibrium). However, it is limited in its use of a relatively coarse, non-interpolated grid of only 131 spectra of mostly Solar metallicity, with potential errors from reddened spectra and correlated errors associated with the photometric calibration.

In lieu of a template library, the previous approach can be conducted using a grid of purely synthetic spectra. By linearly interpolating the spectral grid in $T_{\rm eff}$, $\log g$, and [Fe/H] and fitting to available broadband photometry, $f_{\rm bol}$ can be determined as the total flux from the best-fit spectrum. This was the method employed by Rabus et al. (2019), who used PHOENIX model atmospheres (Husser et al. 2013), assuming [Fe/H] = 0 for all targets (likely to avoid degeneracies between $T_{\rm eff}$ and [Fe/H] for cool star spectra), as well as Huber et al. (2012) using the MARCS grid of model atmospheres (Gustafsson et al. 2008). This technique has the advantage of being unaffected by instrumental or atmospheric effects, and allowing for a much finer grid, but makes the results more susceptible to potential inaccuracies within the models themselves. We note however that synthetic photometry from the MARCS grid has previously been shown to be valid using the colours from both globular and open clusters, across the HR diagram and over a wide range of metallicities ($-2.4 \lesssim$ [Fe/H] $\lesssim +0.3$, Brasseur et al. 2010; VandenBerg et al. 2010).

The final approach to be discussed here, and the one employed for this work, computes $f_{\rm bol}$ using broadband photometry and the appropriate bolometric correction derived from model atmospheres using literature values of $T_{\rm eff}$, $\log g$, and [Fe/H]. This method saw use in Karovicova et al. (2018), and in White et al. (2018) who found it to have excellent consistency with results derived from pure spectrophotometry for all but one of their stars. Casagrande & VandenBerg (2018a) evaluated the validity of using bolometric corrections in this manner by comparing results to the ∼1% precision CALSPEC library (Bohlin 2007) of Hubble Space Telescope spectrophotometry. This demonstrated that bolometric fluxes could be recovered

from computed bolometric corrections to the 2% level, a value typically halved when combining the results from more photometric bands (as we do here, corresponding to roughly ±12.5 K uncertainty on $T_{\rm eff}$ for a 5 000 K star with a 1% error on flux).

Given that all have been demonstrated successfully in the literature, we opt for the bolometric correction technique because of limited available well calibrated photometry for our bright targets. Bolometric fluxes were computed for all stars by way of the `bolometric-corrections`[7] software (Casagrande & VandenBerg 2014, 2018a; Casagrande et al. 2019). For a given set of $T_{\rm eff}$, $\log g$, and [Fe/H] the software produces synthetic bolometric corrections in different filters by interpolating the MARCS grid of synthetic spectra (Gustafsson et al. 2008). $f_{\rm bol}$ is obtained using Equation 2.8 (Casagrande & VandenBerg 2018a):

$$f_{\rm bol} = \frac{\pi L_{\odot}}{1.296 \times 10^{9} \mathrm{au}} 10^{-0.4(\mathrm{BC}_{\zeta} - M_{\mathrm{bol},\odot} + m_{\zeta} - 10)} \tag{2.8}$$

where $f_{\rm bol}$ is the stellar bolometric flux received at Earth in erg s^{-1} cm^{-2}, $L_{\odot}$ is the Solar bolometric luminosity in erg s^{-1} (IAU 2015 Resolution B3, 3.828×10^{33} erg s^{-1}), au is the astronomical unit (IAU 2012 Resolution B2, $1.495978707 \times 10^{13}$ cm), BC_{ζ} and m_{ζ} are the bolometric correction and apparent magnitudes respectively in filter band ζ, and $M_{\rm bol} = 4.75$ is the adopted Solar bolometric magnitude.

Calculation of $f_{\mathrm{bol},\zeta}$ is done at each iteration of the aforementioned bootstrapping and Monte Carlo algorithm for each of $H_{\rm P}$, $B_{\rm T}$, and $V_{\rm T}$ filter bands using the sampled stellar parameters and magnitudes, overwhelmingly consistent to within 1σ uncertainties. An instantaneous value of $f_{\rm bol,final}$ is calculated by averaging the fluxes obtained from each filter, with final values obtained as the mean and standard deviation of the respective distributions. Note that, with the goal of consistency in mind, *Gaia* G, $B_{\rm P}$, and $R_{\rm P}$ were avoided due to saturation for a portion of our sample (and a magnitude-dependent offset for bright targets as noted in Casagrande & VandenBerg 2018b).

The final calculated bolometric fluxes for each band are reported in Table A.1 and visualised in Figure A.1, with the adopted average values in Table 2.4.

2.4.5 Fundamental Stellar Properties

The strength of measuring stellar angular diameters through interferometry is the ability to measure $T_{\rm eff}$ independent of distance in an almost entirely model independent way (the exceptions being the adopted limb darkening law, and ∼1% precision bolometric fluxes). With measures of stellar angular diameter and flux, $T_{\rm eff}$ can be calculated as follows:

$$T_{\rm eff} = \left(\frac{4 f_{\rm bol}}{\sigma \theta_{\rm LD}{}^{2}} \right)^{1/4} \tag{2.9}$$

where $T_{\rm eff}$ is the stellar effective temperature in K, $f_{\rm bol}$ is the bolometric stellar flux in ergs s^{-1} cm^{-2}, and σ is the Stefan-Boltzmann constant, taken to be $\sigma = 5.6704{\times}10^{-5}$ ergs s^{-1} cm^{-2} K^{-4}.

The same measure of flux can be combined with the distance to the star to calculate the

[7] https://github.com/casaluca/bolometric-corrections

Table 2.4: Final fundamental stellar parameters

Star	θ_{UD} (mas)	θ_{LD} (mas)	$R_\star$ ($R_\odot$)	f_{bol} (10^{-8} ergs s^{-1} cm^{-2})	T_{eff} (K)	$L_\star$ ($L_\odot$)
τ Cet	2.005 ± 0.011	2.054 ± 0.011	0.796 ± 0.004	115.0 ± 1.2	5347 ± 18	0.47 ± 0.01
α Hyi	1.436 ± 0.016	1.460 ± 0.016	3.040 ± 0.058	179.0 ± 3.0	7087 ± 47	21.00 ± 0.75
χ Eri	2.079 ± 0.011	2.134 ± 0.011	3.993 ± 0.027	104.0 ± 4.0	5115 ± 49	9.84 ± 0.39
95 Cet A	1.244 ± 0.012	1.280 ± 0.012	8.763 ± 0.128	26.2 ± 1.7	4678 ± 75	33.18 ± 2.27
ϵ Eri	2.087 ± 0.011	2.144 ± 0.011	0.738 ± 0.003	99.8 ± 2.5	5052 ± 33	0.32 ± 0.01
δ Eri	2.343 ± 0.009	2.411 ± 0.009	2.350 ± 0.010	123.2 ± 3.4	5022 ± 34	3.17 ± 0.09
40 Eri A	1.449 ± 0.012	1.486 ± 0.012	0.804 ± 0.006	50.8 ± 0.9	5126 ± 30	0.40 ± 0.01
37 Lib	1.639 ± 0.009	1.684 ± 0.010	5.133 ± 0.043	50.6 ± 2.6	4809 ± 62	12.71 ± 0.69
β TrA	1.438 ± 0.013	1.462 ± 0.013	1.976 ± 0.021	188.2 ± 2.1	7171 ± 35	9.30 ± 0.17
λ Sgr	3.910 ± 0.014	4.060 ± 0.015	11.234 ± 0.181	283.9 ± 8.7	4768 ± 36	58.79 ± 2.61
δ Pav	1.785 ± 0.025	1.828 ± 0.025	1.197 ± 0.016	107.2 ± 2.5	5571 ± 48	1.24 ± 0.03
ϵ Ind	1.758 ± 0.012	1.817 ± 0.013	0.711 ± 0.005	51.5 ± 3.7	4649 ± 84	0.21 ± 0.02
HD131977	1.098 ± 0.014	1.130 ± 0.014	0.715 ± 0.009	17.6 ± 1.1	4505 ± 76	0.19 ± 0.01
η Sco	1.392 ± 0.017	1.416 ± 0.017	3.307 ± 0.050	121.6 ± 2.0	6533 ± 46	17.94 ± 0.45
β Aql	2.079 ± 0.011	2.133 ± 0.012	3.064 ± 0.020	100.3 ± 2.9	5071 ± 37	5.60 ± 0.17
HR7221	1.088 ± 0.014	1.117 ± 0.015	4.428 ± 0.058	26.5 ± 0.7	5023 ± 47	11.24 ± 0.33

bolometric luminosity:

$$L_\star = 4\pi f_{bol} D^2 \tag{2.10}$$

where D is again the distance to the star. Dividing this value by $L_\odot$ gives the luminosity in Solar units.

Finally, the measured angular diameter and distance can be combined to determine the physical radius of a star:

$$R_\star = \frac{1}{2}\theta_{LD} D \tag{2.11}$$

and its uncertainty:

$$\sigma_{R_\star} = R_\star \sqrt{\left(\frac{\sigma_\theta}{\theta_{LD}}\right)^2 + \left(\frac{\sigma_D}{D}\right)^2} \tag{2.12}$$

where $R_\star$ is the physical radius of the star, θ_{LD} is the limb darkened angular diameter, D is the distance to the star, and σ_θ and σ_D are their respective uncertainties. These can be put into Solar units using pc= 3.0857×10^{13} km, and $R_\odot = 6.957 \times 10^5$ km.

These parameters, alongside the final angular diameters, are reported in Table 2.4.

2.5 Discussion

2.5.1 Comparison with Previous Interferometric Measurements

Six of our sample, HD 131977, 40 Eri A, ϵ Ind, τ Ceti, β Aql, and ϵ Eri, have literature angular diameter measurements (Table 2.5), which we find to be consistent with our own to within $\sim 1\sigma$ uncertainties for all but one star (Figure 2.4). Our value for ϵ Ind however is substantially discrepant to the VINCI diameter by $\sim 4\sigma$. Comparing our V^2 fits to the literature results in Demory et al. (2009) reveal that we place tighter constraints on the angular diameter

Table 2.5: Comparison of angular diameters reported here with stars measured previously in the literature.

Star	$\theta_{\rm LD}$ (mas)	Facility	Instrument	Ref
τ Cet	1.971 ± 0.05	VLTI	VINCI	1
	2.078 ± 0.031	VLTI	VINCI	2
	2.015 ± 0.011	CHARA	FLUOR	3
ϵ Eri	2.148 ± 0.029	VLTI	VINCI	2
	2.126 ± 0.014	CHARA	FLUOR	3
	2.153 ± 0.028	NPOI	NPOI	4
40 Eri A	1.437 ± 0.039	VLTI	AMBER	5
ϵ Ind	1.881 ± 0.017	VLTI	VINCI	5
HD131977	1.177 ± 0.029	VLTI	VINCI	5
β Aql	2.18 ± 0.09	NPOI	NPOI	6

References. 1. Pijpers et al. (2003); 2. Di Folco et al. (2004); 3. di Folco et al. (2007); 4. Baines & Armstrong (2011); 5. Demory et al. (2009); 6. Nordgren et al. (1999)

by better resolving the star down to V^2 of ~0.2 versus ~0.5 for previous results. We expect the discrepancy is largely caused by this, plus the fact that these observations were taken at lower sensitivity using two 35 cm test siderostats during the early years of the VLTI rather than the four 1.8 m ATs we have access to now.

None of these prior measurements were made with PIONIER, meaning that our results offer high precision agreement between not only different VLTI beam combiners (AMBER and VINCI), but also as different facilities altogether (NPOI[8] and CHARA/FLUOR). Given the relatively sparse overlaps however, we are not able to say anything substantial about potential systematics. We await the upcoming White et al. (in prep) which will be able to compare PIONIER to CHARA/PAVO for τ Cet, ϵ Eri, δ Eri, 37 Lib, and β Aql. This study will also possibly enable the ability to investigate the effect of limb darkening at different wavelengths since PAVO is an R-band instrument, thus significantly improving the sensitivity to systematic errors. Furthermore, PAVO data for additional dwarf and giant stars, including β Aql, but also many stars not observed here, is to be published soon in Karovicova et al. (in prep.) and a following series of papers.

2.5.2 Comparison with Colour-$\theta_{\rm LD}$ Relations

Figure 2.5 shows a comparison between our fitted diameters, and the $(V-W3)$, $(V-W4)$, and the [Fe/H] dependent $(B-V)$ colour-θ_{LD} relations from Boyajian et al. (2014) used to predict calibrator angular diameters. All three sets of relations are consistent within errors with our results (despite several of our sample being marginally too red for the [Fe/H] dependent $(B-V)$ relation), which bodes well for the accuracy of the relations. However, there appears a clear systematic offset for the $(V-W3)$ relation, plus a less severe offset for the $(V-W4)$ relation. There does not appear to be a trend in either [Fe/H] with any of these relations.

[8]Note that for simplicity NPOI is used here to refer to both the *Navy Prototype Optical Interferometer* (per Nordgren et al. 1999) and the *Navy Optical Interferometer* (per Baines & Armstrong 2011) given the facility changed names between the two measurements referenced here, and is now known as the *Navy Precision Optical Interferometer*.

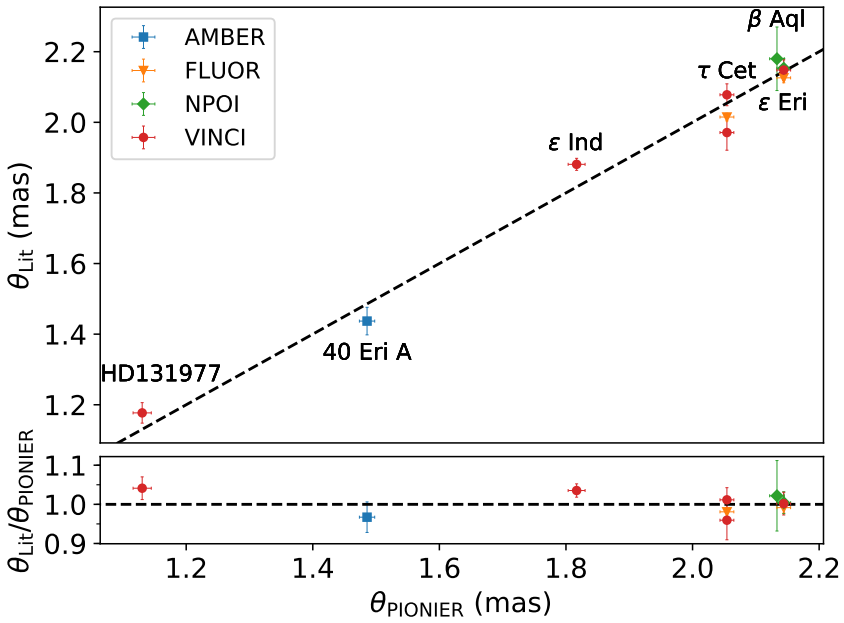

Figure 2.4: Comparison of PIONIER diameters as reported here, to stars with literature measurements from other interferometers or beam-combiners

2.5.3 $T_{\rm eff}$ From Empirical Relations

Unfortunately comparison of the $T_{\rm eff}$ values derived here to those from infrared flux method (Casagrande et al. 2010) is not possible due to saturated *2MASS* photometry - the critical source of infrared photometry. Another source of comparison is to use the empirical relations provided by the same study, which give an empirical mapping between select colour indices and $T_{\rm eff}$. Figure 2.6 presents $T_{\rm eff}$ as a function of $(B_{\rm T} - V_{\rm T})$, uncertainties ±79 K, and demonstrates 1σ agreement for all stars, with the exceptions of HD 131977 and β TrA. Inspecting the photometry for both stars, values of $f_{\rm bol}$ derived from different filter bands are consistent, and rotation does not appear to be a significant factor when considering literature $v \sin i$ presented Table 2.1. We note however that our interferometric temperatures are consistent with the literature spectroscopic values also listed in Table 2.1 for these two stars.

2.6 Conclusions

We have used long-baseline optical interferometry to measure the angular diameters for a sample of 16 southern stars (6 dwarf, 5 sub-giant, and 5 giants) with exquisite precision using the PIONIER instrument on the VLTI. The limb darkened diameters reported have a mean uncertainty of ~0.82%, and were obtained using a robust calibration strategy, and a data analysis pipeline implementing both bootstrapping and Monte Carlo sampling to take into account correlated uncertainties in the interferometric data. In addition to this, we also report derived $T_{\rm eff}$, physical radii, bolometric fluxes, and luminosities for all stars, with mean uncertainties of ~0.9%, ~1.0%, ~3.3%, and ~3.7% respectively.

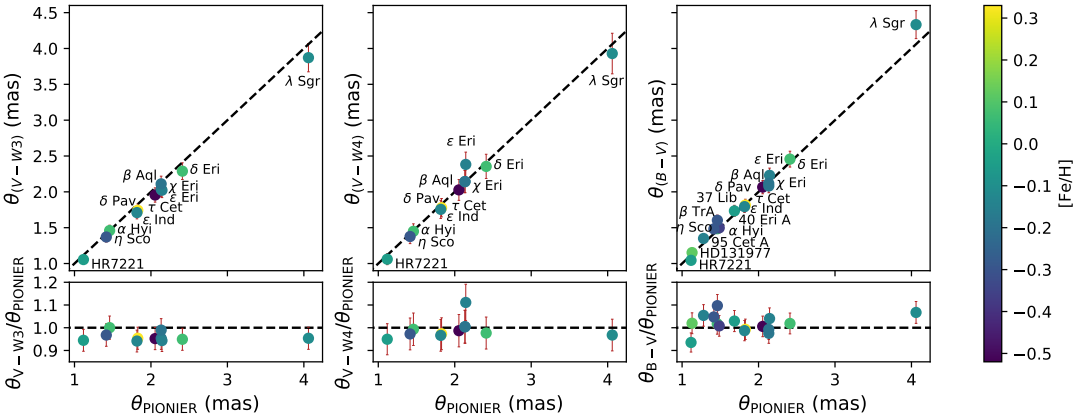

Figure 2.5: Comparison of $\theta_{\rm LD}$ as reported here as compared to predicted diameters from Boyajian et al. (2014). **Left:** $(V-W3)$ relation, **Centre:** $(V-W4)$ relation, **Right:** [Fe/H] dependent $(B-V)$ relation. Note that not all stars have *WISE* photometry, whereas all stars have available *Tycho-2* magnitudes.

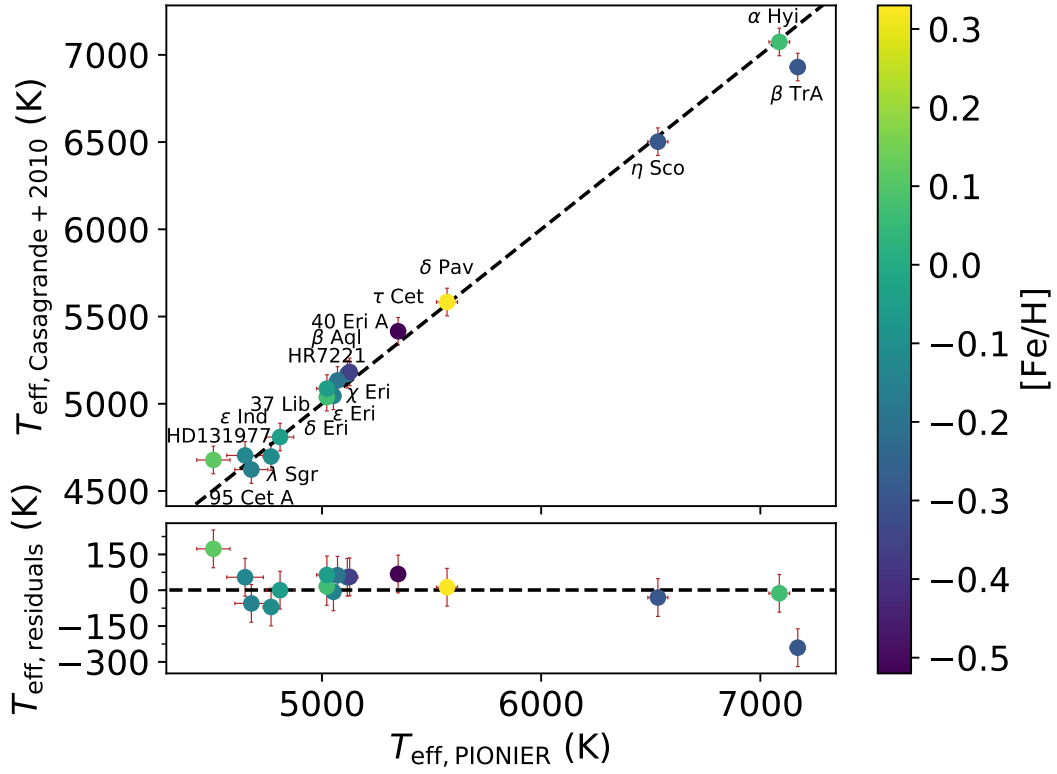

Figure 2.6: Comparison of $T_{\rm eff}$ as reported here and those calculated from $(B_{\rm T}-V_{\rm T})$ using the empirical relations of Casagrande et al. (2010)

Ten of these stars did not have measured angular diameters prior to the results presented here, and the majority of the remaining six have values in agreement with previous literature measurements, with the sole outlier being observed at higher resolution and with greater sensitivity here. These are some of the closest and most well studied stars, and this work hopes to elevate them further to the level of spectral type standards, where they can provide constraints to theoretical models and empirical relations.

Acknowledgements

ADR acknowledges support from the Australian Government Research Training Program, and the Research School of Astronomy & Astrophysics top up scholarship. We acknowledge Australian Research Council funding support through grants DP170102233. LC is the recipient of an ARC Future Fellowship (project number FT160100402). Based on observations obtained under ESO program IDs 099.D-2031(A), 0101.D-0529(A), and 0102.D-0562(A). This research has made use of the `PIONIER data reduction package` of the Jean-Marie Mariotti Center[9]. This research has made use of the *Washington Double Star Catalog* maintained at the U.S. Naval Observatory. This work made use of the *SIMBAD* and *VIZIER* astrophysical database from CDS, Strasbourg, France and the bibliographic information from the NASA Astrophysics Data System. We thank the anonymous referee for their helpful comments.

Software: `Astropy` (Astropy Collaboration et al. 2013), `NumPy` (Harris et al. 2020), `SciPy` (Jones et al. 2016), `iPython` (Perez & Granger 2007), `Pandas` (McKinney 2010), `Matplotlib` (Hunter 2007).

[9]Available at https://www.jmmc.fr/pionier

Chapter 3

The FunnelWeb Survey Tiling Algorithm

Spectroscopic surveys beyond a certain scale require the ability to observe multiple objects—be they stars or galaxies—during each pointing of the telescope. This is largely a matter of efficiency, particularly when observing fainter objects or using high dispersion instruments. Both require longer exposure times, and with sufficiently large target lists, serial observations in a reasonable span of time become simply untenable. Consider the following efficiency metric:

$$E = N_O \cdot A_T \cdot \eta \cdot O_F \tag{3.1}$$

where E is the survey efficiency metric, N_O is the number of objects able to be observed simultaneously, A_T is the collecting area of the telescope in m^2, η is the combined fractional throughput of the telescope and instrument, and O_F is the fractional useful observing time at the site (e.g. due to weather, maintenance, or time sharing). Surveys with a higher E value are more efficient—having the capacity to observe many objects at once, having shorter exposure times that come with larger telescopes or more efficient instrumentation, along with less weather or maintenance related downtime.

Fibre-fed spectrographs are critical to maximise this metric. They allow for spectra to be taken for hundreds of arbitrary positions across a given field, limited only by detector size, the number of fibres, and the technique used to place them. Technology has improved over the decades, and while early fibre positioners often involved hours of manual labour to prepare a single field, their modern equivalents are faster and largely robotic, allowing for the surveys that employ them to be increasingly ambitious.

The 1.2 m UK-Schmidt Telescope at Siding Spring Observatory has hosted several generations of multi-object, fibre-fed spectrographs—each faster and more technologically complex than the last. These include FLAIR (Watson 1988; Watson et al. 1990), which took an experienced operator 4-6 hr to manually glue 90 fibres into position; FLAIR II (Watson & Parker 1994), an upgrade to FLAIR that reduced field configuration times to 3-4 hr and largely eliminated the use of UV curing glue through magnetic buttons; 6dF (6 Degree Field, Watson et al. 1998, Watson et al. 2000), a fully automated fibre positioner taking less than an hour to configure its 150 fibres in serial; and most recently TAIPAN (Kuehn et al. 2014), which uses the novel Starbug technology (Gilbert et al. 2012) to allow parallel positioning of 150–300 fibres in under 10 mins.

6dF in particular enabled two highly-influential spectroscopic surveys: one stellar and one extragalactic. RAVE (the RAdial Velocity Experiment, Steinmetz et al. 2006) was a wide-field stellar survey targeting 450 000 randomly selected stars with $9 < m_I < 12$ which delivered stellar parameters, abundances, and radial velocities (RVs). Its counterpart was the 6dF Galaxy Survey (Jones et al. 2004), which determined the redshifts for 125 000 galaxies, and the peculiar velocities, masses, and bulk motions for a roughly 9 000 galaxy subsample. These surveys continue to have legacy value today, both scientifically and as pathfinders for current and future generations of spectroscopic surveys.

With increasing survey complexity and ambition, however, there is ever greater need for efficient observing strategies to optimise telescope usage and maximise science potential. This is particularly true for the FunnelWeb Survey, a planned successor to RAVE using a refurbished UK-Schmidt Telescope and new rapid fibre positioner and spectrograph known as TAIPAN (Kuehn et al. 2014; Staszak et al. 2016b,a). As originally planned, FunnelWeb had the goal of observing two million of the brightest stars in the Milky Way in just two years, a task only possible with an efficient algorithm for allocating its fixed observing fields—a task known as 'sky tiling'.

The details of this algorithm, along with an overview of FunnelWeb and its eventual cancellation, form the basis of this chapter. We begin with an overview of comparable approaches for past and upcoming surveys in Section 3.1. This is followed by an overview of the two next generation surveys on the UK-Schmidt Telescope and the enabling TAIPAN instrument in Section 3.2, an overview of FunnelWeb itself in Section 3.3, the observing strategy in Section 3.3.4, the implemented algorithm in Section 3.3.5, and a retrospective view of the survey in Section 3.4.

3.1 Survey Sky Tiling

The details and complexity of a given sky tiling algorithm depends on **a)** telescope and instrument specifications like field of view, number of fibres, and minimum on-sky fibre separation; and **b)** the survey science objectives, which include things like the total number of targets—both per field and for the survey as a whole—as well as specific completion requirements. As such, surveys and instruments tend to have their own implementations to suit their individual needs (e.g. 6dFGS, Campbell et al. 2004; 2dF/GAMA Robotham et al. 2010; LAMOST, Yuan et al. 2012, Luo et al. 2015; 4MOST, Tempel et al. 2020a, DESI, Smith et al. 2019), though there remain methods published intended to be more general purpose (e.g. Tempel et al. 2020b).

However, it is important to consider what unforeseen effects perhaps seemingly simple algorithmic choices can have. For instance, Miszalski et al. (2006) investigated how tiling algorithms can imprint subtle selection effects or structure into surveys that would not otherwise be present, an effect that can be mitigated at the expense of additional computation. In terms of survey completeness, Smith et al. (2019) found that the geometry of the fibre positioners themselves—in that fibres cannot be placed arbitrarily close to each other—can limit completion in dense fields, which can accounted for using additional rules for target prioritisation. Given these concerns, it is important to run survey simulations which tile and 'observe' a realistic input catalogue to completion in order to evaluate the results against the survey science goals.

3.2 A New Generation of Surveys with the UK-Schmidt Telescope

The early 2010s saw the first planning for the next generation of spectroscopic surveys on the UK-Schmidt Telescope to succeed RAVE and the 6dF Galaxy Survey. In addition to the aforementioned long field reconfiguration times, a major weakness of both surveys was their highly labour intensive operating model along with increasing maintenance costs. This was largely the result of ageing equipment with multiple single points of failure, limited-to-no available spares, and the fact that 6dF was fundamentally a semi-manual instrument. From an instrument perspective, 6dF was also restricted in its wavelength coverage and throughput, which limited its science potential and the depth it could effectively observe. Thus, the plans for successor surveys to RAVE and 6dFGS were not just a problem of survey design, but also one of new instrumentation and telescope refurbishment.

From this came the TAIPAN instrument—a new robotic fibre positioner and spectrograph. TAIPAN's key innovation was its ability to *rapidly* and *automatically* reposition its fibres in *parallel*, thus greatly reducing survey and observing overheads. With TAIPAN as the foundation, along with a refurbished UK-Schmidt Telescope, two successor surveys were planned: the Taipan Galaxy Survey (da Cunha et al. 2017) and the FunnelWeb Stellar Survey—both following in the tradition of other Australian surveys donning wildlife monikers. The primary goal of Taipan was to be a 1% measurement of the Hubble Constant, H_0, along with a peculiar velocity survey, and studies of galaxy evolution, transitions, environments, and fuelling. FunnelWeb's goal on the other hand was to undertake a magnitude-limited survey of the southern hemisphere, with key science cases being the identification of young or extremely-metal-poor stars, the characterisation of exoplanet hosts, and radial velocities for stars too faint for *Gaia*. While not the largest telescope or highest spectral resolution, what both surveys critically had working in their favour was time—it would be years before any competitors with similar total objects per night capability got on-sky, by which point Taipan and FunnelWeb would be standard and well-cited resources for extragalactic and stellar science respectively.

3.2.1 The TAIPAN Instrument

The TAIPAN Instrument (Kuehn et al. 2014; Staszak et al. 2016b,a) is the robotic fibre positioner and spectrograph designed for the recently refurbished 1.2 m UK Schmidt Telescope at Siding Spring Observatory. Developed at the Australian Astronomical Observatory (AAO), TAIPAN is able to reconfigure its 150 optical fibres in parallel, a process taking fewer than five minutes. This is accomplished through the use of so-called 'Starbugs' (Gilbert et al. 2012): miniature piezoelectric 'walking' robots, capable of moving several millimetres per second, and held via vacuum to the underside of a transparent field plate.

Starbugs are adhered by pressure differential to a 330 mm diameter kinematically-mounted curved glass field plate located at the focal surface of the telescope (Kuehn et al. 2014; Staszak et al. 2016b), which can be seen in Figure 3.1. Each Starbug has a single astronomical fibre payload with 50 μm core diameter (corresponding to 3.3 arcsec diameter on-sky), along with three metrology fibres illuminated via an on-board LED (Lorente et al. 2015, 2016). Each Starbug has an outer diameter of 8mm and a (software-enforced) exclusion radius of 10 mm, limiting the proximity of neighbouring fibres to $\approx$10 arcmin. Positioning feedback is provided

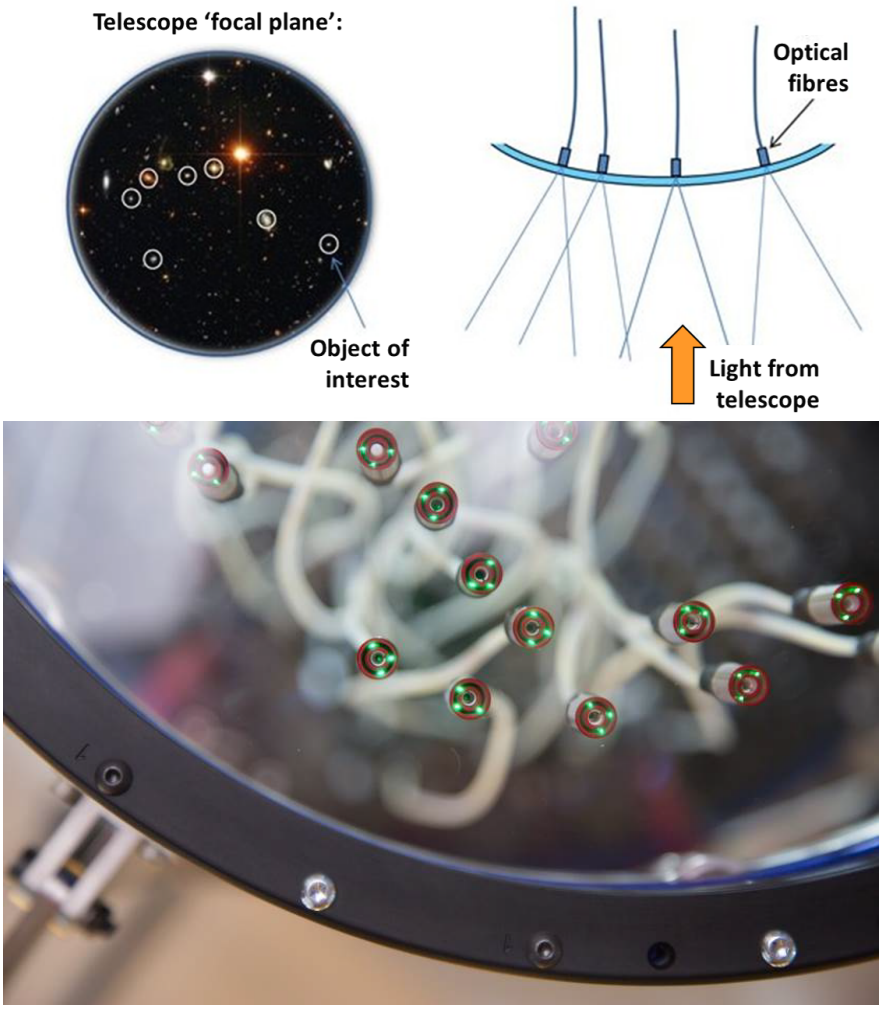

Figure 3.1: The TAIPAN Instrument. **Top:** Schematic view of telescope focal plane. **Bottom:** Field plate with Starbugs in place. Reproduced from da Cunha et al. (2017).

by a 29 megapixel CCD machine vision camera to better than 4.5 μm - equivalent to better than 0.3 arcsec on-sky, or 2% relative science flux loss in 1.5 arcsec seeing conditions. Additionally, the field plate itself has a set of 16 similarly illuminated fiducials about its perimeter.

The TAIPAN spectrograph is an entirely refractive design with a 300 fibre input slit (Staszak et al. 2016a). It has an average resolution of R~2 350 and is composed of two arms: a blue (3 700 $< \lambda <$ 5 920 Å) and a red (5 800 $< \lambda <$ 8 700 Å) arm, with an overlapping region of 5 800 – 5 920 Å. Spectra for each of these cameras, split by a dichroic mirror, are imaged onto separate 2k×2k E2V detectors. The entire instrument is housed in a temperature controlled room to ±1.5° to ensure stability of wavelength calibrations.

TAIPAN began commissioning at Siding Spring Observatory in mid–2017 with 150 science fibres and 9 guide bundles, with scope to upgrade the instrument to 300 science fibres in the future—thereby doubling survey efficiency. Furthermore, the instrument serves as a prototype for the upcoming massively multiplexed fibre-positioner facility MANIFEST (Goodwin et al.

2012; Lawrence et al. 2016). This facility for the Giant Magellan Telescope will include Starbugs that carry multi-fibre integral field unit payloads.

3.3 The FunnelWeb Survey

The FunnelWeb Survey planned to occupy an as yet unfilled scientific role: a complete, magnitude limited ($5.5 \leq G \leq 12.5$), bright star, broadband (3 700 − 8 700 Å) spectroscopic survey of the least crowded regions of the southern sky ($|b| > 10$) with a signal to noise ratio (SNR) $\gtrsim 100$. In many respects, FunnelWeb sought to restart the magnitude-limited mapping of the sky that halted when programs observing stars "one at a time" (e.g. the Michigan Spectroscopic Survey: Houk & Cowley 1975, Houk 1978, Houk 1982, Houk & Smith-Moore 1988; and before that the Henry Draper (HD) Catalogue: Cannon & Pickering 1918) reached their natural limit at about 350 000 stars.

FunnelWeb aimed for 99% completeness at the $G = 12.5$ level (excluding only the most crowded regions of the Galactic plane, $|b| \leq 10$). The intent was to produce high-quality spectra and detailed stellar parameters for every star observed, including $T_{\rm eff}$, $\log g$, [Fe/H], and [α/Fe]), and to make both those parameters, and the spectra they were derived from, publicly available. While the TAIPAN instrument parameters (chiefly the resolution of $R{\sim}2\,350$) were initially optimised for galaxy spectroscopy via the Taipan Survey, they were also appropriate for FunnelWeb's science goals when stellar spectra are obtained at high SNR. Indeed, the low resolution SEGUE (Yanny et al. 2009) and LAMOST (Cui et al. 2012) surveys have successfully returned stellar parameters for most of their stars—along with abundances for a few elements in certain cases—in spite of only moderate typical SNR (∼30 per resolution element).

3.3.1 Survey Science Goals

Observing two million of the brightest stars in the Milky Way opens up a huge array of science cases, even considering the low spectral resolution FunnelWeb would have observed at. While these science cases won't be discussed in detail here, the most compelling were as follows:

- Stellar parameters, activity measures, and RVs for 60 000 M-dwarfs;
- Identification of young members of moving groups via emission features and lithium absorption, and determination of RVs to complete their kinematics and enable dynamical studies;
- Spectrosopic follow-up of 3 000+ extremely metal poor (EMP) star candidates as identified by *SkyMapper* photometry (per Da Costa et al. 2019);
- Stellar parameters for every southern *TESS* Object of Interest (TOI, Guerrero et al. 2021)—the stars around which *TESS* will find planets;
- Studying the relationship between age, chemistry, and kinematics in the nearby Galactic disk in combination with *Gaia* data;
- Spectroscopic stellar parameters (specifically [Fe/H] and [α/H]) to complement asteroseismic data of pulsating stars from *TESS*.

Table 3.1: FunnelWeb main survey predicted yield based on Galaxia models (Sharma et al. 2011), for $\delta \leq 0°$, $|b| \geq 10°$, $5.5 \leq I \leq 12.5$, and using dwarf/giant cuts as per Sharma et al. (2018).

Class	# Objects	SpT	Dwarf	Giant
Total Stars	2 964 614	O	0	0
< 15 Myr	20 283	B	11 978	71
< 100 Myr	331 407	A	134 617	386
Thin Disk	2 305 017	F	928 080	1 335
Thick Disk	628 032	G	386 339	53 750
Halo	26 021	K	142 003	1 235 891
Bulge	5 542	M	1 457	68 705

Predicted Survey Yield

To assess the yield of the FunnelWeb main survey, Galaxia (Sharma et al. 2011, based on Bescanon model predictions Robin et al. 2003, Marshall et al. 2006, Robin et al. 2012, Robin et al. 2014), was used to generate a synthetic survey of the Milky Way for $\delta \leq 0°$, $|b| \geq 10°$, $5.5 \leq I \leq 12.5$—the results of which can be seen in Table 3.1. Note the comparatively low number of M dwarfs present in the main survey, which necessitated dedicated supplementary surveys for these faint stars as discussed in Section 3.3.3.

3.3.2 Input Catalogue

To simplify implementation and operations, all FunnelWeb targets (whether from the main survey, priority, or supplementary surveys) were to be selected from a single source known as the Input Catalogue, as prepared by Dr Dougal Mackey. The base for this catalogue was *Gaia* DR2 (Brown et al. 2018) as it satisfied four key requirements: **i)** a rigorous astrometric solution across the entire sky, including precise proper motions (Lindegren et al. 2018); **ii)** extremely high completeness over the magnitude range of interest, even in very crowded regions; **iii)** uniform high-quality photometric measurements in optical passbands (Evans et al. 2018); and **iv)** the availability of pre-computed cross-matches with various external catalogues (Marrese et al. 2019) including *2MASS* (Skrutskie et al. 2006) and *AllWISE* (Wright et al. 2010; Cutri & et al. 2013). As *Gaia* DR2 is known to be somewhat incomplete at bright magnitudes (Brown et al. 2018), the Input Catalogue was supplemented with the 323 *UCAC4* sources (Zacharias et al. 2013) with $J \leq 7$ without a match in *Gaia* DR2.

The Input Catalogue consisted of all *Gaia* DR2 sources with $G \leq 14.5$ and $\delta \leq +30°$. This was just over 19.4×10^6 stars, of which 98.2% had a *2MASS* point-source match and 82.0% an *AllWISE* match. In addition, 78.5% had some estimate of the stellar parameters from Apsis (Andrae et al. 2018), 28.2% a *Gaia* radial velocity measurement (Katz et al. 2019), and 0.6% were flagged as variable.

Dark Sky Positions Catalogue

To enable for sky subtraction, FunnelWeb needed a catalogue of so called 'dark sky positions' uncontaminated by starlight. Assuming on average a 2 arcsec Moffatt seeing profile, each

Table 3.2: FunnelWeb main, priority, and supplementary survey details.

Name	**Type**	**# Stars**
FunnelWeb Main Survey (G≤12.5, $\delta \leq 10°$, $\lvert b\rvert \geq 10°$)	Main	1 800 000
Standard Star and Crossover Survey Targets (GALAH)	Priority	29 500
Standard Star and Crossover Survey Targets (*Gaia* Benchmarks, South)	Priority	13
M Dwarf Survey ($G < 12.5$)	Priority	14 000
Extremely Metal-Poor Stars ($G < 12.5$)	Priority	900
Standard Star and Crossover Survey Targets (*Gaia* Benchmarks, North)	Supplementary	13
M Dwarf Survey ($12.5 < G < 14.5$)	Supplementary	46 000
Extremely Metal-Poor Stars ($12.5 < G < 14.5$)	Supplementary	2 400
Young Stars	Supplementary	1 000

star—even those fainter than FunnelWeb's magnitude limit—has a magnitude–dependent zone of avoidance where its light can still be detected. This catalogue was generated by Dr Sanjib Sharma by generating a list of random positions uniformly over the sky, and cross matching with a deep catalogue that contains both bright and faint stars (i.e. *Gaia* DR1, Gaia Collaboration et al. 2016b), a catalogue of suitably dark positions can be created. The resulting catalogue has a density of at least 10 dark sky positions per square degree (for the most crowded regions), with the majority of the sky exceeding 32 such positions per square degree—more than sufficient for sky subtraction.

3.3.3 Survey Design

FunnelWeb planned to employ a strategy of having a single *main* survey, alongside selected *priority* and *supplementary* surveys. The main survey was simply all stars in the input catalogue required to meet FunnelWeb's completeness requirements, observed with standard priority. Priority surveys on the other hand consisted of those targets prioritised for early observation for either scientific or calibration reasons. Finally, supplementary surveys were for additional targets not included as part of the main survey due to declination, galactic latitude, or magnitude constraints, but still relevant for either scientific or calibration reasons. The expected surveys as last planned are summarised in Table 3.2.

3.3.4 Observing Strategy

Both the FunnelWeb and Taipan Surveys planned to share access to the UK-Schmidt and TAIPAN Instrument, with observations being somewhat interleaved throughout any given month. FunnelWeb would be observing whenever the moon was above the horizon (i.e. all bright time, and some grey time) or when the conditions at Siding Spring were ill-suited to observations of faint galaxies (i.e. thin cloud cover), but still appropriate for the brighter FunnelWeb fields. As such, flexibility in automated scheduling was critical for both surveys.

Stars observed by FunnelWeb had the potential to vary by as much as 9 magnitudes in *Gaia* G, corresponding to a nearly 4 000-fold difference in observed flux. This meant that a novel solution was required to efficiently tile the sky. The adopted solution in order to optimise both survey completion and SNR for all targets was to group stars into a into a series of overlapping magnitude bins, optimise exposure times for the faintest stars in a given bin, and to use a variable priority scale. By having overlapping bins, FunnelWeb could assess bin *completion* for only the

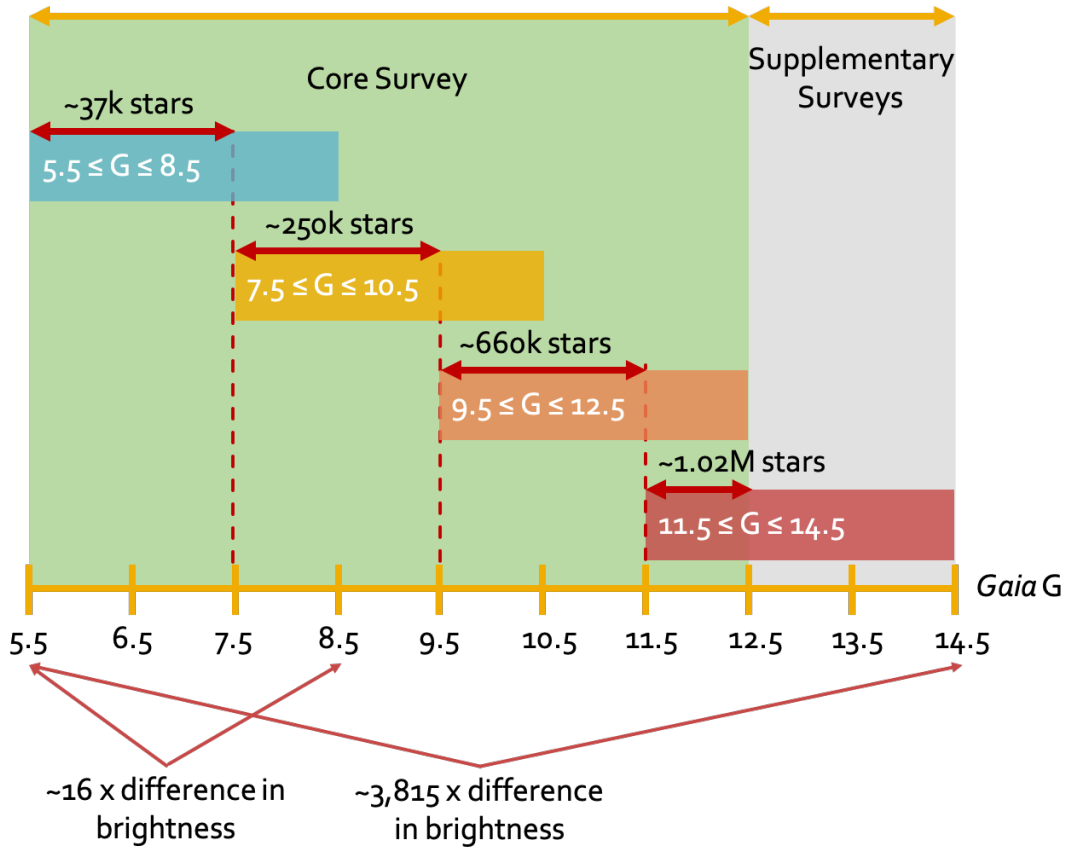

Figure 3.2: Overview of FunnelWeb's observing strategy highlighting its four different magnitude bins (each of which with a priority magnitude range), the number of stars in each bin, and the separation between core and supplementary surveys.

brightest stars in a given bin, preferring fainter stars to be observed in the overlapping fainter magnitude bin at higher SNR. The selected bin sizes were: G = [5.5, 8.5], [7.5. 10.5], [9.5, 12.5], [11.5, 14.5], with FunnelWeb aiming for 99% completion of its main survey for all stars with 5.5 ≤G≤ 12.5. This is summarised in Figure 3.2, along with the number of stars in each bin.

In addition to science targets, the observing strategy also had to take into account both guiding and calibration. Guiding is achieved using TAIPAN's complement of nine guide fibre bundles, separate to its 150 general use Starbugs (Staszak et al. 2016b). Targets for these bundles are known as *guides* and are drawn from the set of moderately bright stars in the input catalogue ($9 \leq G \leq 13$). For calibration, FunnelWeb planned to reserve a set of the 150 ordinary Starbugs to enable for flux calibration and sky subtraction during data reduction, known as *standard* and *sky* fibres respectively. Standards were selected based on a colour cut *Gaia* $G - J \leq 0.5$, with the intent to select hot, smooth–spectrum stars to aid with telluric correction and flux calibration. Sky fibres on the other hand were assigned from a separate input catalogue of dark sky positions, the details of which are outlined in Section 3.3.2. Although standards and guides were to be be drawn from the same input catalogue as the science targets,

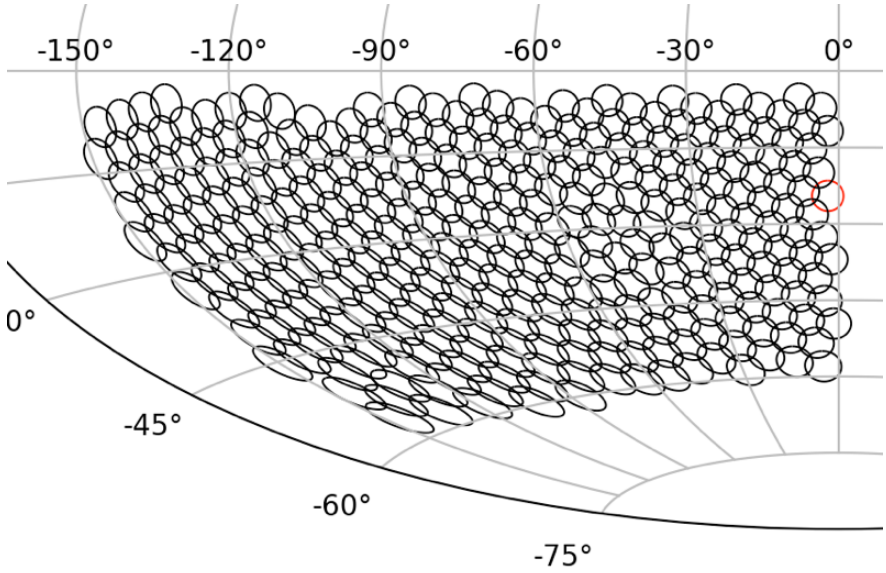

Figure 3.3: Tile overlap for example partial tiling with 2 040 tiles over the entire sky (Hardin, Sloane, & Smith 1994, 2000). Note that FunnelWeb planned to use a factor of ~2 greater tiling density than plotted here.

there was to be no constraint on repeat observations.

3.3.5 Sky Tiling Algorithm

The success of any multi-object survey—especially one targeting objects as bright and numerous as FunnelWeb—depends on efficient use of the instrument's multi-object potential. Both FunnelWeb and Taipan planned to divide the sky into a set of overlapping icosahedrally symmetric circular fields with constant central coordinates in right ascension and declination (see Figure 3.3 for an example, Hardin, Sloane, & Smith 1994, 2000[1]). The collection of targets for a given pointing of the telescope—along with the selection of standard, guide, and sky fibres—is known as a *tile*, with every science object possessing a given *priority*. Accordingly, the process whereby tiles are generated for whole Southern Hemisphere using the survey input catalogue is known as *tiling*.

The Python tiling code was initially written by Dr Marc White to suit the requirements of the Taipan Survey (see Section 4.4 of da Cunha et al. 2017)[2]. The specifics of FunnelWeb, however, required the implementation of a more complex algorithm[3] built from the core Taipan code, the implementation and testing of which forms the core contribution of this chapter.

FunnelWeb's tiling code implements a greedy algorithm to select the highest weighted tiles—based on the aggregate priorities of the objects contained within—and proceeds until a given completion target is reached. The main algorithmic complexity stems from the fact

[1] http://neilsloane.com/icosahedral.codes/
[2] https://github.com/marc-white/taipan-tiling
[3] https://github.com/adrains/taipan-tiling

that each tile overlaps with its neighbours, which removes the notion of viewing any individual field or tile in isolation, and complicates efforts to parallelise the problem. Regardless, for FunnelWeb, tiling is conducted a single magnitude range at a time, bright through faint, and can be summarised as follows:

1. Generate a set of tiles covering the sky (i.e. one tile per field) with allocated science, standard, guide, and sky targets (or positions). Allow targets to be duplicated between tiles.
2. Select the highest ranked tile from this set, and add it to the final set of telescope schedulable tiles.
3. Remove allocated science targets from further consideration in this tiling run.
4. Replace the removed tile, and reallocate all neighbouring (i.e. overlapping) tiles to ensure every science target is only observed a single time per tiling.
5. Recalculate the completion metric.
6. Repeat 2-5 until no useful tiles remain, or the completeness target is reached.
7. Repeat 1-6 for each magnitude range, until no magnitude ranges remain.

To facilitate the ranking of targets and tiles, every star in the input catalogue is given an integer priority between 0 and 5. This affects how likely it is to be incorporated into a given tile, and the resulting score of the tile itself. Targets that have not been observed before or those that are members of priority/supplementary surveys, will possess higher initial priorities, with the rankings labelled as 0 - Desperate, 1 - Marginal, 2 - Normal, 3 - Preferred, 4 - Required, and 5 - Priority. Fibre assignment takes into account, in order: target priority, target difficulty (higher for more crowded regions of sky), and proximity to the Starbug home position when assigning a given tile. For greedy selection of tiles, the tiles are given a score calculated as the exponential sum (base 3) of the priorities of each assigned target:

$$\text{tile score} = \sum_{i=1}^{N} 3^{P_i} \tag{3.2}$$

where N is the total number of science targets assigned to the tile, i is the target index, and P_i is the integer priority of target i. This has the effect of weighting heavily towards tiles with more higher priority targets.

Rather than being removed from consideration entirely, already observed targets would instead see their priority number drop to 0 or 1 (dependent on data quality and SNR). This reduced the likelihood they would be reobserved in subsequent tilings, but left open the possibility should a fibre remain vacant. Additionally, in order to preferentially observe all targets with the greatest SNR, the brightest stars within a given magnitude bin would see their priority temporarily increase. This can be seen in Figure 3.2, with the selected priority magnitude ranges marked by the thick red arrows: G = [5.5, 7.5], [7.5, 9.5], [9.5, 11.5], [11.5, 12.5].

FunnelWeb aimed to re-tile the sky with updated target priorities to account for observed targets and newly identified scientific priorities at least once per lunation. Targets for which

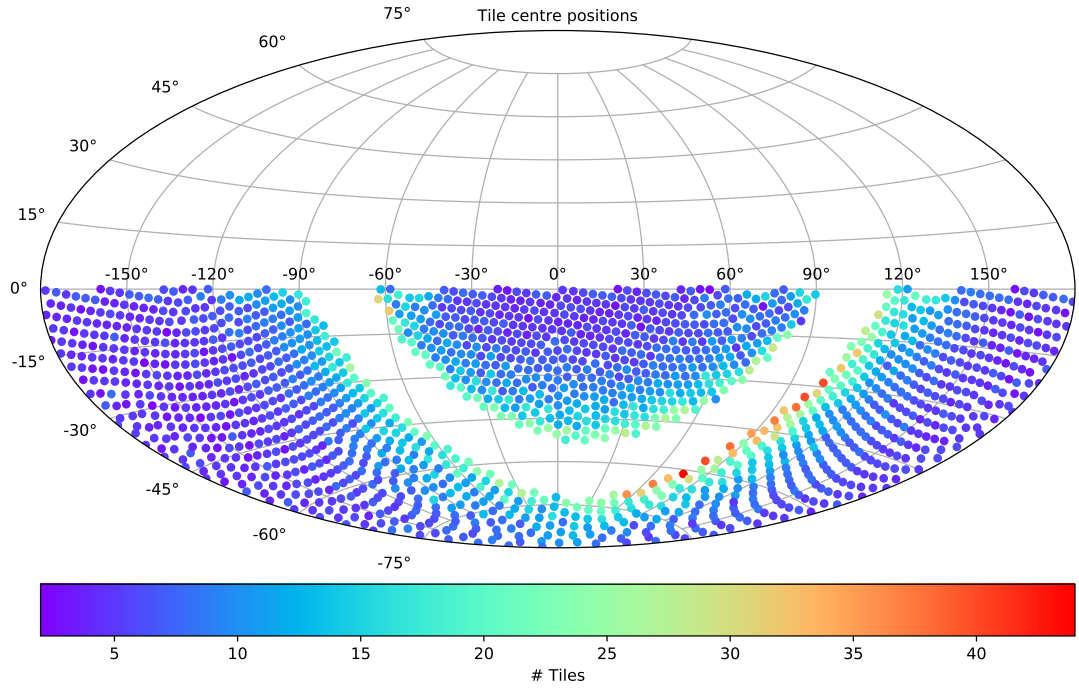

Figure 3.4: Simulated main survey tile density for each of the ~2 000 observed fields, as produced from a 99% completion ($|b| \geq 10$, DEC $< 0°$) tiling run which resulted in more than 15 000 tiles. Note that marker size here does not correspond to field size.

repeat observations would be scientifically valuable would have seen their priorities remain unchanged following a successful observation, allowing them to be re-observed each tiling run at an observational cadence of approximately once per month. However, the efficiency of repeat observations was strongly dependent on the tile density of the target's field. Figure 3.4 shows the tile density for a 99% completion tiling run with DEC$< 0°$, $|b| \geq 10$—more than 15 000 total tiles. As can be seen, most fields at higher Galactic latitudes would have been observed at most a few times per magnitude bin over the entire duration of the survey. Given this, re-observing these fields beyond the point where all other targets had been observed would have extended the total length of the survey, so any potential science gain would have had to be weighted against survey completion time.

Tiling Performance

There were a number of possible metrics available to evaluate the performance of FunnelWeb's tiling code. Broadly, however, these could be broken into: **a)** how effective the tiling algorithm was at aligning with the survey strategy and FunnelWeb's science goals, and **b)** computational efficiency affecting how often the tiling could be rerun.

The effectiveness of the tiling code in achieving the former metric can be seen in Figure 3.5, summarising the same 99% completion tiling run as displayed in Figure 3.4. Displayed are a series of histograms detailing the composition of the final set of schedulable tiles (in terms of allocated science, standard, guide, and sky fibres) for each magnitude bin. FunnelWeb

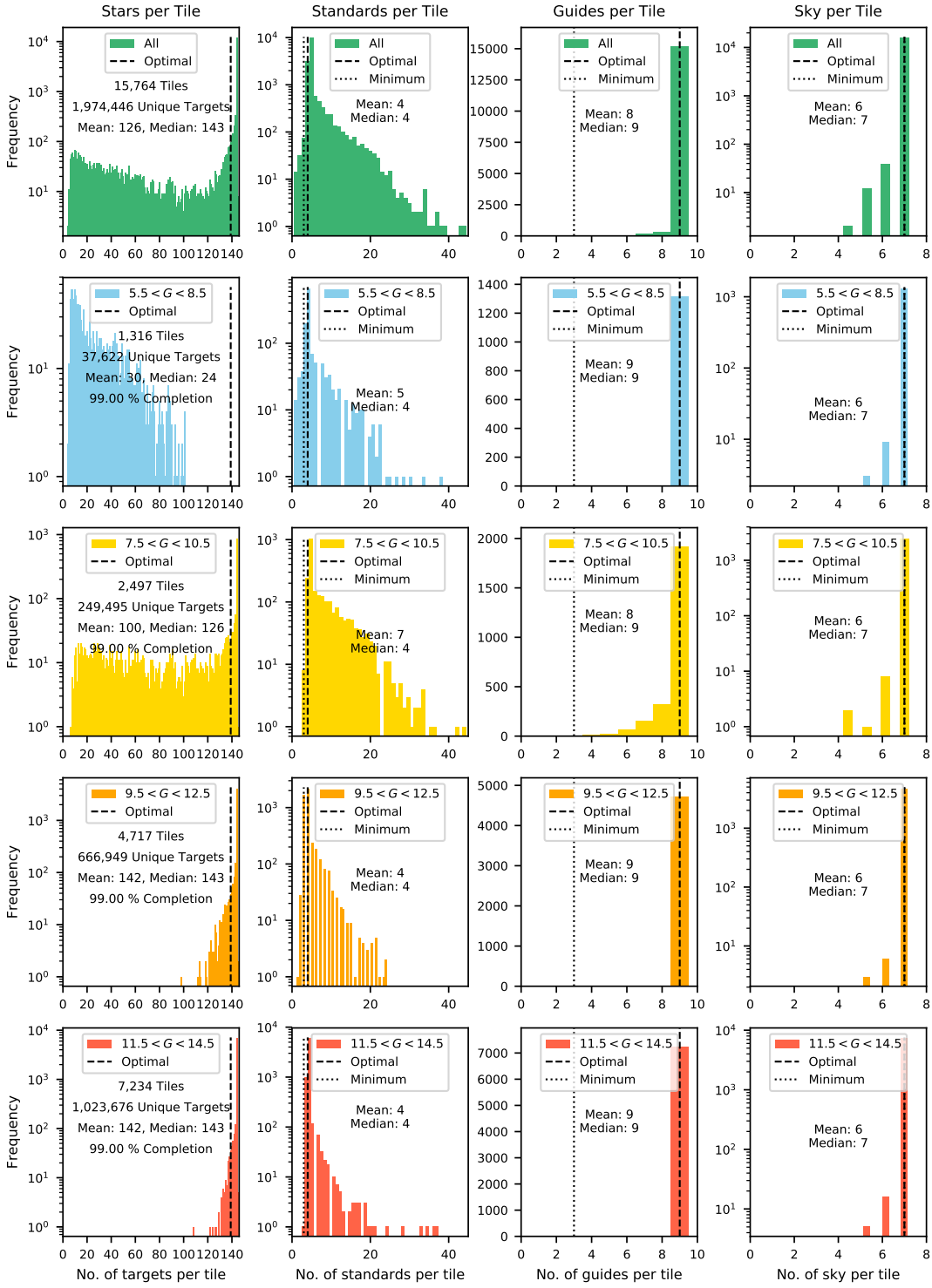

Figure 3.5: A grid of histograms summarising the results of a 99% completion tiling run. Each row represents a different magnitude bin and the corresponding distribution of assigned science, standard, guide, and sky fibres, with the first row being for the survey as a whole. Dotted lines represent minimal and optimal fibre assignments for each type of target. Of note is that FunnelWeb draws its standards from its science targets, and thus it is possible to have more than the 'optimal' number observed as standards function as repeated science observations.

required each tile to have at minimum three allocated standard and guide fibres (ideally four and nine respectively), along with seven sky fibres—all to meet its calibration goals. An optimally filled fibre would be one with all 139 remaining fibres filled, but as can be seen this was not often achieved for the brighter bins with lower on-sky densities of appropriate stars. While unfortunate, this was to be expected when targeting bright stars. Overall—considering that fainter fields have more tiles—the median tile was optimally filled, pointing to the efficiency of the algorithm.

The more difficult challenge to address, however, was the second metric: *computational* efficiency. The FunnelWeb input catalogue was large, and taking into account the overlap between the roughly 2 000 fields even a greedy algorithm such as this was incredibly computationally expensive—taking several weeks of computational time to run to completion in serial using Python. Substantial gains were made by profiling the code in operation, removing duplication and unnecessary calls, and making changes such as using more efficient data structures for look-up like hash-based sets rather than unordered lists. Whilst the algorithm in principle was easy to parallelise by farming out a given tile, its overlapping neighbours and all targets within these fields to sub-processes, in practice this was found to be ineffective in Python. The resulting parallel tiling code actually ran *slower* due to overheads associated with copying data between processes. Further gains were likely possible, especially if the algorithm was ported to a faster language like C, but this was ultimately not deemed worthwhile. As it was, the combination of only needing to retile once per lunation, and not needing to run to completion each time meant the serial implementation was adopted for initial use.

3.3.6 Closing the Loop: Scheduling, Fibre Allocation, and Data Verification

The final part of FunnelWeb's planning and observing loop involved how tiles were scheduled to be observed, which fibres were actually allocated, and the resulting data vetting to determine whether a target was observed with sufficient quality. When properly closed, this feedback loop ensured that FunnelWeb was properly achieving its science goals.

FunnelWeb's sheduling code, written by Dr Maruša Žerjal, served to be the interface between the tiling code and the telescope. To be considered for observation, a tile needed to be: within two hours of the local meridian, not already observed successfully, above 27° in elevation, not within 5° of zenith (for reasons related to dome rotation), not within 20° of the Moon, and above the current limiting magnitude given weather conditions at the time. Tiles meeting these conditions were then weighted by altitude, telescope slew time, moon distance, density (weighting lower density regions higher), fractional completion of the magnitude range in question, and the tile score as outputted from the tiling code. The final observed tile was the one closest to the local meridian from the top 5% highest weighted tiles.

Routing 150 Starbugs in parallel without collisions or tangled fibres was an understandably non-trivial problem. Just because a tile had all fibres allocated was no guarantee that the automated fibre scheduler and routing code on the telescope would actually be able to allocate all fibres in practice (Fernando et al. 2020). It was found to be a simpler solution to simply not allocate the most problematic fibres where a collision-free path not found, rather than devoting more time to optimisation or routing overheads. Thus, in addition to general data quality vetting, each target needed to be considered on an individual basis when marking it observed,

rather than considering the tile as a whole.

Taking all this into account, Dr Žerjal simulated the scheduler running for the duration of the survey, taking into account realistic SSO weather conditions and assuming a field reconfiguration time of 2 – 5 min. The result was a two year primary survey observing on average 3 300 targets a night.

3.4 Retrospective

Ultimately however, continued complexities and delays in TAIPAN's commissioning, the availability of research funds, and the timelines of upcoming spectroscopic surveys led to the cancellation of FunnelWeb in November 2019, and Taipan in December 2020. This loss represents a real blow to the Australian astronomical community—not limited to just the astronomers, instrument scientists, and engineers directly involved, but the many more people (including future students) who would have benefited from the data and science potential. At the time of writing, TAIPAN remains a prototype for MANIFEST and is still actively being commissioned on the UK-Schmidt Telescope. The promise of rapid parallel reconfiguration of fibres using Starbugs is still real, and it is hoped that the experience with TAIPAN will allow MANIFEST to meet with success.

From the FunnelWeb perspective however, it wasn't a complete loss. In late-2018 survey funding was reallocated to support a smaller scale replacement spectroscopic survey for one of FunnelWeb's core science programs: suspected pre-main sequence stars. Conducted from the ANU 2.3 m Telescope and using WiFeS (the Wide Field Spectrograph, Dopita et al. 2007) and the now decommissioned Echelle Spectrograph, this program was led by Dr Maruša Žerjal with the goal of identifying young stars through chromospheric emission features and lithium absorption. Over 64 nights, 756 overluminous late K and early M star candidates were observed, and while a manual, one at a time survey is an obvious step down from what TAIPAN offered, the targets were able to be observed at higher spectral resolution. In total, 346 stars were found to have detectable lithium absorption—318 of which were new detections—with Hα and Ca H&K emission measures and RVs reported, published as Žerjal et al. (2021).

From this survey—initially sharing observing time, later an independent program—grew another survey for one of FunnelWeb's core science cases: *TESS* cool dwarf candidate planet hosts. The goal of this program was to spectroscopically characterise the stellar hosts, and use the resulting stellar parameters in modelling the *TESS* transit light curves to determine candidate planet radii. In total 92 such stars were observed with 100 candidate planets between them. This work was published as Rains et al. (2021) and is the subject of the next chapter.

A discussion of the larger scientific implications of the cancellation of FunnelWeb can be found in the future work section of Chapter 5, specifically Section 5.2.3. In particular, this section discusses whether FunnelWeb-style survey is even scientifically competitive in light of *Gaia* DR3 and other upcoming surveys. Regardless of this setback, the future of observational stellar astrophysics looks bright.

Chapter 4

Spectroscopic Characterisation of 92 Southern TESS Candidate Planet Hosts

This paper was originally published as **A. D. Rains**, M. Žerjal, M. J. Ireland, T. Nordlander, M. S. Bessell, L. Casagrande. C. A. Onken, M. Joyce, J. Kammerer, H. Abbot, 2021, *'Characterization of 93 Southern TESS Candidate Planet Hosts and a New Photometric [Fe/H] Relation for Cool Dwarfs'*, MNRAS, 504, 5788.

4.1 Abstract

We present the results of a medium resolution optical spectroscopic survey of 92 cool ($3\,000 \lesssim T_{\rm eff} \lesssim 4\,500$ K) southern *TESS* candidate planet hosts, and describe our spectral fitting methodology used to recover stellar parameters. We quantify model deficiencies at predicting optical fluxes, and while our technique works well for $T_{\rm eff}$, further improvements are needed for [Fe/H]. To this end, we developed an updated photometric [Fe/H] calibration for isolated main sequence stars built upon a calibration sample of 69 cool dwarfs in binary systems, precise to ± 0.19 dex, from super-solar to metal poor, over $1.51 < Gaia\ (B_P - R_P) < 3.3$. Our fitted $T_{\rm eff}$ and $R_\star$ have median precisions of 0.8% and 1.7%, respectively and are consistent with our sample of standard stars. We use these to model the transit light curves and determine exoplanet radii for 100 candidate planets to 3.5% precision and see evidence that the planet-radius gap is also present for cool dwarfs. Our results are consistent with the sample of confirmed *TESS* planets, with this survey representing one of the largest uniform analyses of cool *TESS* candidate planet hosts to date.

4.2 Introduction

Low mass stars are the most common kind of star in the Galaxy, comprising more than two thirds of all stars (Chabrier 2003), and dominating the Solar Neighbourhood population (e.g. Henry et al. 1994, 2006; Winters et al. 2015; Henry et al. 2018). This abundance alone makes them prime targets for planet searches, with microlensing surveys, which have very little bias

on host star masses, revealing that there is at least one bound planet per Milky Way star (Cassan et al. 2012). Results from the Kepler Mission (Borucki et al. 2010) also bear this out, showing that a large number of planets remain undiscovered around cool dwarfs (Morton & Swift 2014), and that such cool stars are actually more likely to host small planets ($2 < R_P < 4\,R_\oplus$, where R_P and $R_\oplus$ are the planet and earth radius respectively) than their hotter counterparts (Howard et al. 2012; Dressing & Charbonneau 2015).

However, the inherent faintness of these stars complicates the study of both them and their planets. While we now know of over 4 000 confirmed planets orbiting stars other than our own (overwhelmingly discovered by transiting exoplanet surveys), almost an equal number await confirmation[1]. Exoplanet transit surveys like Kepler and *TESS* (Ricker et al. 2015) are able to place tight constraints on planetary radii given a known stellar radius, but follow-up precision radial velocity observations are required to provide planetary mass constraints. This is the second reason why planet searches around low mass stars are critical: their smaller radii and lower masses make the transit signals and radial velocities of higher amplitudes for any planets they host as compared to the same planets around more massive host stars. This is especially important when looking for planets with terrestrial radii or masses respectively.

Many planet host stars have never been targeted by a spectroscopic survey, leaving their properties to be estimated through photometry alone. For instance, the *TESS* input catalogue (Stassun et al. 2018, 2019) based its stellar parameters primarily on photometry, having spectroscopic properties for only about 4 million stars of the nearly 700 million with photometrically estimated equivalents. While stars warmer than 4 000 K are well suited to bulk estimation of properties from photometry (see e.g. Carrillo et al. 2020), special care must be taken for cool dwarfs whose faintness and complex atmospheres make such relations more complex to develop and implement (e.g. see Muirhead et al. 2018 for the K and M dwarf specific approach taken from the *TESS* input catalogue).

NASA's *TESS* Mission, by virtue of being all sky, has given us a wealth of bright candidates which are now being actively followed up by ground based spectroscopic surveys. While multi-epoch radial velocity observations are required to determine planetary masses, these surveys are typically biased towards the brightest stars and smallest planets. As such, there remains a need for single-epoch spectroscopic follow-up of fainter targets to provide reliable host star properties (primarily $T_{\rm eff}$, $\log g$, [Fe/H], and the stellar radius $R_\star$) and allow radial constraints to be placed on transiting planet candidates. Indeed, the LAMOST Survey (Zhao et al. 2012) undertook targeted low resolution spectroscopic follow-up of stars in the Kepler field (De Cat et al. 2015) with the goal of deriving spectroscopic stellar properties. Considering the goal of planet radii determination specifically, Dressing et al. (2019) used medium-resolution near-infrared (NIR) spectra, and Wittenmyer et al. (2020) high-resolution optical spectra to follow-up K2 (Howell et al. 2014) transiting planet candidate hosts and place radius constraints on both planets and their hosts.

Even without mass estimates, much can be learned about exoplanet demographics from their radii alone. As demonstrated by Fulton et al. (2017), Fulton & Petigura (2018), Van Eylen et al. (2018), Kruse et al. (2019), Hardegree-Ullman et al. (2020), Cloutier & Menou (2020), and Hansen et al. (2021), having a large sample of precise planet radii allows insight into

[1] https://exoplanetarchive.ipac.caltech.edu/

the exoplanet radius distribution, which appears to be bimodal with an observable gap in the super-Earth regime ($\sim 1.8\,R_\oplus$). This is thought to be the result of physical phenomena like photoevaporation (where flux from the parent star strips away weakly held atmospheres, e.g. Owen & Wu 2013; Lee et al. 2014; Lopez & Fortney 2014; Lee & Chiang 2016; Owen & Wu 2017; Lopez & Rice 2018), or core-powered mass loss (where a cooling rocky core erodes light planetary atmospheres via its cooling luminosity, e.g. Ikoma & Hori 2012; Ginzburg et al. 2018; Gupta & Schlichting 2019, 2020), and its location likely has a dependence on stellar host mass (e.g. Cloutier & Menou 2020). As such, improving the sample of planets with radius measurements allows us to place observational constraints on planet formation channels and the mechanisms that sculpt planets throughout their lives.

The scientific importance of searching for planets around low-mass stars to study their demographics is thus clear. However, the exact approach for understanding the stars themselves is less obvious, as cool dwarfs are not as well understood as their prevalence would suggest. Their inherent faintness and atmospheric complexity has lead to long standing issues observing representative sets of standard stars, generating synthetic spectra accounting for molecular absorption as well as consistently modelling their evolution (see e.g. Allard et al. 1997; Chabrier 2003).

Analysis of spectra from warmer stars is made simpler by the existence of regions of spectral continuum where atomic or molecular line absorption is minimal, allowing one to disentangle within reasonable uncertainties the effect of [Fe/H] and $T_{\rm eff}$ on an emerging spectrum. This is not the case for cool dwarfs for which there is no continuum at shorter wavelengths, with the deepest absorption caused by most notably TiO in the optical and water in the NIR, but also various other oxides or hydrides. The strength of these features is a function of *both* temperature and [Fe/H], making it difficult to ascribe a unique $T_{\rm eff}$-[Fe/H] pair to a given star.

Despite this complexity, it is possible to take advantage of the relative [Fe/H]-insensitivity of NIR K band magnitudes alongside [Fe/H]-sensitive optical photometry to probe cool dwarf [Fe/H]. This was predicted by theory (see e.g. Allard et al. 1997, Baraffe et al. 1998, and Chabrier & Baraffe 2000 for summaries), confirmed observationally (Delfosse et al. 2000), and later formalised into various empirical calibrations (Bonfils et al. 2005; Johnson & Apps 2009; Schlaufman & Laughlin 2010; Neves et al. 2012; Hejazi et al. 2015; Dittmann et al. 2016).

The last decade has seen a number of studies using low-medium resolution (mostly NIR) spectra, often focused on the development of [Fe/H] relations based on spectral indices (e.g. optical-NIR: Mann et al. 2013b,c, 2015; Kuznetsov et al. 2019; NIR: Newton et al. 2014; H band: Terrien et al. 2012; K band: Rojas-Ayala et al. 2010, 2012). Other studies have opted to use high-resolution spectra which gives access to unblended atomic lines that are not accessible to lower resolution observations (e.g. optical: Bean et al. 2006a,b; Rajpurohit et al. 2014; Passegger et al. 2016; Y band: Veyette et al. 2017; optical-NIR: Woolf & Wallerstein 2005, 2006; Passegger et al. 2018; J band: Önehag et al. 2012; H band: Souto et al. 2017).

Finally, on the point of M-dwarf evolutionary models (and low-mass, cool main sequence stars more generally), there has long been contention between model radii and observed radii (e.g. Kraus et al. 2015). This is often attributed to magnetic fields (and/or the mixing length parameter, which simplistically parameterizes the effects of magnetic fields among other energy transport mechanisms in 1D stellar structure and evolution programs) and is related to the difficulty in accurately modelling convection (e.g. Feiden & Chaboyer 2012; Joyce & Chaboyer

2018a). Fortunately, due to the aforementioned insensitivity of NIR K band photometry to [Fe/H], empirical mass and radius relations have been developed and calibrated on interferometric diameters and dynamical masses (e.g. Henry & McCarthy 1993; Delfosse et al. 2000; Benedict et al. 2016; Mann et al. 2015, 2019).

Here we conduct a moderate resolution spectroscopic survey of 92 southern cool ($T_{\rm eff} \lesssim 4,500$ K) *TESS* candidate planet hosts with the WiFeS instrument (Dopita et al. 2007) on the ANU 2.3 m Telescope at Siding Spring Observatory (NSW, Australia). We combine our spectroscopic observations with literature optical photometry and trigonometric parallaxes from *Gaia* DR2 (Gaia Collaboration et al. 2016b; Brown et al. 2018), infrared photometry from *2MASS* (Skrutskie et al. 2006), optical photometry from SkyMapper DR3 (Keller et al. 2007, Onken et al. 2019, DR3 DOI: 10.25914/5f14eded2d116), empirical relations from (Mann et al. 2015, 2019), and synthetic MARCS model atmospheres (Gustafsson et al. 2008) in order to produce stellar $T_{\rm eff}$, $\log g$, [Fe/H], bolometric flux ($f_{\rm bol}$), $R_\star$, and stellar mass ($M_\star$). By modelling the transit light curves of these host stars, we are additionally able to produce precision planetary radii for 100 candidate planets, which represents one of the largest uniform analyses of cool *TESS* hosts to date. Our observations and data reduction are described in Section 4.3, our photometric [Fe/H] relation in Section 4.4, our host star characterisation methodology and resulting parameters in Section 4.5, our transit light curve fitting and results in Section 4.6, discussion of results in Section 4.7, and concluding remarks in Section 4.8.

4.3 Observations and data reduction

4.3.1 Target Selection

Our initial target selection of southern cool dwarf TOIs was done in August 2019, including stars with $T_{\rm eff} \leq 4\,500$ K in the *TESS* input catalogue and unblended *2MASS* photometry. In order to have reliable parallaxes, we impose the additional requirement that our stars have a *Gaia* DR2 Renormalised Unit Weight Error (RUWE)[2] of < 1.4, as recommended by the *Gaia* team[3]. Adding extra targets sourced in August 2020, and removing those identified as false-positives through community follow-up observations (as listed on NASA's Exoplanet Follow-up Observing Program for *TESS*, ExoFOP-*TESS*, website[4]), we are left with a sample of 92 southern candidate planet hosts spread across the sky with 8.7 < apparent *Gaia* $G < 15.8$. These targets are listed in Table 4.1, and plotted on a colour-magnitude diagram in Figure 4.1, noting that a few appear distinctly above the main sequence. These stars are thus overluminous because they are young and still contracting to the main sequence, or because they are unresolved binaries.

All our targets have *Gaia* DR2 G, B_P, R_P, and *2MASS* J, H, K_S photometry, and most have at least one of *SkyMapper* DR3 r, i, z (noting that the survey is still ongoing, so not all bands

[2]Expected to be approximately 1.0 in cases where the single star model provides a good fit for the astrometric data. See: https://gea.esac.esa.int/archive/documentation/GDR2/Gaia_archive/chap_datamodel/sec_dm_main_tables/ssec_dm_ruwe.html

[3]Though we do accept TIC 158588995 with a marginal RUWE~1.47 as it sits on the main sequence and does not appear overluminous.

[4]https://exofop.ipac.caltech.edu/tess/

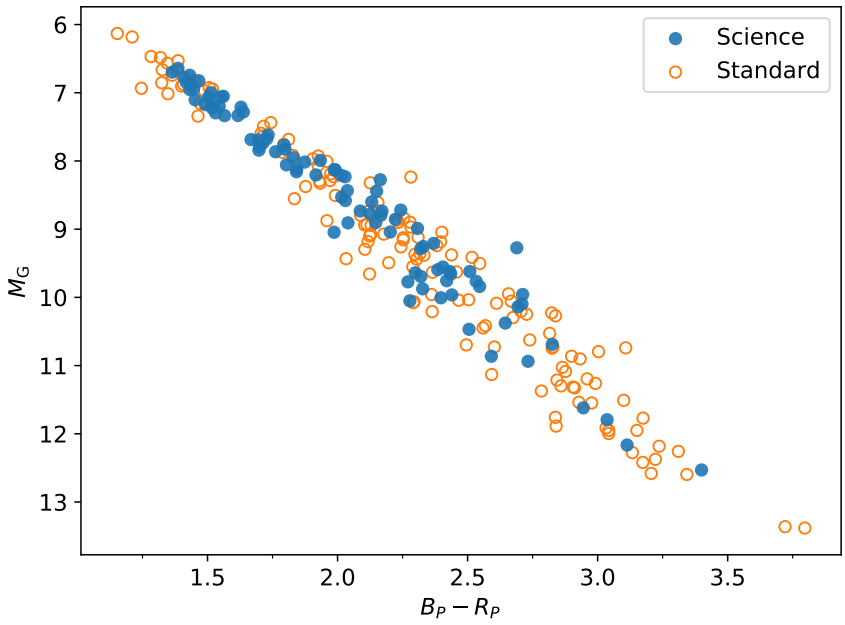

Figure 4.1: *Gaia* DR2 M_G versus $(B_p - R_p)$ colour magnitude diagram for science targets (filled blue circles) and cool dwarf standards (orange open circles).

are available for all targets). We calculate distances from *Gaia* DR2 parallaxes, incorporating the systematic parallax offset of -82 ± 33 μas found by Stassun & Torres (2018).

To correct for reddening we use the 3D dust map of Leike et al. (2020), implemented within the python package `dustmaps` (Green 2018). Targeting bright, cool dwarfs as we do here automatically means our stars will be relatively close, and we take those within the Local Bubble, two thirds of our sample, to be unreddened ($\lesssim 70$ pc, e.g. Leroy 1993; Lallement et al. 2003) so long as the *Gaia* G band extinction reported by the dust map is consistent with zero ($A_G < 0.01$). Nominal extinction coefficients were sourced from Casagrande & VandenBerg (2014) for the *2MASS* JHK_S bands and Casagrande et al. (2019) for *SkyMapper* $uvgriz$, with *Gaia* G, B_P, and R_P coefficients computed from the relation given in Casagrande et al. (2020) for $B_P - R_P = 2.03$, the median value for our sample.

4.3.2 Standard Selection

Given the complexities involved in determining the properties of cool dwarfs, we also observed a set of 136 well characterised late K and early–mid M dwarf standards from the literature. Broadly these standards have parameters from at least one of the following sources:

1. [Fe/H] from a companion with spectral type F/G/K,
2. [Fe/H] from low resolution NIR spectra,
3. $T_{\rm eff}$ from interferometry.

Table 4.1: Science targets

TOI[a]	TIC[b]	*2MASS*[c]	*Gaia* DR2[d]	RA[d] (hh mm ss.ss)	DEC[d] (dd mm ss.ss)	G^d (mag)	$B_p - R_p{}^d$ (mag)	Plx[d] (mas)	ruwe[d]	E($B-V$)	N^e_{pc}
741	359271092	09213761-6016551	5299440441521812992	09 21 35.86	-61 43 07.68	8.68	2.03	95.63 ± 0.03	1.1	0.00	1
731	34068865	09442986-4546351	5412250540681250560	09 44 29.16	-46 13 15.60	9.15	2.32	106.21 ± 0.03	1.1	0.00	1
260	37749396	00190556-0957530	2428162410789155328	00 19 05.52	-10 02 01.68	9.31	1.70	49.51 ± 0.06	0.9	0.00	1
836	440887364	15001942-2427147	6230733559097425152	15 00 19.18	-25 32 44.88	9.39	1.55	36.33 ± 0.04	1.0	0.01	2
562	413248763	09360161-2139371	5664814198431308288	09 36 01.80	-22 20 05.64	9.88	2.40	105.88 ± 0.06	1.1	0.00	3
455	98796344	03015142-1635356	5153091836072107136	03 01 51.00	-17 24 19.80	10.05	2.59	145.55 ± 0.08	1.1	0.00	2
139	62483237	22253655-3454346	6598814657249555328	22 25 36.58	-35 05 25.08	10.08	1.45	23.55 ± 0.04	1.0	0.00	1
253	322063810	00571629-5135048	4928367189956040960	00 57 16.44	-52 24 52.92	10.18	1.71	32.39 ± 0.03	1.0	0.00	1
134	234994474	23200751-6003545	6491962296196145664	23 20 06.86	-61 56 03.48	10.23	2.03	39.73 ± 0.04	1.0	0.00	1
544	50618703	05290957-0020331	3220926542276901888	05 29 09.62	-1 39 25.56	10.40	1.57	24.29 ± 0.04	1.1	0.01	1
486	260708537	06334998-5831426	5482827676662168832	06 33 49.18	-59 28 30.00	10.53	2.43	65.70 ± 0.03	1.2	0.00	1
177	262530407	01214538-4642518	4933912198893332224	01 21 45.22	-47 17 07.08	10.55	2.17	44.46 ± 0.05	1.0	0.00	1
129	201248411	00004490-5449498	4923860051276772608	00 00 44.54	-55 10 09.12	10.59	1.39	16.16 ± 0.02	1.1	0.00	1
175	307210830	08180763-6818468	5271055243163629056	08 18 07.90	-69 41 07.80	10.60	2.51	94.14 ± 0.03	1.1	0.00	3
824	193641523	14483982-5735175	5880886001621564928	14 48 39.72	-58 24 39.96	10.72	1.36	15.61 ± 0.03	1.1	0.02	1
133	219338557	23373497-5857166	6489346046933733632	23 37 35.38	-59 02 41.64	10.72	1.53	20.53 ± 0.03	1.0	0.00	1
1130	254113311	19053021-4126151	6715688452614516736	19 05 30.24	-42 33 44.64	10.88	1.55	17.14 ± 0.05	1.1	0.01	2
198	12421862	00090428-2707196	2333676738049780352	00 09 05.16	-28 52 41.88	10.92	1.99	42.12 ± 0.05	1.0	0.00	1
833	362249359	09423526-6228346	5250780970316845696	09 42 34.92	-63 31 26.76	11.05	1.83	23.94 ± 0.02	0.8	0.01	1
178	251848941	00291228-3027133	2318295979126499200	00 29 12.48	-31 32 45.24	11.15	1.49	15.92 ± 0.05	1.2	0.00	3
279	122613513	02444524-3212391	5063070558501465856	02 44 45.24	-33 47 20.40	11.20	1.44	13.42 ± 0.04	1.1	0.00	1
704	260004324	06042035-5518468	5500061456275483776	06 04 21.60	-56 41 18.60	11.23	2.22	33.48 ± 0.03	1.0	0.00	1
1078	370133522	20274210-5627262	6468968316900356736	20 27 42.86	-57 32 15.72	11.24	2.32	49.06 ± 0.05	1.0	0.00	1
969	280437559	07403284+0205561	3087206553745290624	07 40 32.81	+2 05 54.96	11.25	1.47	12.92 ± 0.05	1.4	0.01	1
620	296739893	09284158-1209551	5738284016370287616	09 28 41.62	-13 49 58.08	11.31	2.24	30.25 ± 0.05	1.0	0.00	1
910	369327947	19205439-8233170	6347643496607835520	19 20 57.10	-83 26 24.72	11.42	2.73	80.09 ± 0.04	1.1	0.00	1
713	167600516	06480517-6537252	5285060409961261696	06 48 05.14	-66 22 32.52	11.42	1.52	14.39 ± 0.02	0.9	0.01	2
932	260417932	06234590-5434414	5499671713762981248	06 23 45.82	-55 25 19.20	11.42	1.41	11.68 ± 0.02	0.8	0.01	2
240	101948569	00590112-4409389	4982951791883929472	00 59 01.18	-45 50 20.76	11.43	1.50	13.33 ± 0.03	1.1	0.00	1
696	77156829	04324261-3947112	4864160624337973248	04 32 42.96	-40 12 32.76	11.54	2.28	50.28 ± 0.02	1.1	0.00	2
244	118327550	00421695-3643053	5001098681543159040	00 42 16.75	-37 16 55.20	11.55	2.55	45.36 ± 0.07	1.3	0.00	1

Notes: [a] TESS Object of Interest ID, [b] TESS Input Catalogue ID (Stassun et al. 2018, 2019),[c] 2MASS (Skrutskie et al. 2006), [c] Gaia (Brown et al. 2018) - note that Gaia parallaxes listed here have been corrected for the zeropoint offset, [d] Number of candidate planets, NASA Exoplanet Follow-up Observing Program for TESS

Table 4.1: – *continued*

TOI[a]	TIC[b]	*2MASS*[c]	*Gaia* DR2[d]	RA[d] (hh mm ss.ss)	DEC[d] (dd mm ss.ss)	G^d (mag)	$B_p - R_p{}^d$ (mag)	Plx[d] (mas)	ruwe[d]	E($B-V$)	N^e_{pc}
270	259377017	04333970-5157222	4781196115469953024	04 33 39.86	-52 02 33.36	11.63	2.33	44.46 ± 0.03	1.0	0.00	3
912	406941612	15172165-8028225	5772442647192375808	15 17 18.86	-81 31 36.12	11.64	2.40	38.27 ± 0.02	1.1	0.01	1
475	100608026	05465951-3231592	2901089987127041920	05 46 59.59	-33 28 03.00	11.70	1.76	16.99 ± 0.02	1.0	0.01	1
442	70899085	04164560-1205023	3189306030970782208	04 16 45.65	-13 54 54.36	11.73	1.99	18.98 ± 0.04	1.2	0.00	1
761	165317334	11570326-3806169	3460168250866990848	11 57 03.12	-39 53 42.72	11.73	1.73	14.94 ± 0.04	1.2	0.01	1
870	219229644	04131645-5056400	4782093729275660160	04 13 16.63	-51 03 20.52	11.78	1.99	18.56 ± 0.02	1.1	0.00	1
904	261257684	05572938-8307486	4620844400530949376	05 57 29.11	-84 52 13.08	11.84	2.02	21.67 ± 0.02	1.0	0.01	1
732	36724087	10183516-1142599	3767281845873242112	10 18 34.78	-12 16 55.92	11.85	2.69	45.46 ± 0.08	1.1	0.00	2
656	36734222	10193800-0948225	3767805209112436736	10 19 37.97	-10 11 36.96	11.89	1.63	11.50 ± 0.04	1.1	0.01	1
1075	351601843	20395334-6526579	6426188308031756288	20 39 53.09	-66 33 01.08	12.05	1.84	16.24 ± 0.02	1.2	0.00	1
700	150428135	06282325-6534456	5284517766615492736	06 28 22.97	-66 25 17.04	12.06	2.39	32.10 ± 0.02	1.1	0.00	3
727	149788158	08425684-0229529	3072157538091829120	08 42 56.86	-3 30 05.04	12.07	2.15	23.24 ± 0.03	1.1	0.00	1
249	179985715	00561930-3856552	4987729474846997248	00 56 19.20	-39 03 02.88	12.08	1.70	14.13 ± 0.03	1.1	0.00	1
1201	29960110	02485926-1432152	5157183324996790272	02 48 59.45	-15 27 45.72	12.10	2.37	26.37 ± 0.04	1.1	0.00	1
875	14165625	05120890-3742313	4820828591913853696	05 12 08.93	-38 17 29.40	12.12	1.51	9.39 ± 0.02	1.0	0.01	1
929	175532955	03033741-3955515	5044287532642519680	03 03 37.73	-40 04 09.12	12.13	1.42	8.71 ± 0.02	1.1	0.01	1
493	19025965	07583071+1253005	3151371883379694720	07 58 30.65	+12 52 59.88	12.19	1.56	9.29 ± 0.04	1.1	0.01	1
1216	141527965	05505139-7541200	4648441970589471104	05 50 51.55	-76 18 41.04	12.31	1.62	10.02 ± 0.03	1.2	0.01	1
233	415969908	22545039-1854426	2402715141877299584	22 54 50.06	-19 05 15.36	12.41	2.27	29.58 ± 0.04	1.0	0.00	2
711	38510224	04100386-6156326	4676789514954240768	04 10 03.86	-62 03 26.28	12.45	1.45	8.43 ± 0.02	1.0	0.01	1
876	32497972	05362611-2414377	2963392606627366912	05 36 26.23	-25 45 20.16	12.47	1.87	12.76 ± 0.03	1.1	0.01	1
785	374829238	05532099-6538022	4755884700667639296	05 53 20.95	-66 21 59.40	12.51	2.04	15.23 ± 0.02	1.0	0.01	1
406	153065527	03170297-4214323	4851053999056603904	03 17 03.02	-43 45 21.24	12.55	2.71	32.17 ± 0.04	1.2	0.00	2
714	219195044	06093401-5349245	5500474185452572032	06 09 34.18	-54 10 37.20	12.56	2.04	18.54 ± 0.02	1.2	0.01	2
900	210873792	16233735-3122228	6037266684232926208	16 23 37.22	-32 37 35.04	12.59	1.52	8.23 ± 0.05	0.9	0.03	1
557	55488511	03560411-1016192	3193508849745633280	03 56 04.27	-11 43 40.80	12.60	1.92	13.14 ± 0.04	1.1	0.01	1
864	231728511	05254662-5121253	4772266186971169792	05 25 46.42	-52 38 34.80	12.66	2.42	26.22 ± 0.03	1.1	0.01	1
256	92226327	00445930-1516166	2371032916186181760	00 44 59.66	-16 43 33.24	12.67	3.04	66.70 ± 0.07	1.1	0.00	2
702	237914496	03444203-6511567	4672700190692201088	03 44 41.98	-66 48 06.12	12.68	1.80	11.82 ± 0.03	1.1	0.01	1
1082	261108236	05330624-8048563	4621526273835900288	05 33 06.19	-81 11 04.20	12.68	1.70	9.95 ± 0.03	1.1	0.01	1

Table 4.1: – *continued*

TOI[a]	TIC[b]	*2MASS*[c]	*Gaia* DR2[d]	RA[d] (hh mm ss.ss)	DEC[d] (dd mm ss.ss)	G^d (mag)	$B_p - R_p{}^d$ (mag)	Plx[d] (mas)	ruwe[d]	E($B-V$)	N^e_{pc}
672	151825527	11115769-3919400	5396580575830873728	11 11 57.82	-40 40 18.84	12.72	2.13	14.92 ± 0.03	1.1	0.01	1
806	33831980	04134003-7605515	4627952094666051072	04 13 39.86	-77 54 07.20	12.77	1.67	9.55 ± 0.02	1.3	0.01	1
797	271596225	07141480-7436089	5262540590756812032	07 14 15.14	-75 23 48.84	12.78	2.20	17.77 ± 0.02	1.1	0.01	2
663	54962195	10401596-0830385	3762515188088861184	10 40 15.82	-9 29 20.04	12.81	2.13	15.54 ± 0.04	1.0	0.01	2
540	200322593	05051443-4756154	4785886941312921344	05 05 14.33	-48 03 45.00	12.89	3.11	71.39 ± 0.04	1.0	0.00	1
285	220459976	04584731-5623385	4764216563561182336	04 58 47.33	-57 36 22.32	13.07	1.79	8.61 ± 0.02	0.9	0.01	1
674	158588995	10582099-3651292	5400949450924312576	10 58 20.78	-37 08 30.84	13.08	2.53	21.67 ± 0.05	1.5	0.01	1
789	300710077	07410444-7118157	5264306681309492864	07 41 04.85	-72 41 46.32	13.15	2.44	23.01 ± 0.03	1.3	0.01	1
873	237920046	03465622-6320142	4673392195823039744	03 46 56.78	-64 39 47.16	13.16	2.09	12.97 ± 0.02	1.3	0.01	1
698	141527579	05505661-7637132	4647922867959139072	05 50 57.38	-77 22 49.44	13.26	2.33	15.75 ± 0.03	1.2	0.01	1
136	410153553	22415815-6910089	6385548541499112448	22 41 59.09	-70 49 40.44	13.39	3.40	67.15 ± 0.05	1.1	0.00	1
269	220479565	05032306-5410378	4770828304936109056	05 03 23.11	-55 49 20.28	13.41	2.30	17.51 ± 0.02	1.1	0.01	1
654	35009898	10585379-0532468	3788670679927991296	10 58 53.90	-6 27 09.00	13.42	2.51	17.29 ± 0.05	1.1	0.01	1
782	429358906	12154108-1854365	3518374197418907648	12 15 40.90	-19 05 22.92	13.55	2.71	19.01 ± 0.07	1.2	0.01	1
521	27649847	08132251+1213181	649852779797683968	08 13 22.63	+12 13 19.56	13.58	2.44	16.38 ± 0.06	1.3	0.00	1
203	259962054	02520450-6741155	4647534190597951232	02 52 04.34	-68 18 46.80	13.59	2.94	40.31 ± 0.05	1.4	0.00	1
532	144700903	05401918+1133463	3340265717587057536	05 40 19.22	+11 33 45.36	13.63	1.93	7.38 ± 0.03	1.1	0.02	1
756	73649615	12482523-4528140	6129327525817451648	12 48 24.89	-46 31 46.20	13.66	2.31	11.58 ± 0.04	1.2	0.02	1
302	229111835	01095538-5214219	4927215760764862976	01 09 55.51	-53 45 37.80	13.71	1.64	5.10 ± 0.01	1.0	0.01	1
435	44647437	03573850-2511238	5082797618168232320	03 57 38.54	-26 48 36.36	13.75	1.73	6.02 ± 0.02	1.1	0.01	1
1067	201642601	19144126-5934458	6638412919991750912	19 14 41.28	-60 25 14.16	13.82	1.43	3.76 ± 0.02	1.0	0.03	1
210	141608198	05555049-7359046	4650160717726370816	05 55 50.83	-74 00 52.92	13.84	2.83	23.33 ± 0.05	1.3	0.01	1
1073	158297421	19095625-4939538	6658373007402886400	19 09 56.26	-50 20 06.36	14.31	1.43	3.30 ± 0.04	1.0	0.04	1
468	33521996	05523523-1901539	2966680597368750720	05 52 35.23	-20 58 06.24	14.34	2.01	5.88 ± 0.04	1.2	0.01	1
122	231702397	22114728-5856422	6411096106487783296	22 11 47.57	-59 03 14.04	14.34	2.64	16.07 ± 0.06	1.2	0.00	1
507	348538431	08063103-1545526	5724250571514167424	08 06 31.10	-16 14 07.08	14.48	2.69	8.99 ± 0.06	1.3	0.01	1
551	192826603	05305145-3637508	4821739369794767744	05 30 51.41	-37 22 08.40	14.83	1.84	4.56 ± 0.02	1.0	0.02	1
552	44737596	04034783-2524320	5082914338199586560	04 03 47.86	-26 35 27.96	14.87	2.15	5.10 ± 0.03	1.1	0.01	1
234	12423815	00101648-2616566	2335244779070099200	00 10 16.54	-27 43 03.36	15.69	2.17	3.98 ± 0.07	1.1	0.01	1
555	170849515	04412154-3219128	4877426575724467456	04 41 21.55	-33 40 46.56	15.71	1.80	2.56 ± 0.04	1.0	0.04	1
142	425934411	00182539-6250523	4901321849613348736	00 18 25.42	-63 09 07.56	15.77	2.16	3.09 ± 0.04	1.0	0.01	1

With the exception of available interferometric $T_{\rm eff}$ standards, we additionally wanted to source standards from large uniform catalogues due to the known problem of systematics between different spectroscopic techniques (e.g. Lebzelter et al. 2012; Hinkel et al. 2016). With this in mind, the bulk of our M/late-K dwarf standards come from the works of Rojas-Ayala et al. (2012) and Mann et al. (2015), with interferometric targets from von Braun et al. (2012), Boyajian et al. (2012b), von Braun et al. (2014), Rabus et al. (2019), and Rains et al. (2020); and F/G/K companion [Fe/H] compiled by Newton et al. (2014) from Valenti & Fischer (2005), Sousa et al. (2006) and Sozzetti et al. (2009). Our mid-K dwarf calibrators do not come from a single uniform catalogue; they are instead pulled from the works of Woolf & Wallerstein (2005), Sousa et al. (2008), Prugniel et al. (2011), Sousa et al. (2011), Tsantaki et al. (2013), Luck (2017), Luck (2018) and Montes et al. (2018).

These stars were observed with the same instrument settings as our science targets (but at higher SNR), with the intent to provide checks against our analysis techniques for this notoriously complex set of stars.

4.3.3 Spectroscopic Observations

Observations were conducted using the WiFeS instrument (Wide-Field Spectrograph, Dopita et al. 2007) on the ANU 2.3 m Telescope at Siding Spring Observatory, Australia between August 2019 and September 2020. WiFeS, a dual camera integral field spectrograph, is an effective stellar survey instrument due to its high throughput and broad wavelength coverage. Using the B3000 and R7000 gratings, and RT480 beam splitter, we obtain low resolution blue spectra ($3\,500 \leq \lambda \leq 5\,700$ Å, $\lambda/\Delta\lambda \sim 3\,000$) and moderate resolution red spectra ($5\,400 \leq \lambda \leq 7\,000$ Å, $\lambda/\Delta\lambda \sim 7\,000$) with median signal to noise ratios (SNR) per spectral pixel of 16 and 58 respectively. Exposure times ranged from 20 sec to 30 min, and were chosen on the basis of 0.5 magnitude bins in *Gaia G*.

Target observations were bracketed hourly with NeAr Arc lamp exposures, telluric standards were observed every few hours, and flux standards were observed several times throughout each night. Data reduction was done using the standard PyWiFeS pipeline (Childress et al. 2014) with the exception of custom flux calibration due to PyWiFeS' poor performance with R7000 spectra. Science target observations are listed in Table B.1, and standard star observations in Table B.2.

4.3.4 Radial velocity determination

Radial velocities of the WiFeS R7000 spectra were determined from a least squares minimisation of a set of synthetic template spectra varying in temperature (see Section 4.5.1 for details of model grid). We use a coarsely sampled version of this grid, computed at R~7 000 over $5\,400 \leq \lambda \leq 7\,000$ for $3\,000 \leq T_{\rm eff} \leq 5\,500$ K, $\log g = 4.5$, and [Fe/H]= 0.0, with $T_{\rm eff}$ steps of 100 K for radial velocity determination. For further information on our RV fitting formalism, see Žerjal et al. (2021)[5].

[5]Our RV fitting code, along with all other code for this project, can be found at https://github.com/adrains/plumage

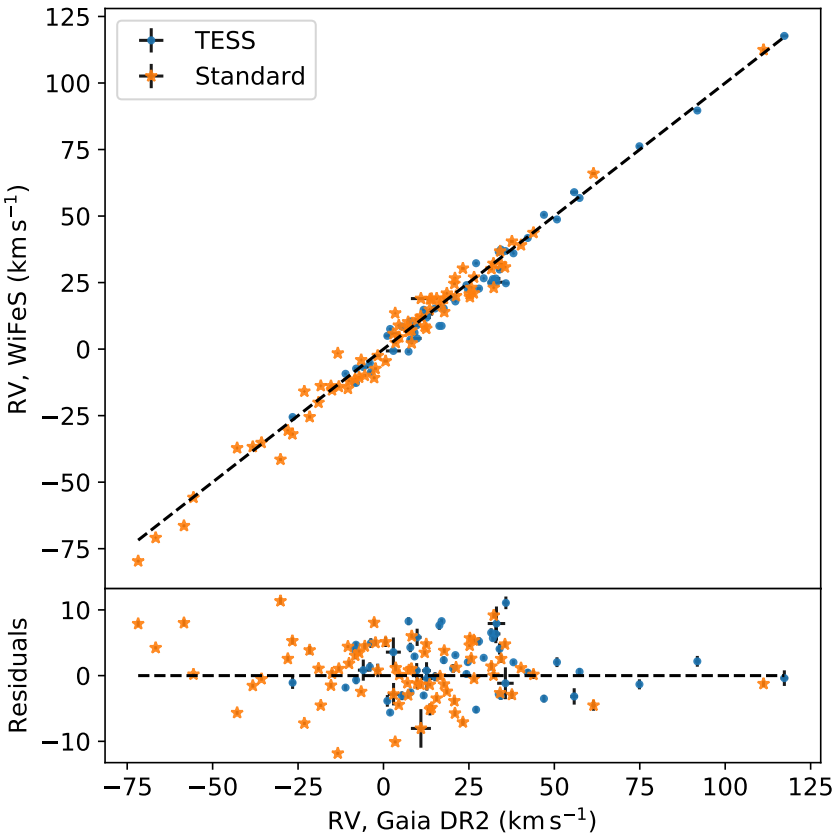

Figure 4.2: Comparison between those stars with radial velocities in *Gaia* DR2 and our work here, from which we determine a scatter of ~4.5 km s^{-1}.

Statistical uncertainties on this approach are median ~410 m s^{-1}, though comparison to *Gaia* DR2 in Figure 4.2 reveals a larger scatter with standard deviation ~4.5 km s^{-1}, computed from a median absolute deviation, which we add in quadrature with our statistical uncertainties. Higher uncertainties are consistent with the work of Kuruwita et al. (2018) who found that WiFeS varies on shorter timescales than our hourly arcs can account for. While they additionally improved precision by calibrating using oxygen B-band absorption, RV uncertainties of ~4.5 km s^{-1} are sufficient for this work. Our final values are reported in Table B.1 for science targets, and Table B.2 for standards.

4.4 Photometric Metallicity Calibration

As established earlier, cool dwarf metallicities are notoriously difficult to determine, particularly when working with optical spectra. Bonfils et al. (2005) initially proposed empirical calibrations to determine [Fe/H] from a star's position in $M_K - (V - K)$ space, a technique which was later iterated on by Johnson & Apps (2009), Schlaufman & Laughlin (2010), and Neves et al. (2012). Such relations are based on the fact that once on the main sequence, low mass stars do not

evolve (and hence change in brightness and temperature) appreciably on moderate timescales as compared to their higher mass and faster evolving counterparts. Thus, assuming no extra scatter from unresolved binaries and standard helium enrichment (e.g. Pagel & Portinari 1998), a star's position above or below the mean main sequence is directly correlated with its chemical composition (Baraffe et al. 1998).

These relations are benchmarked on what is considered the gold standard for M-dwarf metallicities: [Fe/H] from a hotter F/G/K companion taken to have formed at the same time and thus have the same chemical composition. This chemical homogeneity is now well established for F/G/K–F/G/K pairs (e.g. Desidera et al. 2004; Hawkins et al. 2020). The process of determining which stars on the sky are likely associated has now been greatly simplified with the release of *Gaia* DR2, which has provided precision parallax measurements and proper motions for nearly all nearby M-dwarfs, with our sample of secondaries having median 0.17 % parallax precision.

We take as input the sample of F/G/K–K/M-dwarf pairs compiled by Mann et al. (2013a) and Newton et al. (2014). These combine primary star [Fe/H] measurements from high resolution spectra sourced from a variety of previous surveys (Mishenina et al. 2004; Luck & Heiter 2005; Valenti & Fischer 2005; Bean et al. 2006a; Ramírez et al. 2007; Robinson et al. 2007; Fuhrmann 2008; Casagrande et al. 2011; da Silva et al. 2011; Mann et al. 2013a), with Mann et al. (2013a) correcting for inter-survey systematics to place them on a common [Fe/H] scale. To this set we add the metal-poor, cool subdwarf VB12 to extend our metallicity coverage, taking the [Fe/H] reported by Ramírez et al. (2007) for its primary HD 219617 AB (and correcting for the systematic reported by Mann et al. 2013a). This provided 128 total pairs, which was reduced to 69 after crossmatching with both *Gaia* DR2 and *2MASS*, and removing those stars with missing or poor photometry (*2MASS* Qflg≠'AAA', where 'AAA' is the highest photometric quality rating and corresponds to JHK_S respectively); those flagged on SIMBAD[6] as spectroscopic binaries; those with poor *Gaia* astrometry (*Gaia* dup flag=1, RUWE > 1.4); those pairs with M dwarf primaries; or whose parallaxes, astrometry, and RVs indicate they aren't associated with the putative primary. These 69 stars are listed in Table B.4, and span $-1.28 < \mathrm{[Fe/H]} < +0.56$.

From this sample we follow the approaches of Johnson & Apps (2009) and Schlaufman & Laughlin (2010) and use a polynomial to trace the mean main sequence in M_{K_S}−colour space, though using $(B_P - K_S)$ instead of $(V - K_S)$. For our main sequence fit, we use the complete Mann et al. (2015) sample of cool dwarfs with *Gaia* parallaxes, which spans a wider range in $(B_P - K_S)$ and is less sparse than the assembled sample of M-dwarf secondaries. We find the following third order polynomial sufficient to describe the main sequence:

$$(B_P - K_S) = a_3 M_{K_S}^3 + a_2 M_{K_S}^2 + a_1 M_{K_S} + a_0 \tag{4.1}$$

where $a_3 = 0.05385$, $a_2 = -1.08356$, $a_1 = 7.76175$, and $a_0 = -14.54705$. We then calculate the offset in $(B_P - K_S)$ from this polynomial (as a colour offers greater discriminatory power than M_{K_S}, Schlaufman & Laughlin 2010), and use least squares to find the best fitting linear relation for [Fe/H]:

$$\mathrm{[Fe/H]} = b_1 \Delta(B_P - K_S) + b_0 \tag{4.2}$$

[6] http://simbad.u-strasbg.fr/simbad/

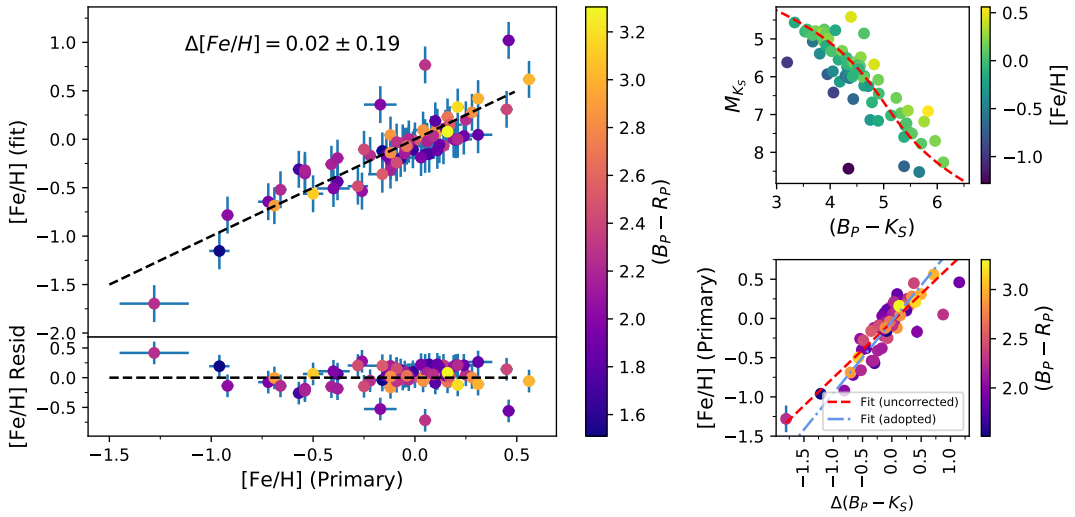

Figure 4.3: **Left:** Cool dwarf secondary [Fe/H] calculated from our photometric calibration vs [Fe/H] from the associated F/G/K primary star, colour coded by *Gaia* $(B_P - R_P)$. The standard deviation of the residuals, and our adopted uncertainty for the relation, is ±0.19 dex. See Table B.4 for further information on this F/G/K–K/M binary calibration sample. **Top Right:** $M_{K_S} - (B_P - K_S)$ colour magnitude diagram for the calibration sample of cool dwarf secondaries colour coded by host star [Fe/H]. The dashed red line is a third order polynomial representing the main sequence, fitted to the Mann et al. (2015) sample of cool dwarfs. **Bottom Right:** Fitted [Fe/H] as a function $\Delta(B_P - K_S)$ offset from the mean main sequence polynomial. The dashed red line is the initial uncorrected linear least squares fit, and the dash-dotted blue line is the adopted fit after correcting for the remaining trend in the residuals

where b_1 and b_0 are the linear polynomial coefficients. After correcting for a remaining trend in the residuals, our adopted coefficients are $b_1 = 0.71339$, and $b_0 = -0.04301$. This relation is valid for stars with $1.51 < (B_P - R_P) < 3.3$ (based on the hottest and coolest secondaries respectively), and has an uncertainty of ±0.19 dex (from the standard deviation in the residuals). We stress that the relation should only be used for stars that pass the same quality cuts we use to build the relation: unsaturated photometry, not flagged as a duplicate source in *Gaia*, RUWE < 1.4, and not a known/suspected spectroscopic binary or pre-main sequence star. Our [Fe/H] recovery and fits can be seen in Figure 4.3.

4.5 Spectroscopic Analysis

The *TESS* candidate planet host observing program described here developed from an ANU 2.3 m/WiFeS survey of potential young stars (Žerjal et al. 2021) to identify signs of youth (via Balmer Series and Ca II H&K emission, and Li 6 708 Å absorption) and determine RVs to enable kinematic analysis with `Chronostar` (Crundall et al. 2019) when combined with *Gaia* astrometry. While their spectral type coverage ($1.27 < B_P < 2.6$) was relatively similar to our own, instrument setup however prioritised higher spectral resolution for improved velocity

precision and coverage of the key wavelength regions of interest. These regions are firmly in the optical, where M-dwarf spectral features are strongly blended and heavily dominated by molecular absorption from hydrides (e.g. MgH, CaH, SiH) and oxides (e.g. TiO, VO, ZrO). This is in contrast to most of the previous low-medium resolution studies of M-dwarfs which work in the NIR where the absorption is less severe and many more [Fe/H] sensitive features are available.

Here we describe our attempts to derive reliable atmospheric parameters from our spectra using a model based approach. Our investigation ultimately revealed substantial systematics and degeneracies when fitting to model optical spectra, resulting in our inability to recover log g or [Fe/H]. While the spectra are included in our temperature fitting routine, they are primarily used for RV determination, identification of peculiarities (such as signs of youth), and for testing model fluxes. The details of our findings are covered below, and we await follow-up work to explore a standard-based or data-driven approach (e.g. similar to the work of Birky et al. 2020, but in the optical) to take full advantage of the information in our now large library of optical cool dwarf spectra.

4.5.1 Selection of Model Atmosphere Grid

While synthetic spectra show better agreement for F/G/K stars, the onset of strong molecular features such as TiO and H_2O in the atmospheres of late K and M dwarfs makes the task of modelling their spectra far more complex. There are known historical issues, for instance, when computing optical colours from synthetic spectra (e.g. difficulties in computing accurate V band magnitudes, Leggett et al. 1996), and the line lists required are considerably more complicated. Thus, before using models in our automatic fitting routine, we first investigate their performance at different wavelengths to flag regions requiring special consideration. For the purposes of this comparison, we check the MARCS grid of stellar atmospheres against the BT-Settl grid (Allard et al. 2011), both of which are described in detail below.

Our template grid of 1D LTE MARCS spectra was previously described by Nordlander et al. (2019) and computed using the TURBOSPECTRUM code (v15.1; Alvarez & Plez 1998; Plez 2012) and MARCS model atmospheres (Gustafsson et al. 2008). The spectra are computed with a sampling resolution of 1 km s^{-1}, corresponding to a resolving power of R~300 000, with a microturbulent velocity of 1 km s^{-1}. We adopt the solar chemical composition and isotopic ratios from Asplund et al. (2009), except for an alpha enhancement that varies linearly from $[\alpha/\mathrm{Fe}] = 0$ when $[\mathrm{Fe/H}] \geq 0$ to $[\alpha/\mathrm{Fe}] = +0.4$ when $[\mathrm{Fe/H}] \leq -1$. We use a selection of atomic lines from VALD3 (Ryabchikova et al. 2015) together with roughly 15 million molecular lines representing 18 different molecules, the most important of which for this work are CaH (Plez, priv. comm.), MgH (Kurucz 1995; Skory et al. 2003), and TiO (Plez 1998, with updates via VALD3).

MARCS model fluxes were developed for usage over a range of spectral types including both cool giants and, critically for our work here, cool dwarfs. Recent work fitting cool dwarf stellar atmospheres however have mostly used high-resolution NIR spectra (J band: Önehag et al. 2012; Lindgren et al. 2016; Lindgren & Heiter 2017; H band: Souto et al. 2017, 2018) rather than the medium resolution optical spectra we use here.

For BT-Settl, we use the most recently published grid (Allard et al. 2012a,b; Baraffe et al.

2015)[7] which uses abundances from Caffau et al. (2011) and covers $1\,200 < T_{\rm eff} < 7\,000$ K, $2.5 < \log g < 5.5$, [M/H]= 0.0. Note that while older grids have a wider range of [M/H], they are also less complete in terms of physics and line lists, so we opt for the newest grid for our comparison here, and limit ourselves to testing on stars with approximately Solar [Fe/H].

BT-Settl atmospheres have been developed with a focus on cool dwarfs and have a strong history of use for studying these stars at a variety of wavelengths and resolutions (e.g. Rojas-Ayala et al. 2012; Muirhead et al. 2012; Mann et al. 2012; Rajpurohit et al. 2013; Lépine et al. 2013; Gaidos et al. 2014; Mann et al. 2013c, 2015; Veyette et al. 2016, 2017; Souto et al. 2018). Most noteworthy for our comparison are tests by Reylé et al. (2011) and Mann et al. (2013c), which examined model performance at optical wavelength regions $> 5\,500$ Å common to our WiFeS R7000 spectra.

For each of our standard stars we combined and normalised our flux calibrated B3000 and R7000 spectra to give a single spectrum with $3\,500 < \lambda < 7\,000$ Å. To this we compared synthetic MARCS fluxes interpolated to literature values of $T_{\rm eff}$, $\log g$, and [Fe/H], as well as the BT-Settl equivalent for those with close to Solar [Fe/H]. Given our large library of standards we were able to observe model performance as a function of both stellar parameters and wavelength. A representative comparison (with overplotted filter bandpasses) is shown in Figure 4.4, and our main conclusions are summarised as follows:

- Both MARCS and BT-Settl models severely overpredict (worsening with decreasing $T_{\rm eff}$) flux blueward of ~5 400 Å. The MARCS systematic offset is also a strong function of [Fe/H], an effect also observed in Joyce & Chaboyer (2015), and while this is likely also true for BT-Settl, we cannot comment definitively while limited to the Solar [Fe/H] grid.

- BT-Settl additionally underpredicts flux at ~6 500 Å (as expected from Reylé et al. 2011 and Mann et al. 2013c).

- Synthetic photometry generated in *SkyMapper* v, g, r, and *Gaia* B_P is thus systematically brighter than the observed equivalents for reasonable assumptions of $T_{\rm eff}$, $\log g$, and [Fe/H] for the star under consideration.

We are able to quantify these systematics by integrating photometry from our flux calibrated observed spectra and comparing to the MARCS synthetic equivalents generated at the literature parameters for each star. Our wavelength coverage allows us to check the magnitude offsets Δv, Δg, Δr and ΔB_P, corresponding to v, g, r, and B_P respectively. We note that for the purpose of this comparison we do not account for inaccuracies in our flux calibration, telluric absorption, nor for WiFeS not covering the bluest ~200 Å of B_P. However, checks with synthetic spectra show that this region accounts for less than 0.25 % of B_P flux at 3 000 K where our correction is greatest, and remains less than 0.5 % of flux at 4 500 K where our correction is more modest. These offsets are shown for g, r, and B_P in Figure 4.5, and fit separately for each filter by the following linear relation in observed *Gaia* DR2 $(B_P - R_P)$:

$$\Delta m_\zeta = a_1(B_P - R_P) + a_0 \tag{4.3}$$

[7] https://phoenix.ens-lyon.fr/Grids/BT-Settl/CIFIST2011_2015/

where Δm_ζ is the magnitude offset in filter ζ; a_1 equals 0.116, 0.084, and 0.034 for g, r, and B_P fits respectively; and a_0 equals -0.072, -0.069, and -0.037 for g, r, and B_P fits respectively. Computing the standard deviation for the residuals shows 0.10, 0.05, and 0.02 uncertainties in magnitude (equivalent to roughly 10%, 5%, and 2% uncertainties in flux) for g, r, and B_P respectively. From this we conclude that while the corrections to r, and B_P are modest, g is likely too affected to prove useful.

Following this both qualitative and quantitative investigation comparing model fluxes to our library of standard star spectra, we make the following decisions for our synthetic fitting methodology:

- Given similar observed systematics for both MARCS and BT-Settl model fluxes, we adopt the MARCS grid to enable fitting for [Fe/H] as well as $T_{\rm eff}$ and $\log g$.
- Only use our R7000 spectra ($5\,400 \leq \lambda \leq 7\,000$ Å) for fitting, additionally masking out the two regions worst affected by missing opacities (5 498–5 585 Å and 6 029–6 159 Å).
- Apply an *observed* $(B_P - R_P)$ dependent systematic offset to our generated synthetic B_P and r photometry per Equation 4.3.
- Given the widespread historical use and success of studying M-dwarfs at NIR wavelengths, we use R_P, i, z, J, H, and K_S photometry assuming no substantial model systematics.
- However, to account for remaining model uncertainties, we add conservative ±0.011 magnitude (1% in flux) uncertainties in quadrature with the observed uncertainties for R_P, i, z; and the fitted ±0.02 for r, and ±0.05 for B_P.

4.5.2 Synthetic Fitting

Our approach to spectral fitting was developed specifically to work with the complicated spectra of our cool star sample and incorporates nine distinct sources of information. While it was hoped that this methodology would be sufficient to disentangle the strong degeneracy between $T_{\rm eff}$ and [Fe/H] and accurately recover *distant–independent* [Fe/H] for our standard sample, this ultimately proved not to be the case. While we are able to tightly constrain $T_{\rm eff}$, we must resort to using the photometric [Fe/H] relation developed in Section 4.4 to fix [Fe/H] during the fit. The information included in our fit is as follows:

1. Medium resolution R7000 optical spectra from WiFeS,
2. Observed *Gaia* B_P, R_P; *2MASS* J, H, and K_S; and *SkyMapper* DR3 r, i, z photometry,
3. Empirical cool dwarf radius relations from Mann et al. (2015)—valid for K7-M7 stars, and used to estimate $\log g$,
4. Empirical cool dwarf mass relations from Mann et al. (2019)—valid for $0.075\,M_\odot < M_\star < 0.70\,M_\odot$, and used to estimate $\log g$,

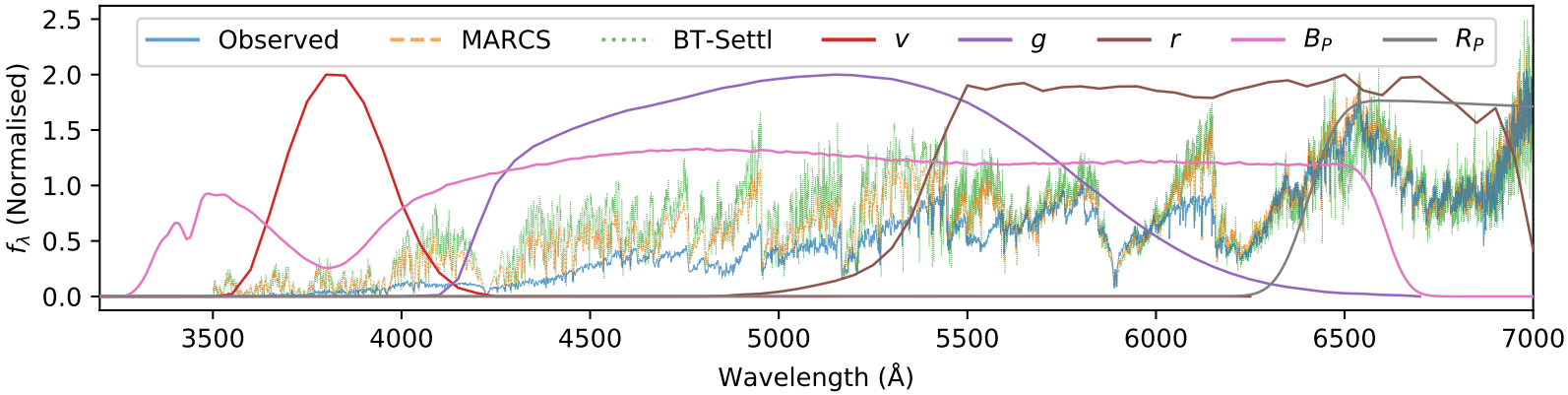

Figure 4.4: Observed WiFeS B3000 and R7000 spectra for GJ 447, along with a MARCS synthetic spectrum interpolated to the parameters from Mann et al. 2015 ($T_{\rm eff}$ = 3192 K, log g = 5.04, [Fe/H] = −0.02), and a PHOENIX/BT-Settl spectrum at the closest grid point available ($T_{\rm eff}$ = 3200 K, log g = 5.0, [Fe/H] = 0.0). *SkyMapper* v, g, r, and *Gaia* B_P and R_P filters are overplotted for reference. Note the severe model disagreement below 5 400 Å.

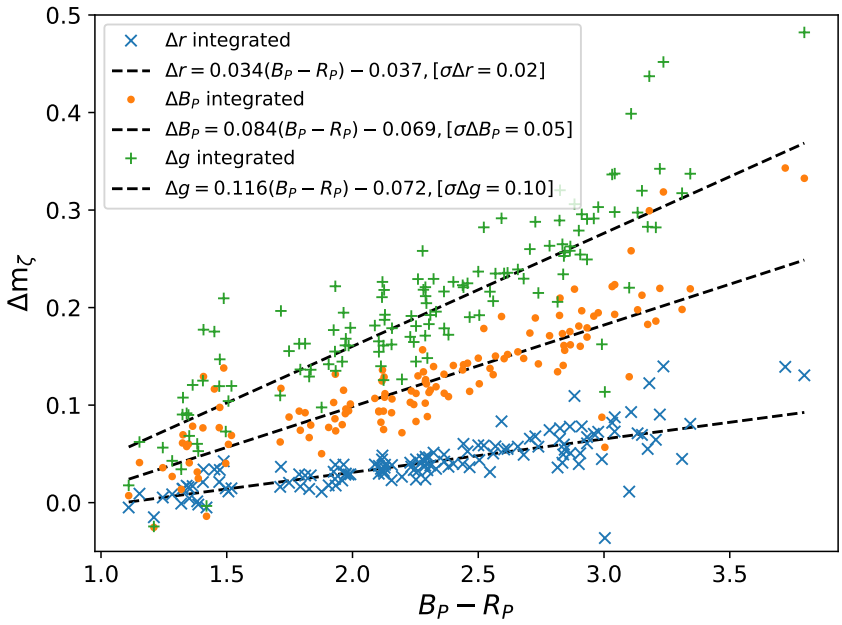

Figure 4.5: *Gaia* B_P, and *SkyMapper* gr systematic offsets between integrated flux calibrated WiFeS spectra and MARCS model integrated spectra at literature parameters for our standard stars, plotted as a function of observed *Gaia* $B_P - R_P$. Stars redder in $B_P - R_P$ have systematically more flux at bluer wavelengths, with the best fit linear magnitude offset plotted for each filter, and the standard deviation in magnitude noted.

5. Synthetic MARCS model spectra (for spectral fitting, interpolated to the resolution and wavelength grid of WiFeS)

6. MARCS model fluxes (for photometric fitting),

7. Stellar parallaxes from *Gaia* DR2,

8. The interstellar dust map from Leike et al. (2020),

9. A set of reference stellar standards with known parameters for testing and validation purposes (see Section 4.3.2 for details).

We found that least squares fitting between real and synthetic spectra alone consistently underestimated expected $\log g$ values of our sample by up to 0.3 dex–physical for a set of young stars, but not realistic for our overwhelmingly main sequence sample. To counter this, we calculate $\log g$ using the absolute K_S band radius and mass relations of Mann et al. (2015) and Mann et al. (2019)[8] respectively, and fix it during fitting. We then use a two step iterative procedure, with the first fit fixing $\log g$ to the value from empirical relations, and a second and final fit using our interim measured radius and a mass from Mann et al. (2019). All of our *TESS* targets

[8]Calculated using the Python code available at: https://github.com/awmann/M_-M_K-

fall within the stated $4 < M_{K_S} < 11$ limits for the mass relation. Although the relation is only valid for main sequence stars, we employ it with caution for two suspected young stars TOI 507 (TIC 348538431) and TOI 142 (425934411), both discussed in more detail in Section 4.7.5, on the assumption that the resulting value of $\log g$ will still be more accurate than an unconstrained synthetic fit. Additionally, we suspect TOI 507 of being a near-equal mass binary, and as such treat it as 0.75 magnitudes fainter (or half as bright) for the purpose of using the relation, equivalent to determining the mass for only a single component.

While this now solves the $\log g$ issue, we are still left with two issues arising from the spectra themselves. The first is that certain wavelength regions of our MARCS model spectra are a poor match compared to our reference sample with known $T_{\rm eff}$, $\log g$, and [Fe/H]—particularly at cooler temperatures. As discussed in Section 4.5.1, we account for this by using only spectra from the red arm of WiFeS with $\lambda > 5\,400$ A, and masking out remaining regions with poor agreement.

The second remaining issue is that of the degeneracy between $T_{\rm eff}$ and [Fe/H] when fitting spectra. This effect is caused by both the temperature and metallicity influencing the strength of atmospheric molecular absorbers or opacity sources (predominantly TiO in the optical, but also various hydrides). What this means in practice is that there often isn't a single minimum or optimal set of atmospheric parameters when fitting synthetic spectra, but instead there exists a range of good fits (or even multiple minima) at different combinations of $T_{\rm eff}$ and [Fe/H]—possibly separated by several 100 K in $T_{\rm eff}$ or several 0.1 dex in [Fe/H].

In an attempt to overcome this, we include photometry from redder wavelengths that are less dominated by absorption than optical wavelengths, meaning that $T_{\rm eff}$ and [Fe/H] are less degenerate. While we do not have NIR spectra for our science or reference sample, we do have *Gaia*, *SkyMapper*, and *2MASS* photometry in the form of B_P, R_P, r, i, z, J, H, and K_S which together give us almost continuous wavelength coverage out to nearly 2.4 μm and covers the bulk of stellar emission for our cool stars.

We thus modified our fitting methodology to also compute the uncertainty weighted residuals between observed and synthetic stellar photometry. In order to compare synthetic photometry to its observed equivalent we formulate the fit as follows:

$$m_{\zeta,m} = \mathrm{BC}_\zeta(T_{\rm eff}, \log g, [\mathrm{Fe/H}]) + m_{\rm bol} \tag{4.4}$$

where $m_{\zeta,m}$ is the model magnitude in filter ζ; BC_ζ is the bolometric correction (i.e. the total flux outside of a filter ζ) as a function of $T_{\rm eff}$, $\log g$, and [Fe/H] in filter ζ; and $m_{\rm bol}$ is the apparent bolometric magnitude (i.e. the apparent magnitude of the star over all wavelengths). In this implementation $m_{\rm bol}$ serves as a physically meaningful free parameter used to scale synthetic magnitudes to their observed equivalents and ultimately allow computation of the apparent bolometric flux $f_{\rm bol}$. This is done using the well tested `bolometric-corrections`[9] software (Casagrande & VandenBerg 2014, 2018a,b) to interpolate a grid of bolometric corrections from MARCS fluxes in different filters for the stellar parameters at each fitting call. By fitting for $m_{\rm bol}$ and using bolometric corrections, we are thus directly able to compare an observed magnitude, $m_{\zeta,o}$, from *Gaia*, *SkyMapper*, or *2MASS* directly with its MARCS synthetic equivalent. With

[9] https://github.com/casaluca/bolometric-corrections

$\log g$ fixed, we now have a three term fit in terms of $T_{\rm eff}$, [Fe/H], and $m_{\rm bol}$, the latter of which allows for direct computation of the bolometric flux (and thus the stellar radius).

This fitting procedure is equivalent to minimising the following relation (performed using the least_squares function from `scipy`'s optimize module):

$$R(\theta) = \sum_{i=1}^{M} \left(\frac{1}{C\sqrt{\chi_f^2}} \frac{f_{o,i} - f_{m,i}}{\sigma_{f_{o,i}}} \right)^2 + \sum_{\zeta=1}^{N} \left(\frac{1}{\sqrt{\chi_m^2}} \frac{m_{\zeta,o} - (m_{\zeta,m} + \Delta m_\zeta)}{\sigma_{m_\zeta}} \right)^2 \tag{4.5}$$

with model uncertainties taken into account via:

$$\sigma_{m_\zeta} = \sqrt{\sigma_{m_{\zeta,o}}^2 + \sigma_{m_{\zeta,m}}^2} \tag{4.6}$$

where $R(\theta)$ are the combined spectral and photometric squared residuals as a function of θ, a vector of $T_{\rm eff}$, $\log g$, [Fe/H], $m_{\rm bol}$); M is the total number of spectral pixels, i is the spectral pixel index, $f_{\rm o,i}$ and $f_{\rm m,i}$ are the observed and model spectral fluxes respectively at pixel i, normalised by their respective medians in the range $6\,200 \leq \lambda \leq 7\,000$ Å; $\sigma_{f_{\rm o,i}}$ is the observed flux uncertainty at pixel i; N is the total number of photometric filters; ζ is the filter index, $m_{\zeta,o}$ and $m_{\zeta,m}$ are the observed and model magnitudes respectively in filter ζ; Δm_ζ is the systematic model magnitude offset in filter ζ (per Equation 4.3 for r and B_P, and 0 for all other filters); $\sigma_{m_{\zeta,o}}$ and $\sigma_{m_{\zeta,m}}$ are the uncertainties on the observed and model magnitudes respectively, added in quadrature to give the total magnitude uncertainty σ_{m_ζ}; χ_f^2 and χ_m^2 are the *global* minimum χ^2 values computed from the spectral and photometry residuals respectively (i.e. global fit using only R7000 spectra, without photometry, and a separate global photometric fit without spectra) used to normalise the two sets of residuals in the case of poor fits and place them on a similar scale; and C, set to 20, is a constant used to account for the spectra having many more pixels than the number of photometric points. This value of C was chosen by visually inspecting the residuals of our spectral fits and means that we assume, on average, every 20 spectral pixels are correlated and do not contain unique information.

We test the accuracy of our fitted [Fe/H] using a set of cool star stellar standards in Figure 4.6. It is immediately clear that, despite the tight constraint on $T_{\rm eff}$ that our broad wavelength coverage from photometry allows, we are unable to recover [Fe/H] for our standard sample to better precision than our photometric [Fe/H] relation from Section 4.4. Our fits systematically overpredict [Fe/H] for the coolest stars in our sample, which might be similar to what was observed in Figure 3 of Rojas-Ayala et al. 2012 (using BT-Settl models), where they find even metal-rich models fail to reproduce the depth of certain features. This has also previously been observed for cool, metal-poor clusters when using evolutionary models (e.g. Joyce & Chaboyer 2015), and observed for isochrones (e.g. Joyce & Chaboyer 2018a). From this we conclude that a simple least squares fit to our medium resolution optical spectra, unweighted to [Fe/H] sensitive regions, and using models with both known and unknown systematics is not sufficient to accurately determine [Fe/H] for cool dwarfs.

Given this, it is clear a three parameter fit to $T_{\rm eff}$, [Fe/H], and $m_{\rm bol}$ is unreasonable. Our final reported parameters are thus a two parameter fit to $T_{\rm eff}$, and $m_{\rm bol}$, fixing [Fe/H] to the value from our relation in Section 4.4 for those stars falling within the $(B_P - R_P)$ range, and the mean value for the Solar Neighbourhood of [Fe/H] = −0.14 (Schlaufman & Laughlin 2010)

for stars outside this range, or suspected of binarity or being young. To further account for both model and zeropoint uncertainties, we add a 1% flux uncertainty in quadrature with our fitted statistical uncertainties on $m_{\rm bol}$. Our standard star $T_{\rm eff}$ recovery for the two parameter fit is shown in Figure 4.7.

We compute the apparent bolometric flux $f_{\rm bol}$ from our fitted value of $m_{\rm bol}$ using Equation 3 from Casagrande & VandenBerg (2018a), from which we then compute the stellar radius $R_\star$. Figure 4.8 shows a comparison between our radii and those from our interferometric standard sample, and final values for *TESS* science targets and stellar standards are reported in Tables 4.2 and B.3 respectively.

4.6 Candidate Planet Parameters

4.6.1 Transit Light Curve Analysis

We now present results for all TOIs not ruled out as false positives (e.g. due to background stars, or eclipsing binaries) by the *TESS* Team and exoplanet community, as listed on the NASA ExoFOP-*TESS* website.

Transit light curves for targets across all *TESS* sectors were downloaded from NASA's Mikulski Archive for Space Telescopes (MAST) service. For all high-cadence data, we used the Pre-search Data Conditioning Simple Aperture Photometry (PDCSAP) fluxes, which have already had some measure of processing to remove systematics. All light curves were downloaded and manipulated using the python package `LightKurve` (Lightkurve Collaboration et al. 2018).

Many stars in our sample show some amount of stellar variability, with periods ranging from days to many weeks. We remove this using `LightKurve`'s flatten function, which applies a Savitzky-Golay filter (Savitzky & Golay 1964) to the data to remove low frequency trends. When applying the filter we mask out all planetary transits by known TOIs. Once flattened, the light curves are then phase folded using either the period provided by NASA ExoFOP-*TESS* (for most stars), or our own fitted period (for stars revisited in the *TESS* extended mission whose long time baseline reveals the ExoFOP-*TESS* period to be incorrect). We use the provided measurement of transit duration to select only photometry from the transit itself, plus 10% of a duration either side for use in model fitting.

Model fitting is implemented using the python package `BATMAN` (Kreidberg 2015), which is capable of generating model transit light curves for a given set of orbital elements (scaled by the stellar radius $R_\star$) and limb darkening coefficients. We use a four term limb darkening law, interpolating the PHOENIX grid provided by Claret (2017) using values of $T_{\rm eff}$ and $\log g$ from Table 4.2. The resulting coefficients are in Table B.5.

Transit photometry alone is not sufficient to uniquely constrain the planet orbit and radius when fitting for the scaled semi-major axis $a_{R_\star} = \frac{a}{R_\star}$, the planetary radius ratio $R_{P,R_\star} = \frac{R_P}{R_\star}$, the inclination i, the eccentricity e, and the longitude of periastron ω (Kipping 2008). While we can use our measurements of $M_\star$, $R_\star$, and T to constrain the semi-major axis of a circular orbit (Equation 4.7), we do not have the precision required to fit for eccentric orbits. As such, we fix $e = 0$ and $\omega = 0$ during our fit, and include our calculated value $a_{R_{\star,c}}$—the value $a_{R_\star}$ assuming a circular orbit, as a prior during fitting. In cases where $e \sim 0$, we expect the fitted

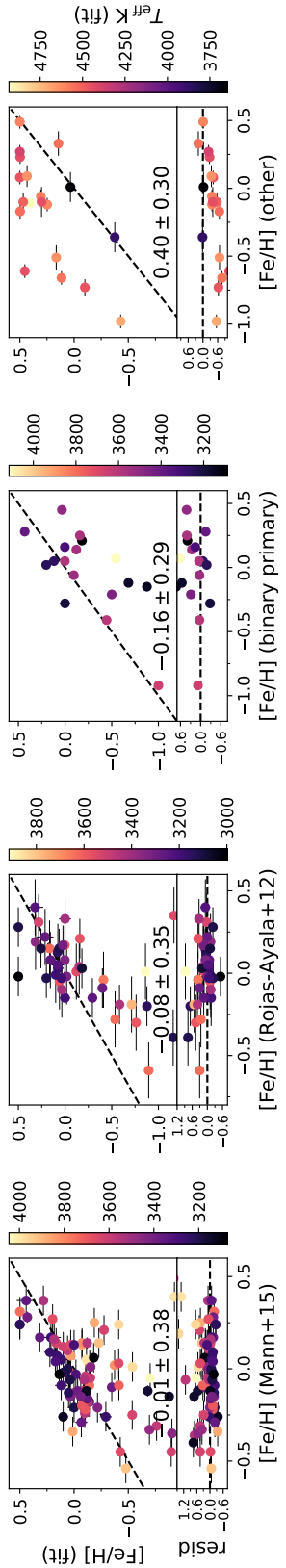

Figure 4.6: [Fe/H] recovery for our 3 parameter fit in $T_{\rm eff}$, [Fe/H], $m_{\rm bol}$ for our four sets of [Fe/H] standards: Mann et al. 2015, Rojas-Ayala et al. 2012, primary star [Fe/H] for cool dwarfs in binaries, and mid-K dwarfs. The median and standard deviation of each set of residuals is annotated. Note the inability of the 3 parameter fit to reliably recover [Fe/H], with the scatter on our recovered [Fe/H] for the binary sample (the most reliable set of [Fe/H] standards) being larger than the scatter on our photometric [Fe/H] relation.

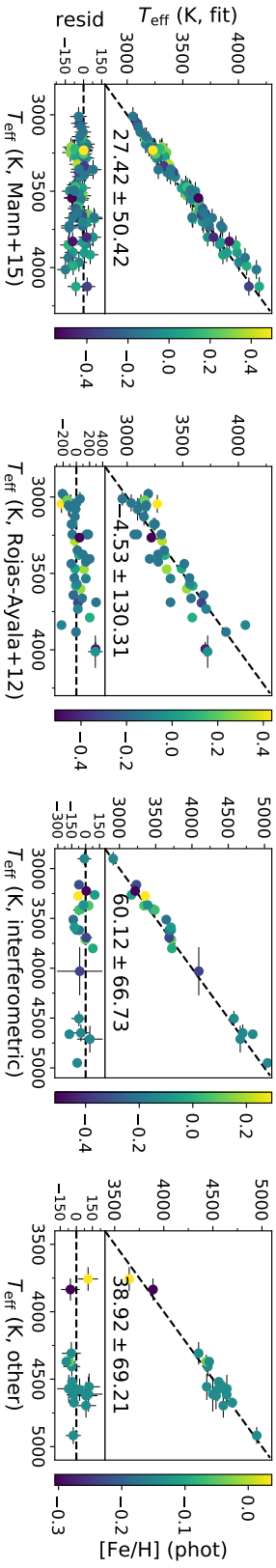

Figure 4.7: $T_{\rm eff}$ recovery for our 2 parameter fit in $T_{\rm eff}$, and $m_{\rm bol}$ for our four sets of $T_{\rm eff}$ standards: Mann et al. 2015, Rojas-Ayala et al. 2012, interferometry, and mid-K dwarfs. [Fe/H] is from our photometric [Fe/H] relation where appropriate, or fixed to the mean Solar Neighbourhood [Fe/H] if not. The median and standard deviation of each set of residuals is annotated (note that these values have not yet been corrected for the systematic, as discussed in Section 4.7.2).

Table 4.2: Final results for TESS candidate exoplanet hosts

TOI	TIC	$T_{\rm eff}$ (K)	$\log g$	[Fe/H]	M ($M_\odot$)	$R_\star$ ($R_\odot$)	$m_{\rm bol}$	$f_{\rm bol}$ (10^{-12} ergs s^{-1} cm^{-2})	EW(Hα) Å	$\log R'_{\rm HK}$
136	410153553	2988 ± 30	5.06 ± 0.02	-	0.155 ± 0.004	0.192 ± 0.004	12.05 ± 0.01	384.4 ± 3.9	-0.05	-5.37
540	200322593	3104 ± 30	5.07 ± 0.02	-0.10	0.164 ± 0.004	0.197 ± 0.004	11.71 ± 0.01	528.3 ± 5.3	2.49	-
256	92226327	3150 ± 30	5.01 ± 0.02	-0.13	0.182 ± 0.005	0.220 ± 0.004	11.55 ± 0.01	611.8 ± 6.1	-0.22	-5.53
203	259962054	3169 ± 30	5.01 ± 0.02	-0.07	0.200 ± 0.005	0.232 ± 0.004	12.49 ± 0.01	255.4 ± 2.6	0.56	-4.98
507	348538431	3279 ± 30	4.76 ± 0.02	-	0.383 ± 0.010	0.424 ± 0.008	14.28 ± 0.01	49.2 ± 0.5	2.24	-4.49
910	369327947	3282 ± 30	4.97 ± 0.02	-0.04	0.262 ± 0.008	0.278 ± 0.005	10.46 ± 0.01	1656.2 ± 16.6	-0.27	-5.47
210	141608198	3284 ± 30	4.90 ± 0.02	0.21	0.312 ± 0.008	0.326 ± 0.006	12.78 ± 0.01	195.8 ± 2.0	-0.23	-5.84
122	231702397	3326 ± 30	4.86 ± 0.02	-0.07	0.316 ± 0.008	0.345 ± 0.006	13.42 ± 0.01	109.3 ± 1.1	-0.21	-
455	98796344	3330 ± 30	4.97 ± 0.02	-0.27	0.248 ± 0.006	0.271 ± 0.005	9.16 ± 0.01	5507.5 ± 54.8	-0.29	-5.39
732	36724087	3354 ± 30	4.83 ± 0.02	0.13	0.364 ± 0.009	0.382 ± 0.007	10.91 ± 0.01	1103.5 ± 11.0	-0.23	-5.55
674	158588995	3355 ± 30	4.77 ± 0.02	-	0.419 ± 0.010	0.443 ± 0.008	12.19 ± 0.01	338.7 ± 3.4	-0.45	-5.58
406	153065527	3369 ± 30	4.83 ± 0.02	0.21	0.380 ± 0.009	0.392 ± 0.007	11.58 ± 0.01	594.6 ± 5.9	-0.15	-5.40
175	307210830	3381 ± 30	4.94 ± 0.02	-0.24	0.293 ± 0.007	0.304 ± 0.005	9.78 ± 0.01	3099.8 ± 31.1	-0.31	-5.47
782	429358906	3390 ± 30	4.81 ± 0.02	0.25	0.401 ± 0.010	0.413 ± 0.008	12.57 ± 0.01	237.3 ± 2.4	-0.37	-6.38
244	118327550	3422 ± 30	4.82 ± 0.02	0.10	0.402 ± 0.010	0.407 ± 0.007	10.69 ± 0.01	1349.2 ± 13.5	-0.30	-5.36
789	300710077	3434 ± 30	4.86 ± 0.02	-0.16	0.360 ± 0.009	0.371 ± 0.007	12.34 ± 0.01	294.0 ± 2.9	-0.28	-
654	35009898	3436 ± 30	4.77 ± 0.02	0.07	0.425 ± 0.010	0.445 ± 0.008	12.56 ± 0.01	239.6 ± 2.4	-0.33	-8.10
864	231728511	3452 ± 30	4.82 ± 0.02	-0.10	0.392 ± 0.010	0.403 ± 0.007	11.86 ± 0.01	460.0 ± 4.6	-0.37	-5.21
562	413248763	3456 ± 30	4.88 ± 0.02	-0.22	0.347 ± 0.008	0.353 ± 0.006	9.11 ± 0.01	5758.7 ± 57.3	-0.25	-5.93
486	260708537	3467 ± 30	4.81 ± 0.02	0.03	0.424 ± 0.010	0.424 ± 0.007	9.74 ± 0.01	3239.2 ± 32.4	-0.40	-5.39
700	150428135	3467 ± 30	4.80 ± 0.02	-	0.416 ± 0.010	0.426 ± 0.007	11.28 ± 0.01	783.3 ± 7.8	-0.35	-5.36
521	27649847	3468 ± 30	4.80 ± 0.02	-0.01	0.416 ± 0.010	0.424 ± 0.008	12.74 ± 0.01	203.5 ± 2.0	-0.30	-5.49
1078	370133522	3486 ± 30	4.83 ± 0.02	-0.24	0.383 ± 0.009	0.392 ± 0.007	10.51 ± 0.01	1583.2 ± 15.8	-0.34	-6.54
912	406941612	3488 ± 30	4.80 ± 0.02	-0.03	0.424 ± 0.010	0.427 ± 0.007	10.87 ± 0.01	1143.7 ± 11.4	-0.31	-5.19
270	259377017	3493 ± 30	4.88 ± 0.02	-0.25	0.364 ± 0.009	0.361 ± 0.006	10.90 ± 0.01	1111.3 ± 11.1	-0.29	-5.40
696	77156829	3496 ± 30	4.92 ± 0.02	-0.45	0.321 ± 0.008	0.327 ± 0.006	10.84 ± 0.01	1170.5 ± 11.7	-0.22	-6.08
269	220479565	3518 ± 30	4.83 ± 0.02	-0.25	0.391 ± 0.010	0.396 ± 0.007	12.69 ± 0.01	214.2 ± 2.1	-0.30	-
233	415969908	3527 ± 30	4.88 ± 0.02	-0.31	0.371 ± 0.009	0.365 ± 0.006	11.72 ± 0.01	522.8 ± 5.2	-0.31	-5.21
698	141527579	3540 ± 30	4.76 ± 0.02	0.04	0.473 ± 0.011	0.474 ± 0.008	12.49 ± 0.01	255.5 ± 2.5	-0.39	-5.12
731	34068865	3543 ± 30	4.77 ± 0.02	-0.03	0.458 ± 0.011	0.463 ± 0.008	8.41 ± 0.01	11008.1 ± 109.5	-0.39	-5.24
1201	29960110	3546 ± 30	4.75 ± 0.02	0.11	0.484 ± 0.012	0.488 ± 0.008	11.31 ± 0.01	757.8 ± 7.6	-0.13	-4.74

Table 4.2: Final results for TESS candidate exoplanet hosts

TOI	TIC	$T_{\rm eff}$ (K)	$\log g$	[Fe/H]	M ($M_\odot$)	$R_\star$ ($R_\odot$)	$m_{\rm bol}$	$f_{\rm bol}$ (10^{-12} ergs s^{-1} cm^{-2})	EW(Hα) Å	$\log R'_{\rm HK}$
756	73649615	3581 ± 30	4.71 ± 0.02	0.11	0.509 ± 0.012	0.522 ± 0.009	12.90 ± 0.01	175.4 ± 1.7	-0.42	-4.90
704	260004324	3596 ± 30	4.69 ± 0.02	-0.05	0.506 ± 0.012	0.533 ± 0.009	10.54 ± 0.01	1540.8 ± 15.4	-0.41	-5.01
177	262530407	3613 ± 30	4.70 ± 0.02	-	0.519 ± 0.013	0.532 ± 0.009	9.91 ± 0.01	2762.3 ± 27.5	0.00	-4.45
797	271596225	3618 ± 30	4.76 ± 0.02	-	0.475 ± 0.011	0.476 ± 0.008	12.13 ± 0.01	356.5 ± 3.5	-0.45	-4.92
727	149788158	3634 ± 30	4.74 ± 0.02	-0.11	0.499 ± 0.012	0.501 ± 0.008	11.42 ± 0.01	686.3 ± 6.8	-0.40	-5.02
142	425934411	3647 ± 30	4.55 ± 0.02	-	0.594 ± 0.016	0.675 ± 0.016	15.09 ± 0.01	23.4 ± 0.2	0.98	-4.25
663	54962195	3658 ± 30	4.72 ± 0.02	-0.10	0.514 ± 0.012	0.521 ± 0.009	12.18 ± 0.01	341.4 ± 3.4	-0.49	-
234	12423815	3668 ± 30	4.70 ± 0.02	0.13	0.545 ± 0.015	0.546 ± 0.013	14.99 ± 0.01	25.7 ± 0.3	-0.51	-4.97
620	296739893	3669 ± 30	4.70 ± 0.02	0.19	0.547 ± 0.014	0.547 ± 0.009	10.62 ± 0.01	1437.2 ± 14.3	-0.45	-5.07
672	151825527	3678 ± 30	4.67 ± 0.02	0.01	0.544 ± 0.013	0.563 ± 0.009	12.08 ± 0.01	375.7 ± 3.7	-0.34	-4.62
873	237920046	3682 ± 30	4.72 ± 0.02	-0.09	0.521 ± 0.013	0.519 ± 0.009	12.55 ± 0.01	243.2 ± 2.4	-0.39	-4.81
714	219195044	3698 ± 30	4.77 ± 0.02	-0.33	0.474 ± 0.011	0.468 ± 0.008	11.98 ± 0.01	410.0 ± 4.1	-0.47	-5.22
134	234994474	3722 ± 30	4.60 ± 0.02	-	0.590 ± 0.015	0.633 ± 0.010	9.65 ± 0.01	3512.5 ± 35.0	-0.47	-4.69
468	33521996	3738 ± 30	4.60 ± 0.02	-	0.588 ± 0.015	0.634 ± 0.012	13.75 ± 0.01	80.4 ± 0.8	-0.55	-4.93
785	374829238	3740 ± 30	4.67 ± 0.02	-0.02	0.559 ± 0.014	0.572 ± 0.009	11.92 ± 0.01	432.7 ± 4.3	-0.39	-4.52
552	44737596	3742 ± 30	4.65 ± 0.02	0.21	0.579 ± 0.014	0.594 ± 0.011	14.19 ± 0.01	53.6 ± 0.5	-0.42	-4.19
904	261257684	3752 ± 30	4.71 ± 0.02	-0.17	0.533 ± 0.013	0.537 ± 0.009	11.28 ± 0.01	778.7 ± 7.8	-0.39	-4.60
741	359271092	3763 ± 30	4.73 ± 0.02	-0.17	0.527 ± 0.013	0.520 ± 0.008	8.12 ± 0.01	14329.1 ± 142.6	-0.46	-5.03
198	12421862	3770 ± 30	4.86 ± 0.02	-	0.447 ± 0.011	0.413 ± 0.007	10.39 ± 0.01	1769.6 ± 17.7	-0.42	-5.14
442	70899085	3831 ± 30	4.63 ± 0.02	0.09	0.598 ± 0.015	0.620 ± 0.010	11.17 ± 0.01	867.7 ± 8.6	-0.40	-4.53
557	55488511	3845 ± 30	4.67 ± 0.02	-0.15	0.570 ± 0.014	0.581 ± 0.009	12.09 ± 0.01	371.3 ± 3.7	-0.51	-4.69
870	219229644	3847 ± 30	4.63 ± 0.02	0.11	0.601 ± 0.015	0.618 ± 0.010	11.21 ± 0.01	836.3 ± 8.3	-0.38	-4.54
551	192826603	3871 ± 30	4.67 ± 0.02	-0.28	0.563 ± 0.014	0.577 ± 0.010	14.35 ± 0.01	46.4 ± 0.5	-0.54	-4.60
876	32497972	3888 ± 30	4.63 ± 0.02	-0.08	0.595 ± 0.015	0.615 ± 0.010	11.98 ± 0.01	410.9 ± 4.1	-0.55	-4.85
532	144700903	3903 ± 30	4.62 ± 0.02	0.07	0.610 ± 0.015	0.630 ± 0.011	13.09 ± 0.01	147.8 ± 1.5	-0.68	-5.39
1075	351601843	3916 ± 30	4.69 ± 0.02	-	0.575 ± 0.014	0.571 ± 0.009	11.59 ± 0.01	588.2 ± 5.9	-0.50	-4.66
833	362249359	3945 ± 30	4.65 ± 0.02	-0.13	0.595 ± 0.015	0.601 ± 0.009	10.60 ± 0.01	1458.0 ± 14.5	-0.49	-4.49
702	237914496	3966 ± 30	4.69 ± 0.02	-0.24	0.577 ± 0.014	0.566 ± 0.009	12.24 ± 0.01	323.3 ± 3.2	-0.56	-4.65
555	170849515	3993 ± 30	4.63 ± 0.02	-0.06	0.615 ± 0.017	0.626 ± 0.015	15.25 ± 0.01	20.1 ± 0.2	-0.40	-4.76
285	220459976	3995 ± 30	4.62 ± 0.02	0.00	0.625 ± 0.015	0.643 ± 0.010	12.61 ± 0.01	229.2 ± 2.3	-0.60	-4.71
475	100608026	4003 ± 30	4.66 ± 0.02	-0.18	0.601 ± 0.015	0.599 ± 0.009	11.29 ± 0.01	775.1 ± 7.7	-0.54	-4.62
253	322063810	4039 ± 30	4.65 ± 0.02	-	0.617 ± 0.015	0.618 ± 0.009	9.79 ± 0.01	3087.3 ± 30.8	-0.60	-4.87

Table 4.2: Final results for TESS candidate exoplanet hosts

TOI	TIC	$T_{\rm eff}$ (K)	$\log g$	[Fe/H]	M ($M_\odot$)	$R_\star$ ($R_\odot$)	$m_{\rm bol}$	$f_{\rm bol}$ (10^{-12} ergs s^{-1} cm $^{-2}$)	EW(Hα) Å	$\log R^{'}_{\rm HK}$
435	44647437	4079 ± 30	4.64 ± 0.02	-0.13	0.621 ± 0.015	0.627 ± 0.010	13.34 ± 0.01	116.9 ± 1.2	-0.56	-4.57
1082	261108236	4096 ± 30	4.65 ± 0.02	-0.24	0.610 ± 0.015	0.609 ± 0.009	12.31 ± 0.01	302.8 ± 3.0	-0.61	-4.76
260	37749396	4097 ± 30	4.70 ± 0.02	-0.28	0.598 ± 0.015	0.575 ± 0.009	8.96 ± 0.01	6614.9 ± 65.9	-0.60	-4.75
761	165317334	4121 ± 30	4.64 ± 0.02	-0.15	0.623 ± 0.015	0.629 ± 0.010	11.34 ± 0.01	740.9 ± 7.4	-0.60	-4.49
249	179985715	4128 ± 30	4.71 ± 0.02	-	0.589 ± 0.015	0.561 ± 0.008	11.70 ± 0.01	531.3 ± 5.3	-0.56	-4.61
806	33831980	4137 ± 30	4.68 ± 0.02	-0.29	0.607 ± 0.015	0.592 ± 0.009	12.42 ± 0.01	274.5 ± 2.7	-0.62	-4.65
1216	141527965	4217 ± 30	4.61 ± 0.02	-0.13	0.649 ± 0.016	0.664 ± 0.010	11.98 ± 0.01	410.5 ± 4.1	-0.67	-4.68
302	229111835	4227 ± 30	4.59 ± 0.02	-0.03	0.661 ± 0.016	0.684 ± 0.011	13.36 ± 0.01	115.2 ± 1.2	-0.73	-4.60
656	36734222	4241 ± 30	4.58 ± 0.02	-0.07	0.662 ± 0.016	0.690 ± 0.010	11.57 ± 0.01	595.9 ± 6.0	-0.61	-4.46
1130	254113311	4275 ± 30	4.55 ± 0.02	-0.12	0.670 ± 0.017	0.716 ± 0.011	10.60 ± 0.01	1463.9 ± 14.6	-0.73	-4.78
133	219338557	4276 ± 30	4.64 ± 0.02	-0.22	0.646 ± 0.016	0.639 ± 0.009	10.45 ± 0.01	1673.5 ± 16.7	-0.71	-5.06
544	50618703	4292 ± 30	4.66 ± 0.02	-0.24	0.641 ± 0.016	0.623 ± 0.009	10.13 ± 0.01	2253.9 ± 22.4	-0.64	-4.56
836	440887364	4308 ± 30	4.62 ± 0.02	-0.15	0.658 ± 0.016	0.659 ± 0.009	9.12 ± 0.01	5710.9 ± 56.9	-0.68	-4.61
240	101948569	4333 ± 30	4.59 ± 0.02	-	0.676 ± 0.017	0.693 ± 0.010	11.16 ± 0.01	876.1 ± 8.8	-0.68	-4.60
713	167600516	4340 ± 30	4.64 ± 0.02	-0.25	0.648 ± 0.016	0.637 ± 0.009	11.17 ± 0.01	868.0 ± 8.7	-0.74	-5.09
900	210873792	4347 ± 30	4.63 ± 0.02	-0.23	0.653 ± 0.016	0.649 ± 0.010	12.32 ± 0.01	300.0 ± 3.0	-0.71	-5.46
493	19025965	4360 ± 30	4.59 ± 0.02	-0.05	0.677 ± 0.017	0.690 ± 0.010	11.92 ± 0.01	434.7 ± 4.3	-0.73	-4.87
178	251848941	4366 ± 30	4.64 ± 0.02	-	0.649 ± 0.016	0.639 ± 0.009	10.91 ± 0.01	1095.3 ± 10.9	-0.75	-4.85
875	14165625	4404 ± 30	4.59 ± 0.02	-0.13	0.675 ± 0.017	0.689 ± 0.010	11.85 ± 0.01	463.0 ± 4.6	-0.69	-4.57
711	38510224	4433 ± 30	4.64 ± 0.02	-	0.653 ± 0.016	0.638 ± 0.009	12.22 ± 0.01	327.6 ± 3.3	-0.73	-4.77
139	62483237	4434 ± 30	4.61 ± 0.02	-	0.673 ± 0.016	0.674 ± 0.009	9.88 ± 0.01	2827.2 ± 28.2	-0.69	-4.47
1073	158297421	4481 ± 30	4.62 ± 0.02	-	0.666 ± 0.017	0.664 ± 0.014	14.09 ± 0.01	58.6 ± 0.6	-0.69	-4.60
929	175532955	4482 ± 30	4.59 ± 0.02	-	0.684 ± 0.017	0.693 ± 0.010	11.92 ± 0.01	432.7 ± 4.3	-0.79	-10.15
969	280437559	4503 ± 30	4.59 ± 0.02	-	0.682 ± 0.017	0.693 ± 0.010	11.06 ± 0.01	960.4 ± 9.6	-0.72	-4.60
932	260417932	4508 ± 30	4.58 ± 0.02	-	0.689 ± 0.017	0.705 ± 0.010	11.23 ± 0.01	817.5 ± 8.1	-0.80	-5.22
1067	201642601	4510 ± 30	4.57 ± 0.02	-	0.698 ± 0.018	0.721 ± 0.012	13.61 ± 0.01	91.7 ± 0.9	-0.76	-
279	122613513	4512 ± 30	4.61 ± 0.02	-	0.677 ± 0.017	0.673 ± 0.009	11.03 ± 0.01	986.9 ± 9.8	-0.76	-4.61
129	201248411	4569 ± 30	4.57 ± 0.02	-	0.697 ± 0.018	0.721 ± 0.010	10.42 ± 0.01	1721.3 ± 17.2	-0.77	-4.50
824	193641523	4589 ± 30	4.60 ± 0.02	-	0.688 ± 0.018	0.691 ± 0.009	10.57 ± 0.01	1505.7 ± 15.0	-0.81	-4.76

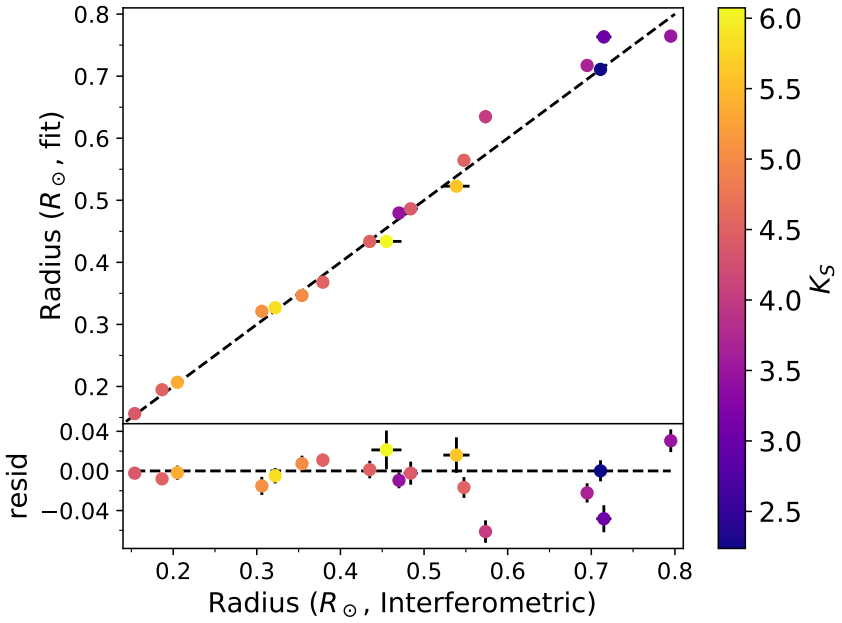

Figure 4.8: Radius comparison for those targets with interfometric radii to better than 5% precision. The median distance precision for these targets is 0.04 %. We find generally good agreement between literature measurements and our own, though noting that the brightness of this sample (see apparent *2MASS* K_S magnitude on the colour bar) results in photometry that is either saturated or has lower precision and thus may be the cause of some of the scatter observed.

semi-major axis $a_{R_\star,f}$ to approach $a_{R_\star,c}$. For cases with a discrepancy between the two, we flag the planet as an indication of a possibly eccentric orbit in Table 4.3.

This measured semi-major axis, calculated using our Mann et al. (2015) absolute K_S band $M_\star$, and T from NASA ExoFOP, can be constrained as follows:

$$a = \sqrt[3]{\frac{GM_\star T^2}{4\pi^2}} \tag{4.7}$$

where a is the semi-major axis, G is the gravitational constant, $M_\star$ is the stellar mass (with $M_\star >> M_p$, the planetary mass), and T is the planet orbital period—all of which we assume are independent quantities.

Now with a prior on the semi-major axis, we again use the least_squares function from `scipy`'s optimize module to perform least squares fitting to minimise the following expression:

$$R_t = \left(\frac{a_{R_\star,m} - a_{R_\star,f}}{\sigma_{a_{R_\star,m}}} + \sum_j^N \frac{t_{\text{obs, j}} - t_{\text{model, j}}}{\sigma_{t_{\text{obs, j}}}} \right)^2 \tag{4.8}$$

where R_t are the light curve and prior residuals (as a function of $R_{p,R_\star}$, $a_{R_\star,f}$, and i), $a_{R_\star,m}$ the measured scaled semi-major axis, $a_{R_\star,f}$ the fitted scaled semi-major axis, $\sigma_{a_{R_\star,m}}$ the

uncertainty on the measured scaled semi-major axis, j is the time step, N the total number of epochs, $t_{\mathrm{obs,\ j}}$ is the observed flux at time step j, $t_{\mathrm{model,\ j}}$ the model flux at time step j, and $\sigma_{t_{\mathrm{obs,\ j}}}$ is the measured flux uncertainty at time step j.

Results from this fitting procedure are presented in Table 4.3, a comparison with confirmed planets in Figure 4.11, and a histogram of the resulting planet candidate radii in Figure 4.12. Note that we do not fit the light curves for some candidates: TOIs 256.01 and 415969908.02 have only two and one transits respectively; TOI 507.01 is a suspected equal mass binary; TOIs 302.01 and 969.01 do not have PDCSAP two minute cadence data; and TOIs 203.01, 253.01, 285.01, 696.02, 785.01, 864.01, 1216.01, 260417932.02, and 98796344.02 have transits observed only at low SNR.

4.7 Discussion

4.7.1 Radial Velocities

Just over half our *TESS* sample have radial velocities in *Gaia* DR2, with the remaining 42 therefore having an incomplete set of positional and kinematic data. Our RVs are consistent with *Gaia* DR2 for our overlap sample and accurate to within ~4.5 km s^{-1} (Section 4.3.4), thus providing RVs for the remainder and enabling insight into Galactic population, or kinematic analysis using tools such as `Chronostar` (Crundall et al. 2019) to determine ages for those that are found to be members of stellar associations. These results are especially interesting given the planet–hosting nature of these stars.

4.7.2 Standard Star Parameter Recovery

Comparing our T_{eff} results to those of Mann et al. (2015) reveals excellent agreement for our two parameter fit (Figure 4.7), with the scatter on our residuals being smaller than their mean reported uncertainty of 60 K and only a relatively small systematic of ~30 K observed. Such consistency is encouraging given that this represents our largest uniform set of comparison stars, a set whose temperatures have already been successfully benchmarked against those from interferometry and should be much less sensitive to model limitations than our own.

When comparing to Rojas-Ayala et al. (2012), the results are less consistent, though we observe a similar effect to Mann et al. (2015) in that Rojas-Ayala et al. (2012) overestimates temperatures for the warmest stars. These temperatures, however, come solely from measurement of the H_2O-K2 index in the K band in conjunction with BT-Settl model atmospheres—much more limited in wavelength coverage than Mann et al. (2015) or our work here.

The interferometric sample shows good agreement, though we observe a ~70 K temperature systematic of the same sign as for the Mann et al. (2015) sample. However, due to the bias of interferometry towards close and thus bright targets, these are also the brightest stars we observe and they have correspondingly high photometric uncertainties due to saturation. This is particularly acute in the *2MASS* bands, where less than half the sample have the photometric quality flag (Qflg) of 'AAA', in contrast to the rest of the standard sample where all but two of 117 stars has Qflg 'AAA', and the entirety of the *TESS* sample. Nonetheless, our derived radii for the interferometric standards (Figure 4.8) are consistent when allowing for additional scatter from poor quality photometry on bright stars that will not be present for our science targets.

Table 4.3: Final results for TESS candidate exoplanets.

TOI	TIC	Sector/s	Period (days)	$R_p/R_\star$	$a/R_\star$	e flag	i (°)	R_p ($R_\oplus$)
122.01	231702397	1,27-28	5.07803 †	0.0797 ± 0.0022	24.63 ± 0.49	0	88.337 ± 0.001	3.00 ± 0.10
129.01	201248411	1-2,28-29	0.98097 †	0.3223 ± 0.0884	5.15 ± 0.04	0	76.381 ± 0.018	25.35 ± 6.96
133.01	219338557	1,28	8.19918 †	0.0269 ± 0.0010	23.15 ± 0.41	0	88.470 ± 0.002	1.88 ± 0.07
134.01	234994474	1,28	1.40153 †	0.0223 ± 0.0006	6.98 ± 0.16	0	84.566 ± 0.005	1.54 ± 0.05
136.01	410153553	1,27-28	0.46293 †	0.0587 ± 0.0006	6.80 ± 0.17	1	90.000 ± 5.000	1.23 ± 0.03
139.01	62483237	1,28	11.07083 †	0.0346 ± 0.0008	27.20 ± 0.56	0	88.549 ± 0.001	2.54 ± 0.07
142.01	425934411	1-2,28-29	0.85335 †	0.1809 ± 0.0184	4.74 ± 0.11	0	79.385 ± 0.012	13.31 ± 1.39
175.01	307210830	2,5,8-12,28-29,32	3.69066 †	0.0397 ± 0.0003	21.32 ± 0.47	0	88.809 ± 0.002	1.32 ± 0.03
175.02	307210830	2,5,8-12,28-29,32	7.45075 †	0.0446 ± 0.0006	34.59 ± 0.75	0	88.483 ± 0.001	1.48 ± 0.03
175.03	307210830	2,5,8-12,28-29,32	2.25310 †	0.0238 ± 0.0003	15.76 ± 0.34	0	88.133 ± 0.003	0.79 ± 0.02
177.01	262530407	2-3,29	2.85310 †	0.0385 ± 0.0005	12.70 ± 0.26	0	86.765 ± 0.002	2.24 ± 0.05
178.01	251848941	2,29	6.55770 †	0.0365 ± 0.0009	19.97 ± 0.36	0	88.506 ± 0.002	2.54 ± 0.07
178.02	251848941	2,29	20.70950 †	0.0439 ± 0.0023	42.94 ± 0.70	0	88.821 ± 0.001	3.06 ± 0.16
178.03	251848941	2,29	9.96188 †	0.0252 ± 0.0013	26.40 ± 0.45	0	88.855 ± 0.002	1.76 ± 0.09
178 b	251848941	2,29	1.91456 †	0.0197 ± 0.0008	8.78 ± 0.15	0	89.745 ± 0.094	1.37 ± 0.06
178 c	251848941	2,29	3.23845 †	0.0231 ± 0.0008	12.47 ± 0.22	0	88.423 ± 0.007	1.61 ± 0.06
178 f	251848941	2,29	15.23191 †	0.0314 ± 0.0011	35.01 ± 0.59	0	88.904 ± 0.001	2.19 ± 0.08
198.01	12421862	2,29	20.43021 †	0.0291 ± 0.0012	58.19 ± 1.14	0	89.374 ± 0.001	1.31 ± 0.06
210.01	141608198	1-5,7-13,27-32	9.01056 †	0.0629 ± 0.0007	37.78 ± 0.66	0	89.531 ± 0.002	2.24 ± 0.05
233.01	415969908	2,29	11.66993 †	0.0457 ± 0.0013	42.65 ± 0.82	0	89.606 ± 0.002	1.82 ± 0.06
234.01	12423815	2,29	2.83927 †	0.1932 ± 0.0045	12.63 ± 0.28	0	86.641 ± 0.003	11.50 ± 0.39
240.01	101948569	2,29	19.47241 †	0.0388 ± 0.0013	38.59 ± 0.59	0	89.278 ± 0.001	2.93 ± 0.10
244.01	118327550	2,29	7.39719 †	0.0321 ± 0.0012	29.05 ± 0.56	0	88.382 ± 0.001	1.42 ± 0.06
249.01	179985715	2,29	6.61542 †	0.0329 ± 0.0018	22.18 ± 0.38	0	88.757 ± 0.003	2.01 ± 0.11
256.02	92226327	3,30	3.77796 †	0.0480 ± 0.0010	25.61 ± 0.59	0	90.000 ± 5.000	1.15 ± 0.03
260.01	37749396	3	13.470018	0.0265 ± 0.0010	34.87 ± 0.60	0	88.758 ± 0.001	1.66 ± 0.07
269.01	220479565	3-6,10,13,30-32	3.69770 †	0.0691 ± 0.0012	18.65 ± 0.31	0	87.384 ± 0.001	2.99 ± 0.07
270.01	259377017	3-5,30,32	5.66054 †	0.0581 ± 0.0004	26.06 ± 0.55	0	89.210 ± 0.002	2.29 ± 0.04
270.02	259377017	3-5,30,32	11.37960 †	0.0535 ± 0.0004	41.87 ± 0.78	0	89.707 ± 0.002	2.11 ± 0.04
270.03	259377017	3-5,30,32	3.36014 †	0.0301 ± 0.0005	18.65 ± 0.37	0	89.218 ± 0.005	1.18 ± 0.03
279.01	122613513	3-4	11.494122	0.0361 ± 0.0013	27.95 ± 0.45	0	88.583 ± 0.001	2.65 ± 0.10

Notes: Periods denoted by † are not as reported by ExoFOP, and have been refitted here. These are overwhelmingly systems with TESS extended mission data, thus having longer time baselines with which to constrain orbital periods. Our fitted periods however are generally consistent within uncertainties of their ExoFOP values, and as such we do not report new uncertainties here. Additionally, our least squares fits to 7 of our light curves proved insenstive to non-edge-on inclinations. As such, we report conservative uncertanties of ±5° for these planets.

Table 4.3: – *continued*

TOI	TIC	Sector/s	Period (days)	$R_p/R_\star$	$a/R_\star$	e flag	i (°)	R_p ($R_\oplus$)
406.01	153065527	3-4,30-31	13.17573 †	0.0430 ± 0.0013	43.35 ± 0.87	0	89.303 ± 0.001	1.84 ± 0.06
435.01	44647437	4-5,31	3.35293 †	0.0583 ± 0.0016	12.82 ± 0.23	0	88.622 ± 0.007	3.99 ± 0.12
442.01	70899085	5,32	4.05203 †	0.0741 ± 0.0007	14.48 ± 0.25	0	86.865 ± 0.002	5.02 ± 0.09
455.01	98796344	4,31	5.35880 †	0.0467 ± 0.0009	29.82 ± 1.22	0	89.391 ± 0.005	1.38 ± 0.04
468.01	33521996	6,32	3.32527 †	0.1735 ± 0.0014	12.63 ± 0.25	0	87.382 ± 0.003	12.01 ± 0.24
475.01	100608026	5-6,32	8.26159 †	0.0307 ± 0.0014	24.22 ± 0.42	0	89.006 ± 0.003	2.00 ± 0.10
486.01	260708537	1-6,8-13,27-32	1.74468 †	0.0128 ± 0.0003	10.82 ± 0.21	0	88.585 ± 0.008	0.59 ± 0.02
493.01	19025965	7	5.947773	0.0518 ± 0.0020	17.60 ± 0.25	0	87.987 ± 0.003	3.90 ± 0.16
521.01	27649847	7	1.542131	0.0463 ± 0.0028	9.89 ± 0.17	0	86.478 ± 0.006	2.15 ± 0.14
532.01	144700903	6	2.326811	0.0876 ± 0.0020	9.96 ± 0.14	0	87.050 ± 0.004	6.02 ± 0.17
540.01	200322593	4-6,31-32	1.23914 †	0.0366 ± 0.0010	13.48 ± 0.32	0	87.063 ± 0.003	0.78 ± 0.03
544.01	50618703	6,32	1.54835 †	0.0281 ± 0.0006	7.80 ± 0.14	0	85.103 ± 0.004	1.91 ± 0.05
551.01	192826603	5-6,32	2.64730 †	0.3387 ± 1.1540	11.60 ± 0.17	0	84.411 ± 0.118	21.32 ± 72.62
552.01	44737596	4-5,31	2.78864 †	0.1552 ± 0.0014	11.57 ± 0.19	0	87.675 ± 0.003	10.05 ± 0.20
555.01	170849515	5,31-32	1.94163 †	0.1548 ± 0.0028	8.92 ± 0.20	0	87.380 ± 0.008	10.57 ± 0.32
557.01	55488511	5,31	3.34499 †	0.0388 ± 0.0025	13.43 ± 0.21	0	86.264 ± 0.002	2.46 ± 0.16
562.01	413248763	8	3.930792	0.0329 ± 0.0007	20.86 ± 0.41	0	88.691 ± 0.002	1.27 ± 0.03
620.01	296739893	8	5.098373	0.0597 ± 0.0015	18.65 ± 0.35	0	87.394 ± 0.001	3.56 ± 0.11
654.01	35009898	9	1.527419	0.0513 ± 0.0019	9.44 ± 0.16	0	87.873 ± 0.010	2.49 ± 0.10
656.01	36734222	9	0.813470	0.1608 ± 0.0005	4.67 ± 0.03	0	81.396 ± 0.002	12.11 ± 0.19
663.01	54962195	9	2.598654	0.0408 ± 0.0017	12.24 ± 0.17	0	88.685 ± 0.010	2.32 ± 0.11
663.02	54962195	9	4.698465	0.0433 ± 0.0023	18.16 ± 0.25	0	88.488 ± 0.004	2.46 ± 0.14
672.01	151825527	9-10	3.633618	0.0889 ± 0.0008	14.44 ± 0.20	0	87.932 ± 0.002	5.45 ± 0.10
674.01	158588995	9-10	1.977238	0.1174 ± 0.0009	11.35 ± 0.17	0	86.352 ± 0.002	5.67 ± 0.11
696.01	77156829	4-5,31-32	0.86024 †	0.0221 ± 0.0008	7.96 ± 0.16	0	84.721 ± 0.004	0.79 ± 0.03
698.01	141527579	1-5,7-13,27-32	15.08666 †	0.0436 ± 0.0010	42.17 ± 0.68	0	89.058 ± 0.001	2.26 ± 0.07
700.01	150428135	1,3-11,13,27-28,30-31	16.05110 †	0.0573 ± 0.0010	47.21 ± 0.89	0	88.902 ± 0.000	2.66 ± 0.07
700.02	150428135	1,3-11,13,27-28,30-31	37.42475 †	0.0272 ± 0.0008	82.17 ± 1.66	0	90.000 ± 5.307	1.26 ± 0.04
700.03	150428135	1,3-11,13,27-28,30-31	9.97701 †	0.0181 ± 0.0009	34.16 ± 0.66	0	89.885 ± 0.014	0.84 ± 0.04
702.01	237914496	1-4,7,11,27,29-31	3.56809 †	0.0280 ± 0.0010	14.46 ± 0.24	0	87.421 ± 0.002	1.73 ± 0.07
704.01	260004324	1-5,7-13,27-32	3.81431 †	0.0208 ± 0.0004	15.38 ± 0.28	0	87.419 ± 0.002	1.21 ± 0.03
711.01	38510224	1-5,7-8,11-12,28-32	18.38384 †	0.0301 ± 0.0012	39.90 ± 0.64	0	89.221 ± 0.001	2.09 ± 0.09
713.01	167600516	1-8,10-13,27-32	35.99988 †	0.0315 ± 0.0006	62.37 ± 0.95	0	89.724 ± 0.001	2.19 ± 0.05
713.02	167600516	1-8,10-13,27-32	1.87150 †	0.0155 ± 0.0007	8.69 ± 0.13	0	84.872 ± 0.003	1.07 ± 0.05
714.01	219195044	4-8,11-12,28,31-32	4.32378 †	0.0260 ± 0.0010	18.59 ± 0.31	0	88.556 ± 0.003	1.33 ± 0.06

Table 4.3: – *continued*

TOI	TIC	Sector/s	Period (days)	$R_p/R_\star$	$a/R_\star$	e flag	i (°)	R_p ($R_\oplus$)
714.02	219195044	4-8,11-12,28,31-32	10.17742 †	0.0307 ± 0.0011	32.90 ± 0.51	0	89.108 ± 0.001	1.57 ± 0.06
727.01	149788158	8	4.726090	0.0293 ± 0.0020	18.76 ± 0.31	0	89.435 ± 0.014	1.60 ± 0.11
731.01	34068865	9	0.321941	0.0133 ± 0.0005	3.29 ± 0.07	0	85.081 ± 0.031	0.67 ± 0.03
732.01	36724087	9	0.768418	0.0311 ± 0.0011	6.59 ± 0.13	0	90.000 ± 5.000	1.30 ± 0.05
732.02	36724087	9	12.254218	0.0607 ± 0.0022	41.84 ± 0.74	0	88.868 ± 0.001	2.53 ± 0.10
741.01	359271092	9-10	7.576262	0.0160 ± 0.0009	25.25 ± 0.62	0	88.472 ± 0.002	0.91 ± 0.05
756.01	73649615	10-11	1.23952 †	0.0548 ± 0.0019	7.43 ± 0.10	0	85.039 ± 0.005	3.12 ± 0.12
761.01	165317334	10	10.563348	0.0417 ± 0.0016	27.53 ± 0.41	0	89.196 ± 0.003	2.86 ± 0.12
782.01	429358906	10	16.047203	0.0659 ± 0.0040	47.81 ± 0.69	0	89.070 ± 0.001	2.97 ± 0.19
789.01	300710077	1-3,5-13,27-32	5.44693 †	0.0274 ± 0.0011	24.99 ± 0.44	0	89.127 ± 0.003	1.11 ± 0.05
797.01	271596225	1-13,27-32	1.80078 †	0.0256 ± 0.0006	10.21 ± 0.17	0	86.580 ± 0.003	1.33 ± 0.04
797.02	271596225	1-13,27-32	4.14002 †	0.0292 ± 0.0011	17.78 ± 0.30	0	87.236 ± 0.001	1.52 ± 0.06
806.01	33831980	1-3,5-6,8-9,12-13,27-29,32	21.91625 †	0.0347 ± 0.0011	47.14 ± 0.66	0	89.479 ± 0.001	2.24 ± 0.08
824.01	193641523	11-12	1.392930	0.0436 ± 0.0007	6.69 ± 0.10	0	83.665 ± 0.004	3.29 ± 0.07
833.01	362249359	9-11	1.042241	0.0190 ± 0.0007	6.02 ± 0.10	0	89.977 ± 1.790	1.24 ± 0.05
836.01	440887364	11	8.593935	0.0346 ± 0.0006	23.32 ± 0.30	0	88.727 ± 0.001	2.49 ± 0.06
836.02	440887364	11	3.817115	0.0240 ± 0.0008	13.59 ± 0.23	0	87.727 ± 0.003	1.72 ± 0.06
870.01	219229644	3-5,30-32	22.03813 †	0.0330 ± 0.0012	45.25 ± 0.81	0	89.013 ± 0.001	2.22 ± 0.09
873.01	237920046	1-4,11,28-31	5.93122 †	0.0279 ± 0.0012	21.26 ± 0.38	0	90.000 ± 5.000	1.58 ± 0.07
875.01	14165625	5-6	11.020153	0.0277 ± 0.0021	26.47 ± 0.36	0	90.000 ± 5.000	2.08 ± 0.16
876.01	32497972	5-6,32	38.69629 †	0.0367 ± 0.0044	65.85 ± 1.39	0	89.254 ± 0.001	2.46 ± 0.30
900.01	210873792	12	4.844050	0.0426 ± 0.0026	15.81 ± 0.26	0	90.000 ± 5.000	3.01 ± 0.19
904.01	261257684	12-13	18.35654 †	0.0342 ± 0.0017	43.55 ± 0.79	0	90.000 ± 5.000	2.00 ± 0.10
910.01	369327947	12-13,27	2.02911 †	0.0311 ± 0.0007	15.53 ± 0.31	0	87.229 ± 0.002	0.94 ± 0.03
912.01	406941612	12-13	4.679100	0.0414 ± 0.0008	20.71 ± 0.32	0	88.819 ± 0.002	1.93 ± 0.05
929.01	175532955	30-31	5.83010 †	0.0314 ± 0.0015	17.32 ± 0.28	0	89.396 ± 0.012	2.37 ± 0.12
932.01	260417932	28-29,31-32	19.310700	0.0337 ± 0.0009	38.00 ± 0.62	0	89.463 ± 0.002	2.59 ± 0.08
1067.01	201642601	13,27	3.13167 †	0.1071 ± 0.0012	11.13 ± 0.20	0	89.174 ± 0.012	8.42 ± 0.17
1073.01	158297421	13,27	3.92282 †	0.1799 ± 0.0039	13.88 ± 0.27	0	86.903 ± 0.002	13.04 ± 0.39
1075.01	351601843	13,27	0.60474 †	0.0286 ± 0.0006	4.39 ± 0.08	0	85.023 ± 0.014	1.78 ± 0.05
1078.01	370133522	13,27	0.51824 †	0.0274 ± 0.0004	5.04 ± 0.10	0	85.016 ± 0.010	1.17 ± 0.03
1082.01	261108236	12-13,27-28,31	16.34646 †	0.0399 ± 0.0012	37.72 ± 0.63	0	89.448 ± 0.002	2.65 ± 0.09
1201.01	29960110	4,31	2.49197 †	0.0389 ± 0.0009	12.46 ± 0.24	0	87.967 ± 0.004	2.07 ± 0.06
153065527.02	153065527	3-4,30-31	3.30745 †	0.0270 ± 0.0013	17.26 ± 0.33	0	87.940 ± 0.003	1.16 ± 0.06

Encouragingly however Mann et al. (2015), which we are in agreement with, integrated their own photometry from low resolution flux calibrated spectra and found a good match between their results and their own interferometric sample.

Finally, our results are consistent with our sample of mid-K-dwarfs in the temperature range of our warmest science targets. The observed higher scatter (than e.g. the Mann et al. 2015 sample) is to be expected due to inter-study systematics, as these targets were not pulled from a single uniform catalogue.

While the exact cause of the Mann et al. (2015) and interferometric systematic is unclear, its appearance in both samples suggests it is not an artefact. As such, we apply a −30 K correction to the observed temperature systematic. Although our remaining scatter is consistent with the scatter in our external reference catalogues, we add a further ±30 K $T_{\rm eff}$ uncertainty in quadrature with our statistical uncertainties to account for the unknown origin of the observed systematic. Given these corrections, we are confident our fitting methodology is able to recover both accurate and precise stellar temperatures and radii for stars in the range 3 000 K$\lesssim T_{\rm eff} \lesssim$ 4 500 K—critical for insight into the radii of their transiting planets.

4.7.3 Model Limitations

The inability of cool dwarf atmospheric models to reproduce optical fluxes is significant. Such wavelengths are among the most easily accessible, and understanding them is required to take full advantage of photometry from surveys like *Gaia* and *SkyMapper*. Thus anyone relying directly (e.g. spectral fitting) or indirectly (e.g. isochrone fitting with colours) on models for cool stellar atmospheres must do so with caution (for specifics on isochone systematics, see e.g. VandenBerg et al. 2006 for the Victoria-Regina models, Dotter et al. 2008 and Joyce & Chaboyer 2018a for DSEP, and Dotter 2016 for MIST).

We identify two key areas for improvement with our models and methods as implemented. The first relates to TiO, the dominant opacity source at optical wavelengths. Comparing high-resolution spectra of M dwarfs to PHOENIX models and TiO templates, Hoeijmakers et al. (2015) concluded that 'the modelled spectrum of TiO is not representative of the real TiO'. McKemmish et al. (2019) confirmed this discrepancy in the process of validating their updated TiO line list, with their comparisons showing significant improvements in both predicted TiO wavelengths and line depths across the optical when using the updated line list. McKemmish et al. (2019) was not yet published at the time our MARCS models were generated, and although they note that there remains room for further work, this represents a significant improvement on the previous state of the art. While recomputing our library of synthetic spectra with the new line list would constitute a significant computational effort, we will endeavour to do this in future work.

The second issue concerns proper consideration of the relative abundances of C and O—constituents of the dominant molecular opacity sources in cool dwarf atmospheres—denoted here as [(O-C)/Fe]. As described by Veyette et al. (2016), it is not just $T_{\rm eff}$ and [Fe/H] that affects the location of the pseudo-continuum, but also [(O-C)/Fe]. The principal reason for this is that [(O-C)/Fe] influences the concentrations of C- and O-based molecules, affecting the flux of the pseudo-continuum and apparent strength of metal lines. They conclude that ultimately the inferred value of [Fe/H] depends on [(O-C)/Fe], and that much better spectral fits

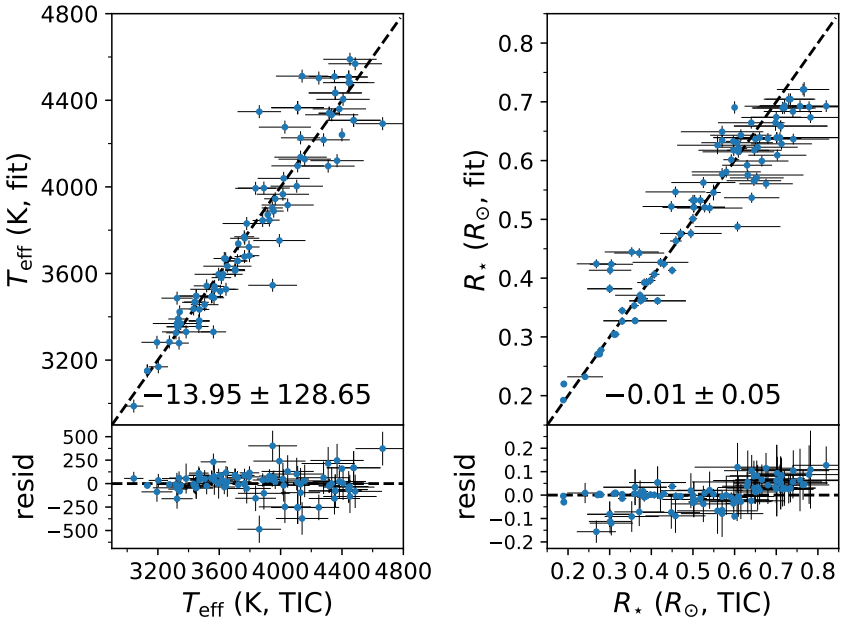

Figure 4.9: Comparison of $T_{\rm eff}$ and $R_\star$ as reported here compared to those from the *TESS* Input Catalogue. The median and standard deviation of each set of residuals is annotated.

are possible when allowing [(O-C)/Fe] to vary. An important note is that empirical calibrations based on F/G/K–M binaries such as Rojas-Ayala et al. (2012), Mann et al. (2013a), and our own photometric [Fe/H] relation should remain valid as statistical [Fe/H] indicators due to the tight Solar Neighbourhood [Fe/H]–[C/O] correlation. Per the recommendation of Veyette et al. (2016), this issue is significant enough to merit new models with [C/Fe] and [O/Fe] as independent parameters.

That said, there is an ever increasing empirical knowledge of M-dwarfs meaning that, even in the absence of accurate models, empirical or data driven approaches should be possible, especially if methods to break the [Fe/H]–[(O-C)/Fe] degeneracy can be found. For instance, see Birky et al. (2020) which demonstrates that a data driven approach, at least in the *H* band, is possible for M-dwarfs. The very small rate of evolution for these low-mass stars means we can rely on mass and chemical composition to derive the fundamental parameters of the star, thus making for a more tractable problem.

4.7.4 *TESS* Input Catalogue Stellar Parameters

The *TESS* Input Catalogue is often the first stellar parameter reference for newly alerted TOIs. As these parameters are mostly derived from empirical relations using literature photometry, we thought it useful to compare these predictions with our fits to inspect for remaining catalogue systematics. Figure 4.9 displays this comparison for $T_{\rm eff}$ and $R_\star$, and while the TIC temperatures are broadly consistent, TIC radii for the warmest stars in our sample appear systematically large. This stellar radii systematic is noteworthy as it would bias any predicted exoplanet radii around mid-K dwarfs.

4.7.5 Emission Features in *TESS* Candidates

While model limitations prevented us from taking full advantage of our spectra during fitting, our wide wavelength coverage allows us to look for spectral peculiarities. In the current study, these take the form of emission in the hydrogen Balmer series or Ca II H&K (both signs of stellar activity and youth), as well as absorption in the Li 6 708 Å (another sign of youth). While none of our *TESS* planet hosts show detectable Lithium absorption, we report Hα equivalent widths and $\log R'_{\rm HK}$ in Table 4.2, calculated using the methodology of Žerjal et al. (2021). 53 stars in our sample have EWH$\alpha > -0.5$ Å (adopted as the limiting bound for activity, noting as well that this is strongly dependent on $T_{\rm eff}$ and thus somewhat approximate), and 35 have $\log R'_{\rm HK} > -4.75$ (the lower bound for active stars used in Gray et al. 2006).

Of particular note are our two most active stars, the first of which is TOI 507 (TIC 348538431). TOI 507 appears substantially overluminous in Figure 4.1, and presents with strong emission across the Balmer series and in Ca II H&K. Visual inspection of its spectrum, along with comparison to the cool dwarf standard HIP 103039 which is very similar in $T_{\rm eff}$, indicates that it is actually a double-lined spectroscopic binary. Transit depths appear similar for both primary and secondary eclipses, which points to the system being composed of roughly equal mass components. Taking a ~0.75 mag offset into account due to binarity, TOI 507 still sits slightly above the main sequence, meaning that it remains a potentially young touchstone system amenable to characterisation as in e.g. Murphy et al. (2020). The mass, radius, $m_{\rm bol}$, and flux reported in Table 4.2 have been derived for a single component of this binary system, assuming equal mass and brightness.

The second star is TOI 142 (425934411) which is also overluminous and displays strong emission features. Interestingly, it appears to host a giant planet ($R_P = 13.31 \pm 1.39\,R_\oplus$) on a short period ($T \approx 0.85$ day)—see Figure 4.10. While this is unusual for such a cool star, it is not unheard of, such as K2 32b which is a known short period super-Neptune orbiting a pre-main sequence star (David et al. 2016; Mann et al. 2016). Further characterisation of the system however, whilst scientifically interesting, is likely to be hampered by the faintness of the host star (G~15.8).

4.7.6 Planet Parameter Recovery

Table B.6 collates literature parameters for previously characterised planets in our sample. These planets have typically had follow-up radial velocity observations which not only allows for planetary mass determination, but helps constrain their orbits when combined with the *TESS* light curves we use here (or additional time series photometric follow up). Figure 4.11 compares these results to our own for $R_P/R_\star$, $a/R_\star$, i, and R_P. We find our results consistent with the literature, aside from a few exceptions discussed below.

LHS 3844 b

Vanderspek et al. (2019) reports a larger value of $Rp/R_\star$ for LHS 3844 b (TOI 136.01) than we do here, a difference we can attribute to our access to an extra sector of *TESS* data. While they also have ground based data, the extra *TESS* sector amounts to some 60 extra transits, which should give us improved precision.

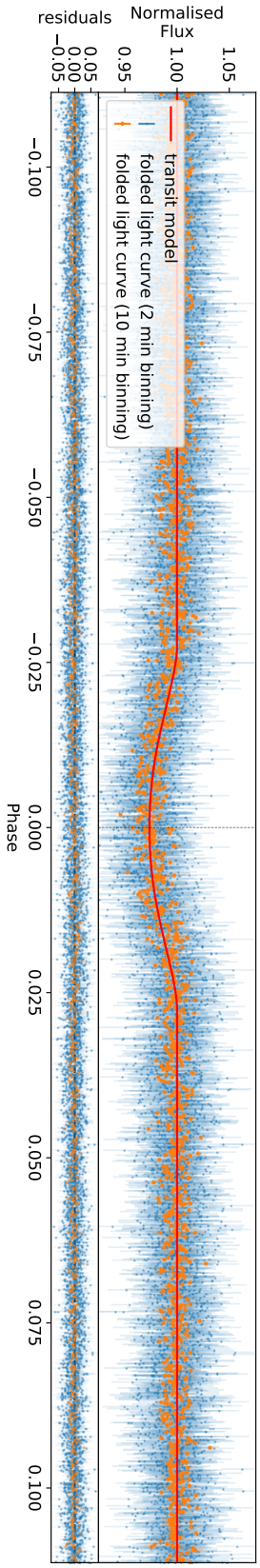

Figure 4.10: Phase folded light curve with best fitting transit model for TOI 142.01.

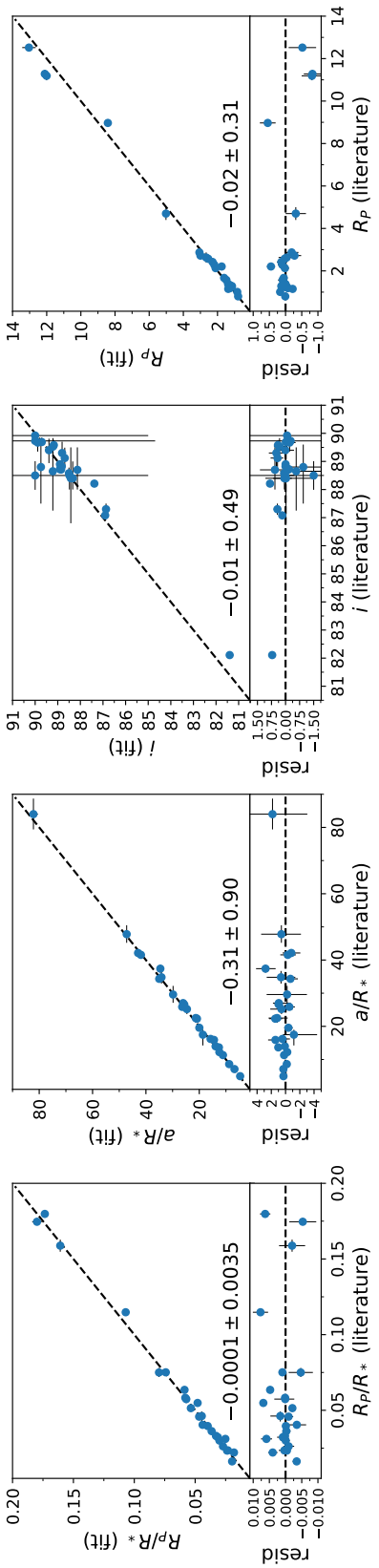

Figure 4.11: Comparison of $R_P/R_\star$, $a/R_\star$, i, and R_P to literature results in Table B.6. Our two largest literature planets, TOIs 129.01 and 551.01, are hot Jupiters in a grazing configuration which leaves their radii poorly constrained. As such, they have been left off for clarity, though our results are consistent within uncertainties. The median and standard deviation of each set of residuals is annotated and excludes these two planets.

HATS-48 A b, TOI 178 b/e, LHS 1140 c

Comparison with HATS-48 A b (TOI 1067.01) from Hartman et al. (2020) shows an inconsistent value of $R_P/R_\star$, indicating a difference in how we have modelled the light curves. While we have access to an additional sector of *TESS* data, the difference primarily appears to come from **a)** including RVs in their fit, and **b)** their use of an additional 'dilution factor' when fitting to account for nearby unresolved stars. Such nearby stars have the effect of diluting the transit and making the transit appear shallower than it would were only the flux from the host star observed. Our transit fits, by comparison, rely on the quality of the detrending and correction for crowding already done by the *TESS* team and provided in their PDCSAP fluxes.

Leleu et al. (2021) reports parameters for six planets orbiting TOI 178, of which only three were alerted on as TOIs. Our parameters are consistent for all but two of these, TOI 178 b (not alerted on) and TOI 178.03, both of which are relatively low SNR detections by *TESS*. Although our analysis includes an additional *TESS* sector of data, they employ higher precision data from CHEOPS to which we attribute the difference.

The analysis of LHS 1140 c (TOI 256.02) by Ment et al. (2019) results in a value of $R_P/R_\star$ discrepant with our own. While our analysis makes use of an additional sector of *TESS* data, we consider their results more reliable as they conducted a joint RV and transit photometry analysis, including additional ground based data alongside high-precision *Spitzer* data.

WASP-43 b and HATS-6 b

We find a consistent $R_P/R_\star$ with Esposito et al. (2017) for WASP-43 b (TOI 656.01), though our value of R_P is smaller. This difference is attributable to their larger and less precise stellar $T_{\rm eff}$, with which they obtain a smaller stellar radius—resulting in a smaller planetary radii. As discussed, we are confident with our $T_{\rm eff}$ and $R_\star$ recovery, and consider the difference the result of differing approaches to stellar parameter determination.

For HATS-6 b (TOI 468.01) we find our $R_P/R_\star$ and $T_{\rm eff}$ consistent, but a different value for R_P as compared to Hartman et al. (2015). This difference again arises from a smaller literature value of $R_\star$. We consider our approach to radius determination using stellar fluxes more direct than the modelling based approach used here, especially given our access to precision *Gaia* parallaxes.

4.7.7 Candidate Planet Radii Distribution

We plot a histogram of our candidate planet radii in Figure 4.12, which shows the existence of the planet radius gap, first identified by Fulton et al. (2017), at $\sim 1.65 - 2.0\,R_\oplus$ at a $\sim 1\sigma$ level. As we remain limited by our small sample size, we do not perform any additional analysis and leave such investigations for future studies based on a larger sample of *TESS* planets.

Our results however do provide encouraging further evidence for the radius gap being present around planets orbiting low-mass stars. Its detection for the stellar mass range considered here is similar to the work of Cloutier & Menou (2020) who investigated a set of confirmed and candidate planets from Kepler and K2 orbiting stars with $T_{\rm eff} < 4\,700$ K, with their sample being roughly a factor of ~4.5 larger than our own. Separating their planets into bins of different stellar mass, they demonstrated that the bimodality in the radius distribution vanishes as stellar

mass decreases, corresponding to the population of rocky planets beginning to dominate that of their more gas rich counterparts. They note, however, that a much larger sample of planets is required in order to properly distinguish between the various possible formation channels for the radius valley (e.g. photoevaporation, core-powered mass loss), particularly when further subdividing the sample by stellar mass. It is hoped that our results here can contribute to a larger future analysis combining *Kepler*, *K2*, *and TESS* planets, perhaps also looking into correlations with stellar activity using activity measures such as we provide.

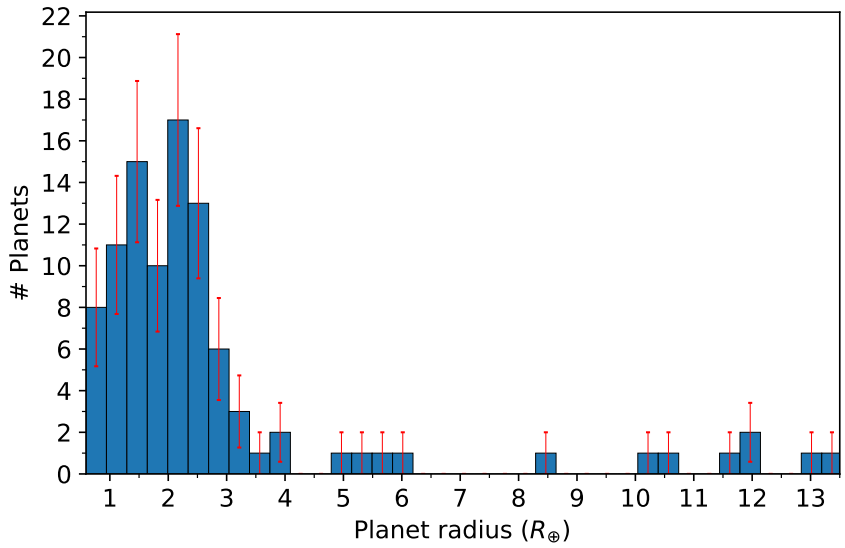

Figure 4.12: Histogram of candidate planet radii with $R_P < 14\,R_\oplus$, with $0.35\,R_\oplus$ width bins and Poisson uncertainties. Note that we detect the exoplanet radius gap at approximately a $\sim 1\sigma$ level, though remain limited by our small sample size.

4.8 Conclusions

In the work presented above, we have described our ANU 2.3 m/WiFeS observing program to characterise 92 southern *TESS* candidate planet hosts with $3\,000 \lesssim T_{\rm eff} \lesssim 4\,500$ K in order to precisely determine the radii of 100 transiting planets they host. In the process of doing so we investigated cool dwarf model atmosphere systematics, as well as developed a new photometric [Fe/H] calibration. The main conclusions from our work are as follows:

- Cool dwarf MARCS model atmospheres systematically overestimate flux in the optical relative to the well produced spectral regions 5 585-6 029 Å and 6 159-7 000 Å, with agreement being worse the cooler the star or bluer the wavelength. We report a simple linear relation parameterising the offset as a function of the observed *Gaia* $(B_P - R_P)$ colour, enabling the correction of synthetic *Gaia* B_P, and *SkyMapper* g and r magnitudes. We recommend that future work consider updated molecular line lists (McKemmish et al. 2019) and non-solar scaled chemical abundances (see Veyette et al. 2016).

- Using the same models, a general least squares fitting approach to medium resolution optical spectra and literature photometry is not sufficient to accurately recover [Fe/H] for cool dwarfs. We instead develop an updated photometric [Fe/H] calibration for cool dwarfs, built using a sample of 69 M and K dwarfs with F/G/K binary companions having reliable [Fe/H] measurements. By relating the position of these isolated main sequence KM stars in $M_{K_S} - (B_P - K_S)$ space to the F/G/K companion, and thus system, [Fe/H], our relation can determine metallicity to a precision of ±0.19 dex for stars with $1.51 < (B_P - R_P) < 3.3$. This relation expands on the work of Bonfils et al. (2005), Johnson & Apps (2009), and Schlaufman & Laughlin (2010), and takes advantage of precision *Gaia* parallaxes (for precise distances) and kinematics (for binary identification) for the first time.

- We determine $T_{\rm eff}$ and $R_\star$ for our 92 *TESS* candidate planet hosts with a median precision of 0.8% and 1.7% respectively, as well as radial velocities to $\sim$4.5 km s^{-1}. 42 of these targets did not previously have radial velocities from *Gaia* DR2, thus completing completing the kinematics for these stars.

- We report Hα equivalent widths and Ca II H&K $\log R'_{\rm HK}$ for our sample, both signs of activity and youth. None of our stars display detectable Lithium 6 708 Å absorption.

- We use our derived stellar parameters to fit the *TESS* light curves for our 100 planet candidates in order to determine R_P with a median precision of 3.5%. Our planet properties are consistent with the 30 already confirmed by other studies. We additionally see evidence of the planet radius gap at a $\sim 1\sigma$ level for our low-mass stellar sample, with the robustness of the detection only limited by the small sample size.

- We report the existence of two likely young systems based on stellar emission and location above the main sequence: TOI 507 (TIC 348538431) and TOI 142 (425934411). The former appears to be a near-equal mass, double-lined eclipsing binary with $T_{\rm eff} \approx 3\,300$ K, potentially amenable to characterisation as a pre-main sequence benchmark system. TOI 142 on the other hand has a giant planet ($R_P = 13.31 \pm 1.39\,R_\oplus$) on a short period ($T \approx 0.85$ day) orbit.

This is one of the largest uniform analyses of cool *TESS* candidate planet hosts to date, and the first cool dwarf photometric [Fe/H] calibration based on *Gaia* data. Given the major difficulties encountered using model atmospheres for [Fe/H] determination, we plan to conduct follow-up work investigating empirical or data driven approaches built upon our now large collection of cool dwarf standard spectra.

Acknowledgements

We acknowledge the traditional custodians of the land on which the ANU 2.3 m Telescope stands, the Gamilaraay people, and pay our respects to elders past and present. We also acknowledge helpful early conversations with George Zhou about target selection and observing strategy, as well as the efforts of Andy Casey in developing a prototype data-driven model which

ultimately proved out of scope for this study. We thank the anonymous referee for their helpful comments.

ADR acknowledges support from the Australian Government Research Training Program, and the Research School of Astronomy & Astrophysics top up scholarship. MŽ and MJI acknowledge funding from the Australian Research Council (grant DP170102233). LC is the recipient of the ARC Future Fellowship FT160100402. MJ was supported the Research School of Astronomy and Astrophysics at the Australian National University and funding from Australian Research Council grant No. DP150100250. Parts of this research were conducted by the Australian Research Council Centre of Excellence for All Sky Astrophysics in 3 Dimensions (ASTRO 3D), through project number CE170100013.

This research has made use of the Exoplanet Follow-up Observation Program website, which is operated by the California Institute of Technology, under contract with the National Aeronautics and Space Administration under the Exoplanet Exploration Program. This paper includes data collected by the *TESS* mission. Funding for the *TESS* mission is provided by the NASA Explorer Program. This work has made use of data from the European Space Agency (ESA) mission *Gaia* (`https://www.cosmos.esa.int/gaia`), processed by the *Gaia* Data Processing and Analysis Consortium (DPAC, `https://www.cosmos.esa.int/web/gaia/dpac/consortium`). Funding for the DPAC has been provided by national institutions, in particular the institutions participating in the *Gaia* Multilateral Agreement. This publication makes use of data products from the Two Micron All Sky Survey, which is a joint project of the University of Massachusetts and the Infrared Processing and Analysis Center/California Institute of Technology, funded by the National Aeronautics and Space Administration and the National Science Foundation. The national facility capability for *SkyMapper* has been funded through ARC LIEF grant LE130100104 from the Australian Research Council, awarded to the University of Sydney, the Australian National University, Swinburne University of Technology, the University of Queensland, the University of Western Australia, the University of Melbourne, Curtin University of Technology, Monash University and the Australian Astronomical Observatory. *SkyMapper* is owned and operated by The Australian National University's Research School of Astronomy and Astrophysics. The survey data were processed and provided by the *SkyMapper* Team at ANU. The *SkyMapper* node of the All-Sky Virtual Observatory (ASVO) is hosted at the National Computational Infrastructure (NCI). Development and support for the *SkyMapper* node of the ASVO has been funded in part by Astronomy Australia Limited (AAL) and the Australian Government through the Commonwealth's Education Investment Fund (EIF) and National Collaborative Research Infrastructure Strategy (NCRIS), particularly the National eResearch Collaboration Tools and Resources (NeCTAR) and the Australian National Data Service Projects (ANDS). This research made use of Lightkurve, a Python package for Kepler and *TESS* data analysis.

Software: `Astropy` (Astropy Collaboration et al. 2013), `batman` (Kreidberg 2015), `iPython` (Perez & Granger 2007), `dustmaps` (Green 2018), `lightkurve` (Lightkurve Collaboration et al. 2018), `Matplotlib` (Hunter 2007), `NumPy` (Harris et al. 2020), `Pandas` (McKinney 2010), `SciPy` (Jones et al. 2016).

Chapter 5

Conclusions and Future Work

In this thesis I have expanded the library of benchmark stars available to stellar astrophysics; implemented a sky-tiling algorithm suitable for an all-sky massively-multiplexed spectroscopic survey of bright stars like the FunnelWeb Survey; and characterised a set of cool dwarf exoplanet hosts and their planets using a model-based spectral fitting methodology calibrated by stellar standards. Here I summarise each of these projects in Section 5.1, discuss how each fits into stellar and exoplanetary astrophysics along with future work in Section 5.2, before concluding in Section 5.3.

5.1 Summary of Thesis

5.1.1 Precision Angular Diameters with VLTI/PIONIER

Long-baseline optical interferometry presents the most direct method of determining stellar temperatures and radii in a near-model-independent way. These stars are then able to serve as benchmarks for astrophysics more broadly, and are critical to calibrating spectroscopic surveys, developing empirical relations, and testing theoretical models. In Chapter 2, published as Rains et al. (2020), I describe my work using the PIONIER beam combiner on the Very Large Telescope Interferometer (VLTI) to measure the angular diameters, stellar radii, and effective temperatures for 16 southern stars.

PIONIER is the shortest-wavelength beam combiner on the VLTI, thus making it the highest spatial resolution instrument in the Southern Hemisphere and well suited for this work. High angular resolution is necessary to resolve the diameters of dwarf stars in the Solar Neighbourhood, particularly the low-mass regime which has few reliable measurements. The stars in my sample consisted of a variety of stellar temperatures and evolutionary states—six dwarf, five subgiant, and five giant stars—ten of which were new to interferometry. The remaining six served as a check on cross beam-combiner systematics—important given the care required to calibrate for instrumental effects and the fundamental nature of the technique. With this in mind, I increased the robustness of the standard PIONIER data reduction pipeline by adding bootstrapping and Monte Carlo steps to account for correlated uncertainties, which was able to produce $\sim$1% precision angular diameters, stellar radii, and effective temperatures for my sample. These results were entirely consistent with past measurements (mostly VLTI beam combiners), and observed with greater sensitivity than those from the literature—encouraging results for the consistency of the southern set of stellar temperature and radius standards.

5.1.2 A Sky Tiling Algorithm for Massively-Multiplexed Spectroscopic Surveys

As stellar spectroscopic surveys become increasingly multiplexed, and target ever larger samples of stars across a broad range in magnitudes, the optimisation of survey strategy with respect to efficiency and completeness becomes a more critical consideration. In Chapter 3 I discuss my work developing the sky tiling algorithm for the now cancelled FunnelWeb Survey—an ambitious multiplexed low-resolution optical spectroscopic survey of two million of the brightest stars in the Southern Hemisphere.

The key technological innovation driving FunnelWeb was the TAIPAN robotic fibre positioner, able to rapidly reposition 150 optical fibres in parallel across the wide 6° field of the UK-Schmidt Telescope. This pairing is what made an all–sky, bright–star survey of the Southern Hemisphere possible, and was excellently timed to synergise with modern astrophysical datasets in a variety of ways. A few key science cases included: a census of nearby pre-main sequence stars identified through spectral features of youth; stellar temperatures, gravities, and metallicities for nearby dwarf stars to inform the input catalogue and follow-up efforts for NASA's Transiting Exoplanet Survey Satellite (*TESS*); spectral identification or confirmation of all bright southern extremely metal-poor (EMP) stars, or stars with anomalous abundance patterns, such as carbon enhanced metal-poor stars (CEMP); among a variety of other science cases.

FunnelWeb's tiling algorithm thus had to take into account not only prioritisation of these various science cases, but also how to efficiently observe and allocate fibres for two million stars differing in brightness by up to 9 magnitudes—a factor of nearly 4 000 in flux. The resulting scheme, described in Chapter 3, utilised a uniformly distributed set of overlapping 6° tiles, four overlapping magnitude bins, a six step priority scale, and a greedy allocation algorithm to ensure survey efficiency, completeness, and optimal target signal-to-noise. Ultimately, however, continued delays in the commissioning of the TAIPAN instrument, the availability of research funds and personnel and, perhaps most critically, the timelines of other upcoming large spectroscopic surveys such as *Gaia* DR3 and SDSS-V, led to the cancellation of the FunnelWeb Survey in November 2019.

5.1.3 Characterisation of Southern TESS Candidate Exoplanet Hosts

NASA's *TESS* mission, by virtue of observing nearly the entire sky, is discovering the majority of the short-period, high signal-to-noise exoplanets transiting bright stars—overwhelmingly around low-mass, cool dwarfs. While many of these planets will be subject to detailed characterisation and multi-epoch precision radial velocity (RV) follow-up observations, there remains a need for single-epoch spectroscopic observations to characterise the properties of the stellar hosts. In Chapter 4, I describe a survey of 92 southern cool ($T_{\rm eff} \lesssim 4\,500\,{\rm K}$) dwarf candidate exoplanet hosts with the WiFeS instrument on the ANU 2.3 m Telescope, as well as the accompanying investigation into obtaining cool dwarf metallicities from optical spectra.

The properties of transiting planets can be known only as well as one knows the properties of their host stars. While broadband photometry can be used to determine precise stellar temperatures, spectroscopic characterisation remains essential in order to gain insight into bulk stellar metallicities, elemental abundances, and stellar youth– or activity–based emission features. Since the analysis of exoplanet transit light curves yields only the *ratio* of exoplanetary

to stellar radii, the most critical parameter to determine is the stellar radius, which in turn gives the planet radius. If this is done uniformly for a large sample of transiting planets, one can then begin to study planet demographics—something not possible with only a small sample. This was the goal motivating the survey of southern cool dwarf planet hosts as described in Rains et al. (2021)—stellar characterisation to enable exoplanet demographics. I implemented a model-based spectral fitting routine, calibrated by stellar standards, to determine stellar parameters from WiFeS spectra and literature photometry, followed by exoplanet transit light curve modelling for planet properties. This resulted in 0.8% and 1.7% precision stellar temperatures and radii—consistent with interferometric standards—and 3.5% precision exoplanet radii—precise enough to provide tentative further evidence that the so called 'exoplanet radius valley' is also present for cool dwarfs. This feature, first observed by Fulton et al. (2017) for planets around stars of spectral type F/G/K, consists of a region of 'forbidden exoplanet radii' and is thought to be a sign of exoplanet atmospheric mass loss.

This analysis however was made difficult by the well-known complexity of optical cool dwarf atmospheres, and limitations present even in modern synthetic spectral libraries. Extensive molecular absorption in the atmospheres of cool dwarfs makes disentangling the effects of temperature and metallicity challenging, and incomplete line lists or opacity tables in model spectra only compound this. As such, the project also used observed cool dwarf standards to quantify and correct for optical flux systematics in broadband photometry, as well as developing a new optical photometric relation to estimate cool dwarf metallicity independently of spectroscopy. Thus, while a model-based approach was ultimately successful in characterising cool dwarfs and their planets, the success was in large part due to the strength of standard-based calibrations and empirical relations, and highlights the challenges in working with these stars.

5.2 Future Work

I've stated before that this PhD was an interdisciplinary one, and that is reflected by the length of this chapter and the very existence of this overview. To that end, I discuss outstanding issues in the topics of stellar benchmarking and parameter determination more generally in Section 5.2.1; how non-traditional analysis techniques continue to be deployed in Section 5.2.2; the future of spectroscopic surveys and what that looks like in the absence of FunnelWeb in Section 5.2.3; and the future of studying planet demographics around low-mass stars in Section 5.2.4.

5.2.1 Stellar Parameters and Standards

Thanks to surveys like *Gaia*, *SkyMapper*, *SDSS*, *PANSTARS*, *2MASS*, and *WISE*, soon all but the very brightest or faintest stars will have optical-through-IR photometry. The infrared flux method (IRFM), alongside *Gaia* parallaxes and reddening estimates from modern 3D dust maps (e.g. Green et al. 2019, built from *Gaia*, *Pan-STARRS*, and *2MASS* photometry), can give few % level precision temperatures for this sample for roughly $4\,000 < T_{\rm eff} < 8\,000\,\mathrm{K}$ (e.g. Casagrande et al. 2020). With these temperatures and parallaxes, plus bolometric fluxes from broadband photometry, precision radii can be calculated for this sample—thus leaving only the chemical and mass dimensions unknown.

To ensure however that the technique is built upon solid foundations, it must be benchmarked

against a wide variety of stellar standards. Whilst the accuracy and precision of the IRFM obviates the need to obtain interferometric temperatures and radii for all stars, the standards we do have should adequately cover the possible temperature–radius–chemistry space. This includes: hot stars (e.g. Maestro et al. 2013), cool stars (e.g. Boyajian et al. 2012b; Rabus et al. 2019), metal-poor stars (e.g. Karovicova et al. 2018, 2020), and asteroseismic standards (e.g. Huber et al. 2012; White et al. 2013) to name a few.

However, there are known angular diameter and temperature disagreements in the literature between the IRFM and certain interferometric standards, as reported by Casagrande et al. (2014). This disagreement can be up to as much as 10%, and is systematically worse for those stars less well resolved by the interferometer, with White et al. (2018) reporting similar findings when comparing results from different interferometric beam combiners. More recently, Tayar et al. (2020) compared angular diameters of stars with measurements in common between different beam combiners on the CHARA array (specifically CLASSIC, MIRC, VEGA, and PAVO), and also found systematic differences of up to 10% — again worst for the least resolved stars. While my work in Rains et al. (2020) showed much better agreement between the PIONIER and VINCI beam combiners on the VLTI, there clearly needs to be more effort to validate our existing library of interferometric standards, in addition to generally expanding the library to new regions of the parameter space.

Absent from this discussion on the IRFM are cool dwarfs — the most common kind of star in the Galaxy. The development and use of the IFRM, plus other photometric relations, in M and late-K dwarfs ($T_{\rm eff} \lesssim 4\,500$ K) is made challenging by strong molecular absorption in their atmospheres. This absorption is a function of **both** stellar temperature and chemical composition, meaning that photometric colours, the basis for the aforementioned temperature relations, are also a function of both. This is why, for example, the most precise M-dwarf relations in Mann et al. (2015) employed two terms in their empirical temperature relations: one optical colour to parameterise temperature, and either the metallicity (if known) or another near-IR colour to act as its proxy. Further complicating matters is that the location of the 'pseudocontinuum', and thus stellar colours, is not just affected by the bulk metallicity, but also by specific elemental abundances. Veyette et al. (2016) demonstrated that independently changing carbon and oxygen abundances by just ±0.2 dex can result in inferred metallicity ranging over a full order of magnitude (> 1 dex), and that typical metallicity indicators show a strong dependence on the C/O ratio. These limitations, in combination with incomplete line-lists present in current generation libraries of model spectra, mean that it is far from simple to produce accurate cool dwarf temperatures, radii, and *especially* metallicities en masse—let alone individual elemental abundances. While updated line lists of important molecules like TiO seem to improve the situation (McKemmish et al. 2019), there remains a lag between these being initially developed and them becoming widely available in updated models.

My work in Rains et al. (2021) has demonstrated it is possible to use synthetic optical spectra, however flawed, to obtain precise temperatures for these stars by using only reliable wavelength regions in spectroscopic fits, correcting for systematic offsets in synthetic optical broadband photometry, and employing empirical relations to reduce the dimensionality of the problem. This approach isn't a purely model based one, but a hybrid model-empirical methodology, whose accuracy is only as good as the stars it has been benchmarked upon—be they interferometric temperature standards, metallicities from warmer companion stars, or

additional surveys themselves benchmarked on these standards. As stated, however, more than just temperature, radius, and bulk metallicity are required to properly characterise an M dwarf, so more detailed spectroscopic work is necessary to understand the chemistry of our existing benchmarks—particularly for those stars outside the Solar Neighbourhood where Solar trends in abundance cease to hold.

This makes it more important to have a library of cool dwarf standards to compare to, but is made difficult by the small size and inherent faintness of these stars. Interferometric cool dwarf standards are particularly challenging, as there is a very small sample of bright stars that have large enough angular sizes to be targeted by current interferometers—biased towards the brightest, and thus typically warmest, stars. To resolve these small targets, there is no better facility than the CHARA Array when using its optical beam combiner PAVO (Ireland et al. 2008). Early attempts in 2008 and 2009 to undertake a dedicated M dwarf observing program with PAVO were unfortunately put on hold due to insufficient sensitivity and calibration difficulties. Not only have these issues since been resolved, but CHARA has also completed the installation of adaptive optics systems on each of its telescopes, further improving sensitivity. In November 2020 we obtained the first high-SNR optical fringes *ever* of dwarfs with $T_{\rm eff} \lesssim 4,100\,{\rm K}$, using PAVO. This was followed by a further successful April 2021 observing run, which reobserved some targets, and added new ones to the list. Given it took four observing proposals and 6 unsuccessful nights of no data over several years to get to this point, it remains a long–term project to both obtain new precision cool dwarf diameters and validate existing ones.

Understanding elemental abundances of cool dwarfs—rather than just the bulk metallicity—is also important, but requires high-resolution spectra to do so. A number of studies have begun this important work (e.g. Tsuji & Nakajima 2014; Tsuji et al. 2015; Tsuji & Nakajima 2016; Tsuji 2016; Veyette et al. 2016, 2017; Souto et al. 2017, 2018, 2020), but not many so far (e.g. Ishikawa et al. 2020) benchmark using the gold standard of M dwarfs in binary systems with warmer F/G/K companions under the assumption of common chemistry. These systems are typically selected using a combination of parallax, proper motion, and radial velocity to assess whether the stars are in fact bound and common formation and chemistry can be assumed. With the advent of ground-based proper motion surveys like SUPERBLINK (Lépine 2005; Lépine & Gaidos 2011), space-based astronometric missions like *Hipparcos* and *Gaia*, and increasingly more stars with RVs from a variety of sources, the number of such systems known has only increased over the years. *Gaia* specifically is an incredible boon for this style of calibration, as *Gaia* DR3 will provide astrometry, RVs, and high-resolution spectra for all bright systems—available to the entire astronomy community.

Due to the complexity of cool stellar atmospheres—both dwarf and giant—they are often not well handled by the standard data analysis pipelines of large spectroscopic surveys like GALAH, finding their parameters either flagged or ignored entirely (Kos et al. 2017; Buder et al. 2021). GALAH in particular has a library of many thousands of unanalysed cool dwarf and giant spectra with temperatures less than ~4 000 K, ill-suited to their traditional analysis pipeline. Working with Dr Maruša Žerjal and Dr Thomas Nordlander, in July 2020 we obtained a calibration sample of cool dwarf wide-binary pairs as part of a pilot program to develop metallicity and abundance calibrations suitable for the GALAH wavelength bands, and open up analysis of *all* kinds of cool stars. While no analysis has yet begun, these benchmarks will prove

an incredibly powerful tool for unlocking the chemistry of cool stars near and far—something all spectroscopic surveys should consider.

Finally, all of this assumes that such stellar properties remain unchanging on human timescales. Many stars however are active, with magnetic fields and spots that vary over the course of an activity cycle, and these are known to alter the equivalent widths of absorption lines. Spina et al. (2020) observed this effect for 211 Sun-like stars over the course of their activity cycles, and found, for the most active in the sample, that spectroscopic determinations of temperature and metallicity are systematically underestimated. This has implications for studies of stellar associations, and young stars more generally, and likely active cooler dwarfs as well (see work by Lafarga et al. 2021, focused not on stellar parameters, but instead on monitoring various activity measures and the RV jitter of M dwarfs). There is a need to incorporate this knowledge into how we establish benchmarks and plan stellar surveys for stars continue to prove complicated.

5.2.2 Non-Traditional Analysis Techniques

Employing data-driven techniques like the Cannon (Ness et al. 2015) on FunnelWeb data, or on its replacement WiFeS data from the young star (Žerjal et al. 2021) and cool dwarf planet host (Rains et al. 2021) ANU 2.3 m Telescope surveys, was originally planned to be a core focus of the PhD. This was reflected in the planning for all three surveys, which placed emphasis on observing a wide range of benchmarks to enable the development of such techniques. These benchmarks included not only a variety of the aforementioned cool dwarf standards, but also the young spectral type standards (e.g. Herczeg & Hillenbrand 2014), and cool giant standards (e.g. Baines et al. 2018) necessary to work with pre-main sequence stars in the process of contraction.

Unlike the situation for warmer stars, the problem of 'missing labels' posed a key hurdle for a data driven pipeline working on cool dwarfs—and especially *young* cool pre-main sequence 'dwarfs'. Missing labels in this context refers to not having a complete and well-constrained set of stellar parameters, e.g. in $T_{\rm eff}$, $\log g$, and [Fe/H]. Interferometric standards for instance might have precision $T_{\rm eff}$, but [Fe/H] remains difficult to determine in the absence of binary or NIR constraints. On the other hand, cool dwarfs in binary systems might have well constrained chemistry, but their temperatures do not have model-independent constraints. Thus, unlike more 'traditional' Cannon implementations, a more robust method of handling uncertainties would be required to work with cool stars in the optical.

A functional prototype was developed using the probabilistic Stan programming language, called from Python, in late 2019 thanks to the not-insubstantial efforts of Dr Andy Casey at Monash University. Early tests showed promise (with [Fe/H] recovery comparable to the photometric relation from Rains et al. 2021), but the typical quadratic Cannon model struggled to capture the complexity of M-dwarf spectra given the rapid onset of molecular features with cooler temperatures. At the time this was put aside in favour of getting a model-based approach working which, in true research spirit, *also* proved more complex than anticipated leaving the data-driven approach out of scope for Rains et al. (2021).

However, with the investigation in Rains et al. (2021) revealing the troubling extent of model systematics—including the functional uselessness of the WiFeS B3000 spectra in a

model-based approach—the case for developing a functional *optical* data-driven model for cool atmospheres is stronger than ever. Just from the perspective of the two ANU 2.3 m surveys, there are near 1 000 science targets whose spectra have not been fully exploited—and indeed *cannot be* fully exploited with a model-based approach. There are some 180 benchmarks already observed at high-SNR available to calibrate such an algorithm, and it would be revealing to compare to the the *H* band Cannon implementation on M dwarfs in Birky et al. (2020). More importantly however, this would be an important proof of concept for when *Gaia* DR3 releases Radial Velocity Spectrometer (RVS) spectra for what will be *tens of thousands* of cool stars.

Further to this is the aforementioned GALAH pilot study involving F/G/K–K/M benchmark systems and thousands of archival, unanalysed spectra. Given the challenges of model based analysis, a machine learning or data-driven approach might be highly effective at first developing an [Fe/H] calibration applicable for *all* GALAH cool dwarfs. Beyond this however, this calibration could be extended to other abundances, and potentially even propagated to cool giants whose models share similar problems—all calibrated on these benchmark systems.

These are just two problems that will likely benefit from a non-traditional approach. As large surveys continue to produce ever more data, such algorithms will continue to be useful to fill gaps that current generations of models cannot, or help point us in interesting directions. As always though, care must be taken to remember that these algorithms are tools, and it is easy to misuse them. For instance Ting & Weinberg (2021) shows that predicting, rather than measuring, abundances cannot take advantage of—and indeed destroys—small patterns like covariances which could otherwise be exploited. Nonetheless, there remains untapped potential for machine learning or data-driven implementations, with some caveats.

5.2.3 The Future of Bright Ground-Based Stellar Spectroscopic Surveys

The state of stellar spectroscopic surveys is now very different to what it was when FunnelWeb was first proposed in 2011. At that point in time FunnelWeb's goal—spectroscopic stellar parameters and radial velocities for two million of the brightest stars in the Southern Hemisphere—was high-impact from a scientific perspective: competitor spectroscopic surveys were at least 5 years away, *Gaia* had not yet had a data release, and *TESS* had not yet launched. Fast forward to now, where large spectroscopic surveys like *SDSS-V* and *4MOST* are only a few years away from beginning operations, *Gaia* is about to have its third full data release (including spectra for all bright stars), and *TESS* has finished its primary mission. Thus, the science case for a FunnelWeb-style low-resolution survey of all bright stars is much diminished, as the main advantage FunnelWeb had was time.

Gaia DR3 in particular will soon deliver the single largest blow to the relevance of a FunnelWeb-style survey. Unlike previous data releases which released broadband photometry, astrometry, and RVs, *Gaia* DR3 will provide the low and high resolution spectra that are the basis for such photometry and velocities. Although very low-resolution for typical stellar science, *Gaia*'s spectrophotometry will provide the spectral energy distributions of **one billion** stars down to $G \sim 20$ for $330 < \lambda < 1\,040$ nm and in doing so will be able to place strong constrains on stellar $T_{\rm eff}$ and extinction, and to a lesser extent $\log g$ and [Fe/H] (Liu et al. 2012). *Gaia*'s RVS (R∼11 200, Cropper et al. 2018) on the other hand will target the Ca II NIR triplet ($847 < \lambda < 874$ nm) to produce RVs for some 150 million stars, and stellar $T_{\rm eff}$, $\log g$, [M/H],

and [α/Fe] for several 10s of millions of stars. For a further five million sources, even with its limited wavelength coverage, *Gaia* will be able to produce abundances of Fe, Ca, Mg, Ti, and Si at 0.1 dex precision (Recio-Blanco et al. 2016). Beyond a few specific science cases, this renders any need for a FunnelWeb-style magnitude-limited survey of bright stars unnecessary.

However, there remain science cases for which a multiplexed low-resolution spectroscopic survey remains valuable. Such cases capitalise on the ability to *rapidly* and *cheaply* obtain spectra for a large number of stars, with science able to be done even with only modest SNR. For example, Ting et al. (2017) used low–resolution (R~1 800) LAMOST spectra with SNR $\gtrsim$ 30 per spectral pixel to measure 14 elemental abundances to ~0.1 dex precision when using a training sample of ~500 high–SNR stars cross–matched with APOGEE. This demonstrates the utility of easy–to–obtain low–resolution spectra for Galactic archaeology work—commonly thought to be the sole domain of medium–to–high resolution surveys like APOGEE or GALAH.

While every star in FunnelWeb's main survey will have spectra and stellar parameters from *Gaia*, targeting stars fainter than this ($G > 14.5$) with longer exposure times would allow for an effective reconnaissance survey of stars with chemical peculiarities, such as stars with enhanced r or s-process abundances, lithium absorption, EMP stars, or CEMP stars. Currently follow-up of *SkyMapper* candidate extremely metal poor stars is done manually, one star at a time using WiFeS on the ANU 2.3 m Telescope, having observed some several thousand stars over several hundred nights of observing time (Da Costa et al. 2019). With a limiting magnitude of $g \approx 16$, exposure times are long and the survey incredibly inefficient. Due to this, the adopted photometric selection criteria for EMP stars is quite strict, and actively selects against CEMP stars—which appear metal rich with the selection function—as well as dwarf stars. This bottleneck all but disappears with a multiplexed instrument like TAIPAN, which would be able to observe all interesting candidates in a given 6° field in a single pointing and exposure, thus greatly increasingly the chances of finding rare and interesting objects.

Moving to other populations of rare stars with chemical peculiarities, lithium absorption, typically probed by the Li 6 708 Å line, is not accessible to *Gaia*. While this is useful in searching for the very youngest of stars (e.g. Žerjal et al. 2019, 2021), it is also of interest for the study of lithium-rich giants (e.g. Martell et al. 2021)—a rare and poorly understood population of stars who have undergone one of several possible independent methods of lithium enrichment. Planning for FunnelWeb concluded that a modest SNR $\gtrsim$ 50 would be sufficient to measure Li equivalent widths of $\mathrm{EW_{Li}} \gtrsim 0.2$ Å from R~2 000 spectra.

Finally, active stars with photospheric emission in the NIR Ca II triplet region—the location of the *Gaia* RVS spectra—will likely prove difficult for *Gaia* to determine the chemical composition of. These stars would thus benefit from additional spectroscopy in order to constrain their chemistry and to observe additional emission features missed by *Gaia* (e.g. Hα, or Ca II H&K in the blue). Additionally, emission is an inherently time-varying phenomenon, and the short period evolution of which will not be well-captured by *Gaia*'s RVS observational cadence of ~5 – 6 weeks (see Section 5.2 from Gaia Collaboration et al. 2016a for further information about *Gaia*'s scanning law). A FunnelWeb-like stellar survey could prioritise frequent (e.g. at a monthly, weekly, or even nightly cadence) multi-epoch spectroscopic coverage of active targets relatively cheaply—especially compared to activity studies at higher resolution (e.g. with CARMENES, Lafarga et al. 2021), and would complement the multi-epoch photometric observations of upcoming surveys like LSST (Ivezić et al. 2019). Experience observing ac-

tivity measures in Žerjal et al. (2021), while done at higher spectral resolution than TAIPAN, indicates that emission is able to be quantified even at low SNR (e.g. Ca II H&K from spectra with median SNR ≈ 13, and Hα from spectra with median SNR ≈ 31[1]) due to how the emission itself is brighter and thus observed at higher SNR than the surrounding spectrum.

Incidentally, most of these were originally FunnelWeb supplementary surveys to some degree, and the fact that they aren't yet solved problems shows that even a survey as ambitious as *Gaia* will not be sufficient to answer all the outstanding questions of stellar and Galactic astrophysics. While upcoming surveys like SDDS-V (Kollmeier et al. 2017), 4MOST (de Jong et al. 2019), and WEAVE (Dalton et al. 2016) will have both high and low resolution modes, these modes operate from the same telescope and will compete for time, reducing the capacity for the science described here. Thus, there remains a strong need for observations of niche science cases, and small-medium sized telescopes equipped with novel instrumentation are perfect for this.

5.2.4 Exoplanet Demographics Around Low-Mass Stars

Limitations in our understanding of stellar astrophysics are likely a greater impediment to understanding the planets around cool dwarfs than for any other spectral type—which presents an obvious problem given these are the most likely stars to host planets. The key complexity, as has been touched on already, is the difficulty in determining the chemical composition of such stars, which in turn limits our ability to determine accurate temperatures and radii or investigate abundance patterns. Given that we can only know the radius of a transiting planet as well as we do its stellar host, this places a fundamental limit on how well we can know the radii and densities of *most* planets. Thus, for the planet hosts studied here, but also for those already known, greater effort must be devoted to constraining their chemical composition, temperatures, and radii—and how stellar activity affects these parameters.

For the planets themselves, especially those studied here, higher-sensitivity time series photometry is required. *TESS* is a fantastic instrument to initially identify transiting systems, but its sensitivity is far below that of other space missions like *Kepler* and *CHEOPS*[2]. As a result, it is estimated that *TESS* has missed many additional planets belonging to tight multiple systems that lie below its level of detection (Ballard 2019). Assuming stellar parameters are precise, high SNR transit photometry of both known and new transiting planets will have the precision to investigate non-circular orbits or timing effects. For those systems bright or interesting enough, precision radial-velocities will add critical planet mass constraints and allow the determination of exoplanet densities—giving us the greatest insight into these planets until future atmospheric characterisation using next generation telescopes.

All of this benefits the study of exoplanet demographics—better stellar host and planet parameters, as well as a more complete set of planets. Critically though these must be put on a uniform scale in order to account for systematics between different techniques, and the host stars need to be given just as much attention during analysis as the planets themselves. Only then can we confidently investigate planet demographics, such as the location of the exoplanet

[1] Assuming Poisson uncertainties, binning these spectra to a TAIPAN–equivalent spectral resolution increases the SNR values to roughly 16 and 58 respectively.

[2] *TESS* has factors of ~78x and ~9x less collecting area when compared to *Kepler* and *CHEOPS* respectively.

radius gap, its sensitivity to stellar mass, and what information it records about planet formation and evolution.

The exoplanet radius valley was first discovered by Fulton et al. (2017) from a population of *Kepler* planets with host stars having $6\,500 > T_{\rm eff} > 4\,700$ K—i.e. spectral types F/G/K. The population of confirmed or candidate planets around stars of lower mass than this is far lower, and while some studies of the radius gap have included cooler stars (e.g. Hardegree-Ullman et al. 2020), only Cloutier & Menou (2020) has done an analysis *solely* on cool dwarfs ($T_{\rm eff} < 4\,700$ K). Their results, using both *Kepler* and *K2* planets, were the first to find evidence that the radius valley persists around mid-K to mid-M dwarfs, and that the bimodality in the distribution disappears when moving to lower mass stars as the population of rocky planets comes to dominate that of their non-rocky counterparts. One of their main conclusions was that in order to distinguish between the various proposed physical mechanisms sculpting the gap in this stellar mass regime—and how this compares to warmer stars—many more planets are required.

TESS will dramatically improve this situation, with the sample of planets analysed in Rains et al. (2021) representing only a fraction of the southern sample of *TESS* planets. A key implication from this work is that for isolated main sequence cool dwarfs, photometry and distances alone are sufficient—when properly calibrated—to reliably determine the parameters necessary for transit light curve analysis of candidate planets. That is to say that this work can *already* be done—without spectra—on the joint northern and southern *TESS* set of cool dwarfs which, when combined with the existing *Kepler* and *K2* samples, will allow for more in depth demographic studies than have been possible to date.

Beyond generally expanding the sample, further work must be done to investigate the true depth of the gap and what kinds of planets—if any—fill it. While this could involve comprehensive efforts to further reduce planet radius uncertainties to better resolve the gap, perhaps more detailed forward modelling properly taking the existing uncertainties into account would be sufficient. Some of this will require additional chemical constraints like the C/O ratio, which affects the formation of so called 'carbon–rich' or 'diamond' planets (e.g. Kuchner & Seager 2005). Fortney (2012), however, notes that high measured values of C/O for Solar Neighbourhood stars are likely overestimates, and that stars with C/O > 1.0 are rare—thus making 'carbon–rich' planets far more uncommon than originally suspected. Other work involves determining planet densities to place limits on their composition, useful to study the prevalence of lower density planets like 'water worlds' which could more easily fill the radius valley than their rocky counterparts or even populate the second peak of the radius distribution (e.g. Zeng et al. 2019; Venturini et al. 2020). There is clearly still much to learn about planets and their evolution and, to bring it full circle, our knowledge of planet properties remains limited by how well we understand their stellar hosts—particularly for cool dwarfs.

5.3 Final Remarks

Stellar and exoplanetary astrophysics is now, and will continue to be, rich in both data and potential. Much of these data are or will be publicly available, as are catalogues of benchmark stars, ever more reliable stellar models, and many libraries of helpful open–source software. On top of this, there remains machine learning and statistics knowledge that has not yet made

its way to our metaphorical astrophysical shores—if only we could make smart use of it.

It's both a good and interesting time to be working in these fields and making the connections between them stronger. Perhaps most importantly though, there remain a great many questions to be answered, key among them being:

1. How severe are the issues with existing main sequence interferometric benchmarks, and how much effort is required to unify and expand this library?
2. What is the ultimate precision of cool dwarf stellar properties determined from photometry and distances alone, and how does stellar rotation affect this precision?
3. What insights into Galactic chemical or dynamical structure will be revealed by having a better understanding of the chemistry of cool stars both dwarf and giant?
4. How deep is the exoplanet radius gap and what planets, if any, fill it?

While the future will hopefully bring us answers, it will also inevitably deliver us new questions. Our understanding of astrophysics has a ways to go yet, but I can only hope I've helped in some small way here.

Bibliography

Abolfathi B., et al., 2018, The Astrophysical Journal Supplement Series, 235, 42

Allard F., Hauschildt P. H., Alexander D. R., Starrfield S., 1997, Annual Review of Astronomy and Astrophysics, 35, 137

Allard F., Homeier D., Freytag B., 2011, in ASP Conference Series. p. 91, http://adsabs.harvard.edu/abs/2011ASPC..448...91A

Allard F., Homeier D., Freytag B., Sharp C. M., 2012a, in EAS Publications Series. Roscoff, France, pp 3–43, doi:10.1051/eas/1257001, http://adsabs.harvard.edu/abs/2012EAS....57....3A

Allard F., Homeier D., Freytag B., 2012b, Philosophical Transactions of the Royal Society of London Series A, 370, 2765

Allende Prieto C., 2016, Living Reviews in Solar Physics, 13, 1

Allende Prieto C., López R. J. G., Lambert D. L., Gustafsson B., 1999, The Astrophysical Journal, 527, 879

Allende Prieto C., Barklem P. S., Lambert D. L., Cunha K., 2004, Astronomy and Astrophysics, 420, 183

Allende Prieto C., Beers T. C., Wilhelm R., Newberg H. J., Rockosi C. M., Yanny B., Lee Y. S., 2006, The Astrophysical Journal, 636, 804

Allende Prieto C., et al., 2008, Astronomische Nachrichten, 329, 1018

Aller L. H., et al., 1982. p. 54, http://adsabs.harvard.edu/abs/1982lbg6.conf.....A

Alonso A., Arribas S., Martinez-Roger C., 1996, Astronomy and Astrophysics, 313, 873

Alvarez R., Plez B., 1998, Astronomy and Astrophysics, 330, 1109

Alves S., et al., 2015, Monthly Notices of the Royal Astronomical Society, 448, 2749

Amarsi A. M., 2016, PhD Thesis, Australian National University, Canberra, ACT, Australia, https://openresearch-repository.anu.edu.au/handle/1885/114541

Andersen J., 1991, Astronomy and Astrophysics Review, 3, 91

Anderson J. A., 1920, The Astrophysical Journal, 51, 263

Andrae R., et al., 2018, Astronomy & Astrophysics, 616, A8

Arnett W. D., Meakin C., Viallet M., Campbell S. W., Lattanzio J. C., Mocák M., 2015, The Astrophysical Journal, 809, 30

Asplund M., 2005, Annual Review of Astronomy and Astrophysics, 43, 481

Asplund M., Nordlund Å., Trampedach R., Allende Prieto C., Stein R. F., 2000, Astronomy and Astrophysics, 359, 729

Asplund M., Grevesse N., Sauval A. J., Scott P., 2009, Annual Review of Astronomy and Astrophysics, 47, 481

Astropy Collaboration et al., 2013, Astronomy and Astrophysics, 558, A33

Auvergne M., et al., 2009, Astronomy & Astrophysics, 506, 411

Bailer-Jones C. A. L., 2000, Astronomy and Astrophysics, 357, 197

Bailer-Jones C. A. L., Irwin M., Von Hippel T., 1998, Monthly Notices of the Royal Astronomical Society, 298, 361

Baines E. K., Armstrong J. T., 2011, The Astrophysical Journal, 744, 138

Baines E. K., McAlister H. A., ten Brummelaar T. A., Turner N. H., Sturmann J., Sturmann L., Goldfinger P. J., Ridgway S. T., 2008, The Astrophysical Journal, 680, 728

Baines E. K., McAlister H. A., ten Brummelaar T. A., Sturmann J., Sturmann L., Turner N. H., Ridgway S. T., 2009, The Astrophysical Journal, 701, 154

Baines E. K., Armstrong J. T., Schmitt H. R., Zavala R. T., Benson J. A., Hutter D. J., Tycner C., Belle G. T. v., 2018, The Astronomical Journal, 155, 30

Bakos G., Noyes R. W., Kovács G., Stanek K. Z., Sasselov D. D., Domsa I., 2004, Publications of the Astronomical Society of the Pacific, 116, 266

Bakos G. Á., et al., 2013, Publications of the Astronomical Society of the Pacific, 125, 154

Baliunas S. L., et al., 1995, The Astrophysical Journal, 438, 269

Ball N. M., Brunner R. J., 2010, International Journal of Modern Physics D, 19, 1049

Ballard S., 2019, The Astronomical Journal, 157, 113

Baraffe I., Chabrier G., Allard F., Hauschildt P. H., 1997, Astronomy and Astrophysics, 327, 1054

Baraffe I., Chabrier G., Allard F., Hauschildt P. H., 1998, Astronomy and Astrophysics, 337, 403

Baraffe I., Homeier D., Allard F., Chabrier G., 2015, Astronomy and Astrophysics, 577, A42

Baranne A., et al., 1996, Astronomy and Astrophysics Supplement Series, 119, 373

Barklem P. S., Stempels H. C., Prieto C. A., Kochukhov O. P., Piskunov N., O'Mara B. J., 2002, Astronomy & Astrophysics, 385, 951

Barnes S. A., 2007, The Astrophysical Journal, 669, 1167

Barnes S. A., 2009, in Proceedings of the International Astronomical Union. pp 345–356, doi:10.1017/S1743921309032001, http://adsabs.harvard.edu/abs/2009IAUS..258..345B

Barnes T. G., Evans D. S., 1976, Monthly Notices of the Royal Astronomical Society, 174, 489

Bastian N., Covey K. R., Meyer M. R., 2010, Annual Review of Astronomy and Astrophysics, 48, 339

Bayliss D., et al., 2018, Monthly Notices of the Royal Astronomical Society, 475, 4467

Bean J. L., Sneden C., Hauschildt P. H., Johns-Krull C. M., Benedict G. F., 2006a, The Astrophysical Journal, 652, 1604

Bean J. L., Benedict G. F., Endl M., 2006b, The Astrophysical Journal Letters, 653, L65

Bedding T. R., et al., 2011, Nature, 471, 608

Behmard A., Petigura E. A., Howard A. W., 2019, The Astrophysical Journal, 876, 68

Behr B. B., Cenko A. T., Hajian A. R., McMillan R. S., Murison M., Meade J., Hindsley R., 2011, The Astronomical Journal, 142, 6

Bell R. A., Gustafsson B., 1989, Monthly Notices of the Royal Astronomical Society, 236, 653

Bell R. A., Edvardsson B., Gustafsson B., 1985, Monthly Notices of the Royal Astronomical Society, 212, 497

Belokurov V., Erkal D., Evans N. W., Koposov S. E., Deason A. J., 2018, Monthly Notices of the Royal Astronomical Society, 478, 611

Benedict G. F., et al., 2016, The Astronomical Journal, 152, 141

Bensby T., Feltzing S., Lundström I., 2003, Astronomy & Astrophysics, 410, 527

Bensby T., Feltzing S., Oey M. S., 2014, Astronomy and Astrophysics, 562, A71

Bergemann M., Lind K., Collet R., Magic Z., Asplund M., 2012, Monthly Notices of the Royal Astronomical Society, 427, 27

Bergemann M., et al., 2016, Astronomy and Astrophysics, 594, A120

Berger D. H., et al., 2006, The Astrophysical Journal, 644, 475

Berger T. A., Huber D., van Saders J. L., Gaidos E., Tayar J., Kraus A. L., 2020, The Astronomical Journal, 159, 280

Bessell M. S., 2000, Publications of the Astronomical Society of the Pacific, 112, 961

Bessell M. S., Castelli F., Plez B., 1998, Astronomy and Astrophysics, 333, 231

Birky J., Hogg D. W., Mann A. W., Burgasser A., 2020, The Astrophysical Journal, 892, 31

Blackwell D. E., Lynas-Gray A. E., 1998, Astronomy and Astrophysics Supplement Series, 129, 505

Blackwell D. E., Shallis M. J., 1977, Monthly Notices of the Royal Astronomical Society, 180, 177

Blackwell D. E., Willis R. B., 1977, Monthly Notices of the Royal Astronomical Society, 180, 169

Blackwell D. E., Shallis M. J., Selby M. J., 1979, Monthly Notices of the Royal Astronomical Society, 188, 847

Blackwell D. E., Petford A. D., Shallis M. J., 1980, Astronomy and Astrophysics, 82, 249

Blanco-Cuaresma S., Soubiran C., Jofré P., Heiter U., 2014a, Astronomy and Astrophysics, 566, A98

Blanco-Cuaresma S., Soubiran C., Heiter U., Jofré P., 2014b, Astronomy & Astrophysics, 569, A111

Boden A. F., Creech-Eakman M. J., Queloz D., 2000, The Astrophysical Journal, 536, 880

Boden A. F., Torres G., Hummel C. A., 2005, The Astrophysical Journal, 627, 464

Bohlin R. C., 2007, in Astronomical Society of the Pacific Conference Series. Blankenberge, Belgium, p. 315, http://adsabs.harvard.edu/abs/2007ASPC..364..315B

Böhm-Vitense E., 1958, Zeitschrift fur Astrophysik, 46, 108

Bonfils X., Delfosse X., Udry S., Santos N. C., Forveille T., Ségransan D., 2005, Astronomy and Astrophysics, 442, 635

Bonneau D., et al., 2006, Astronomy and Astrophysics, 456, 789

Bonneau D., Delfosse X., Mourard D., Lafrasse S., Mella G., Cetre S., Clausse J.-M., Zins G., 2011, Astronomy and Astrophysics, 535, A53

Borucki W. J., et al., 2010, Science, 327, 977

Bouquin J.-B. L., et al., 2011, Astronomy & Astrophysics, 535, A67

Boyajian T. S., et al., 2012a, The Astrophysical Journal, 746, 101

Boyajian T. S., et al., 2012b, The Astrophysical Journal, 757, 112

Boyajian T. S., et al., 2013, The Astrophysical Journal, 771, 40

Boyajian T. S., van Belle G., von Braun K., 2014, The Astronomical Journal, 147, 47

Brasseur C. M., Stetson P. B., VandenBerg D. A., Casagrande L., Bono G., Dall'Ora M., 2010, The Astronomical Journal, 140, 1672

Bressan A., Marigo P., Girardi L., Salasnich B., Dal Cero C., Rubele S., Nanni A., 2012, Monthly Notices of the Royal Astronomical Society, 427, 127

Brewer J. M., Fischer D. A., Basu S., Valenti J. A., Piskunov N., 2015, The Astrophysical Journal, 805, 126

Brown T. M., Gilliland R. L., 1994, Annual Review of Astronomy and Astrophysics, 32, 37

Brown A. G. A., et al., 2018, Astronomy & Astrophysics, 616, A1

Brown A. G. A., et al., 2021, Astronomy & Astrophysics, 649, A1

Buder S., et al., 2018, Monthly Notices of the Royal Astronomical Society, 478, 4513

Buder S., et al., 2021, Monthly Notices of the Royal Astronomical Society

Burke C. J., Pinsonneault M. H., Sills A., 2004, The Astrophysical Journal, 604, 272

Caffau E., Ludwig H.-G., Steffen M., Freytag B., Bonifacio P., 2011, Solar Physics, 268, 255

Campbell L., Saunders W., Colless M., 2004, Monthly Notices of the Royal Astronomical Society, 350, 1467

Cannon A. J., Pickering E. C., 1918, Annals of Harvard College Observatory, 91, 1

Cantat-Gaudin T., et al., 2018, Astronomy & Astrophysics, 618, A93

Cardelli J. A., Clayton G. C., Mathis J. S., 1989, The Astrophysical Journal, 345, 245

Cardini D., Cassatella A., 2007, The Astrophysical Journal, 666, 393

Carrillo A., Hawkins K., Bowler B. P., Cochran W., Vanderburg A., 2020, Monthly Notices of the Royal Astronomical Society, 491, 4365

Casagrande L., VandenBerg D. A., 2014, Monthly Notices of the Royal Astronomical Society, 444, 392

Casagrande L., VandenBerg D. A., 2018a, Monthly Notices of the Royal Astronomical Society, 475, 5023

Casagrande L., VandenBerg D. A., 2018b, Monthly Notices of the Royal Astronomical Society, 479, L102

Casagrande L., Portinari L., Flynn C., 2006, Monthly Notices of the Royal Astronomical Society, 373, 13

Casagrande L., Ramírez I., Meléndez J., Bessell M., Asplund M., 2010, Astronomy and Astrophysics, 512, A54

Casagrande L., Schönrich R., Asplund M., Cassisi S., Ramírez I., Meléndez J., Bensby T., Feltzing S., 2011, Astronomy and Astrophysics, 530, A138

Casagrande L., et al., 2014, Monthly Notices of the Royal Astronomical Society, 439, 2060

Casagrande L., Wolf C., Mackey A. D., Nordlander T., Yong D., Bessell M., 2019, Monthly Notices of the Royal Astronomical Society, 482, 2770

Casagrande L., et al., 2020, arXiv:2011.02517 [astro-ph]

Cassan A., et al., 2012, Nature, 481, 167

Castelli F., Kurucz R. L., 2003, in Proceedings of the IAU Symp. No 210; IAU Symp. No 210, Modelling of Stellar Atmospheres. p. A20, http://adsabs.harvard.edu/abs/2003IAUS..210P.A20C

Chabrier G., 2003, Publications of the Astronomical Society of the Pacific, 115, 763

Chabrier G., Baraffe I., 2000, Annual Review of Astronomy and Astrophysics, 38, 337

Chabrier G., Baraffe I., Plez B., 1996, The Astrophysical Journal Letters, 459, L91

Chambers K. C., et al., 2016, arXiv:1612.05560 [astro-ph]

Chaplin W. J., Miglio A., 2013, Annual Review of Astronomy and Astrophysics, 51, 353

Chen Y., Girardi L., Bressan A., Marigo P., Barbieri M., Kong X., 2014, Monthly Notices of the Royal Astronomical Society, 444, 2525

Childress M. J., Vogt F. P. A., Nielsen J., Sharp R. G., 2014, Astrophysics and Space Science, 349, 617

Choi J., Dotter A., Conroy C., Cantiello M., Paxton B., Johnson B. D., 2016, The Astrophysical Journal, 823, 102

Christensen-Dalsgaard J., 1984, in Proceedings of Space Research Prospects in Stellar Activity and Variability. Meudon, France, p. 11, http://adsabs.harvard.edu/abs/1984srps.conf...11C

Christensen-Dalsgaard J., 2002, Reviews of Modern Physics, 74, 1073

Christensen-Dalsgaard J., 2004, in Proceedings of the SOHO 14 / GONG 2004 Workshop (ESA SP-559). New Haven, Connecticut, p. 1, http://adsabs.harvard.edu/abs/2004ESASP.559....1C

Chung S.-J., et al., 2017, The Astrophysical Journal, 838, 154

Claret A., 2000, Astronomy and Astrophysics, 363, 1081

Claret A., 2017, Astronomy and Astrophysics, 600, A30

Claret A., Bloemen S., 2011, Astronomy and Astrophysics, 529, A75

Cloutier R., Menou K., 2020, The Astronomical Journal, 159, 211

Code A. D., Bless R. C., Davis J., Brown R. H., 1976, The Astrophysical Journal, 203, 417

Cowan J. J., Thielemann F.-K., Truran J. W., 1991, Annual Review of Astronomy and Astrophysics, 29, 447

Cox J. P., 1980, Theory of Stellar Pulsation. Princeton Series in Astrophysics, Princeton University Press

Cropper M., et al., 2018, Astronomy and Astrophysics, 616, A5

Crundall T. D., Ireland M. J., Krumholz M. R., Federrath C., Žerjal M., Hansen J. T., 2019, Monthly Notices of the Royal Astronomical Society, 489, 3625

Cui X.-Q., et al., 2012, Research in Astronomy and Astrophysics, 12, 1197

Cushing M. C., et al., 2011, The Astrophysical Journal, 743, 50

Cutri R. M., et al. 2013, VizieR Online Data Catalog, 2328

Czekala I., Andrews S. M., Jensen E. L. N., Stassun K. G., Torres G., Wilner D. J., 2015, The Astrophysical Journal, 806, 154

Czekala I., Andrews S. M., Torres G., Jensen E. L. N., Stassun K. G., Wilner D. J., Latham D. W., 2016, The Astrophysical Journal, 818, 156

Czekala I., et al., 2017, The Astrophysical Journal, 851, 132

Da Costa G. S., et al., 2019, Monthly Notices of the Royal Astronomical Society, 489, 5900

Dalton G., et al., 2016, in Ground-based and Airborne Instrumentation for Astronomy VI. International Society for Optics and Photonics, p. 99081G, doi:10.1117/12.2231078, https://www.spiedigitallibrary.org/conference-proceedings-of-spie/9908/99081G/Final-design-and-progress-of-WEAVE--the-next-generation/10.1117/12.2231078.short

Daniel S. F., Connolly A., Schneider J., Vanderplas J., Xiong L., 2011, The Astronomical Journal, 142, 203

David T. J., et al., 2016, Nature, 534, 658

Davis J., Tango W. J., Booth A. J., ten Brummelaar T. A., Minard R. A., Owens S. M., 1999, Monthly Notices of the Royal Astronomical Society, 303, 773

De Cat P., et al., 2015, The Astrophysical Journal Supplement Series, 220, 19

De Silva G. M., et al., 2015, Monthly Notices of the Royal Astronomical Society, 449, 2604

Delfosse X., Forveille T., Ségransan D., Beuzit J.-L., Udry S., Perrier C., Mayor M., 2000, Astronomy and Astrophysics, 364, 217

Delgado Mena E., Tsantaki M., Adibekyan V. Z., Sousa S. G., Santos N. C., González Hernández J. I., Israelian G., 2017, Astronomy and Astrophysics, 606, A94

Demarque P., Woo J.-H., Kim Y.-C., Yi S. K., 2004, The Astrophysical Journal Supplement Series, 155, 667

Demory B.-O., et al., 2009, Astronomy and Astrophysics, 505, 205

Desidera S., et al., 2004, Astronomy and Astrophysics, 420, 683

Di Folco E., Thévenin F., Kervella P., Domiciano de Souza A., Coudé du Foresto V., Ségransan D., Morel P., 2004, Astronomy and Astrophysics, 426, 601

Dittmann J. A., Irwin J. M., Charbonneau D., Newton E. R., 2016, The Astrophysical Journal, 818, 153

Donati J.-F., Landstreet J., 2009, Annual Review of Astronomy and Astrophysics, 47, 333

Dopita M., Hart J., McGregor P., Oates P., Bloxham G., Jones D., 2007, Astrophysics and Space Science, 310, 255

Dotter A., 2016, The Astrophysical Journal Supplement Series, 222, 8

Dotter A., Chaboyer B., Jevremović D., Kostov V., Baron E., Ferguson J. W., 2008, The Astrophysical Journal Supplement Series, 178, 89

Doyle L. R., et al., 2011, Science, 333, 1602

Dravins D., Nordlund A., 1990, Astronomy and Astrophysics, 228, 184

Dravins D., Lindegren L., Nordlund A., 1981, Astronomy and Astrophysics, 96, 345

Dreizler S., et al., 2020, Astronomy & Astrophysics, 644, A127

Dressing C. D., Charbonneau D., 2013, The Astrophysical Journal, 767, 95

Dressing C. D., Charbonneau D., 2015, The Astrophysical Journal, 807, 45

Dressing C. D., et al., 2019, The Astronomical Journal, 158, 87

Dupuy T. J., Liu M. C., Ireland M. J., 2009, The Astrophysical Journal, 699, 168

ESA 1997, The HIPPARCOS and TYCHO catalogues. Astrometric and photometric star catalogues derived from the ESA HIPPARCOS Space Astrometry Mission. ESA Special Publication Vol. 1200

Eddington A. S., 1930, The Internal Constitution of the Stars. Cambridge University Press

Edvardsson B., Andersen J., Gustafsson B., Lambert D. L., Nissen P. E., Tomkin J., 1993, Astronomy and Astrophysics, 275, 101

Eisenhauer F., et al., 2011, The Messenger, 143, 16

Erspamer D., North P., 2003, Astronomy & Astrophysics, 398, 1121

Esposito M., et al., 2017, Astronomy and Astrophysics, 601, A53

Evans D. W., et al., 2018, Astronomy and Astrophysics, 616, A4

Feiden G. A., 2015, in Rucinski S. M., Torres G., Zejda M., eds, Astronomical Society of the Pacific Conference Series Vol. 496, Proceedings of Living Together: Planets, Host Stars and Binaries. Litomyšl, Czech Republic, p. 137

Feiden G. A., 2016, Astronomy & Astrophysics, 593, A99

Feiden G. A., Chaboyer B., 2012, The Astrophysical Journal, 757, 42

Fernández D., Figueras F., Torra J., 2008, Astronomy & Astrophysics, 480, 735

Fernando N., Bacigalupo C., Farrell T., Lorente N., 2020, in Advances in Optical Astronomical Instrumentation 2019. International Society for Optics and Photonics, p. 1120316, doi:10.1117/12.2541296, https://www.spiedigitallibrary.org/conference-proceedings-of-spie/11203/1120316/Steering-Starbugs-routing-autonomous-fibre-positioners-for-TAIPAN/10.1117/12.2541296.short

Fischer D. A., Valenti J., 2005, The Astrophysical Journal, 622, 1102

Flores M., González J. F., Arancibia M. J., Buccino A., Saffe C., 2016, Astronomy & Astrophysics, 589, A135

Fortney J. J., 2012, The Astrophysical Journal, 747, L27

Fouque P., Gieren W. P., 1997, Astronomy and Astrophysics, 320, 799

Fressin F., et al., 2013, The Astrophysical Journal, 766, 81

Fritz T. K., et al., 2011, The Astrophysical Journal, 737, 73

Fuhrmann K., 1998, Astronomy and Astrophysics, 338, 161

Fuhrmann K., 2008, Monthly Notices of the Royal Astronomical Society, 384, 173

Fuhrmann K., Chini R., Kaderhandt L., Chen Z., 2017, The Astrophysical Journal, 836, 139

Fulton B. J., Petigura E. A., 2018, The Astronomical Journal, 156, 264

Fulton B. J., et al., 2017, The Astronomical Journal, 154, 109

Gagné J., Faherty J. K., 2018, The Astrophysical Journal, 862, 138

Gagné J., et al., 2018, The Astrophysical Journal, 856, 23

Gaia Collaboration et al., 2016a, Astronomy and Astrophysics, 595, A1

Gaia Collaboration et al., 2016b, Astronomy and Astrophysics, 595, A2

Gaidos E., et al., 2014, Monthly Notices of the Royal Astronomical Society, 443, 2561

Galland F., Lagrange A.-M., Udry S., Chelli A., Pepe F., Queloz D., Beuzit J.-L., Mayor M., 2005, Astronomy & Astrophysics, 443, 337

Gallenne A., et al., 2016, Astronomy and Astrophysics, 586, A35

Gallenne A., et al., 2018, Astronomy & Astrophysics, 616, A68

Gallenne A., et al., 2019, Astronomy and Astrophysics, 622, A164

García R. A., Ballot J., 2019, Living Reviews in Solar Physics, 16, 4

Gilbert J., et al., 2012, in Modern Technologies in Space- and Ground-based Telescopes and Instrumentation II. International Society for Optics and Photonics, p. 84501A, doi:10.1117/12.924502, https://www.spiedigitallibrary.org/conference-proceedings-of-spie/8450/84501A/Starbugs-all-singing-all-dancing-fibre-positioning-robots/10.1117/12.924502.short

Gilbert E. A., et al., 2020, The Astronomical Journal, 160, 116

Gillon M., et al., 2017, Nature, 542, 456

Gilmore G., et al., 2012, The Messenger, 147, 25

Ginzburg S., Schlichting H. E., Sari R., 2018, Monthly Notices of the Royal Astronomical Society, 476, 759

González Hernández J. I., Bonifacio P., 2009, Astronomy & Astrophysics, 497, 497

Goodwin M., et al., 2012, in Ground-based and Airborne Instrumentation for Astronomy IV. International Society for Optics and Photonics, p. 84467I, doi:10.1117/12.925125, https://www.spiedigitallibrary.org/conference-proceedings-of-spie/8446/84467I/MANIFEST-instrument-concept-and-related-technologies/10.1117/12.925125.short

Gray D. F., 1994, Publications of the Astronomical Society of the Pacific, 106, 1248

Gray D. F., Johanson H. L., 1991, Publications of the Astronomical Society of the Pacific, 103, 439

Gray R. O., Corbally C. J., Garrison R. F., McFadden M. T., Robinson P. E., 2003, The Astronomical Journal, 126, 2048

Gray R. O., Corbally C. J., Garrison R. F., McFadden M. T., Bubar E. J., McGahee C. E., O'Donoghue A. A., Knox E. R., 2006, The Astronomical Journal, 132, 161

Green G. M., 2018, The Journal of Open Source Software, 3, 695

Green G. M., et al., 2015, The Astrophysical Journal, 810, 25

Green G. M., et al., 2018, Monthly Notices of the Royal Astronomical Society, 478, 651

Green G. M., Schlafly E., Zucker C., Speagle J. S., Finkbeiner D., 2019, The Astrophysical Journal, 887, 93

Groenewegen M. a. T., 2007, Astronomy & Astrophysics, 474, 975

Güdel M., Guinan E. F., Skinner S. L., 1997, The Astrophysical Journal, 483, 947

Guerrero N. M., et al., 2021, The Astrophysical Journal Supplement Series, 254, 39

Gulati R. K., Gupta R., Gothoskar P., Khobragade S., 1994, The Astrophysical Journal, 426, 340

Günther M. N., et al., 2019, Nature Astronomy, 3, 1099

Gupta A., Schlichting H. E., 2019, Monthly Notices of the Royal Astronomical Society, 487, 24

Gupta A., Schlichting H. E., 2020, Monthly Notices of the Royal Astronomical Society, 493, 792

Gustafsson B., Jørgensen U. G., 1994, The Astronomy and Astrophysics Review, 6, 19

Gustafsson B., Edvardsson B., Eriksson K., Jørgensen U. G., Nordlund Å., Plez B., 2008, Astronomy and Astrophysics, 486, 951

Haguenauer P., et al., 2010, in Optical and Infrared Interferometry II. International Society for Optics and Photonics, p. 773404, doi:10.1117/12.857070, https://www.spiedigitallibrary.org/conference-proceedings-of-spie/7734/773404/The-very-large-telescope-Interferometer-2010-edition/10.1117/12.857070.short

Hanbury Brown R., Davis J., Lake R. J. W., Thompson R. J., 1974, Monthly Notices of the Royal Astronomical Society, 167, 475

Hansen J. T., Casagrande L., Ireland M. J., Lin J., 2021, Monthly Notices of the Royal Astronomical Society, 501, 5309

Hardegree-Ullman K. K., Cushing M. C., Muirhead P. S., Christiansen J. L., 2019, The Astronomical Journal, 158, 75

Hardegree-Ullman K. K., Zink J. K., Christiansen J. L., Dressing C. D., Ciardi D. R., Schlieder J. E., 2020, The Astrophysical Journal Supplement Series, 247, 28

Harris C. R., et al., 2020, Nature, 585, 357

Hartkopf W. I., Mason B. D., Worley C. E., 2001, The Astronomical Journal, 122, 3472

Hartman J. D., et al., 2015, The Astronomical Journal, 149, 166

Hartman J. D., et al., 2020, The Astronomical Journal, 159, 173

Hawkins K., et al., 2020, Monthly Notices of the Royal Astronomical Society, 492, 1164

Hayashi C., 1961, Publications of the Astronomical Society of Japan, 13, 450

Haywood R. D., et al., 2014, International Journal of Astrobiology, 13, 155

Haywood M., Di Matteo P., Lehnert M. D., Snaith O., Khoperskov S., Gómez A., 2018, The Astrophysical Journal, 863, 113

Heiter U., Eriksson K., 2006, Astronomy & Astrophysics, 452, 1039

Heiter U., Soubiran C., Netopil M., Paunzen E., 2014, Astronomy & Astrophysics, 561, A93

Heiter U., Jofré P., Gustafsson B., Korn A. J., Soubiran C., Thévenin F., 2015, Astronomy and Astrophysics, 582, A49

Hejazi N., De Robertis M. M., Dawson P. C., 2015, The Astronomical Journal, 149, 140

Hekker S., Christensen-Dalsgaard J., 2017, The Astronomy and Astrophysics Review, 25, 1

Hekker S., Meléndez J., 2007, Astronomy and Astrophysics, 475, 1003

Helmi A., Babusiaux C., Koppelman H. H., Massari D., Veljanoski J., Brown A. G. A., 2018, Nature, 563, 85

Henry T. J., McCarthy Jr. D. W., 1993, The Astronomical Journal, 106, 773

Henry T. J., Kirkpatrick J. D., Simons D. A., 1994, The Astronomical Journal, 108, 1437

Henry T. J., Jao W.-C., Subasavage J. P., Beaulieu T. D., Ianna P. A., Costa E., Méndez R. A., 2006, The Astronomical Journal, 132, 2360

Henry T. J., et al., 2018, The Astronomical Journal, 155, 265

Henyey L. G., Lelevier R., Levée R. D., 1955, Publications of the Astronomical Society of the Pacific, 67, 154

Herbig G. H., 1985, The Astrophysical Journal, 289, 269

Herczeg G. J., Hillenbrand L. A., 2014, The Astrophysical Journal, 786, 97

Hindsley R. B., Bell R. A., 1989, The Astrophysical Journal, 341, 1004

Hinkel N. R., et al., 2016, The Astrophysical Journal Supplement Series, 226, 4

Ho A. Y. Q., Ness M., Hogg D. W., Rix H.-W., 2016, The Cannon: Data-driven method for determining stellar parameters and abundances from stellar spectra, http://adsabs.harvard.edu/abs/2016ascl.soft02010H

Ho A. Y. Q., et al., 2017, The Astrophysical Journal, 836, 5

Hoeijmakers H. J., Kok R. J. d., Snellen I. a. G., Brogi M., Birkby J. L., Schwarz H., 2015, Astronomy & Astrophysics, 575, A20

Høg E., et al., 2000, Astronomy and Astrophysics, 355, L27

Hon M., Stello D., Yu J., 2018, Monthly Notices of the Royal Astronomical Society, 476, 3233

Hotelling H., 1936, Biometrika, 28, 321

Houdashelt M. L., Bell R. A., Sweigart A. V., 2000, The Astronomical Journal, 119, 1448

Houk N., 1978, Michigan catalogue of two-dimensional spectral types for the HD stars. Michigan Catalogue of Two-dimensional Spectral Types for the HD stars. Vol. 2, Ann Arbor, MI (USA): Department of Astronomy, University of Michigan, http://adsabs.harvard.edu/abs/1978mcts.book.....H

Houk N., 1982, Michigan Catalogue of Two-dimensional Spectral Types for the HD stars. Volume_3. Declinations -40_?0 to -26_?0.. Michigan Catalogue of Two-dimensional Spectral Types for the HD stars Vol. 3, Ann Arbor, MI (USA): Department of Astronomy, University of Michigan, http://adsabs.harvard.edu/abs/1982mcts.book.....H

Houk N., Cowley A. P., 1975, University of Michigan Catalogue of two-dimensional spectral types for the HD stars. Volume I. Declinations -90_ to -53_?0.. Michigan Catalogue of Two-dimensional Spectral Types for the HD stars Vol. 1, Ann Arbor, MI (USA): Department of Astronomy, University of Michigan, http://adsabs.harvard.edu/abs/1975mcts.book.....H

Houk N., Smith-Moore M., 1988, Michigan Catalogue of Two-dimensional Spectral Types for the HD Stars. Volume 4, Declinations -26°.0 to -12°.0.. Michigan Catalogue of Two-dimensional Spectral Types for the HD stars Vol. 4, Ann Arbor, MI (USA): Department of Astronomy, University of Michigan, http://adsabs.harvard.edu/abs/1988mcts.book.....H

Howard A. W., et al., 2012, The Astrophysical Journal Supplement Series, 201, 15

Howell S. B., et al., 2014, Publications of the Astronomical Society of the Pacific, 126, 398

Hsu D. C., Ford E. B., Ragozzine D., Ashby K., 2019, The Astronomical Journal, 158, 109

Hsu D. C., Ford E. B., Terrien R., 2020, Monthly Notices of the Royal Astronomical Society, 498, 2249

Huang C. X., et al., 2020, The Astrophysical Journal, 892, L7

Hubeny I., Mihalas D., 2014, Theory of stellar atmospheres: An introduction to astrophysical non-equilibrium quantitative spectroscopic analysis. Princeton University Press, https://arizona.pure.elsevier.com/en/publications/theory-of-stellar-atmospheres-an-introduction-to-astrophysical-no

Huber D., et al., 2012, The Astrophysical Journal, 760, 32

Hunter J. D., 2007, Computing in Science Engineering, 9, 90

Husser T.-O., Wende-von Berg S., Dreizler S., Homeier D., Reiners A., Barman T., Hauschildt P. H., 2013, Astronomy and Astrophysics, 553, A6

Ikoma M., Hori Y., 2012, The Astrophysical Journal, 753, 66

Ireland M. J., et al., 2008, in Optical and Infrared Interferometry. International Society for Optics and Photonics, p. 701324, doi:10.1117/12.788386, https://www.spiedigitallibrary.org/conference-proceedings-of-spie/7013/701324/Sensitive-visible-interferometry-with-PAVO/10.1117/12.788386.short

Irwin J., Bouvier J., 2009, in The Ages of Stars. Baltimore, MD, USA, pp 363–374, doi:10.1017/S1743921309032025, http://adsabs.harvard.edu/abs/2009IAUS..258..363I

Irwin J., Charbonneau D., Nutzman P., Falco E., 2008, Proceedings of the International Astronomical Union, 4, 37

Ishikawa H. T., Aoki W., Kotani T., Kuzuhara M., Omiya M., Reiners A., Zechmeister M., 2020, Publications of the Astronomical Society of Japan, 72, 102

Ivezić Ž., et al., 2019, The Astrophysical Journal, 873, 111

Jacoby G. H., Hunter D. A., Christian C. A., 1984, The Astrophysical Journal Supplement Series, 56, 257

Jehin E., et al., 2011, The Messenger, 145, 2

Jenkins J. S., et al., 2011, Astronomy and Astrophysics, 531, A8

Jewitt D., Luu J., 2019, The Astrophysical Journal, 886, L29

Jofré P., et al., 2017, Astronomy & Astrophysics, 601, A38

Jofré P., Heiter U., Soubiran C., 2019, Annual Review of Astronomy and Astrophysics, 57, 571

Johnson J. A., Apps K., 2009, The Astrophysical Journal, 699, 933

Johnson J. A., Aller K. M., Howard A. W., Crepp J. R., 2010, Publications of the Astronomical Society of the Pacific, 122, 905

Johnson J. A., et al., 2017, The Astronomical Journal, 154, 108

Jolliffe I. T., 2002, Principal Component Analysis, 2 edn. Springer Series in Statistics, Springer-Verlag, New York, doi:10.1007/b98835, https://www.springer.com/gp/book/9780387954424

Jones D. H., et al., 2004, Monthly Notices of the Royal Astronomical Society, 355, 747

Jones E., Oliphant T., Peterson P., 2016, SciPy: Open source scientific tools for Python, 2001

Jordi C., et al., 2010, Astronomy & Astrophysics, 523, A48

Joyce M., Chaboyer B., 2015, The Astrophysical Journal, 814, 142

Joyce M., Chaboyer B., 2018a, The Astrophysical Journal, 856, 10

Joyce M., Chaboyer B., 2018b, The Astrophysical Journal, 864, 99

Kaiser N., et al., 2002, in Survey and Other Telescope Technologies and Discoveries. International Society for Optics and Photonics, pp 154–164, doi:10.1117/12.457365, https://www.spiedigitallibrary.org/conference-proceedings-of-spie/4836/0000/Pan-STARRS-a-large-synoptic-survey-telescope-array/10.1117/12.457365.short

Kaiser N., et al., 2010, in Ground-based and Airborne Telescopes III. International Society for Optics and Photonics, p. 77330E, doi:10.1117/12.859188, https://www.spiedigitallibrary.org/conference-proceedings-of-spie/7733/77330E/The-Pan-STARRS-wide-field-opticalNIR-imaging-survey/10.1117/12.859188.short

Karovicova I., et al., 2018, Monthly Notices of the Royal Astronomical Society

Karovicova I., White T. R., Nordlander T., Casagrande L., Ireland M., Huber D., Jofré P., 2020, Astronomy & Astrophysics, 640, A25

Katz D., Soubiran C., Cayrel R., Adda M., Cautain R., 1998, Astronomy and Astrophysics, 338, 151

Katz D., et al., 2019, Astronomy and Astrophysics, 622, A205

Keller S. C., et al., 2007, Publications of the Astronomical Society of Australia, 24, 1

Kervella P., Thévenin F., Di Folco E., Ségransan D., 2004a, Astronomy and Astrophysics, 426, 297

Kervella P., Bersier D., Mourard D., Nardetto N., Fouqué P., 2004b, Astronomy & Astrophysics, 428, 587

Kervella P., Bigot L., Gallenne A., Thévenin F., 2017, Astronomy and Astrophysics, 597, A137

Kippenhahn R., Weigert A., Weiss A., 2012, Stellar Structure and Evolution, 2 edn. Astronomy and Astrophysics Library, Springer-Verlag, Berlin Heidelberg, doi:10.1007/978-3-642-30304-3, https://www.springer.com/gp/book/9783642302558

Kipping D. M., 2008, Monthly Notices of the Royal Astronomical Society, 389, 1383

Kirkpatrick J. D., 2005, Annual Review of Astronomy and Astrophysics, 43, 195

Kirkpatrick J. D., Henry T. J., McCarthy Jr. D. W., 1991, The Astrophysical Journal Supplement Series, 77, 417

Kirkpatrick J. D., Henry T. J., Simons D. A., 1995, The Astronomical Journal, 109, 797

Kirkpatrick J. D., et al., 1999, The Astrophysical Journal, 519, 802

Köhler R., Ratzka T., Leinert C., 2012, Astronomy & Astrophysics, 541, A29

Koleva M., Prugniel P., Bouchard A., Wu Y., 2009, Astronomy & Astrophysics, 501, 1269

Kollmeier J. A., et al., 2017, arXiv:1711.03234 [astro-ph]

Konacki M., Muterspaugh M. W., Kulkarni S. R., Hełminiak K. G., 2010, The Astrophysical Journal, 719, 1293

Kos J., et al., 2017, Monthly Notices of the Royal Astronomical Society, 464, 1259

Kostov V. B., et al., 2019, The Astronomical Journal, 158, 32

Kounkel M., Covey K., 2019, The Astronomical Journal, 158, 122

Kovtyukh V. V., Soubiran C., Belik S. I., Gorlova N. I., 2003, Astronomy & Astrophysics, 411, 559

Kraus A. L., Tucker R. A., Thompson M. I., Craine E. R., Hillenbrand L. A., 2011, The Astrophysical Journal, 728, 48

Kraus A. L., Cody A. M., Covey K. R., Rizzuto A. C., Mann A. W., Ireland M. J., 2015, The Astrophysical Journal, 807, 3

Kreidberg L., 2015, Publications of the Astronomical Society of the Pacific, 127, 1161

Kruse E., Agol E., Luger R., Foreman-Mackey D., 2019, The Astrophysical Journal Supplement Series, 244, 11

Kuchner M. J., Seager S., 2005, arXiv:astro-ph/0504214 [astro-ph]

Kudritzki R.-P., Urbaneja M. A., Rix H.-W., 2020, The Astrophysical Journal, 890, 28

Kuehn K., et al., 2014, in Ground-based and Airborne Instrumentation for Astronomy V. International Society for Optics and Photonics, p. 914710, doi:10.1117/12.2055677, https://www.spiedigitallibrary.org/conference-proceedings-of-spie/9147/914710/TAIPAN-optical-spectroscopy-with-StarBugs/10.1117/12.2055677.short

Kurucz R. L., 1995, Kurucz CD-ROM, 15. Cambridge, Mass.: Smithsonian Astrophysical Observatory

Kurucz R. L., 2011, Canadian Journal of Physics, 89, 417

Kuruwita R. L., Ireland M., Rizzuto A., Bento J., Federrath C., 2018, Monthly Notices of the Royal Astronomical Society, 480, 5099

Kuznetsov M. K., del Burgo C., Pavlenko Y. V., Frith J., 2019, The Astrophysical Journal, 878, 134

Lachaume R., Rabus M., Jordán A., 2014, in Optical and Infrared Interferometry IV. International Society for Optics and Photonics, p. 914631, doi:10.1117/12.2057447, https://www.spiedigitallibrary.org/conference-proceedings-of-spie/9146/914631/An-accurate-assessment-of-uncertainties-in-model-fits-of-interferometric/10.1117/12.2057447.short

Lachaume R., Rabus M., Jordán A., Brahm R., Boyajian T., von Braun K., Berger J.-P., 2019, Monthly Notices of the Royal Astronomical Society, 484, 2656

Lacy C. H., 1977, The Astrophysical Journal Supplement Series, 34, 479

Lafarga M., et al., 2021, arXiv:2105.13467 [astro-ph]

Lallement R., Welsh B. Y., Vergely J. L., Crifo F., Sfeir D., 2003, Astronomy & Astrophysics, 411, 447

Lawrence J. S., et al., 2016, in Ground-based and Airborne Instrumentation for Astronomy VI. International Society for Optics and Photonics, p. 99089O, doi:10.1117/12.2232412, https://www.spiedigitallibrary.org/conference-proceedings-of-spie/9908/99089O/The-MANIFEST-prototyping-design-study/10.1117/12.2232412.short

Lebreton Y., Montalbán J., 2009, in Proc. of the IAU Symp. 258 "The Ages of Stars". Baltimore, MD, USA, pp 419–430, doi:10.1017/S1743921309032074, http://adsabs.harvard.edu/abs/2009IAUS..258..419L

Lebzelter T., et al., 2012, Astronomy & Astrophysics, 547, A108

Lee E. J., Chiang E., 2016, The Astrophysical Journal, 817, 90

Lee Y. S., et al., 2008, The Astronomical Journal, 136, 2022

Lee E. J., Chiang E., Ormel C. W., 2014, The Astrophysical Journal, 797, 95

Leggett S. K., Allard F., Berriman G., Dahn C. C., Hauschildt P. H., 1996, The Astrophysical Journal Supplement Series, 104, 117

Leike R. H., Glatzle M., Enßlin T. A., 2020, Astronomy and Astrophysics, 639, A138

Leleu A., et al., 2021, Astronomy & Astrophysics, 649, A26

Lépine S., 2005, The Astronomical Journal, 130, 1247

Lépine S., Gaidos E., 2011, The Astronomical Journal, 142, 138

Lépine S., Hilton E. J., Mann A. W., Wilde M., Rojas-Ayala B., Cruz K. L., Gaidos E., 2013, The Astronomical Journal, 145, 102

Leroy J. L., 1993, Astronomy and Astrophysics, 274, 203

Lightkurve Collaboration et al., 2018, Lightkurve: Kepler and TESS time series analysis in Python, http://adsabs.harvard.edu/abs/2018ascl.soft12013L

Lind K., 2010, PhD Thesis, Ludwig-Maximilians-Universität München, https://edoc.ub.uni-muenchen.de/12097/

Lind K., Asplund M., Barklem P. S., 2009, Astronomy & Astrophysics, 503, 541

Lind K., Bergemann M., Asplund M., 2012, Monthly Notices of the Royal Astronomical Society, 427, 50

Lindegren L., et al., 2018, Astronomy & Astrophysics, 616, A2

Lindgren S., Heiter U., 2017, Astronomy and Astrophysics, 604, A97

Lindgren S., Heiter U., Seifahrt A., 2016, Astronomy and Astrophysics, 586, A100

Liu Y. J., Zhao G., Shi J. R., Pietrzyński G., Gieren W., 2007, Monthly Notices of the Royal Astronomical Society, 382, 553

Liu C., Bailer-Jones C. A. L., Sordo R., Vallenari A., Borrachero R., Luri X., Sartoretti P., 2012, Monthly Notices of the Royal Astronomical Society, 426, 2463

Lopez E. D., Fortney J. J., 2014, The Astrophysical Journal, 792, 1

Lopez E. D., Rice K., 2018, Monthly Notices of the Royal Astronomical Society, 479, 5303

López-Morales M., 2007, The Astrophysical Journal, 660, 732

Lorente N. P. F., Vuong M., Satorre C., Hong S. E., Shortridge K., Goodwin M., Kuehn K., 2015, in Proceedings of Astronomical Data Analysis Software an Systems XXIV (ADASS XXIV). Astronomical Society of the Pacific, Calgary, Alberta Canada, p. 265, http://adsabs.harvard.edu/abs/2015ASPC..495..265L

Lorente N. P. F., et al., 2016, in Software and Cyberinfrastructure for Astronomy IV. International Society for Optics and Photonics, p. 99130U, doi:10.1117/12.2233685, https://www.spiedigitallibrary.org/conference-proceedings-of-spie/9913/99130U/AAO-Starbugs-software-control-and-associated-algorithms/10.1117/12.2233685.short

Lovis C., Fischer D., 2010, in , Exoplanets. University of Arizona Press, Tucson, AZ, pp 27–53, http://adsabs.harvard.edu/abs/2010exop.book...27L

Luck R. E., 2017, The Astronomical Journal, 153, 21

Luck R. E., 2018, The Astronomical Journal, 155, 111

Luck R. E., Heiter U., 2005, The Astronomical Journal, 129, 1063

Ludwig H.-G., Freytag B., Steffen M., 1999, Astronomy and Astrophysics, 346, 111

Luo A.-L., et al., 2015, Research in Astronomy and Astrophysics, 15, 1095

Luque R., et al., 2019, Astronomy and Astrophysics, 628, A39

Lyra W., 2005, Astronomy & Astrophysics, 431, 329

Maestro V., et al., 2013, Monthly Notices of the Royal Astronomical Society, 434, 1321

Magic Z., Collet R., Asplund M., Trampedach R., Hayek W., Chiavassa A., Stein R. F., Nordlund Å., 2013, Astronomy & Astrophysics, 557, A26

Magic Z., Weiss A., Asplund M., 2015, Astronomy and Astrophysics, 573, A89

Majewski S. R., et al., 2017, The Astronomical Journal, 154, 94

Makarov V. V., 2007, The Astrophysical Journal Supplement Series, 169, 105

Mallik S. V., Parthasarathy M., Pati A. K., 2003, Astronomy and Astrophysics, 409, 251

Mamajek E. E., 2009, in Proceedings of the International Astronomical Union. Baltimore, USA, pp 375–382, doi:10.1017/S1743921309032037, http://adsabs.harvard.edu/abs/2009IAUS..258..375M

Mamajek E. E., Hillenbrand L. A., 2008, The Astrophysical Journal, 687, 1264

Mann A. W., Gaidos E., Lépine S., Hilton E. J., 2012, The Astrophysical Journal, 753, 90

Mann A. W., Brewer J. M., Gaidos E., Lépine S., Hilton E. J., 2013a, The Astronomical Journal, 145, 52

Mann A. W., Brewer J. M., Gaidos E., Lépine S., Hilton E. J., 2013b, Astronomische Nachrichten, 334, 18

Mann A. W., Gaidos E., Ansdell M., 2013c, The Astrophysical Journal, 779, 188

Mann A. W., Feiden G. A., Gaidos E., Boyajian T., von Braun K., 2015, The Astrophysical Journal, 804, 64

Mann A. W., et al., 2016, The Astronomical Journal, 152, 61

Mann A. W., et al., 2019, The Astrophysical Journal, 871, 63

Marrese P. M., Marinoni S., Fabrizio M., Altavilla G., 2019, Astronomy & Astrophysics, 621, A144

Marshall D. J., Robin A. C., Reylé C., Schultheis M., Picaud S., 2006, Astronomy & Astrophysics, 453, 635

Martell S. L., et al., 2021, Monthly Notices of the Royal Astronomical Society, 505, 5340

Martig M., et al., 2016, Monthly Notices of the Royal Astronomical Society, 456, 3655

Martínez-Arnáiz R., Maldonado J., Montes D., Eiroa C., Montesinos B., 2010, Astronomy & Astrophysics, 520, A79

Mason B. D., Wycoff G. L., Hartkopf W. I., Douglass G. G., Worley C. E., 2001, The Astronomical Journal, 122, 3466

Massarotti A., Latham D. W., Stefanik R. P., Fogel J., 2008, The Astronomical Journal, 135, 209

Masseron T., et al., 2014, Astronomy & Astrophysics, 571, A47

Mayor M., Queloz D., 1995, Nature, 378, 355

Mayor M., et al., 2003, The Messenger, 114, 20

Mayor M., et al., 2011, arXiv:1109.2497 [astro-ph]

Mazumdar A., 2005, Astronomy & Astrophysics, 441, 1079

McGurk R. C., Kimball A. E., Ivezić Ž., 2010, The Astronomical Journal, 139, 1261

McKemmish L. K., Masseron T., Hoeijmakers H. J., Pérez-Mesa V., Grimm S. L., Yurchenko S. N., Tennyson J., 2019, Monthly Notices of the Royal Astronomical Society, 488, 2836

McKinney W., 2010, in Proceedings of the 9th Python in Science Conference. pp 51–56, doi:10.25080/Majora-92bf1922-00a, http://conference.scipy.org/proceedings/scipy2010/mckinney.html

Meech K. J., et al., 2017, Nature, 552, 378

Meingast S., Alves J., 2019, Astronomy & Astrophysics, 621, L3

Meléndez J., Asplund M., Gustafsson B., Yong D., 2009, The Astrophysical Journal, 704, L66

Ment K., et al., 2019, The Astronomical Journal, 157, 32

Mentuch E., Brandeker A., van Kerkwijk M. H., Jayawardhana R., Hauschildt P. H., 2008, The Astrophysical Journal, 689, 1127

Michelson A. A., Pease F. G., 1921, The Astrophysical Journal, 53

Mishenina T. V., Soubiran C., Kovtyukh V. V., Korotin S. A., 2004, Astronomy and Astrophysics, 418, 551

Miszalski B., Shortridge K., Saunders W., Parker Q. A., Croom S. M., 2006, Monthly Notices of the Royal Astronomical Society, 371, 1537

Montes D., et al., 2018, Monthly Notices of the Royal Astronomical Society, 479, 1332

Montet B. T., Crepp J. R., Johnson J. A., Howard A. W., Marcy G. W., 2014, The Astrophysical Journal, 781, 28

Morales J. C., Ribas I., Jordi C., 2008, Astronomy & Astrophysics, 478, 507

Morales J. C., et al., 2009, The Astrophysical Journal, 691, 1400

Morgan W. W., Keenan P. C., Kellman E., 1943, An atlas of stellar spectra, with an outline of spectral classification. The University of Chicago Press, Chicago, USA, http://adsabs.harvard.edu/abs/1943assw.book.....M

Morton T. D., Swift J., 2014, The Astrophysical Journal, 791, 10

Mould J., Clementini G., Da Costa G., 2019, Publications of the Astronomical Society of Australia, 36, e001

Mozurkewich D., et al., 2003, The Astronomical Journal, 126, 2502

Muirhead P. S., Hamren K., Schlawin E., Rojas-Ayala B., Covey K. R., Lloyd J. P., 2012, The Astrophysical Journal Letters, 750, L37

Muirhead P. S., Dressing C. D., Mann A. W., Rojas-Ayala B., Lépine S., Paegert M., De Lee N., Oelkers R., 2018, The Astronomical Journal, 155, 180

Murphy S. J., et al., 2020, Monthly Notices of the Royal Astronomical Society, 491, 4902

Myeong G. C., Vasiliev E., Iorio G., Evans N. W., Belokurov V., 2019, Monthly Notices of the Royal Astronomical Society, 488, 1235

Nakajima T., Oppenheimer B. R., Kulkarni S. R., Golimowski D. A., Matthews K., Durrance S. T., 1995, Nature, 378, 463

Ness M., Hogg D. W., Rix H.-W., Ho A. Y. Q., Zasowski G., 2015, The Astrophysical Journal, 808, 16

Ness M., Hogg D. W., Rix H.-W., Martig M., Pinsonneault M. H., Ho A. Y. Q., 2016, The Astrophysical Journal, 823, 114

Neves V., et al., 2012, Astronomy and Astrophysics, 538, A25

Newton E. R., Charbonneau D., Irwin J., Berta-Thompson Z. K., Rojas-Ayala B., Covey K., Lloyd J. P., 2014, The Astronomical Journal, 147, 20

Ng Y. K., Bertelli G., 1998, Astronomy and Astrophysics, 329, 943

Nielsen L. D., et al., 2020, Astronomy and Astrophysics, 639, A76

Nissen P. E., 2015, Astronomy & Astrophysics, 579, A52

Nissen P. E., Gustafsson B., 2018, The Astronomy and Astrophysics Review, 26, 6

Nissen P. E., Akerman C., Asplund M., Fabbian D., Kerber F., Käufl H. U., Pettini M., 2007, Astronomy & Astrophysics, 469, 319

Nordgren T. E., et al., 1999, The Astronomical Journal, 118, 3032

Nordlander T., et al., 2019, Monthly Notices of the Royal Astronomical Society, 488, L109

Noyes R. W., Hartmann L. W., Baliunas S. L., Duncan D. K., Vaughan A. H., 1984, The Astrophysical Journal, 279, 763

Önehag A., Heiter U., Gustafsson B., Piskunov N., Plez B., Reiners A., 2012, Astronomy and Astrophysics, 542, A33

Onken C. A., et al., 2019, Publications of the Astronomical Society of Australia, 36, e033

Otí Floranes H., Christensen-Dalsgaard J., Thompson M. J., 2005, Monthly Notices of the Royal Astronomical Society, 356, 671

Owen J. E., Wu Y., 2013, The Astrophysical Journal, 775, 105

Owen J. E., Wu Y., 2017, The Astrophysical Journal, 847, 29

Pagel B. E. J., Portinari L., 1998, Monthly Notices of the Royal Astronomical Society, 298, 747

Paladini C., et al., 2018, Nature, 553, 310

Passegger V. M., Wende-von Berg S., Reiners A., 2016, Astronomy and Astrophysics, 587, A19

Passegger V. M., et al., 2018, Astronomy and Astrophysics, 615, A6

Paxton B., Bildsten L., Dotter A., Herwig F., Lesaffre P., Timmes F., 2010, The Astrophysical Journal Supplement Series, 192, 3

Pearson K. F., 1901, The London, Edinburgh, and Dublin Philosophical Magazine and Journal of Science, 2, 559

Pecaut M. J., Mamajek E. E., 2013, The Astrophysical Journal Supplement Series, 208, 9

Pepper J., et al., 2007, Publications of the Astronomical Society of the Pacific, 119, 923

Perez F., Granger B. E., 2007, Computing in Science Engineering, 9, 21

Pérez A. E. G., et al., 2016, The Astronomical Journal, 151, 144

Perryman M. A. C., et al., 1997, Astronomy and Astrophysics, 323, L49

Petigura E. A., Howard A. W., Marcy G. W., 2013, Proceedings of the National Academy of Science, 110, 19273

Piau L., Kervella P., Dib S., Hauschildt P., 2011, Astronomy and Astrophysics, 526, A100

Pickles A. J., 1998, Publications of the Astronomical Society of the Pacific, 110, 863

Pietrinferni A., Cassisi S., Salaris M., Castelli F., 2004, The Astrophysical Journal, 612, 168

Pijpers F. P., Teixeira T. C., Garcia P. J., Cunha M. S., Monteiro M. J. P. F. G., Christensen-Dalsgaard J., 2003, Astronomy and Astrophysics, 406, L15

Pinsonneault M. H., et al., 2014, The Astrophysical Journal Supplement Series, 215, 19

Plez B., 1998, Astronomy and Astrophysics, 337, 495

Plez B., 2012, Turbospectrum: Code for spectral synthesis, http://adsabs.harvard.edu/abs/2012ascl.soft05004P

Plez B., Brett J. M., Nordlund A., 1992, Astronomy and Astrophysics, 256, 551

Pollacco D. L., et al., 2006, Publications of the Astronomical Society of the Pacific, 118, 1407

Pont F., Eyer L., 2004, Monthly Notices of the Royal Astronomical Society, 351, 487

Pourbaix D., et al., 2004, Astronomy and Astrophysics, 424, 727

Prugniel P., Vauglin I., Koleva M., 2011, Astronomy and Astrophysics, 531, A165

Queloz D., et al., 2000, Astronomy and Astrophysics, 354, 99

Quillen A. C., Pettitt A. R., Chakrabarti S., Zhang Y., Gagné J., Minchev I., 2020, Monthly Notices of the Royal Astronomical Society, 499, 5623

Quirrenbach A., et al., 2014, in Ground-based and Airborne Instrumentation for Astronomy V. International Society for Optics and Photonics, p. 91471F, doi:10.1117/12.2056453, https://www.spiedigitallibrary.org/conference-proceedings-of-spie/9147/91471F/CARMENES-instrument-overview/10.1117/12.2056453.short

Rabus M., et al., 2019, Monthly Notices of the Royal Astronomical Society, 484, 2674

Rains A. D., Ireland M. J., White T. R., Casagrande L., Karovicova I., 2020, Monthly Notices of the Royal Astronomical Society, 493, 2377

Rains A. D., et al., 2021, Monthly Notices of the Royal Astronomical Society, 504, 5788

Rajpurohit A. S., Reylé C., Allard F., Homeier D., Schultheis M., Bessell M. S., Robin A. C., 2013, Astronomy and Astrophysics, 556, A15

Rajpurohit A. S., Reylé C., Allard F., Scholz R.-D., Homeier D., Schultheis M., Bayo A., 2014, Astronomy and Astrophysics, 564, A90

Ramírez I., Meléndez J., 2004, The Astrophysical Journal, 609, 417

Ramírez I., Meléndez J., 2005, The Astrophysical Journal, 626, 446

Ramírez I., Allende Prieto C., Lambert D. L., 2007, Astronomy and Astrophysics, 465, 271

Ramírez I., Allende Prieto C., Lambert D. L., 2013, The Astrophysical Journal, 764, 78

Ramírez I., et al., 2014, Astronomy & Astrophysics, 572, A48

Rebolo R., Osorio M. R. Z., Martín E. L., 1995, Nature, 377, 129

Recio-Blanco A., Bijaoui A., De Laverny P., 2006, Monthly Notices of the Royal Astronomical Society, 370, 141

Recio-Blanco A., et al., 2016, Astronomy & Astrophysics, Volume 585, id.A93, 22 pp., 585, A93

Reylé C., Rajpurohit A. S., Schultheis M., Allard F., 2011, in ASP Conference Series. University of Washington, Seattle, Washington, p. 929, http://adsabs.harvard.edu/abs/2011ASPC..448..929R

Ribas I., 2006, Astrophysics and Space Science, 304, 89

Rice M., Brewer J. M., 2020, The Astrophysical Journal, 898, 119

Ricker G. R., et al., 2015, Journal of Astronomical Telescopes, Instruments, and Systems, 1, 014003

Rivera E. J., et al., 2005, The Astrophysical Journal, 634, 625

Robin A. C., Reylé C., Derrière S., Picaud S., 2003, Astronomy & Astrophysics, 409, 523

Robin A. C., Marshall D. J., Schultheis M., Reylé C., 2012, Astronomy & Astrophysics, 538, A106

Robin A. C., Reylé C., Fliri J., Czekaj M., Robert C. P., Martins A. M. M., 2014, Astronomy & Astrophysics, 569, A13

Robinson S. E., Ammons S. M., Kretke K. A., Strader J., Wertheimer J. G., Fischer D. A., Laughlin G., 2007, The Astrophysical Journal Supplement Series, 169, 430

Robotham A., et al., 2010, Publications of the Astronomical Society of Australia, 27, 76

Rockosi C., Beers T. C., Majewski S., Schiavon R., Eisenstein D., 2009, in Proceedings of astro2010: The Astronomy and Astrophysics Decadal Survey. eprint: arXiv:0902.3484, http://adsabs.harvard.edu/abs/2009astro2010S..14R

Rojas-Ayala B., Covey K. R., Muirhead P. S., Lloyd J. P., 2010, The Astrophysical Journal Letters, 720, L113

Rojas-Ayala B., Covey K. R., Muirhead P. S., Lloyd J. P., 2012, The Astrophysical Journal, 748, 93

Rosenfeld K. A., Andrews S. M., Wilner D. J., Stempels H. C., 2012, The Astrophysical Journal, 759, 119

Roweis S. T., Saul L. K., 2000, Science, 290, 2323

Royer F., Zorec J., Gómez A. E., 2007, Astronomy and Astrophysics, 463, 671

Ryabchikova T., Piskunov N., Kurucz R. L., Stempels H. C., Heiter U., Pakhomov Y., Barklem P. S., 2015, Physica Scripta, 90, 054005

Saffe C., Flores M., Miquelarena P., López F. M., Arancibia M. J., Collado A., Jofré E., Petrucci R., 2018, Astronomy & Astrophysics, 620, A54

Sameshima H., et al., 2018, Publications of the Astronomical Society of the Pacific, 130, 074502

Santos N. C., Israelian G., Mayor M., Rebolo R., Udry S., 2003, Astronomy & Astrophysics, 398, 363

Santos N. C., Israelian G., Mayor M., 2004, Astronomy & Astrophysics, 415, 1153

Savitzky A., Golay M. J. E., 1964, Analytical Chemistry, 36, 1627

Schlaufman K. C., Laughlin G., 2010, Astronomy and Astrophysics, 519, A105

Schröder C., Reiners A., Schmitt J. H. M. M., 2009, Astronomy and Astrophysics, 493, 1099

Seager S., ed. 2011, Exoplanets. University of Arizona Press, Tucson : Houston

Serenelli A., et al., 2021, Astronomy and Astrophysics Review, 29, 4

Sharma S., Bland-Hawthorn J., Johnston K. V., Binney J., 2011, The Astrophysical Journal, 730, 3

Sharma S., et al., 2018, Monthly Notices of the Royal Astronomical Society, 473, 2004

Shin I.-G., et al., 2017, The Astronomical Journal, 154, 176

Siess L., Dufour E., Forestini M., 2000, Astronomy and Astrophysics, 358, 593

Silva Aguirre V., et al., 2015, Monthly Notices of the Royal Astronomical Society, 452, 2127

Silva Aguirre V., et al., 2017, The Astrophysical Journal, 835, 173

Simon M., et al., 2017, The Astrophysical Journal, 844, 158

Skory S., Weck P. F., Stancil P. C., Kirby K., 2003, The Astrophysical Journal Supplement Series, 148, 599

Skrutskie M. F., et al., 2006, The Astronomical Journal, 131, 1163

Smiljanic R., et al., 2014, Astronomy and Astrophysics, 570, A122

Smith V. V., Lambert D. L., 1985, The Astrophysical Journal, 294, 326

Smith A., et al., 2019, Monthly Notices of the Royal Astronomical Society, 484, 1285

Sneden C., Kraft R. P., Guhathakurta P., Peterson R. C., Fulbright J. P., 2004, The Astronomical Journal, 127, 2162

Snider S., Prieto C. A., Hippel T. v., Beers T. C., Sneden C., Qu Y., Rossi S., 2001, The Astrophysical Journal, 562, 528

Soderblom D. R., 2010, Annual Review of Astronomy and Astrophysics, 48, 581

Soderblom D. R., Jones B. F., Balachandran S., Stauffer J. R., Duncan D. K., Fedele S. B., Hudon J. D., 1993, The Astronomical Journal, 106, 1059

Soderblom D. R., Hillenbrand L. A., Jeffries R. D., Mamajek E. E., Naylor T., 2014, in Beuther H., Klessen R. S., Dullemond C. P., Henning T., eds, Protostars and Planets VI. p. 219, doi:10.2458/azu_uapress_9780816531240-ch010

Söderhjelm S., 1999, Astronomy and Astrophysics, 341, 121

Sousa S. G., Santos N. C., Israelian G., Mayor M., Monteiro M. J. P. F. G., 2006, Astronomy and Astrophysics, 458, 873

Sousa S. G., et al., 2008, Astronomy and Astrophysics, 487, 373

Sousa S. G., Santos N. C., Israelian G., Mayor M., Udry S., 2011, Astronomy and Astrophysics, 533, A141

Southworth J., Maxted P. F. L., Smalley B., 2005, Astronomy & Astrophysics, 429, 645

Souto D., et al., 2017, The Astrophysical Journal, 835, 239

Souto D., et al., 2018, The Astrophysical Journal Letters, 860, L15

Souto D., et al., 2020, The Astrophysical Journal, 890, 133

Sozzetti A., Torres G., Latham D. W., Carney B. W., Stefanik R. P., Boss A. P., Laird J. B., Korzennik S. G., 2006, The Astrophysical Journal, 649, 428

Sozzetti A., Torres G., Latham D. W., Stefanik R. P., Korzennik S. G., Boss A. P., Carney B. W., Laird J. B., 2009, The Astrophysical Journal, 697, 544

Spina L., Meléndez J., Ramírez I., 2016, Astronomy & Astrophysics, 585, A152

Spina L., Meléndez J., Casey A. R., Karakas A. I., Tucci-Maia M., 2018, The Astrophysical Journal, 863, 179

Spina L., et al., 2020, The Astrophysical Journal, 895, 52

Stassun K. G., Torres G., 2018, The Astrophysical Journal, 862, 61

Stassun K. G., Feiden G. A., Torres G., 2014, New Astronomy Reviews, 60-61, 1

Stassun K. G., et al., 2018, The Astronomical Journal, 156, 102

Stassun K. G., et al., 2019, The Astronomical Journal, 158, 138

Staszak N. F., et al., 2016a, in Advances in Optical and Mechanical Technologies for Telescopes and Instrumentation II. International Society for Optics and Photonics, p. 99121W, doi:10.1117/12.2233583, https://www.spiedigitallibrary.org/conference-proceedings-of-spie/9912/99121W/TAIPAN-instrument-fibre-positioner-and-Starbug-robots-engineering-overview/10.1117/12.2233583.short

Staszak N. F., et al., 2016b, in Advances in Optical and Mechanical Technologies for Telescopes and Instrumentation II. International Society for Optics and Photonics, p. 991223, doi:10.1117/12.2233796, https://www.spiedigitallibrary.org/conference-proceedings-of-spie/9912/991223/TAIPAN-fibre-feed-and-spectrograph-engineering-overview/10.1117/12.2233796.short

Steinmetz M., et al., 2006, The Astronomical Journal, 132, 1645

Storm J., et al., 2011a, Astronomy & Astrophysics, 534, A94

Storm J., Gieren W., Fouqué P., Barnes T. G., Soszyński I., Pietrzyński G., Nardetto N., Queloz D., 2011b, Astronomy & Astrophysics, 534, A95

Takeda Y., Ohkubo M., Sadakane K., 2002, Publications of the Astronomical Society of Japan, 54, 451

Talens G. J. J., Spronck J. F. P., Lesage A.-L., Otten G. P. P. L., Stuik R., Pollacco D., Snellen I. A. G., 2017, Astronomy and Astrophysics, 601, A11

Tayar J., et al., 2017, The Astrophysical Journal, 840, 17

Tayar J., Claytor Z. R., Huber D., van Saders J., 2020, arXiv:2012.07957 [astro-ph]

Tempel E., et al., 2020a, Monthly Notices of the Royal Astronomical Society, 497, 4626

Tempel E., et al., 2020b, Astronomy and Astrophysics, 635, A101

Tennyson J., et al., 2016, Journal of Molecular Spectroscopy, 327, 73

Terrien R. C., Mahadevan S., Bender C. F., Deshpande R., Ramsey L. W., Bochanski J. J., 2012, The Astrophysical Journal Letters, 747, L38

Thévenin F., Idiart T. P., 1999, The Astrophysical Journal, 521, 753

Ting Y.-S., Weinberg D. H., 2021, arXiv:2102.04992 [astro-ph]

Ting Y.-S., Rix H.-W., Conroy C., Ho A. Y. Q., Lin J., 2017, The Astrophysical Journal Letters, 849, L9

Tinney C. G., Butler R. P., Marcy G. W., Jones H. R. A., Penny A. J., Vogt S. S., Apps K., Henry G. W., 2001, The Astrophysical Journal, 551, 507

Tomkin J., Fekel F. C., 2006, The Astronomical Journal, 131, 2652

Torres G., 2010, The Astronomical Journal, 140, 1158

Torres G., Ribas I., 2002, The Astrophysical Journal, 567, 1140

Torres C. a. O., Quast G. R., da Silva L., de La Reza R., Melo C. H. F., Sterzik M., 2006, Astronomy and Astrophysics, 460, 695

Torres G., Andersen J., Giménez A., 2010, Astronomy and Astrophysics Review, 18, 67

Trampedach R., Stein R. F., Christensen-Dalsgaard J., Nordlund Å., Asplund M., 2014, Monthly Notices of the Royal Astronomical Society, 445, 4366

Traven G., et al., 2017, The Astrophysical Journal Supplement Series, 228, 24

Tsantaki M., Sousa S. G., Adibekyan V. Z., Santos N. C., Mortier A., Israelian G., 2013, Astronomy and Astrophysics, 555, A150

Tsuji T., 2016, Publications of the Astronomical Society of Japan, 68

Tsuji T., Nakajima T., 2014, Publications of the Astronomical Society of Japan, 66

Tsuji T., Nakajima T., 2016, Publications of the Astronomical Society of Japan, 68

Tsuji T., Nakajima T., Takeda Y., 2015, Publications of the Astronomical Society of Japan, 67

Tucci Maia M., Meléndez J., Ramírez I., 2014, The Astrophysical Journal, 790, L25

Ulrich R. K., 1986, The Astrophysical Journal Letters, 306, L37

Unno W., 1989, Nonradial Oscillations of Stars. University of Tokyo Press

Valenti J. A., Fischer D. A., 2005, The Astrophysical Journal Supplement Series, 159, 141

Valenti J. A., Piskunov N., 1996, Astronomy and Astrophysics Supplement Series, 118, 595

Van Eylen V., Agentoft C., Lundkvist M. S., Kjeldsen H., Owen J. E., Fulton B. J., Petigura E., Snellen I., 2018, Monthly Notices of the Royal Astronomical Society, 479, 4786

VandenBerg D. A., Bergbusch P. A., Dowler P. D., 2006, The Astrophysical Journal Supplement Series, 162, 375

VandenBerg D. A., Casagrande L., Stetson P. B., 2010, The Astronomical Journal, 140, 1020

Vanderspek R., et al., 2019, The Astrophysical Journal Letters, 871, L24

Venturini J., Guilera O. M., Haldemann J., Ronco M. P., Mordasini C., 2020, Astronomy & Astrophysics, 643, L1

Veyette M. J., Muirhead P. S., Mann A. W., Allard F., 2016, The Astrophysical Journal, 828, 95

Veyette M. J., Muirhead P. S., Mann A. W., Brewer J. M., Allard F., Homeier D., 2017, The Astrophysical Journal, 851, 26

Vitense E., 1953, Zeitschrift fur Astrophysik, 32, 135

Waalkes W. C., et al., 2020, The Astronomical Journal, 161, 13

Watson F. G., 1988, in Proceedings of Fiber optics in astronomy. Tucson, AZ, USA, pp 125–132, http://adsabs.harvard.edu/abs/1988ASPC....3..125W

Watson F. G., Parker Q. A., 1994, in Instrumentation in Astronomy VIII. International Society for Optics and Photonics, pp 65–75, doi:10.1117/12.176786, https://www.spiedigitallibrary.org/conference-proceedings-of-spie/2198/0000/Wide-field-multifiber-spectroscopy-with-FLAIR-II/10.1117/12.176786.short

Watson F. G., Oates A. P., Gray P. M., 1990, in Instrumentation in Astronomy VII. International Society for Optics and Photonics, pp 736–746, doi:10.1117/12.19137, https://www.spiedigitallibrary.org/conference-proceedings-of-spie/1235/0000/FLAIR-wide-field-multiobject-spectroscopy-system/10.1117/12.19137.short

Watson F. G., Parker Q. A., Miziarski S., 1998, in Optical Astronomical Instrumentation. International Society for Optics and Photonics, pp 834–843, doi:10.1117/12.316797, https://www.spiedigitallibrary.org/conference-proceedings-of-spie/3355/0000/6dF--a-very-efficient-multiobject-spectroscopy-system-for-the/10.1117/12.316797.short

Watson F. G., Parker Q. A., Bogatu G., Farrell T. J., Hingley B. E., Miziarski S., 2000, in Optical and IR Telescope Instrumentation and Detectors. International Society for Optics and Photonics, pp 123–129, doi:10.1117/12.395490, https://www.spiedigitallibrary.org/conference-proceedings-of-spie/4008/0000/Progress-with-6dF--a-multi-object-spectroscopy-system-for/10.1117/12.395490.short

Wesselink A. J., 1969, Monthly Notices of the Royal Astronomical Society, 144, 297

Wheatley P. J., et al., 2018, Monthly Notices of the Royal Astronomical Society, 475, 4476

White T. R., et al., 2013, Monthly Notices of the Royal Astronomical Society, 433, 1262

White T. R., et al., 2018, Monthly Notices of the Royal Astronomical Society, 477, 4403

Winn J. N., 2010, in , Exoplanets. University of Arizona Press, Tucson, AZ, p. 25, http://arxiv.org/abs/1001.2010

Winters J. G., et al., 2015, The Astronomical Journal, 149, 5

Winters J. G., et al., 2019, The Astronomical Journal, 158, 152

Wittenmyer R. A., et al., 2020, Monthly Notices of the Royal Astronomical Society, 496, 851

Wittkowski M., et al., 2017, Astronomy and Astrophysics, 601, A3

Woitas J., Tamazian V. S., Docobo J. A., Leinert C., 2003, Astronomy & Astrophysics, 406, 293

Wolszczan A., Frail D. A., 1992, Nature, 355, 145

Woolf V. M., Wallerstein G., 2005, Monthly Notices of the Royal Astronomical Society, 356, 963

Woolf V. M., Wallerstein G., 2006, Publications of the Astronomical Society of the Pacific, 118, 218

Wright E. L., et al., 2010, The Astronomical Journal, 140, 1868

Wu Y., et al., 2011, Research in Astronomy and Astrophysics, 11, 924

Xiang M. S., et al., 2015, Monthly Notices of the Royal Astronomical Society, 448, 822

Yana Galarza J., et al., 2019, Monthly Notices of the Royal Astronomical Society: Letters, 490, L86

Yanny B., et al., 2009, The Astronomical Journal, 137, 4377

Yong D., Lambert D. L., Prieto C. A., Paulson D. B., 2004, The Astrophysical Journal, 603, 697

York D. G., et al., 2000, The Astronomical Journal, 120, 1579

Yuan H., Zhang H., Lei Y., Dong Y., 2012, in Observatory Operations: Strategies, Processes, and Systems IV. International Society for Optics and Photonics, p. 84482A, doi:10.1117/12.925359, https://www.spiedigitallibrary.org/conference-proceedings-of-spie/8448/84482A/The-plate-candidates-and-tiling-method-for-LAMOST-pilot-survey/10.1117/12.925359.short

Zacharias N., Finch C. T., Girard T. M., Henden A., Bartlett J. L., Monet D. G., Zacharias M. I., 2013, The Astronomical Journal, 145, 44

Zari E., Hashemi H., Brown A. G. A., Jardine K., Zeeuw P. T. d., 2018, Astronomy & Astrophysics, 620, A172

Zeng L., et al., 2019, Proceedings of the National Academy of Sciences, 116, 9723

Žerjal M., et al., 2019, Monthly Notices of the Royal Astronomical Society, 484, 4591

Žerjal M., et al., 2021, Monthly Notices of the Royal Astronomical Society, 503, 938

Zhao G., Zhao Y.-H., Chu Y.-Q., Jing Y.-P., Deng L.-C., 2012, Research in Astronomy and Astrophysics, 12, 723

Zhu W., et al., 2016, The Astrophysical Journal, 825, 60

Zuckerman B., Koester D., Reid I. N., Hünsch M., 2003, The Astrophysical Journal, 596, 477

Zwitter T., et al., 2008, The Astronomical Journal, 136, 421

da Cunha E., et al., 2017, Publications of the Astronomical Society of Australia, 34, e047

da Silva R., Milone A. C., Reddy B. E., 2011, Astronomy and Astrophysics, 526, A71

de Jong R. S., 4MOST Consortium 2016, Astronomische Nachrichten, 337, 964

de Jong R. S., et al., 2019, The Messenger, 175, 3

di Benedetto G. P., 1995, The Astrophysical Journal, 452, 195

di Benedetto G. P., 2005, Monthly Notices of the Royal Astronomical Society, 357, 174

di Folco E., et al., 2007, Astronomy and Astrophysics, 475, 243

do Nascimento J. D., Castro M., Meléndez J., Bazot M., Théado S., Mello G. F. P. d., Medeiros J. R. D., 2009, Astronomy & Astrophysics, 501, 687

ten Brummelaar T. A., et al., 2005, The Astrophysical Journal, 628, 453

van Belle G. T., 1999, Publications of the Astronomical Society of the Pacific, 111, 1515

van Belle G. T., von Braun K., 2009, The Astrophysical Journal, 694, 1085

van Belle G. T., et al., 1999, The Astronomical Journal, 117, 521

van Belle G. T., Ciardi D. R., Boden A. F., 2007, The Astrophysical Journal, 657, 1058

van Belle G. T., et al., 2008, The Astrophysical Journal Supplement Series, 176, 276

van der Maaten L., Hinton G., 2008, Journal of Machine Learning Research, 9, 2579

von Braun K., et al., 2011, The Astrophysical Journal Letters, 729, L26

von Braun K., et al., 2012, The Astrophysical Journal, 753, 171

von Braun K., et al., 2014, Monthly Notices of the Royal Astronomical Society, 438, 2413

von Hippel T., Storrie-Lombardi L. J., Storrie-Lombardi M. C., Irwin M. J., 1994, Monthly Notices of the Royal Astronomical Society, 269, 97

Appendix

A Supplementary Information: PIONIER Diameters

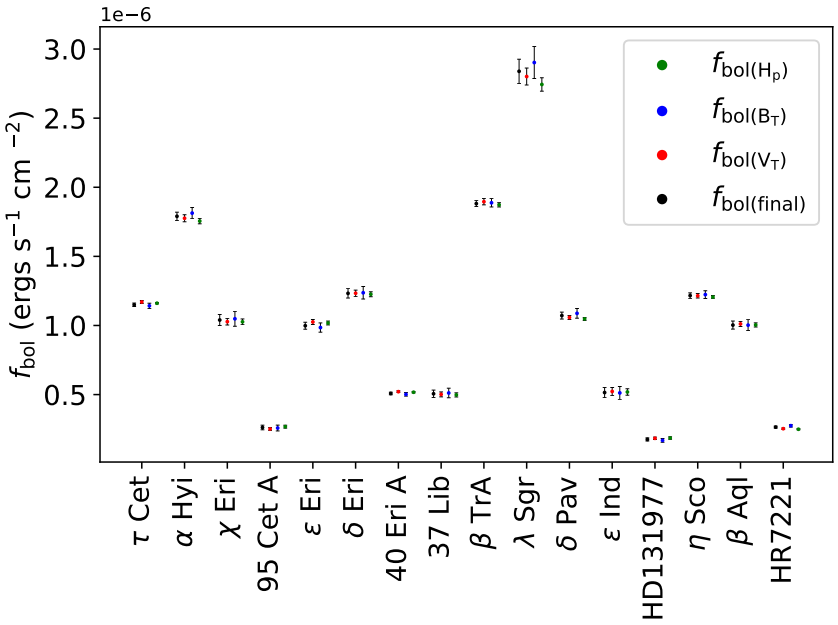

Figure A.1: Comparison of f_{bol} calculated from *Hipparcos-Tycho* H_P, B_T, V_T, as compared to the final average value adopted.

Table A.1: Calculated bolometric fluxes

Star	HD	$f_{\rm bol}$ (MARCS) (10^{-8} ergs s^{-1} cm $^{-2}$)	$\sigma_{f_{\rm bol}}(\zeta)$ (%)
τ Cet	10700	<>: 114.976	1.08
		H_p: 116.099	0.40
		B_T: 114.227	1.64
		V_T: 116.981	0.94
α Hyi	12311	<>: 178.994	1.66
		H_p: 175.530	1.12
		B_T: 181.304	2.23
		V_T: 177.571	1.43
χ Eri	11937	<>: 103.957	3.85
		H_p: 102.641	2.02
		B_T: 104.834	5.15
		V_T: 102.741	2.33
95 Cet A	20559	<>: 26.195	6.37
		H_p: 26.783	3.91
		B_T: 25.803	8.16
		V_T: 25.088	4.65
ϵ Eri	22049	<>: 99.817	2.52
		H_p: 101.793	1.36
		B_T: 98.500	3.40
		V_T: 102.539	1.76
δ Eri	23249	<>: 123.239	2.75
		H_p: 122.583	1.45
		B_T: 123.676	3.66
		V_T: 123.326	1.82
40 Eri A	26965	<>: 50.797	1.84
		H_p: 51.708	0.92
		B_T: 50.189	2.56
		V_T: 52.095	1.31
37 Lib	138716	<>: 50.601	5.23
		H_p: 49.763	3.00
		B_T: 51.159	6.76
		V_T: 50.133	3.54

Table A.1: – *continued*

Star	HD	f_{bol} (MARCS) (10^{-8} ergs s^{-1} cm^{-2})	$\sigma_{f_{bol}}(\zeta)$ (%)
β TrA	141891	<>: 188.174	1.14
		H_p: 187.285	0.82
		B_T: 188.766	1.60
		V_T: 189.549	1.20
λ Sgr	169916	<>: 283.889	3.08
		H_p: 274.369	1.77
		B_T: 290.236	3.99
		V_T: 280.120	2.19
δ Pav	190248	<>: 107.160	2.33
		H_p: 104.741	1.03
		B_T: 108.773	3.23
		V_T: 105.819	1.37
ϵ Ind	209100	<>: 51.481	7.18
		H_p: 51.882	4.50
		B_T: 51.214	9.04
		V_T: 52.269	5.45
HD131977	131977	<>: 17.554	6.40
		H_p: 18.572	4.77
		B_T: 16.876	8.07
		V_T: 18.358	4.82
η Sco	155203	<>: 121.621	1.62
		H_p: 120.550	0.97
		B_T: 122.336	2.28
		V_T: 121.489	1.32
β Aql	188512	<>: 100.299	2.90
		H_p: 100.388	1.49
		B_T: 100.239	3.93
		V_T: 101.120	1.81
HR7221	177389	<>: 26.462	2.81
		H_p: 24.930	1.53
		B_T: 27.484	3.65
		V_T: 25.323	1.92

Table A.2: Calibrator stars

HD	SpT (Actual)[a]	SpT (Adopted)[b]	V_T^c (mag)	H^d (mag)	$E(B-V)$ (mag)	θ_{pred} (mas)	θ_{LD} Rel	Used	Plx (mas)	Target/s
9228	K2III	K2III	6.08	3.13	0.186	1.336 ± 0.07	VW3	Y	5.99 ± 0.06[e]	τ Cet
10148	F0V	F0V	5.61	4.83	0.029	0.461 ± 0.02	VW3	Y	13.89 ± 0.11[e]	τ Cet
18978	A3IV-V	A3IV	4.09	3.54	0.000	0.719 ± 0.04	VW3	Y	38.58 ± 0.39[e]	τ Cet
17206	F7V	F7V	4.52	3.24	0.000	0.904 ± 0.05	VW3	Y	70.74 ± 0.45[e]	τ Cet
18622	-	A3IV	-	-	-	-	-	N[f]	-	α Hyi, χ Eri, τ Cet
1581	F9.5V	F9V	4.29	2.74	0.000	1.151 ± 0.06	VW3	Y	117.17 ± 0.33[e]	α Hyi, χ Eri
15233	F2II/III	F2II	5.40	4.51	0.000	0.543 ± 0.03	VW3	Y	21.01 ± 0.10[e]	α Hyi
19319	F0III/IV	F0III	5.16	4.28	0.000	0.580 ± 0.03	VW3	N[f]	23.36 ± 0.12[e]	α Hyi
11332	K0III	K0III	6.25	3.71	0.004	0.795 ± 0.04	VW3	Y	6.88 ± 0.03[e]	α Hyi, χ Eri
10019	G8III	G8III	6.95	4.76	0.013	0.573 ± 0.03	VW3	Y	5.61 ± 0.03[e]	χ Eri
16970A	A2Vn	A2V	3.55	-	0.000	0.754 ± 0.03	BV-feh	Y	43.60 ± 0.82[e]	δ Eri, ϵ Eri, 95 Cet A
19866	K0III	K0III	7.21	4.73	0.178	0.583 ± 0.03	VW3	Y	5.88 ± 0.04[e]	95 Cet A
20699	K0III	K0III	6.83	4.75	-0.048	0.580 ± 0.03	VW3	Y	6.24 ± 0.04[e]	95 Cet A
19994	F8.5V	F8V	5.13	3.77	0.000	0.785 ± 0.04	VW3	Y	44.37 ± 0.20[e]	95 Cet A
22484	F9IV-V	F9IV	4.35	2.92	0.000	1.127 ± 0.06	VW3	Y	71.62 ± 0.54[c]	40 Eri A, 95 Cet A
21530	K2II/III	K2II	5.85	3.33	-0.177	1.101 ± 0.06	VW3	Y	10.59 ± 0.09[e]	ϵ Eri
25725	M7+II	M7II	8.74	-0.32	-	-	VW4	N[h]	2.28 ± 0.68[c]	ϵ Eri
20010A	F6V	F6V	3.98	2.32	0.000	1.247 ± 0.06	VK	Y	71.68 ± 0.31[e]	δ Eri, ϵ Eri
24555	G6.5III	G6III	4.80	2.47	-0.007	1.414 ± 0.07	VK	Y	10.11 ± 0.24[e]	δ Eri, ϵ Eri
23304	K0III	K0III	7.33	4.88	0.102	0.546 ± 0.03	VW3	Y	5.25 ± 0.07[e]	δ Eri
26464	K1III	K1III	5.81	3.55	-0.011	1.039 ± 0.05	VW3	Y	10.01 ± 0.09[e]	δ Eri, 40 Eri A
24780	K4/5III	K4III	8.49	4.84	0.129	0.664 ± 0.03	VW3	Y	1.66 ± 0.05[e]	40 Eri A
26409	G8III	G8III	5.55	3.59	0.002	1.011 ± 0.05	VW3	Y	9.10 ± 0.11[e]	40 Eri A
27487	G8III	G8III	6.83	4.75	-0.011	0.560 ± 0.03	VW3	Y	4.96 ± 0.04[e]	40 Eri A
33111	A3IV	A3IV	2.78	2.44	0.000	1.241 ± 0.06	VW3	Y	36.50 ± 0.42[c]	40 Eri A

Notes: [a]SIMBAD, [b]Adopted for intrinsic colour grid interpolation,[c]Tycho Høg et al. (2000), [d]2MASS Skrutskie et al. (2006), [e]Gaia Brown et al. (2018), [f]Binarity, [g]IR excess, [h]Inconsistent photometry

Table A.2: – *continued*

HD	SpT (Actual)[a]	(Adopted)[b]	V_T^c (mag)	H^d (mag)	$E(B-V)$ (mag)	θ_{pred} (mas)	θ_{LD} Rel	Used	Plx (mas)	Target/s
136498	K2III	K2III	7.89	4.67	0.222	0.629 ± 0.03	VW3	Y	2.27 ± 0.05[e]	37 Lib
139155	K2/3IV	K2IV	8.64	5.00	0.472	0.548 ± 0.03	VW3	Y	1.69 ± 0.06[e]	37 Lib
149757	O9.2IVnn	O9IV	2.55	2.67	0.335	0.940 ± 0.05	VW3	Y	5.83 ± 1.02[e]	37 Lib
132052	F2V	F2V	4.50	3.82	0.000	0.753 ± 0.04	VW3	Y	36.31 ± 0.26[e]	37 Lib
141795	kA2hA5mA7V	A5V	3.71	3.44	0.000	0.789 ± 0.04	VW3	Y	48.08 ± 0.57[e]	37 Lib
128898	A7VpSrCrEu	A7V	3.19	2.47	0.000	1.157 ± 0.06	VW3	Y	62.94 ± 0.43[e]	β TrA
140018	K1/2III	K1III	7.01	3.97	0.290	0.847 ± 0.04	VW3	Y	1.96 ± 0.03[e]	β TrA
143853	K1III	K1III	7.24	3.92	0.268	0.706 ± 0.04	VW3	Y	2.05 ± 0.04[e]	β TrA
136225	K3III	K3III	7.30	3.66	0.305	0.969 ± 0.05	VW3	Y	1.22 ± 0.04[e]	β TrA
165040	kA4hF0mF2III	F0III	4.36	3.80	0.000	0.681 ± 0.03	VW3	Y	24.78 ± 0.31[e]	β TrA, HR7221
166464	K0III	K0III	5.08	2.71	0.059	1.433 ± 0.07	VW3	Y	12.63 ± 0.24[e]	λ Sgr
167720	K2III	K2III	5.97	2.43	0.392	1.790 ± 0.09	VW3	Y	3.02 ± 0.17[e]	λ Sgr
175191	B2V	B2V	-	-	-	-	-	N[f]	-	λ Sgr
165634	G7:IIIbCN-1CH-3.5HK+1	G7III	4.66	2.19	0.010	1.620 ± 0.08	VW3	Y	9.83 ± 0.34[e]	λ Sgr
169022	B9.5III	B9III	1.81	1.77	0.000	1.569 ± 0.11	VW4	Y	22.76 ± 0.24[c]	λ Sgr
192531	K0III	K0III	6.40	3.85	0.055	0.781 ± 0.04	VW3	Y	7.73 ± 0.03[e]	δ Pav
197051	A7III	A7III	3.43	2.79	0.000	0.982 ± 0.05	VW3	Y	25.64 ± 0.33[e]	δ Pav, ϵ Ind
197359	K0/1III	K0III	6.82	4.47	0.074	0.674 ± 0.03	VW3	Y	6.26 ± 0.03[e]	δ Pav
169326	K2III	K2III	6.09	3.50	0.028	1.089 ± 0.06	VW3	Y	6.66 ± 0.08[e]	δ Pav
191937	K3III	K3III	6.72	3.57	0.157	1.084 ± 0.06	VW3	Y	3.99 ± 0.03[e]	δ Pav
205935	K0II/III	K0II	6.45	3.95	-0.016	0.829 ± 0.04	VW3	Y	4.96 ± 0.03[e]	ϵ Ind
209952	B6V	B6V	1.76	2.03	0.000	1.112 ± 0.08	VW4	Y	32.29 ± 0.21[c]	ϵ Ind
212878	G8III	G8III	6.98	4.81	0.035	0.553 ± 0.03	VW3	Y	5.11 ± 0.04[e]	ϵ Ind
219571	F4V	F4V	4.03	3.08	0.000	1.077 ± 0.05	VW3	Y	42.32 ± 0.25[e]	ϵ Ind
4188	K0III	K0III	4.88	2.67	0.000	1.476 ± 0.08	VW3	Y	14.41 ± 0.37[e]	τ Cet

Table A.2: – *continued*

HD	SpT		V_T^c	H^d	$E(B-V)$	$\theta_{\rm pred}$	$\theta_{\rm LD}$ Rel	Used	Plx	Target/s
	(Actual)[a]	(Adopted)[b]	(mag)	(mag)	(mag)	(mas)			(mas)	
129008	G8III/IV	G8III	7.25	4.88	0.029	0.546 ± 0.03	VW3	Y	5.88 ± 0.05[e]	HD131977
133649	K0III	K0III	7.81	4.96	0.188	0.528 ± 0.03	VW3	Y	2.81 ± 0.05[e]	HD131977
133670	K0III	K0III	6.25	3.83	0.000	0.851 ± 0.04	VW3	Y	15.41 ± 0.06[e]	HD131977
129502	F2V	F2V	3.91	3.07	0.000	1.087 ± 0.06	VW3	Y	54.79 ± 0.51[e]	HD131977
133627	K0III	K0III	6.86	4.33	0.041	0.709 ± 0.04	VW3	Y	6.58 ± 0.05[e]	HD131977
152236	B1Ia-0ek	B1Ia	4.82	3.34	0.615	-	-	N[g]	0.71 ± 0.24[e]	η Sco
152293	F3II	F3II	5.91	4.25	0.294	0.604 ± 0.03	VW3	Y	0.31 ± 0.16[e]	η Sco
158408	B2IV	B2IV	2.62	3.11	0.051	-	-	N[f]	5.66 ± 0.18[c]	η Sco
135382	A1V	A1V	2.85	2.53	0.000	1.090 ± 0.06	VW3	Y	16.50 ± 0.73[e]	η Sco
160032	F4V	F4V	4.80	3.70	0.000	0.743 ± 0.04	VW3	Y	47.10 ± 0.29[e]	η Sco
182835	F2Ib	F2Ib	4.73	2.87	0.339	1.063 ± 0.05	VW3	Y	1.29 ± 0.22[e]	β Aql
193329	K0III	K0III	6.16	3.83	0.091	0.910 ± 0.05	VW3	Y	7.90 ± 0.07[e]	β Aql
189533	G8II	G8II	6.84	3.74	0.295	0.864 ± 0.04	VW3	Y	2.42 ± 0.04[e]	β Aql
189188	K2III	K2III	6.89	3.73	0.071	0.857 ± 0.04	VW3	Y	4.49 ± 0.04[e]	β Aql
194013	G8III-IV	G8III	5.41	3.31	0.038	1.143 ± 0.06	VW3	Y	12.59 ± 0.14[e]	β Aql
172555	A7V	A7V	4.79	4.25	0.000	0.792 ± 0.04	VW3	N[g]	35.29 ± 0.23[e]	HR7221
173948	B2Ve	B2V	4.18	4.32	0.051	0.419 ± 0.02	VW3	Y	4.80 ± 0.45[e]	HR7221
161955	K0/1III	K0III	6.58	4.10	0.100	0.746 ± 0.04	VW3	Y	6.85 ± 0.04[e]	HR7221
188228	A0Va	A0V	3.94	3.76	0.000	0.571 ± 0.03	VW3	Y	31.87 ± 0.33[e]	HR7221

Table A.3: Comparison between $\theta_{\rm LD}$ derived using Claret & Bloemen (2011) linear limb darkening coefficients and Magic et al. (2015) equivalent linear limb darkening coefficients. The absolute median percentage difference is 0.14%, with no obvious systematic observed. The largest discrepancy is for λ Sgr, our most well resolved star.

Star	$\theta_{\rm LD,CB11}$ (mas)	$\theta_{\rm LD,STAGGER}$ (mas)	$\sigma_{\theta_{\rm LD}}$ (%)
τ Cet	2.053 ± 0.011	2.054 ± 0.011	-0.07
χ Eri	2.139 ± 0.012	2.134 ± 0.011	0.25
95 Cet A	1.277 ± 0.012	1.280 ± 0.012	-0.26
ϵ Eri	2.146 ± 0.012	2.144 ± 0.011	0.08
δ Eri	2.413 ± 0.010	2.411 ± 0.009	0.08
40 Eri A	1.489 ± 0.012	1.486 ± 0.012	0.23
37 Lib	1.687 ± 0.010	1.684 ± 0.010	0.14
λ Sgr	4.074 ± 0.019	4.060 ± 0.015	0.35
δ Pav	1.826 ± 0.025	1.828 ± 0.025	-0.07
β Aql	2.137 ± 0.012	2.133 ± 0.012	0.18
HR7221	1.116 ± 0.015	1.117 ± 0.015	-0.14

Table A.4: Limb darkening coefficients

Star	CB11	Equivalent Linear Limb Darkening Coefficient						$\theta_{\rm LD}$ Scaling Term					
	$^{\rm u}\lambda$	$^{\rm u}\lambda_1$	$^{\rm u}\lambda_2$	$^{\rm u}\lambda_3$	$^{\rm u}\lambda_4$	$^{\rm u}\lambda_5$	$^{\rm u}\lambda_6$	$^{\rm s}\lambda_1$	$^{\rm s}\lambda_2$	$^{\rm s}\lambda_3$	$^{\rm s}\lambda_4$	$^{\rm s}\lambda_5$	$^{\rm s}\lambda_6$
τ Cet	-	0.247 ± 0.001	0.234 ± 0.001	0.221 ± 0.001	0.215 ± 0.001	0.210 ± 0.001	0.212 ± 0.001	0.994	0.995	0.995	0.995	0.995	0.995
α Hyi	0.211 ± 0.015	-	-	-	-	-	-	-	-	-	-	-	-
χ Eri	-	0.267 ± 0.006	0.251 ± 0.005	0.233 ± 0.005	0.227 ± 0.004	0.221 ± 0.004	0.226 ± 0.004	0.994	0.994	0.994	0.994	0.995	0.995
95 Cet A	-	0.313 ± 0.007	0.292 ± 0.006	0.268 ± 0.006	0.260 ± 0.006	0.253 ± 0.005	0.253 ± 0.005	0.993	0.993	0.993	0.994	0.994	0.994
ϵ Eri	-	0.275 ± 0.003	0.258 ± 0.002	0.243 ± 0.002	0.237 ± 0.002	0.231 ± 0.002	0.232 ± 0.002	0.994	0.994	0.994	0.994	0.994	0.994
δ Eri	-	0.282 ± 0.004	0.264 ± 0.004	0.245 ± 0.004	0.239 ± 0.003	0.232 ± 0.003	0.237 ± 0.003	0.994	0.994	0.994	0.994	0.994	0.994
40 Eri A	-	0.263 ± 0.002	0.248 ± 0.002	0.234 ± 0.002	0.227 ± 0.002	0.222 ± 0.002	0.224 ± 0.001	0.994	0.994	0.994	0.994	0.995	0.995
37 Lib	-	0.298 ± 0.007	0.279 ± 0.006	0.257 ± 0.006	0.250 ± 0.005	0.243 ± 0.005	0.245 ± 0.005	0.993	0.994	0.994	0.994	0.994	0.994
β TrA	0.209 ± 0.011	-	-	-	-	-	-	-	-	-	-	-	-
λ Sgr	-	0.307 ± 0.004	0.287 ± 0.003	0.263 ± 0.003	0.256 ± 0.003	0.248 ± 0.003	0.249 ± 0.003	0.993	0.993	0.994	0.994	0.994	0.994
δ Pav	-	0.251 ± 0.004	0.239 ± 0.004	0.226 ± 0.004	0.219 ± 0.004	0.213 ± 0.004	0.218 ± 0.003	0.994	0.995	0.995	0.995	0.995	0.995
ϵ Ind	0.382 ± 0.021	-	-	-	-	-	-	-	-	-	-	-	-
HD131977	0.359 ± 0.031	-	-	-	-	-	-	-	-	-	-	-	-
η Sco	0.215 ± 0.017	-	-	-	-	-	-	-	-	-	-	-	-
β Aql	-	0.266 ± 0.005	0.250 ± 0.004	0.233 ± 0.004	0.227 ± 0.004	0.221 ± 0.004	0.225 ± 0.003	0.994	0.994	0.994	0.995	0.995	0.995
HR7221	-	0.290 ± 0.004	0.271 ± 0.003	0.251 ± 0.003	0.245 ± 0.003	0.238 ± 0.003	0.241 ± 0.003	0.993	0.994	0.994	0.994	0.994	0.994

B Supplementary Information: TESS Candidate Planets

Table B.1: Observing log for TESS candidate exoplanet host stars

TIC	UT Date	airmass	exp	RV	SNR	
			(sec)	($km\,s^{-1}$)	(B)	(R)
219338557	19-08-25	1.1	120	36.00 ± 4.50	66	185
201248411	19-08-26	1.1	200	17.92 ± 4.50	52	142
262530407	19-08-26	1.1	200	8.71 ± 4.51	37	114
118327550	19-08-26	1.0	300	6.48 ± 4.53	23	75
410153553	19-08-26	1.3	600	-14.96 ± 4.55	14	63
62483237	19-08-26	1.0	150	6.17 ± 4.50	61	164
259377017	19-08-27	1.3	300	20.21 ± 4.53	26	84
200322593	19-08-27	1.4	600	12.61 ± 4.55	12	46
406941612	19-08-27	1.7	300	2.38 ± 4.52	24	80
193641523	19-08-27	1.7	300	26.62 ± 4.50	54	151
351601843	19-08-28	1.4	300	26.31 ± 4.51	21	71
234994474	19-08-28	1.1	300	24.29 ± 4.51	71	208
251848941	19-10-13	1.0	600	56.79 ± 4.50	72	199
259962054	19-10-14	1.2	300	-11.16 ± 4.54	6	27
101948569	19-10-14	1.0	120	22.63 ± 4.50	28	82
179985715	19-10-14	1.0	120	-12.54 ± 4.51	17	58
37749396	19-10-14	1.1	60	-9.28 ± 4.51	52	149
122613513	19-10-14	1.0	300	8.72 ± 4.50	54	145
229111835	19-10-14	1.1	300	13.15 ± 4.51	12	42
70899085	19-10-15	1.1	300	-12.74 ± 4.51	30	96
98796344	19-10-15	1.1	90	-10.03 ± 4.54	30	96
55488511	19-10-15	1.1	300	89.66 ± 4.51	18	63
271596225	19-10-15	1.4	300	-0.68 ± 4.52	15	53
44647437	19-10-16	1.0	300	14.43 ± 4.51	9	36
237914496	19-10-16	1.2	300	-6.74 ± 4.51	18	58
237920046	19-10-16	1.2	300	8.94 ± 4.51	12	43
201642601	19-10-17	1.3	900	-27.52 ± 4.51	16	57
158297421	19-10-17	1.2	900	-5.31 ± 4.50	14	49
261108236	19-10-17	1.5	600	4.02 ± 4.51	19	69
231702397	19-10-17	1.1	900	-76.33 ± 4.54	7	33
322063810	19-10-17	1.1	150	32.28 ± 4.51	47	137
220479565	19-10-17	1.1	600	30.73 ± 4.53	10	47
220459976	19-10-17	1.2	600	15.25 ± 4.51	20	73
192826603	19-10-17	1.1	1200	95.80 ± 4.52	7	38
44737596	19-10-17	1.1	1200	41.46 ± 4.52	6	36
38510224	19-10-17	1.2	300	29.91 ± 4.50	23	72
33831980	19-10-17	1.4	600	11.84 ± 4.51	25	85
219229644	19-10-17	1.1	300	48.73 ± 4.51	28	91
14165625	19-10-17	1.1	300	22.75 ± 4.50	27	86
32497972	19-10-17	1.0	300	3.57 ± 4.51	16	60
170849515	19-10-18	1.0	1800	4.86 ± 4.52	9	29
100608026	19-10-19	1.0	300	24.98 ± 4.51	29	97
144700903	19-10-19	1.4	700	-0.04 ± 4.51	12	53
12423815	19-11-16	1.0	2000	-11.69 ± 4.52	9	35

Table B.1: – *continued*

TIC	UT Date	airmass	exp (sec)	RV ($km\,s^{-1}$)	SNR (B)	SNR (R)
260708537	20-02-01	1.1	120	25.15 ± 4.53	32	102
35009898	20-02-01	1.2	600	-41.91 ± 4.53	14	52
151825527	20-02-01	1.0	450	-5.31 ± 4.52	23	80
150428135	20-02-01	1.2	360	-4.25 ± 4.53	29	92
260004324	20-02-01	1.1	180	41.76 ± 4.52	32	99
167600516	20-02-01	1.2	300	36.55 ± 4.51	45	136
219195044	20-02-01	1.1	450	117.69 ± 4.52	28	90
73649615	20-02-01	1.0	700	14.53 ± 4.52	12	50
165317334	20-02-01	1.0	150	4.98 ± 4.51	22	80
440887364	20-02-01	1.1	45	-25.52 ± 4.50	46	140
307210830	20-02-03	1.3	120	-5.17 ± 4.53	23	88
141608198	20-02-03	1.4	900	14.91 ± 4.54	8	44
33521996	20-02-03	1.0	900	41.68 ± 4.52	6	37
19025965	20-02-03	1.6	360	46.78 ± 4.50	17	73
27649847	20-02-03	1.4	720	-10.40 ± 4.53	8	44
413248763	20-02-03	1.0	45	-36.03 ± 4.53	22	80
296739893	20-02-03	1.1	300	8.47 ± 4.52	38	118
36734222	20-02-03	1.1	450	-8.65 ± 4.51	24	89
54962195	20-02-03	1.1	450	25.13 ± 4.52	7	44
158588995	20-02-03	1.0	720	7.25 ± 4.53	9	49
141527579	20-02-03	1.4	900	24.59 ± 4.52	20	75
149788158	20-02-03	1.2	360	24.03 ± 4.52	19	73
34068865	20-02-03	1.1	30	50.46 ± 4.52	30	99
36724087	20-02-03	1.1	360	-7.62 ± 4.53	14	60
359271092	20-02-03	1.2	20	37.39 ± 4.51	24	91
429358906	20-02-03	1.1	1200	-1.21 ± 4.54	6	43
374829238	20-02-03	1.2	600	15.29 ± 4.51	19	73
300710077	20-02-03	1.3	660	58.98 ± 4.53	12	60
362249359	20-02-03	1.2	180	14.78 ± 4.51	32	110
210873792	20-02-03	1.4	450	-75.36 ± 4.51	22	78
261257684	20-02-03	1.6	300	7.56 ± 4.51	25	91
280437559	20-02-03	1.3	180	-3.64 ± 4.50	25	91
370133522	20-09-11	1.3	180	-0.93 ± 4.53	20	70
12421862	20-09-11	1.0	180	19.29 ± 4.51	28	97
415969908	20-09-11	1.0	450	24.75 ± 4.52	20	71
92226327	20-09-11	1.1	450	-15.10 ± 4.55	9	44
348538431	20-09-11	2.0	900	-6.72 ± 4.56	15	56
254113311	20-09-12	1.0	180	-7.33 ± 4.50	39	115
29960110	20-09-12	1.0	360	26.52 ± 4.52	17	63
425934411	20-09-12	1.2	1200	-47.79 ± 4.53	11	52
153065527	20-09-12	1.0	450	17.50 ± 4.54	8	41
50618703	20-09-12	1.3	120	10.43 ± 4.50	36	111
77156829	20-09-12	1.0	300	9.06 ± 4.53	21	77
231728511	20-09-12	1.1	450	-5.94 ± 4.53	13	51
369327947	20-09-12	1.6	300	-13.78 ± 4.53	23	79
175532955	20-09-12	1.0	360	76.23 ± 4.50	25	79
141527965	20-09-13	1.4	450	37.43 ± 4.50	29	90
260417932	20-09-13	1.2	300	36.85 ± 4.50	42	116

Table B.2: Observing log for cool dwarf standards

Gaia DR2	UT Date	airmass	exp (sec)	RV ($km\,s^{-1}$)	SNR (B)	SNR (R)
19316224572460416	19-07-22	1.5	5	20.65 ± 4.50	108	251
2306965202564506752	19-07-22	1.0	200	19.60 ± 4.52	180	487
2603090003484152064	19-07-22	1.1	300	-4.68 ± 4.53	100	281
2683023811628007296	19-07-22	1.3	300	19.01 ± 4.51	159	462
2828928008202069376	19-07-22	1.5	200	-30.56 ± 4.51	158	458
5134635708766250752	19-07-22	1.1	300	8.56 ± 4.51	182	529
6553614253923452800	19-07-22	1.0	30	7.13 ± 4.51	117	335
6604147121141267712	19-07-22	1.0	30	8.13 ± 4.50	192	474
2552925644460225152	19-08-26	1.2	10	-14.82 ± 4.50	144	309
2627117287488522240	19-08-26	1.5	60	-18.10 ± 4.53	92	247
2653762573103102592	19-08-26	1.5	90	11.04 ± 4.51	94	271
2702655587447223168	19-08-26	1.6	300	-13.88 ± 4.51	74	219
2739689239311660672	19-08-26	1.2	90	-79.67 ± 4.52	73	213
4282578724832056576	19-08-26	1.7	120	9.19 ± 4.51	82	234
4293318823182081408	19-08-26	1.7	100	30.79 ± 4.52	85	228
6412595290592307840	19-08-26	1.1	6	-42.60 ± 4.50	296	711
6562924609150908416	19-08-26	1.1	60	7.74 ± 4.52	180	492
2611163717366876544	19-08-27	1.2	60	-11.00 ± 4.51	45	139
2815543034682035840	19-08-27	1.6	90	-7.36 ± 4.51	44	136
3209938366665770752	19-08-27	2.6	30	2.25 ± 4.51	66	209
114207651462714880	19-10-12	1.9	300	26.03 ± 4.53	114	346
2515037264041041536	19-10-12	1.2	120	-10.79 ± 4.52	110	309
2560771312759450496	19-10-12	1.2	180	-31.93 ± 4.52	77	227
301785537751949824	19-10-12	2.0	300	-9.94 ± 4.51	65	211
87921523897823872	19-10-12	1.7	300	-4.49 ± 4.52	65	197
145421309108301184	19-10-14	1.7	60	-35.17 ± 4.51	93	282
3210731015767419520	19-10-14	1.2	30	-55.79 ± 4.50	109	278
3339921875389105152	19-10-14	1.4	120	20.00 ± 4.51	108	318
3359074685047632640	19-10-14	1.8	200	-60.17 ± 4.51	91	282
3409711211681795584	19-10-14	1.6	180	23.09 ± 4.52	78	233
1736838805468812160	19-10-15	1.4	30	-70.90 ± 4.50	58	162
3057712188691831936	19-10-15	1.2	90	-20.08 ± 4.51	92	274
4075141768785646848	19-10-15	1.5	60	-9.52 ± 4.55	32	110
4971496564348094336	19-10-15	1.0	90	43.73 ± 4.52	52	148
5006921282807193856	19-10-15	1.0	150	40.49 ± 4.51	61	179
2910909931633597312	19-10-17	1.0	144	53.69 ± 4.52	44	125
2979590513145784192	19-10-17	1.0	144	-15.39 ± 4.52	43	131
3101920046552857728	19-10-17	1.2	90	-11.34 ± 4.52	65	184
3117120863523946368	19-10-17	1.2	90	11.51 ± 4.55	25	91
3136952686035250688	19-10-17	1.4	90	19.87 ± 4.56	25	87
3184351876391975808	19-10-17	1.1	90	-10.63 ± 4.52	44	130
3316364602541746048	19-10-17	1.2	144	24.40 ± 4.54	31	104
5951824121022278144	19-10-17	1.5	108	-8.80 ± 4.53	75	223
3057712223051571200	20-02-01	1.1	12	-13.82 ± 4.50	99	231
4364527594192166400	20-02-01	2.1	15	36.77 ± 4.51	65	195
5378886891122066560	20-02-01	1.0	15	14.90 ± 4.50	81	206
6143175840404555008	20-02-01	1.0	24	-4.07 ± 4.50	35	101

Table B.2: – *continued*

Gaia DR2	UT Date	airmass	exp (sec)	RV ($km\,s^{-1}$)	SNR (B)	SNR (R)
6223456372670070656	20-02-01	1.1	90	18.75 ± 4.50	79	202
6288325222245417856	20-02-01	1.0	15	-36.71 ± 4.50	63	184
1244644727396803584	20-02-03	1.6	60	24.60 ± 4.51	46	152
3089711447388931584	20-02-03	1.2	60	65.99 ± 4.52	44	138
3195919322830293760	20-02-03	1.1	144	-45.15 ± 4.55	41	120
3256334497479041024	20-02-03	1.2	15	13.50 ± 4.50	55	152
3520548825260557312	20-02-03	1.0	60	112.47 ± 4.51	64	158
3550084490721711872	20-02-03	1.1	90	30.33 ± 4.50	51	143
3630092241022731136	20-02-03	1.1	36	-15.90 ± 4.50	51	144
3661492609484469504	20-02-03	1.2	60	-37.17 ± 4.50	75	210
3689602277083844480	20-02-03	1.2	72	8.91 ± 4.51	105	321
3738099879558957952	20-02-03	1.4	72	18.94 ± 4.51	79	240
3741297293732404352	20-02-03	1.5	45	19.02 ± 4.52	80	235
3767878708888402816	20-02-03	1.2	90	26.64 ± 4.51	53	163
3796072592206250624	20-02-03	1.2	120	-34.21 ± 4.54	21	90
3828238392559860992	20-02-03	1.3	120	10.18 ± 4.52	92	268
3855208897392952192	20-02-03	1.3	120	6.61 ± 4.52	70	211
3902785109124370432	20-02-03	1.4	300	20.95 ± 4.51	106	322
4017860992519744384	20-02-03	1.9	120	4.28 ± 4.53	33	118
4330690742322011520	20-02-03	1.4	120	-25.48 ± 4.53	62	195
4364480521350598144	20-02-03	1.8	60	31.88 ± 4.52	39	130
5170039502144332800	20-02-03	1.2	15	-1.55 ± 4.50	58	164
5266270443442455040	20-02-03	1.3	90	18.99 ± 4.50	70	183
614543647497149056	20-02-03	1.6	90	12.23 ± 4.52	36	118
6232511606838403968	20-02-03	1.2	7	27.29 ± 4.50	130	330
6324325225803432320	20-02-03	1.2	144	-1.32 ± 4.54	38	122
116037376250217984	20-09-11	1.9	500	25.26 ± 4.53	28	99
1750765357185849856	20-09-11	1.5	500	-25.65 ± 4.54	25	96
18565464288396416	20-09-11	1.3	240	20.98 ± 4.53	36	112
2029432043779954432	20-09-11	2.4	600	-48.01 ± 4.54	11	52
2316867885320845696	20-09-11	1.0	150	16.65 ± 4.52	35	109
2358524597030794112	20-09-11	1.1	240	18.71 ± 4.56	26	98
2435125446129139712	20-09-11	1.1	450	-30.75 ± 4.53	27	94
2533723464155234176	20-09-11	1.3	150	13.99 ± 4.51	46	144
2595284016771502080	20-09-11	1.0	600	-14.03 ± 4.55	23	86
2640434056928150400	20-09-11	1.2	500	-41.88 ± 4.56	9	64
2817999068780218368	20-09-11	1.6	240	-7.29 ± 4.54	32	103
4145870293808914688	20-09-11	1.1	920	-46.19 ± 4.55	21	66
4177731838628465408	20-09-11	1.2	36	23.09 ± 4.52	43	132
4187836934609063552	20-09-11	1.1	1500	-58.36 ± 4.54	31	102
4303294035005560704	20-09-11	1.5	450	-0.34 ± 4.53	37	117
4339465360508118912	20-09-11	1.2	240	12.31 ± 4.54	34	111
4365609170043180416	20-09-11	1.2	360	-11.77 ± 4.55	31	105
4375233191015944192	20-09-11	1.3	15	-22.90 ± 4.51	65	197
4389844948935164544	20-09-11	1.3	45	-14.11 ± 4.51	47	148
4472832130942575872	20-09-11	1.3	30	-109.09 ± 4.56	29	106
4498055584805914752	20-09-11	1.7	920	-28.75 ± 4.54	32	107
4550763526539955712	20-09-11	1.7	45	-11.93 ± 4.51	38	123

Table B.2: – *continued*

Gaia DR2	UT Date	airmass	exp (sec)	RV ($km\,s^{-1}$)	SNR (B)	SNR (R)
4572835535272064768	20-09-11	2.2	60	2.41 ± 4.51	41	136
4584638930036248192	20-09-11	2.5	600	-2.63 ± 4.52	31	108
5042734468172061440	20-09-11	1.1	240	-41.49 ± 4.52	49	149
5853498713160606720	20-09-11	1.4	60	-26.88 ± 4.56	49	187
6245870673116518784	20-09-11	1.2	180	-2.02 ± 4.53	38	113
6322070093095493504	20-09-11	1.5	120	-9.91 ± 4.53	42	133
6882963066420161664	20-09-11	1.2	150	6.16 ± 4.54	27	96
6885776098199761024	20-09-11	1.2	150	-66.40 ± 4.52	41	131
6890353330746858368	20-09-11	1.2	240	27.46 ± 4.53	42	124
76868614540049408	20-09-11	1.5	240	-34.31 ± 4.56	21	83
102162639019033600	20-09-12	1.9	600	-10.88 ± 4.54	21	79
1784473016438653056	20-09-12	1.6	60	-27.82 ± 4.53	32	106
1809359465717142656	20-09-12	1.6	500	-51.83 ± 4.54	20	64
1810616448010879488	20-09-12	1.6	450	-62.47 ± 4.54	27	98
1814070838668707840	20-09-12	1.8	90	5.78 ± 4.51	40	129
1838855376946302720	20-09-12	1.9	294	-31.81 ± 4.53	30	104
2507016253701863040	20-09-12	1.2	450	21.18 ± 4.54	26	89
2976850598890038784	20-09-12	1.2	240	9.31 ± 4.53	28	95
3187115498866675456	20-09-12	1.4	240	32.96 ± 4.55	23	85
3219851121121855872	20-09-12	1.3	500	31.72 ± 4.52	38	120
3239548631415741440	20-09-12	1.6	360	40.94 ± 4.52	35	111
3288082758293022848	20-09-12	1.7	240	-15.01 ± 4.53	27	88
35398295820372864	20-09-12	1.6	600	-37.31 ± 4.54	20	74
4295619138933719808	20-09-12	1.4	600	19.28 ± 4.54	30	96
4393265392167891712	20-09-12	1.4	600	11.05 ± 4.54	22	76
4508377078422114944	20-09-12	1.5	360	-48.72 ± 4.54	26	82
4512525016089353472	20-09-12	1.7	500	11.51 ± 4.55	31	108
4519789081415296128	20-09-12	1.9	150	30.19 ± 4.53	40	134
4519789321933481856	20-09-12	1.9	150	32.15 ± 4.53	40	135
4535928365908540416	20-09-12	2.2	240	22.56 ± 4.54	17	56
5077642283022422656	20-09-12	1.0	90	31.72 ± 4.51	42	130
2467732906559754496	20-09-13	1.1	500	-5.83 ± 4.56	21	80
2549050931124387456	20-09-13	1.2	600	-5.17 ± 4.53	31	100
2848646203058386560	20-09-13	1.7	450	-48.92 ± 4.53	37	116
2868199402451064064	20-09-13	2.2	600	-15.06 ± 4.56	21	85
2911981886751531648	20-09-13	1.1	240	4.93 ± 4.53	34	106
3011648664439643520	20-09-13	1.1	120	21.03 ± 4.50	46	127
3131777319158582272	20-09-13	1.4	300	-6.02 ± 4.52	28	97
3266980243936341248	20-09-13	1.2	600	82.84 ± 4.52	28	93
4706630501049679744	20-09-13	1.4	60	39.09 ± 4.50	96	243
4871271406553197184	20-09-13	1.0	90	26.97 ± 4.50	53	140
5142772953804963456	20-09-13	1.1	600	-2.48 ± 4.53	38	119
6391176735363140480	20-09-13	1.4	30	4.49 ± 4.50	69	192

Table B.3: Final results for cool dwarf standards

Gaia DR2	$T_{\rm eff}$ (K)	$\log g$	[Fe/H]	M ($M_\odot$)	$R_\star$ ($R_\odot$)	$m_{\rm bol}$	$f_{\rm bol}$ (10^{-12} ergs s^{-1} cm $^{-2}$)
5853498713160606720	2885 ± 30	5.14 ± 0.02	-	0.124 ± 0.003	0.156 ± 0.003	7.36 ± 0.01	28793.2 ± 291.5
2640434056928150400	2927 ± 30	5.20 ± 0.02	-	0.120 ± 0.003	0.144 ± 0.003	11.19 ± 0.01	851.2 ± 8.9
2595284016771502080	3006 ± 30	5.03 ± 0.02	-	0.176 ± 0.004	0.212 ± 0.004	10.25 ± 0.01	2020.5 ± 21.1
2467732906559754496	3022 ± 30	5.10 ± 0.02	-	0.145 ± 0.004	0.178 ± 0.004	11.43 ± 0.01	680.0 ± 7.0
4393265392167891712	3035 ± 30	5.03 ± 0.02	-	0.181 ± 0.004	0.214 ± 0.004	11.71 ± 0.01	524.2 ± 5.4
4145870293808914688	3061 ± 30	5.08 ± 0.02	-	0.153 ± 0.004	0.187 ± 0.004	10.65 ± 0.01	1398.5 ± 14.2
2358524597030794112	3062 ± 30	5.13 ± 0.02	-0.29	0.137 ± 0.003	0.167 ± 0.003	9.24 ± 0.01	5113.3 ± 52.0
1810616448010879488	3064 ± 30	4.99 ± 0.02	-	0.190 ± 0.005	0.231 ± 0.005	10.58 ± 0.01	1488.6 ± 14.8
76868614540049408	3069 ± 30	5.09 ± 0.02	-0.17	0.148 ± 0.003	0.182 ± 0.004	9.45 ± 0.01	4221.2 ± 42.1
2868199402451064064	3088 ± 30	5.06 ± 0.02	-0.15	0.156 ± 0.004	0.192 ± 0.004	11.58 ± 0.01	591.2 ± 5.9
3117120863523946368	3094 ± 30	4.91 ± 0.02	-	0.236 ± 0.006	0.281 ± 0.006	8.29 ± 0.01	12313.6 ± 123.2
1750765357185849856	3121 ± 30	5.04 ± 0.02	-	0.183 ± 0.004	0.215 ± 0.004	11.30 ± 0.01	765.6 ± 7.7
2029432043779954432	3128 ± 30	4.98 ± 0.02	0.23	0.206 ± 0.005	0.242 ± 0.005	11.51 ± 0.01	632.4 ± 6.3
3796072592206250624	3136 ± 30	5.06 ± 0.02	-0.08	0.176 ± 0.004	0.206 ± 0.004	8.47 ± 0.01	10415.1 ± 105.8
2549050931124387456	3139 ± 30	4.72 ± 0.02	-	0.384 ± 0.009	0.445 ± 0.009	12.05 ± 0.01	385.1 ± 3.9
3187115498866675456	3142 ± 30	5.08 ± 0.02	-0.14	0.171 ± 0.004	0.198 ± 0.004	9.56 ± 0.01	3810.3 ± 38.7
3195919322830293760	3160 ± 30	4.94 ± 0.02	-	0.231 ± 0.006	0.269 ± 0.005	8.72 ± 0.01	8276.6 ± 84.2
4512525016089353472	3167 ± 30	4.98 ± 0.02	-	0.207 ± 0.005	0.244 ± 0.005	11.16 ± 0.01	869.9 ± 8.7
102162639019033600	3169 ± 30	4.98 ± 0.02	0.05	0.212 ± 0.005	0.246 ± 0.005	10.39 ± 0.01	1773.4 ± 17.7
6882963066420161664	3173 ± 30	4.97 ± 0.02	-	0.232 ± 0.006	0.261 ± 0.005	9.01 ± 0.01	6339.3 ± 64.0
4472832130942575872	3188 ± 30	5.06 ± 0.02	-0.51	0.160 ± 0.004	0.195 ± 0.004	7.19 ± 0.01	33821.5 ± 338.4
4535928365908540416	3201 ± 30	4.83 ± 0.02	0.65	0.342 ± 0.008	0.370 ± 0.007	9.45 ± 0.01	4204.3 ± 42.0
4075141768785646848	3204 ± 30	5.06 ± 0.02	-0.32	0.177 ± 0.004	0.207 ± 0.004	8.10 ± 0.01	14680.7 ± 146.2
3316364602541746048	3206 ± 30	4.97 ± 0.02	0.05	0.231 ± 0.006	0.262 ± 0.005	8.79 ± 0.01	7711.6 ± 76.7
4187836934609063552	3208 ± 30	4.98 ± 0.02	-0.01	0.230 ± 0.006	0.258 ± 0.005	11.48 ± 0.01	649.8 ± 6.5
1809359465717142656	3221 ± 30	4.92 ± 0.02	-	0.244 ± 0.006	0.282 ± 0.005	11.56 ± 0.01	605.2 ± 6.0
4365609170043180416	3224 ± 30	4.98 ± 0.02	-0.02	0.235 ± 0.006	0.260 ± 0.005	9.90 ± 0.01	2796.5 ± 28.1
2507016253701863040	3227 ± 30	4.97 ± 0.02	0.21	0.256 ± 0.006	0.275 ± 0.005	10.99 ± 0.01	1017.2 ± 10.3
18565464288396416	3234 ± 30	4.92 ± 0.02	0.02	0.252 ± 0.006	0.288 ± 0.005	9.26 ± 0.01	5022.8 ± 50.2
3136952686035250688	3241 ± 30	4.88 ± 0.02	0.44	0.315 ± 0.007	0.336 ± 0.006	8.51 ± 0.01	10006.1 ± 101.8
4339465360508118912	3247 ± 30	5.01 ± 0.02	-	0.209 ± 0.005	0.237 ± 0.004	9.44 ± 0.01	4269.1 ± 42.5
2848646203058386560	3250 ± 30	4.78 ± 0.02	-	0.373 ± 0.009	0.410 ± 0.008	10.73 ± 0.01	1293.0 ± 12.9
3288082758293022848	3250 ± 30	4.81 ± 0.02	-	0.366 ± 0.009	0.393 ± 0.007	9.73 ± 0.01	3258.4 ± 32.9
4508377078422114944	3265 ± 30	4.89 ± 0.02	0.14	0.294 ± 0.007	0.322 ± 0.006	10.09 ± 0.01	2345.5 ± 23.3

Table B.3: – *continued*

Gaia DR2	$T_{\rm eff}$ (K)	$\log g$	[Fe/H]	M ($M_\odot$)	$R_\star$ ($R_\odot$)	$m_{\rm bol}$	$f_{\rm bol}$ (10^{-12} ergs s^{-1} cm^{-2})
4303294035005560704	3277 ± 30	4.82 ± 0.02	-	0.354 ± 0.009	0.383 ± 0.007	10.75 ± 0.01	1279.4 ± 12.7
2435125446129139712	3278 ± 30	4.95 ± 0.02	0.32	0.303 ± 0.008	0.305 ± 0.006	10.93 ± 0.01	1081.2 ± 11.1
116037376250217984	3282 ± 30	4.90 ± 0.02	0.19	0.304 ± 0.007	0.324 ± 0.006	11.41 ± 0.01	692.3 ± 6.9
6324325225803432320	3283 ± 30	4.96 ± 0.02	0.32	0.294 ± 0.008	0.299 ± 0.006	8.80 ± 0.01	7681.5 ± 78.9
4295619138933719808	3299 ± 30	5.01 ± 0.02	-0.37	0.220 ± 0.005	0.242 ± 0.004	10.39 ± 0.01	1781.8 ± 17.9
1784473016438653056	3303 ± 30	4.76 ± 0.02	-	0.395 ± 0.009	0.433 ± 0.008	8.14 ± 0.01	14033.5 ± 139.9
4330690742322011520	3309 ± 30	4.91 ± 0.02	0.07	0.302 ± 0.008	0.321 ± 0.006	7.80 ± 0.01	19231.6 ± 191.5
2603090003484152064	3326 ± 30	4.89 ± 0.02	0.29	0.338 ± 0.008	0.347 ± 0.006	7.79 ± 0.01	19393.6 ± 194.0
35398295820372864	3330 ± 30	4.81 ± 0.02	-	0.370 ± 0.010	0.396 ± 0.009	10.57 ± 0.01	1508.8 ± 15.0
2976850598890038784	3337 ± 30	4.96 ± 0.02	-	0.274 ± 0.007	0.287 ± 0.005	9.66 ± 0.01	3465.4 ± 34.6
2817999068780218368	3344 ± 30	4.83 ± 0.02	0.39	0.381 ± 0.009	0.394 ± 0.007	9.26 ± 0.01	5021.5 ± 50.0
6322070093095493504	3360 ± 30	4.90 ± 0.02	-0.10	0.311 ± 0.008	0.327 ± 0.006	8.52 ± 0.01	9900.6 ± 98.6
6245870673116518784	3360 ± 30	4.69 ± 0.02	-	0.481 ± 0.011	0.515 ± 0.009	9.35 ± 0.01	4619.8 ± 46.8
2911981886751531648	3362 ± 30	4.92 ± 0.02	-0.13	0.305 ± 0.007	0.316 ± 0.006	9.88 ± 0.01	2831.9 ± 28.5
4498055584805914752	3385 ± 30	4.97 ± 0.02	-0.36	0.259 ± 0.006	0.276 ± 0.005	11.28 ± 0.01	785.0 ± 7.8
114207651462714880	3403 ± 30	4.84 ± 0.02	-0.08	0.357 ± 0.009	0.374 ± 0.007	8.60 ± 0.01	9191.7 ± 91.6
5951824121022278144	3435 ± 30	4.88 ± 0.02	-0.13	0.353 ± 0.008	0.359 ± 0.006	7.52 ± 0.01	25039.0 ± 249.3
3219851121121855872	3456 ± 30	4.69 ± 0.02	-	0.498 ± 0.012	0.524 ± 0.009	11.50 ± 0.01	636.8 ± 6.4
4017860992519744384	3459 ± 30	4.79 ± 0.02	0.05	0.423 ± 0.010	0.434 ± 0.008	8.73 ± 0.01	8170.7 ± 81.3
5142772953804963456	3483 ± 30	4.89 ± 0.02	-	0.352 ± 0.008	0.354 ± 0.006	12.06 ± 0.01	379.6 ± 3.8
1838855376946302720	3484 ± 30	4.93 ± 0.02	-	0.311 ± 0.008	0.315 ± 0.006	10.24 ± 0.01	2033.8 ± 20.3
2560771312759450496	3497 ± 30	4.84 ± 0.02	-0.13	0.403 ± 0.010	0.402 ± 0.007	9.17 ± 0.01	5445.7 ± 54.4
2627117287488522240	3505 ± 30	4.77 ± 0.02	0.29	0.465 ± 0.011	0.463 ± 0.008	8.31 ± 0.01	12075.4 ± 120.5
6890353330746858368	3511 ± 30	4.76 ± 0.02	0.17	0.468 ± 0.011	0.470 ± 0.008	9.58 ± 0.01	3738.4 ± 37.5
4584638930036248192	3516 ± 30	4.76 ± 0.02	-0.05	0.448 ± 0.011	0.460 ± 0.008	10.85 ± 0.01	1166.3 ± 11.6
2979590513145784192	3522 ± 30	4.83 ± 0.02	-0.19	0.409 ± 0.010	0.407 ± 0.007	9.23 ± 0.01	5167.2 ± 51.5
3239548631415741440	3530 ± 30	4.48 ± 0.02	-	0.624 ± 0.015	0.747 ± 0.013	10.28 ± 0.01	1955.6 ± 19.5
3101920046552857728	3533 ± 30	4.79 ± 0.02	-0.07	0.441 ± 0.012	0.445 ± 0.008	8.35 ± 0.01	11628.5 ± 115.7
3089711447388931584	3534 ± 30	4.79 ± 0.02	-0.09	0.442 ± 0.011	0.444 ± 0.008	8.40 ± 0.01	11122.0 ± 110.7
3855208897392952192	3540 ± 30	4.81 ± 0.02	-0.11	0.431 ± 0.010	0.429 ± 0.007	7.95 ± 0.01	16866.3 ± 167.9
4519789081415296128	3541 ± 30	4.94 ± 0.02	-	0.319 ± 0.008	0.319 ± 0.005	9.08 ± 0.01	5906.7 ± 58.9
4519789321933481856	3543 ± 30	4.94 ± 0.02	-	0.318 ± 0.008	0.317 ± 0.005	9.09 ± 0.01	5856.8 ± 58.4
3131777319158582272	3545 ± 30	4.65 ± 0.02	-	0.528 ± 0.013	0.566 ± 0.010	10.46 ± 0.01	1659.9 ± 16.5
3184351876391975808	3555 ± 30	4.75 ± 0.02	-	0.470 ± 0.011	0.478 ± 0.008	8.70 ± 0.01	8389.8 ± 83.5
4293318823182081408	3555 ± 30	4.76 ± 0.02	0.07	0.474 ± 0.011	0.476 ± 0.008	7.32 ± 0.01	29932.3 ± 298.2

Table B.3: – *continued*

Gaia DR2	$T_{\rm eff}$ (K)	$\log g$	[Fe/H]	M ($M_\odot$)	$R_\star$ ($R_\odot$)	$m_{\rm bol}$	$f_{\rm bol}$ (10^{-12} ergs s^{-1} cm $^{-2}$)
3409711211681795584	3560 ± 30	4.73 ± 0.02	0.06	0.489 ± 0.012	0.500 ± 0.009	8.24 ± 0.01	12905.3 ± 128.4
2910909931633597312	3582 ± 30	4.71 ± 0.02	0.26	0.517 ± 0.012	0.527 ± 0.009	8.95 ± 0.01	6698.1 ± 66.7
614543647497149056	3583 ± 30	4.75 ± 0.02	-0.07	0.474 ± 0.011	0.478 ± 0.008	8.73 ± 0.01	8157.1 ± 81.2
87921523897823872	3601 ± 30	4.72 ± 0.02	0.10	0.511 ± 0.012	0.518 ± 0.009	8.97 ± 0.01	6591.2 ± 65.6
6885776098199761024	3611 ± 30	4.91 ± 0.02	-0.56	0.355 ± 0.009	0.345 ± 0.006	9.46 ± 0.01	4186.0 ± 41.8
4364480521350598144	3615 ± 30	4.77 ± 0.02	-0.21	0.464 ± 0.011	0.467 ± 0.008	8.53 ± 0.01	9818.2 ± 97.8
6562924609150908416	3615 ± 30	4.81 ± 0.02	-0.22	0.440 ± 0.010	0.434 ± 0.007	7.07 ± 0.01	37591.6 ± 374.6
4971496564348094336	3618 ± 30	4.71 ± 0.02	0.04	0.516 ± 0.012	0.526 ± 0.009	8.71 ± 0.01	8361.5 ± 83.2
2316867885320845696	3622 ± 30	4.71 ± 0.02	0.16	0.525 ± 0.012	0.530 ± 0.009	9.43 ± 0.01	4283.9 ± 42.6
3828238392559860992	3627 ± 30	4.72 ± 0.02	0.03	0.512 ± 0.012	0.518 ± 0.009	7.63 ± 0.01	22534.9 ± 224.3
2515037264041041536	3635 ± 30	4.79 ± 0.02	-0.33	0.449 ± 0.011	0.449 ± 0.008	8.60 ± 0.01	9214.0 ± 92.0
4550763526539955712	3638 ± 30	4.81 ± 0.02	-0.32	0.442 ± 0.010	0.436 ± 0.007	8.12 ± 0.01	14421.3 ± 143.6
3767878708888402816	3647 ± 30	4.70 ± 0.02	-0.01	0.526 ± 0.013	0.538 ± 0.009	8.63 ± 0.01	8991.2 ± 89.5
4177731838628465408	3649 ± 30	4.79 ± 0.02	-0.22	0.466 ± 0.011	0.456 ± 0.008	7.89 ± 0.01	17811.0 ± 177.3
6553614253923452800	3656 ± 30	4.74 ± 0.04	-0.35	0.463 ± 0.034	0.479 ± 0.008	5.91 ± 0.01	109647.8 ± 1093.2
3741297293732404352	3657 ± 30	4.75 ± 0.02	-0.19	0.487 ± 0.011	0.486 ± 0.008	6.97 ± 0.01	41290.1 ± 411.5
5042734468172061440	3660 ± 30	4.77 ± 0.02	-	0.484 ± 0.011	0.476 ± 0.008	9.68 ± 0.01	3399.1 ± 33.9
2739689239311660672	3673 ± 30	4.85 ± 0.02	-0.44	0.413 ± 0.010	0.399 ± 0.007	7.56 ± 0.01	23962.9 ± 238.6
4572835535272064768	3680 ± 30	4.72 ± 0.02	-0.09	0.518 ± 0.012	0.523 ± 0.009	8.19 ± 0.01	13424.8 ± 133.7
2306965202564506752	3683 ± 30	4.90 ± 0.02	-	0.389 ± 0.009	0.368 ± 0.006	7.06 ± 0.01	38086.6 ± 379.9
2828928008202069376	3687 ± 30	4.67 ± 0.02	0.09	0.551 ± 0.013	0.564 ± 0.009	7.12 ± 0.01	36004.7 ± 358.9
3209938366665770752	3693 ± 30	4.58 ± 0.04	-0.02	0.562 ± 0.042	0.635 ± 0.010	6.45 ± 0.01	66571.3 ± 665.3
3738099879558957952	3707 ± 30	4.75 ± 0.02	-0.16	0.505 ± 0.012	0.495 ± 0.008	7.61 ± 0.01	23016.6 ± 229.1
4389844948935164544	3734 ± 30	4.69 ± 0.02	-0.13	0.541 ± 0.014	0.551 ± 0.009	7.96 ± 0.01	16663.8 ± 166.0
3359074685047632640	3746 ± 30	4.79 ± 0.02	-0.44	0.467 ± 0.011	0.454 ± 0.007	8.34 ± 0.01	11698.3 ± 116.7
3266980243936341248	3756 ± 30	4.92 ± 0.02	-	0.376 ± 0.009	0.352 ± 0.006	13.32 ± 0.01	119.5 ± 1.2
2683023811628007296	3802 ± 30	4.67 ± 0.02	-0.05	0.571 ± 0.014	0.578 ± 0.009	7.87 ± 0.01	18086.3 ± 180.1
4282578724832056576	3810 ± 30	4.66 ± 0.02	0.02	0.582 ± 0.014	0.593 ± 0.009	7.92 ± 0.01	17330.6 ± 172.6
3902785109124370432	3813 ± 30	4.68 ± 0.02	-	0.567 ± 0.014	0.571 ± 0.010	8.43 ± 0.01	10831.2 ± 107.8
2611163717366876544	3828 ± 30	4.70 ± 0.02	-0.15	0.557 ± 0.014	0.554 ± 0.009	8.62 ± 0.01	9063.8 ± 90.2
2653762573103102592	3831 ± 30	4.65 ± 0.02	0.06	0.591 ± 0.015	0.604 ± 0.010	8.72 ± 0.01	8284.3 ± 82.4
1814070838668707840	3859 ± 30	4.61 ± 0.03	-	0.604 ± 0.016	0.634 ± 0.017	9.06 ± 0.01	6068.2 ± 60.6
5006921282807193856	3860 ± 30	4.74 ± 0.02	-0.31	0.538 ± 0.013	0.520 ± 0.008	9.38 ± 0.01	4514.1 ± 44.9
2702655587447223168	3866 ± 30	4.64 ± 0.02	0.02	0.599 ± 0.015	0.611 ± 0.010	9.29 ± 0.01	4900.3 ± 48.8
1244644727396803584	3888 ± 30	4.80 ± 0.02	-0.50	0.499 ± 0.012	0.470 ± 0.007	8.66 ± 0.01	8747.3 ± 87.1

Table B.3: – *continued*

Gaia DR2	$T_{\rm eff}$ (K)	$\log g$	[Fe/H]	M ($M_\odot$)	$R_\star$ ($R_\odot$)	$m_{\rm bol}$	$f_{\rm bol}$ (10^{-12} ergs s^{-1} cm^{-2})
301785537751949824	3948 ± 30	4.64 ± 0.02	0.12	0.619 ± 0.015	0.624 ± 0.010	9.13 ± 0.01	5640.6 ± 56.2
5134635708766250752	3958 ± 30	4.66 ± 0.02	0.03	0.608 ± 0.015	0.605 ± 0.009	7.70 ± 0.01	21175.6 ± 211.0
3339921875389105152	3974 ± 30	4.66 ± 0.02	-0.06	0.605 ± 0.015	0.605 ± 0.009	7.75 ± 0.01	20128.4 ± 200.4
2533723464155234176	4030 ± 30	4.68 ± 0.02	-	0.602 ± 0.015	0.591 ± 0.011	9.64 ± 0.01	3540.0 ± 35.3
5077642283022422656	4033 ± 30	4.64 ± 0.02	-0.07	0.617 ± 0.015	0.622 ± 0.009	9.18 ± 0.01	5410.4 ± 54.0
3689602277083844480	4044 ± 30	4.62 ± 0.02	0.10	0.638 ± 0.016	0.648 ± 0.010	7.37 ± 0.01	28564.9 ± 284.8
4375233191015944192	4064 ± 30	4.55 ± 0.03	-0.36	0.611 ± 0.043	0.682 ± 0.010	6.54 ± 0.01	61522.8 ± 614.6
2815543034682035840	4132 ± 30	4.66 ± 0.02	-0.12	0.625 ± 0.015	0.613 ± 0.009	9.27 ± 0.01	4998.8 ± 49.8
3057712188691831936	4154 ± 30	4.66 ± 0.02	-0.13	0.627 ± 0.015	0.616 ± 0.009	7.97 ± 0.01	16501.3 ± 164.5
145421309108301184	4157 ± 30	4.61 ± 0.02	0.08	0.656 ± 0.016	0.668 ± 0.010	7.30 ± 0.01	30485.1 ± 304.2
3630092241022731136	4325 ± 30	4.61 ± 0.02	-	0.665 ± 0.016	0.669 ± 0.009	8.43 ± 0.01	10747.0 ± 107.2
6288325222245417856	4403 ± 30	4.58 ± 0.02	-0.04	0.685 ± 0.017	0.699 ± 0.010	7.44 ± 0.01	26824.7 ± 267.3
6391176735363140480	4408 ± 30	4.60 ± 0.02	-	0.678 ± 0.017	0.686 ± 0.010	7.59 ± 0.01	23309.6 ± 232.2
4364527594192166400	4409 ± 30	4.66 ± 0.02	-	0.655 ± 0.016	0.628 ± 0.009	7.03 ± 0.01	39249.2 ± 391.7
1736838805468812160	4419 ± 30	4.58 ± 0.02	-	0.685 ± 0.017	0.699 ± 0.010	7.57 ± 0.01	23790.6 ± 237.7
3011648664439643520	4433 ± 30	4.72 ± 0.02	-	0.621 ± 0.015	0.568 ± 0.008	10.01 ± 0.01	2513.1 ± 25.0
3661492609484469504	4469 ± 30	4.58 ± 0.02	-	0.691 ± 0.017	0.708 ± 0.010	8.56 ± 0.01	9562.0 ± 95.2
3550084490721711872	4502 ± 30	4.61 ± 0.02	-	0.674 ± 0.017	0.671 ± 0.009	9.32 ± 0.01	4744.6 ± 47.3
4871271406553197184	4517 ± 30	4.63 ± 0.02	-	0.670 ± 0.016	0.660 ± 0.009	9.55 ± 0.01	3842.3 ± 38.3
4706630501049679744	4529 ± 30	4.67 ± 0.02	-	0.653 ± 0.016	0.617 ± 0.008	7.92 ± 0.01	17249.1 ± 171.8
6232511606838403968	4548 ± 30	4.53 ± 0.03	-	0.721 ± 0.045	0.763 ± 0.010	5.22 ± 0.01	207838.3 ± 2069.6
3210731015767419520	4554 ± 30	4.58 ± 0.02	-	0.700 ± 0.018	0.712 ± 0.010	7.07 ± 0.01	37634.1 ± 375.1
5170039502144332800	4571 ± 30	4.54 ± 0.02	-	0.720 ± 0.021	0.756 ± 0.010	7.30 ± 0.01	30580.6 ± 305.1
3256334497479041024	4576 ± 30	4.61 ± 0.02	-	0.686 ± 0.017	0.681 ± 0.009	7.51 ± 0.01	25118.9 ± 250.2
5378886891122066560	4611 ± 30	4.66 ± 0.02	-	0.664 ± 0.016	0.634 ± 0.008	7.25 ± 0.01	32106.9 ± 319.6
6143175840404555008	4612 ± 30	4.57 ± 0.02	-	0.706 ± 0.019	0.724 ± 0.010	7.90 ± 0.01	17587.4 ± 175.1
6604147121141267712	4636 ± 30	4.61 ± 0.03	-	0.690 ± 0.042	0.677 ± 0.009	5.95 ± 0.01	105643.6 ± 1053.2
3520548825260557312	4667 ± 30	4.70 ± 0.02	-	0.642 ± 0.016	0.589 ± 0.008	9.00 ± 0.01	6412.7 ± 63.8
6412595290592307840	4670 ± 30	4.57 ± 0.03	-	0.685 ± 0.041	0.711 ± 0.009	4.22 ± 0.01	523617.3 ± 5227.6
19316224572460416	4808 ± 30	4.53 ± 0.03	-	0.724 ± 0.043	0.765 ± 0.010	5.42 ± 0.01	172178.2 ± 1715.9
3057712223051571200	4917 ± 30	4.56 ± 0.02	-	0.729 ± 0.022	0.739 ± 0.009	6.85 ± 0.01	46403.6 ± 463.8
2552925644460225152	5011 ± 30	4.57 ± 0.03	-	0.702 ± 0.048	0.717 ± 0.009	5.44 ± 0.01	169339.3 ± 1688.1

Table B.4: Stellar pairs and primary [Fe/H] used for photometric [Fe/H] relation

Gaia DR2 ID (s)	$B_P - R_P$	*Gaia* DR2 ID (p)	[Fe/H] ref	[Fe/H] adopted
853820948481913472	1.66	853819947756949120	Valenti & Fischer 2005	−0.07 ± 0.03
3057712188691831936	1.71	3057712223051571200	Valenti & Fischer 2005	0.07 ± 0.03
3732696295305334016	1.73	3732696398384550400	Mann et al. 2013c	−0.57 ± 0.03
3999917031474342016	1.94	3999916962754865152	Ramírez et al. 2007	−0.72 ± 0.05
3936909723803146496	2.03	3936909723803146368	Mann et al. 2013c	−0.12 ± 0.03
3266980243936341248	2.04	3266980170921153920	Mann et al. 2013c	−0.92 ± 0.03
4364480521350598144	2.18	4364527594192166400	Valenti & Fischer 2005	−0.41 ± 0.03
2719475542667351552	2.26	2719475542666622976	Valenti & Fischer 2005	−0.22 ± 0.03
3131777319158582272	2.26	3131777319158581376	Valenti & Fischer 2005	0.25 ± 0.03
3239548631415741440	2.29	3239548665775613056	Valenti & Fischer 2005	0.05 ± 0.03
4584638930036248192	2.32	4584639307993378432	Valenti & Fischer 2005	−0.06 ± 0.03
3101920046552857728	2.33	3101923001490347392	Valenti & Fischer 2005	0.14 ± 0.03
3219851121121855872	2.40	3219847066672970368	Valenti & Fischer 2005	0.45 ± 0.03
4662917874454254 08	2.43	4662942957063417 60	da Silva et al. 2011	−0.25 ± 0.03
1982947131682334848	2.49	1982946891164168576	Valenti & Fischer 2005	0.00 ± 0.03
4303294035005560704	2.68	4303294039306246656	Valenti & Fischer 2005	0.16 ± 0.03
1603272950424941440	2.78	1603267143629157120	Valenti & Fischer 2005	0.11 ± 0.03
116037376250217984	2.83	116037204451525376	Valenti & Fischer 2005	0.28 ± 0.03
18565464288396416	2.86	19316224572460416	Valenti & Fischer 2005	−0.12 ± 0.03
4187836934609063552	2.87	4187837450005193088	Valenti & Fischer 2005	0.05 ± 0.03
1379500928055726848	2.91	1379500756257031808	Valenti & Fischer 2005	−0.69 ± 0.03
581103581886377728	2.92	581100382135253760	Valenti & Fischer 2005	0.10 ± 0.03
704966762213039488	2.99	704967037090946688	Valenti & Fischer 2005	0.31 ± 0.03
3928040341460587904	3.04	3928040444539772800	Valenti & Fischer 2005	0.08 ± 0.03
2029432043779954432	3.18	2029433521248546304	Valenti & Fischer 2005	0.21 ± 0.03
3374633977170787328	1.51	3374633977170787072	Ramírez et al. 2007	−0.96 ± 0.05
3895404602964117504	1.52	3895404602962524544	Mann et al. 2013c	−0.16 ± 0.03
238521872077340416	1.67	238521867779351296	Mann et al. 2013c	−0.01 ± 0.03
248004472671505152	1.72	248004472671281664	Mann et al. 2013c	0.20 ± 0.03
2258411902954640512	1.74	2258413380423390464	Mann et al. 2013c	0.05 ± 0.04
2586715870164766336	1.79	2586715870164766464	Mann et al. 2013c	0.10 ± 0.03
4418849515915901312	1.82	4418850954729363584	Mann et al. 2013c	−0.38 ± 0.03
686996515965961728	1.84	686996756484129664	Robinson et al. 2007	0.31 ± 0.07
2462426800883156480	1.86	2462426800883134336	Valenti & Fischer 2005	0.12 ± 0.03
3907643060733826432	1.87	3907643060733826560	Mann et al. 2013c	0.11 ± 0.03

Table B.4: – *continued*

Gaia DR2 ID (s)	$B_P - R_P$	*Gaia* DR2 ID (p)	[Fe/H] ref	[Fe/H] adopted
6272950819874104960	1.87	6272950029600121984	Mann et al. 2013c	0.15 ± 0.03
716547127913595520	1.89	716546681236997888	Casagrande et al. 2011	0.24 ± 0.08
3630359628505968640	1.89	3630359589851275008	Mann et al. 2013c	−0.14 ± 0.03
3977050728669175040	1.91	3977050728669174912	Mann et al. 2013c	0.46 ± 0.03
1960631100090155264	1.96	1960631100090155008	Robinson et al. 2007	0.03 ± 0.07
238242871001896448	1.98	238195901239543424	Casagrande et al. 2011	−0.40 ± 0.08
1602355133093554560	2.00	1602402034136426752	Casagrande et al. 2011	−0.17 ± 0.08
263916742385357056	2.07	263916708025623680	Valenti & Fischer 2005	0.19 ± 0.03
937667952870488704	2.07	937667952870489856	Mann et al. 2013c	−0.26 ± 0.03
3419636575776307072	2.10	3419824248667573248	Casagrande et al. 2011	−0.03 ± 0.08
3120524882802287616	2.12	3120526738228080256	Mann et al. 2013c	−0.54 ± 0.03
1760208512800938752	2.14	1760204939386236288	Mann et al. 2013c	−0.38 ± 0.03
4595996885151094784	2.15	4595997263108222592	Mann et al. 2013c	−0.05 ± 0.03
3912817529956869248	2.17	3912817907913991424	Mann et al. 2013c	−0.12 ± 0.03
1583101688058584320	2.18	1583101791137799552	Mann et al. 2013c	−0.54 ± 0.03
438829835272390784	2.19	438829629113960704	Valenti & Fischer 2005	0.06 ± 0.03
4549331996760861696	2.20	4549335123497064576	Mann et al. 2013c	−0.09 ± 0.03
1518618835782597888	2.21	1518617358313845888	Mann et al. 2013c	−0.05 ± 0.03
1896261153909224064	2.23	1896449200461155712	Robinson et al. 2007	0.21 ± 0.07
3661352765349351552	2.23	3661352692334448128	Mann et al. 2013c	−0.03 ± 0.03
4471250556472775296	2.23	4471250556472774400	Mann et al. 2013c	−0.66 ± 0.03
1612283585653429632	2.26	1612283585653429760	Mann et al. 2013c	0.09 ± 0.03
769364814652674944	2.28	769365192609825920	Mann et al. 2013c	−0.09 ± 0.03
2517386203182257792	2.44	2517384485195421 44	Ramírez et al. 2007	−0.28 ± 0.05
1391673002811376512	2.45	1391679909118786176	Mann et al. 2013c	−0.09 ± 0.03
1034999982042706048	2.53	1035000055055287680	Mishenina et al. 2004	−0.16 ± 0.07
3223332136283271296	2.53	3223331006703460352	Bean et al. 2006a	0.17 ± 0.06
2383483242516852864	2.66	2383423025770192 64	Mann et al. 2013c	−0.04 ± 0.08
1416123117756120960	2.82	1416124285987232256	Mann et al. 2013c	−0.12 ± 0.03
2005804153064109056	2.85	2005798350576886144	Fuhrmann 2008	0.04 ± 0.05
3641698032930553088	3.00	3641697998570813952	Valenti & Fischer 2005	0.56 ± 0.03
1240498400329095168	3.11	1240498331609669120	Ramírez et al. 2007	−0.50 ± 0.05
2669364200719508352	3.30	2669361142702790272	Valenti & Fischer 2005	0.16 ± 0.03
2411728182287010816	2.26	HD 219617	Ramírez et al. 2007	−1.28 ± 0.17

Table B.5: Nonlinear limb darkening coefficients from Claret (2017)

TIC	a_1	a_2	a_3	a_4
410153553	1.479	0.174	-0.928	0.472
200322593	1.863	-1.754	1.264	-0.374
92226327	1.589	-1.152	0.657	-0.152
259962054	1.558	-1.100	0.609	-0.135
348538431	3.672	-5.444	4.411	-1.347
369327947	3.002	-4.406	3.796	-1.249
141608198	3.261	-4.842	4.096	-1.317
231702397	2.803	-4.078	3.570	-1.193
98796344	3.066	-4.665	4.129	-1.389
36724087	2.629	-3.737	3.274	-1.098
158588995	2.422	-3.290	2.861	-0.957
153065527	2.601	-3.685	3.229	-1.084
307210830	2.917	-4.373	3.869	-1.302
429358906	2.508	-3.496	3.058	-1.026
118327550	2.512	-3.520	3.087	-1.037
300710077	2.591	-3.694	3.251	-1.094
35009898	2.322	-3.115	2.715	-0.911
231728511	2.454	-3.408	2.989	-1.005
413248763	2.640	-3.809	3.361	-1.132
260708537	2.400	-3.297	2.889	-0.971
150428135	2.357	-3.205	2.804	-0.942
27649847	2.366	-3.226	2.823	-0.949
370133522	2.431	-3.373	2.963	-0.997
406941612	2.336	-3.170	2.775	-0.933
259377017	2.574	-3.683	3.252	-1.096
77156829	2.665	-3.881	3.435	-1.159
220479565	3.015	-4.772	4.370	-1.504
415969908	3.485	-5.854	5.429	-1.879
141527579	3.547	-6.087	5.725	-1.999
34068865	3.662	-6.356	5.990	-2.094
29960110	3.689	-6.433	6.079	-2.128
73649615	4.178	-7.459	7.019	-2.441
260004324	4.342	-7.781	7.298	-2.530
262530407	4.247	-7.630	7.197	-2.506
271596225	4.525	-8.332	7.922	-2.774
149788158	4.088	-7.396	7.057	-2.480
425934411	2.687	-4.134	3.849	-1.335
54962195	3.532	-6.228	5.993	-2.122
12423815	3.393	-5.919	5.699	-2.020
296739893	3.399	-5.934	5.715	-2.025
151825527	3.103	-5.267	5.074	-1.801
237920046	3.637	-6.480	6.246	-2.214
219195044	4.137	-7.619	7.353	-2.604
234994474	1.670	-1.949	1.810	-0.638
33521996	2.284	-3.134	2.788	-0.929
374829238	1.984	-2.556	2.312	-0.791
44737596	2.149	-2.875	2.575	-0.868

Table B.5: – *continued*

TIC	a_1	a_2	a_3	a_4
261257684	2.229	-3.030	2.703	-0.909
359271092	2.508	-3.569	3.149	-1.043
12421862	2.213	-3.043	2.756	-0.947
70899085	4.248	-6.917	5.904	-1.852
55488511	3.742	-5.936	5.088	-1.606
219229644	3.596	-5.652	4.851	-1.531
192826603	2.617	-3.752	3.269	-1.051
32497972	1.823	-2.211	1.985	-0.657
144700903	1.418	-1.431	1.340	-0.460
351601843	2.120	-2.828	2.532	-0.833
362249359	3.216	-5.021	4.415	-1.413
237914496	4.173	-7.011	6.189	-1.989
170849515	5.144	-9.201	8.292	-2.710
220459976	5.150	-9.182	8.248	-2.685
100608026	5.481	-10.069	9.214	-3.059
322063810	5.019	-9.160	8.444	-2.812
44647437	3.271	-5.739	5.574	-1.926
261108236	2.771	-4.830	4.877	-1.733
37749396	3.184	-5.778	5.803	-2.064
165317334	2.436	-4.170	4.313	-1.549
179985715	3.242	-6.008	6.095	-2.182
33831980	2.889	-5.229	5.357	-1.921
141527965	1.202	-1.424	1.681	-0.610
229111835	1.276	-1.586	1.836	-0.661
36734222	1.383	-1.809	2.038	-0.725
254113311	1.652	-2.370	2.551	-0.888
219338557	1.617	-2.234	2.373	-0.821
50618703	1.580	-2.170	2.328	-0.808
440887364	1.619	-2.285	2.461	-0.854
101948569	1.667	-2.443	2.644	-0.919
167600516	1.535	-2.143	2.353	-0.820
210873792	1.578	-2.258	2.474	-0.863
19025965	1.692	-2.547	2.774	-0.969
251848941	1.576	-2.286	2.519	-0.882
14165625	1.748	-2.745	3.007	-1.057
38510224	1.616	-2.431	2.685	-0.943
62483237	1.707	-2.645	2.897	-1.016
158297421	1.728	-2.685	2.923	-1.021
175532955	1.767	-2.777	3.012	-1.051
280437559	1.877	-3.038	3.280	-1.147
260417932	1.864	-3.025	3.277	-1.147
201642601	1.870	-3.048	3.303	-1.157
122613513	1.804	-2.898	3.163	-1.111
201248411	3.659	-6.702	6.491	-2.171
193641523	4.062	-7.523	7.206	-2.398

Table B.6: Summary of literature properties for already confirmed planets

TOI	TIC	Name	$R_P/R_\star$	$a/R_\star$	i (°)	R_P ($R_\oplus$)	Reference
122.01	231702397	TOI 122 b	$0.07500^{+0.00300}_{-0.00300}$	$25.20^{+1.50}_{-1.50}$	$88.40^{+0.60}_{-0.40}$	$2.720^{+0.180}_{-0.180}$	Waalkes et al. (2020)
129.01	201248411	HIP 65A b	$0.28700^{+0.08800}_{-0.06800}$	$5.29^{+0.05}_{-0.04}$	$77.18^{+0.92}_{-1.00}$	$22.800^{+6.800}_{-5.500}$	Nielsen et al. (2020)
136.01	410153553	LHS 3844 b	$0.06350^{+0.00090}_{-0.00090}$	$7.11^{+0.03}_{-0.03}$	$88.50^{+0.51}_{-0.51}$	$1.303^{+0.022}_{-0.022}$	Vanderspek et al. (2019)
175.01	307210830	L 98-59 c	$0.03960^{+0.00110}_{-0.00080}$	$22.50^{+1.10}_{-1.40}$	$89.30^{+0.40}_{-0.50}$	$1.350^{+0.080}_{-0.070}$	Kostov et al. (2019)
175.02	307210830	L 98-59 d	$0.04620^{+0.00300}_{-0.00360}$	$37.40^{+1.10}_{-1.20}$	$88.50^{+0.20}_{-0.50}$	$1.570^{+0.140}_{-0.140}$	Kostov et al. (2019)
175.03	307210830	L 98-59 b	$0.02340^{+0.00090}_{-0.00080}$	$16.20^{+0.80}_{-1.00}$	$88.70^{+0.80}_{-0.70}$	$0.800^{+0.050}_{-0.050}$	Kostov et al. (2019)
178.01	251848941	TOI-178 d	$0.03623^{+0.00087}_{-0.00091}$	$19.57^{+0.47}_{-0.49}$	$88.58^{+0.20}_{-0.18}$	$2.572^{+0.075}_{-0.078}$	Leleu et al. (2021)
178.02	251848941	TOI-178 g	$0.04040^{+0.00190}_{-0.00180}$	$42.13^{+1.01}_{-1.06}$	$88.82^{+0.04}_{-0.05}$	$2.870^{+0.140}_{-0.130}$	Leleu et al. (2021)
178.03	251848941	TOI-178 e	$0.03110^{+0.00110}_{-0.00120}$	$25.87^{+0.62}_{-0.65}$	$88.71^{+0.16}_{-0.13}$	$2.207^{+0.088}_{-0.090}$	Leleu et al. (2021)
-	251848941	TOI-178 b	$0.01623^{+0.00097}_{-0.00097}$	$8.61^{+0.21}_{-0.22}$	$88.80^{+0.80}_{-1.30}$	$1.152^{+0.073}_{-0.070}$	Leleu et al. (2021)
-	251848941	TOI-178 c	$0.02350^{+0.00150}_{-0.00130}$	$12.23^{+0.29}_{-0.31}$	$88.40^{+1.10}_{-1.60}$	$1.669^{+0.114}_{-0.099}$	Leleu et al. (2021)
-	251848941	TOI-178 f	$0.03220^{+0.00140}_{-0.00140}$	$34.33^{+0.82}_{-0.87}$	$88.72^{+0.07}_{-0.07}$	$2.287^{+0.108}_{-0.110}$	Leleu et al. (2021)
237.01	305048087	TOI 237 b	$0.06200^{+0.00200}_{-0.00200}$	$34.70^{+2.90}_{-2.90}$	$89.50^{+0.40}_{-0.60}$	$1.440^{+0.120}_{-0.120}$	Waalkes et al. (2020)
256.02	92226327	LHS 1140 c	$0.05486^{+0.00013}_{-0.00013}$	$26.57^{+0.05}_{-0.05}$	$89.92^{+0.06}_{-0.09}$	$1.282^{+0.024}_{-0.024}$	Ment et al. (2019)
270.01	259377017	TOI-270 c	$0.05825^{+0.00079}_{-0.00058}$	$27.01^{+0.60}_{-1.58}$	$89.53^{+0.30}_{-0.42}$	$2.420^{+0.130}_{-0.130}$	Günther et al. (2019)
270.02	259377017	TOI-270 d	$0.05143^{+0.00074}_{-0.00074}$	$41.56^{+0.70}_{-0.83}$	$89.69^{+0.16}_{-0.12}$	$2.130^{+0.120}_{-0.120}$	Günther et al. (2019)
270.03	259377017	TOI-270 b	$0.03000^{+0.00150}_{-0.00110}$	$17.48^{+1.49}_{-3.24}$	$88.65^{+0.85}_{-1.40}$	$1.247^{+0.089}_{-0.083}$	Günther et al. (2019)
442.01	70899085	LP 714-47 b	$0.07510^{+0.00090}_{-0.00090}$	$15.90^{+1.00}_{-0.70}$	$87.30^{+0.20}_{-0.20}$	$4.700^{+0.300}_{-0.300}$	Dreizler et al. (2020)
455.01	98796344	LTT 1445 A b	$0.04580^{+0.00120}_{-0.00110}$	$29.60^{+2.60}_{-2.50}$	$89.40^{+0.41}_{-0.46}$	$1.380^{+0.130}_{-0.120}$	Winters et al. (2019)
468.01	33521996	HATS-6 b	$0.17978^{+0.00077}_{-0.00077}$	$13.65^{+0.15}_{-0.15}$	$88.21^{+0.09}_{-0.09}$	$11.190^{+0.210}_{-0.210}$	Hartman et al. (2015)
551.01	192826603	NGTS-1 b	$0.23900^{+0.10000}_{-0.05400}$	$12.20^{+0.70}_{-0.70}$	$85.27^{+0.02}_{-0.01}$	$14.900^{+6.800}_{-3.700}$	Bayliss et al. (2018)
562.01	413248763	GJ 357 b	$0.03310^{+0.00090}_{-0.00090}$	$22.31^{+0.76}_{-0.90}$	$89.12^{+0.37}_{-0.31}$	$1.217^{+0.084}_{-0.083}$	Luque et al. (2019)
656.01	36734222	WASP-43 b	$0.15880^{+0.00400}_{-0.00400}$	$4.97^{+0.14}_{-0.14}$	$82.11^{+0.09}_{-0.09}$	$11.280^{+0.190}_{-0.190}$	Esposito et al. (2017)
700.01	150428135	TOI-700 c	$0.05740^{+0.00320}_{-0.00260}$	$47.80^{+2.70}_{-2.60}$	$88.90^{+0.08}_{-0.11}$	$2.630^{+0.240}_{-0.230}$	Gilbert et al. (2020)
700.02	150428135	TOI-700 d	$0.02620^{+0.00140}_{-0.00150}$	$84.00^{+4.70}_{-4.60}$	$89.73^{+0.15}_{-0.12}$	$1.190^{+0.110}_{-0.110}$	Gilbert et al. (2020)
700.03	150428135	TOI-700 b	$0.02210^{+0.00110}_{-0.00120}$	$34.80^{+1.90}_{-1.90}$	$89.67^{+0.23}_{-0.32}$	$1.010^{+0.094}_{-0.087}$	Gilbert et al. (2020)
1067.01	201642601	HATS-48 A b	$0.11480^{+0.00200}_{-0.00200}$	$11.33^{+0.05}_{-0.05}$	$89.58^{+0.18}_{-0.18}$	$8.970^{+0.170}_{-0.170}$	Hartman et al. (2020)
1073.01	158297421	HATS-47 b	$0.17460^{+0.00140}_{-0.00140}$	$13.98^{+0.15}_{-0.15}$	$87.08^{+0.06}_{-0.06}$	$12.520^{+0.160}_{-0.160}$	Hartman et al. (2020)
1130.01	254113311	TOI-1130 b	$0.04860^{+0.00111}_{-0.00090}$	$13.75^{+0.31}_{-0.27}$	$87.98^{+0.86}_{-0.46}$	$3.650^{+0.100}_{-0.100}$	Huang et al. (2020)
1130.02	254113311	TOI-1130 c	$0.21800^{+0.03700}_{-0.02900}$	$22.21^{+0.50}_{-0.43}$	$87.43^{+0.16}_{-0.16}$	$16.800^{+3.000}_{-2.500}$	Huang et al. (2020)